

SAND REPORT

SAND2002-3743
Unlimited Release
November 2002

Predicting Function of Biological Macromolecules: A Summary of LDRD activities - Project 10746

PIs: Laura JD Frink and Mark Stevens, Sandia

Co-Authors:

Susan Rempe, Paul Crozier, Shawn Means, Marcus Martin, Mark Sears, Harry Hjalmarson, Sandia

Collaborators:

Frank van Swol, Andrew Salinger, John Shadid, Sandia

Martha Mitchell, New Mexico State University

Henry S. Ashbaugh, D. Asthagiri, and Lawrence R. Pratt, Los Alamos

Joanne N. Bright, Jan Hoh, and Thomas B. Woolf, Johns Hopkins University

Itamar Borukhov, Kun-Chun Lee, Fobijn F. Bruinsma, William M. Gelbart, and

Andrea J. Liu UCLA

R.P. Joshi, Old Dominion University

Prepared by

Sandia National Laboratories

Albuquerque, New Mexico 87185 and Livermore, California 94550

Sandia is a multiprogram laboratory operated by Sandia Corporation, a Lockheed Martin Company, for the United States Department of Energy under Contract DE-AC04-94AL85000.

Approved for public release; further dissemination unlimited.



Sandia National Laboratories

NOTICE: This report was prepared as an account of work sponsored by an agency of the United States Government. Neither the United States Government, nor any agency thereof, nor any of their employees, nor any of their contractors, subcontractors, or their employees, make any warranty, express or implied, or assume any legal liability or responsibility for the accuracy, completeness, or usefulness of any information, apparatus, product, or process disclosed, or represent that its use would not infringe privately owned rights. Reference herein to any specific commercial product, process, or service by trade name, trademark, manufacturer, or otherwise, does not necessarily constitute or imply its endorsement, recommendation, or favoring by the United States Government, any agency thereof, or any of their contractors or subcontractors. The views and opinions expressed herein do not necessarily state or reflect those of the United States Government, any agency thereof, or any of their contractors.

Printed in the United States of America. This report has been reproduced directly from the best available copy.

Available to DOE and DOE contractors from
U.S. Department of Energy
Office of Scientific and Technical Information
P.O. Box 62
Oak Ridge, TN 37831

Telephone: (865) 576-8401
Facsimile: (865) 576-5728
E-Mail: reports@adonis.osti.gov
Online ordering: <http://www.doe.gov/bridge>

Available to the public from
U.S. Department of Commerce
National Technical Information Service
5285 Port Royal Rd
Springfield, VA 22161

Telephone: (800) 553-6847
Facsimile: (703) 605-6900
E-Mail: orders@ntis.fedworld.gov
Online ordering: <http://www.ntis.gov/ordering.htm>



Predicting Function of Biological Macromolecules: A Summary of LDRD activities - Project 10746

Laura Frink, Susan Rempe, and Shawn Means
Computational Biology Department

Mark Stevens, Paul Crozier, Marcus Martin, Mark Sears, and Harry Hjalmarson
Computational Materials and Molecular Biology Department

Sandia National Laboratories
P.O. Box 5800
Albuquerque, NM 87185-0316

Abstract

This LDRD project has involved the development and application of Sandia's massively parallel materials modeling software to several significant biophysical systems. We have been successful in applying the molecular dynamics code LAMMPS to modeling DNA, unstructured proteins, and lipid membranes. We have developed and applied a coupled transport-molecular theory code (Tramonto) to study ion channel proteins with gramicidin A as a prototype. We have used the Towhee configurational bias Monte-Carlo code to perform rigorous tests of biological force fields. We have also applied the MP-Salsa reacting-diffusion code to model cellular systems. Electroporation of cell membranes has also been studied, and detailed quantum mechanical studies of ion solvation have been performed. In addition, new molecular theory algorithms have been developed (in FasTram) that may ultimately make protein solvation calculations feasible on workstations. Finally, we have begun implementation of a combined molecular theory and configurational bias Monte-Carlo code. We note that this LDRD has provided a basis for several new internal (e.g. several new LDRD) and external (e.g. 4 NIH proposals and a DOE/Genomes to Life) proposals.

Contents

1	Executive Summary	5
2	Solvation of Proteins and Ions	8
	Applying the statistical mechanics of inhomogeneous fluids to protein solvation I: A theoretical framework	8
	Hydration of Krypton and Consideration of Clathrate Models of Hydrophobic Effects from the Perspective of Quasi-Chemical Theory	24
3	Ion Transport Proteins	46
	Applying the statistical mechanics of inhomogeneous fluids to protein solvation II: Gramicidin A as a test case	46
4	Interactions and Assembly of Solvated Macromolecules	58
	Simulations of single grafted polyelectrolyte chains: ssDNA and dsDNA	58
	Simple simulations of DNA condensation	70
	Towards understanding the function of unstructured proteins: simulations of charged polymers under confinement	89
	Association of two semiflexible polyelectrolytes by interchain linkers: Theory and simulations	110
	Interactions and assembly of simple solvated polymers models	119
5	Biological Membranes	126
	Coarse-grained models and simulations of bilayer membranes	126
	Electroporation	134
6	Cell Modeling	136
	Intracellular Calcium Dynamics Modeling with Unstructured Finite Element Solution Methods	136
7	Development of Computational Tools	149
	Applying molecular theory to steady-state diffusing systems	149
	Comparison of the Amber, Charmm, Compass, Gromos, OPLS-aa, and TraPPE-UA force fields for the prediction of liquid densities and vapor-liquid coexistence for small organics	167
	A new efficient method for density functional theory calculations of inhomogeneous fluids	178

Predicting Function of Biological Macromolecules: A Summary of LDRD activities - Project 10746

1 Executive Summary

In this summary, we provide a brief sketch of the work performed in this project along with significant findings of that work. All the supporting documentation is included in the following sections. Many different systems were studied in this project because the goal of this project was to develop biophysical modeling expertise at Sandia. Furthermore, since Sandia has a variety of unique computing capabilities utilizing massively parallel computers, the secondary goal was to leverage those tools to solve hard biophysics problems. Along the way there have been 5 publications published 7 publications accepted or submitted. There are also at least 5 additional manuscripts in preparation at the time of this report. Furthermore, this project has been heavily leveraged to further develop computational biology programs at Sandia.

One major scientific effort of this project has been to develop and demonstrate a unique capability for modeling ion channel proteins. We chose to concentrate on gramicidin A which is a small dimer polypeptide with a known high resolution crystal structure. Ion channel proteins in general are very significant biologically because they control ion concentrations levels in cells, and so control the physiological functioning of many cells. Gramicidin A is smaller and simpler than most ion channel proteins, but it is an important test case both because there is a great deal of experimental data published. In addition, the sensor and materials groups at Sandia (Brozik, 1744 and Brinker, 1846) are currently studying Gramicidin A as a stepping stone to building synthetic biomimetic membranes.

The primary tool with which we chose to study ion channels was the molecular theory code Tramonto. This code had previously been built to study solvation, wetting, and phase transitions of inhomogeneous fluids near complex (2 and 3-dimensional) surfaces. In order to apply the code to study protein solvation, it was necessary to be able to describe a "surface" as the atomic coordinates and charge distribution on a given protein. This type of description needed to be based on a suitable biological force field. Therefore, a detailed investigation of various biological force fields was undertaken. Those investigations showed that the Charmm force fields do the best job of reproducing liquid-vapor equilibria for the various methyl capped side chains found in amino acids. Currently all the major biological force fields are available to all of our molecular simulation and theory codes. In addition to force fields, it was necessary to develop a nonequilibrium molecular theory capability to study ion channels. We implemented a spatially varying chemical potential field along with a simple diffusion equation, and performed several detailed studies comparing grand canonical molecular dynamics predictions for diffusion through simple membranes and in various mixtures to the nonequilibrium molecular theory predictions. These calculations demonstrated the feasibility of the nonequilibrium molecular theory approach needed for studying transport through ion channel proteins and addressing patch-clamp experiments that measure ion current through those proteins as a function of applied voltage. One common way to analyze patch clamp experiments

is to develop transition state (or barrier) models for ion transport through channels. One key quantity in such models is the free energy landscape in and around a channel. In statistical mechanics, this quantity is the potential of mean force (PMF). We have developed a firm statistical mechanical basis for computing the potentials of mean force in these systems that can be generalized to any molecular fluid model of interest.

Finally, we performed extensive initial calculations on the gramicidin A channel both in equilibrium and with applied electrostatic potentials across a membrane. We computed potentials of mean force down the channel in both circumstances for both a Poisson-Boltzmann model electrolyte and an explicit 3-component model electrolyte where the ions and the dense solvent all had a finite size. We found that for this system the electrostatic effects dominated packing effects, and so the Poisson-Boltzmann model did a surprisingly good job capturing binding sites and free energy barriers. It became clear with these investigations that two critical pieces of science will be needed for further application of molecular theory tools to simulation of protein systems including ion channels. The first is a more accurate treatment of electrolytes. We plan to perform detailed quantum mechanical studies to pursue these developments, and have hired a new staff member (S. Rempe) to pursue the project. The second critical need is for faster molecular theory algorithms. The real space algorithms developed in the Tramonto code are capable of treating small proteins in large parallel computers. However the ultimate goal will be to treat proteins routinely on workstation platforms. Therefore, we have developed an entirely different algorithmic strategy for solving these systems of equations that we have shown to scale nearly linearly with system size.

This project was also used to study interactions and assembly of biological macromolecules. This work was primarily performed using the LAMMPS code. Simple coarse-grained models were developed to treat DNA, unstructured proteins and lipids. This comprises three of the four major biomolecules (polysaccharides being the fourth). For each case important outstanding problems were used to define and guide the computational research.

A major outstanding problem is "DNA condensation" which is DNA wrapping itself into toroidal structures that can fit into viral capsids and bacteria. Without this collapse of DNA, it would not fit inside a virus or a bacterial cell. The physical mechanism of DNA condensation was not understood. We showed that DNA condensation is a consequence of strong Coulomb interactions that occur in the presence of multivalent ions. More generally, we showed that the competition between the electrostatic interactions, entropy and the stiffness of the DNA determine the possible condensation structures.

In a related work, the aggregation of stiff charged biopolymers was studied in collaboration with Andrea Liu's group at UCLA. Here, the model represent various biopolymers, including actin, a fundamental fibril protein, as well as short DNA. We quantified the number of multivalent ions necessary to bind two charged biopolymers. This work is continuing on to treat multiple chain systems.

One of the major recent experimental techniques is DNA microarrays. The structure of the grafted ssDNA and dsDNA in these devices has not been well characterized. We began to study these systems initially at the single chain level. A key part of this study was the implementation of the 2-dimensional particle mesh Ewald method done by Paul Crozier. The simulations showed the correlation between the ssDNA structure and the counterion distribution. The nature of the ssDNA offers clues concerning better sensors. A collaboration with Prof. Attanosov at UNM who is developing such devices has been started.

Finally, following some work in the literature, we formulated simulations of bilayer lipids in solvent. We showed that our models self-assemble quickly into bilayer membranes. Using parallel computers we can treat system sizes not considered to date and to treat a large variety of interesting phenomena. In particular, treating the biomembrane as a dynamical object is now possible which it has not been and is known to be important. In addition, we demonstrated that we can simulate vesicles.

Again we hired a new LTE (P. Crozier) to assist with these simulations.

Finally, this project funded the start up of a new effort in cell modeling. This effort utilizes the MP-Salsa code to treat cells as a system of reaction diffusion equations. We applied MP-Salsa to calcium dynamics in excitable systems (neurons, cardiac cells, etc.). This application included exploration of spatial distributions otherwise intractable in the experimental laboratory. This project has led to funding from the National Institutes of Health and the University of Maryland for continuation of current work. An LTE (S. Means) was hired to start up this program.

2 Solvation of Proteins and Ions

Applying the statistical mechanics of inhomogeneous fluids to protein solvation I: A theoretical framework

Laura J. Douglas Frink and Frank van Swol

Abstract

Solvation is a critical problem of many biophysics applications. For example protein folding is understood to be critically dependent on interactions of different residues (e.g. hydrophobic vs. hydrophilic) with the solvent. The solvation of proteins and ligands is important to many other applications and system as well including drug and sensor design, protein crystallization, and membrane bound proteins. In this paper we outline how the statistical mechanics of inhomogeneous fluids can be applied to protein solvation. In this approach the protein is treated as a surface or external field in which the fluid must equilibrate. The result is an inhomogeneous density distribution of fluid near the protein. We outline briefly a density functional theory approach that can be used to compute the inhomogeneous density distribution. We discuss the computation of potentials of mean force, present specific potential of mean force calculations for several simple systems, demonstrate application of the theory to solvation of gramicidin A, and discuss more broadly the application of this detailed implicit solvent approach to protein simulations.

Introduction

Solvation of proteins and other biological macromolecules is critically important to their structure and function. Since these macromolecules exhibit unique functions based on specific molecular structures, it is natural to try to take a molecular modeling based approach to understanding the structure and function of proteins. However, there are many pitfalls related to the fluid phase (e.g. an electrolyte or a lipid bilayer) in which the protein is invariably suspended. Specifically, simulating the electrolyte can be quite time consuming. In addition, while an open ensemble would allow for the unknown adsorption of fluid species at the protein surface, most simulations are done with a constant number of ions. Finally, the presence of the small fluid species dictate the time scale accessible to a molecular dynamics simulation. Physical overlaps between fluid particles and large protein segments upon attempted large conformational changes make Monte-Carlo simulations of proteins difficult as well. As a result of these pitfalls, rigorous simulations of many solvated protein systems remain out of reach.

In this paper, we discuss a different approach for treating the solvation of proteins that is based on the statistical mechanics of inhomogeneous fluids. The key observation is that the fluid near a protein is not homogeneous, but rather arranges itself (from hydrogen bonding to double layers to steric ordering) in order to optimize the free energy of the system. In the past 20 years there has been a significant effort in the statistical mechanics community to develop theoretical approaches for inhomogeneous fluids. The principle applications of those approaches to date have centered on materials problems rather than biological systems. Some phenomena that have been investigated quite thoroughly include adsorption, wetting, capillary condensation (Henderson, 1992). More recently, the investigations have turned toward considering fluids near surfaces with more complex chemical patterning (Frink, 1999 and Henderson, 1999) and fluids in disordered porous media (Kierlik, 2001 and Frink, 2002). Clearly these problems are closely related to solvation of biological macromolecules, and in

this paper, we show how the statistical mechanical machinery developed to treat these other problems may also be used to treat protein solvation.

The most closely related approaches to those presented here have been employed by Lagüe et.al. in studies of interactions of membrane bound proteins (Lagüe, 2000), Im et.al. in studies of ion channel proteins (Im, 2000), and Roux and Simonson in a discussion of Implicit solvent models (Roux, 1999). These authors focus on integral equation methods for computing liquid phase structure near proteins. These integral equation theories are closely related to the density functional theory (DFT) methods discussed here.

For the purposes of this discussion, we focus on equilibrium situations where the thermodynamic state of the fluid is known. Nonequilibrium situations will be discussed in the context of ion channel proteins in another paper. We detail the theoretical approach in section II, discuss a specific molecular theory approach (Density Functional Theory, DFT) in section III, and demonstrate the calculation of potentials of mean force, PMF, for both several simple systems and for a gramicidin A channel in a 1:1 electrolyte in section IV.

Statistical Mechanics

In this section we review the statistical mechanics that underpin our computational approach. We also briefly discuss the consequences for performing simulations of biological systems with implicit solvent. In many cases, one would like to perform a simulation with a known protein or protein complex in an electrolyte solution. Since the adsorption at the protein surface for each of the fluid species (e.g. water and ions) is unknown apriori, we choose to consider a semi-grand ensemble which is open to material transport of the fluid atoms/molecules. Thus, we begin our discussion by considering an ensemble with constant $N\mu VT$ where N is the constant number of protein atoms (or surfaces) in the system and μ represents the chemical potentials of all the fluid species in the system. The configurational integral for this ensemble is

$$Z_{N\mu VT} = \int d\mathbf{R}_N e^{U(\mathbf{R}_N)} \times \left\{ \sum_{n=0}^{\infty} \frac{z^n}{n!} \int d\mathbf{r}^n e^{-\beta u(\mathbf{r}_n) - \beta V(\mathbf{r}_n, \mathbf{R}_N)} \right\} \quad (1)$$

where n is the *variable* number of fluid atoms or molecules in the system, U represents the potential energy of the interactions of static protein atoms or surfaces with one another, u represents the potential energy of the fluid-fluid interactions, and V represents the potential energy of all the interactions between the fluid and the static atoms or surfaces.

If we assume that the characteristic time of protein and surfaces motion is much slower than fluid equilibration, then the Born-Oppenheimer approximation can be expected to hold, and from the perspective of the fluid atoms the problem to be solved is fundamentally an inhomogeneous fluids problem where the protein or surfaces are *frozen* and the fluid molecules distribute themselves in response to the external field, $V(\mathbf{r})$, generated by the surfaces and/or protein atoms. The inhomogeneous density distribution, $\rho(\mathbf{r})$ in the fluid minimizes the *free energy* of the system. More specifically, we can identify the integral in the curly brackets as the grand canonical partition function for a fluid in an external field, Ξ where

$$\Xi = \sum_{n \geq 0} \frac{z^n}{(n)!} \int \dots \int e^{-(\beta U(\{\mathbf{r}_n\}) - \beta V(\{\mathbf{r}_n\}))} d\mathbf{r}_1 \dots d\mathbf{r}_n \quad (2)$$

Ξ is related to the grand potential, Ω by

$$\Omega/kT = -\ln \Xi \quad (3)$$

With this definition, Eq.1 can be rewritten in terms of a single configurational integral over the configurations of the protein atoms or surfaces

$$Z_{N\mu VT} = \int d\mathbf{R}_N e^{-\beta U(\mathbf{R}_N)} e^{-\beta \Omega(\mathbf{R}_N)}. \quad (4)$$

It is apparent from Eq. 4 that if both $\Omega(\mathbf{R}_N)$ and $U(\mathbf{R}_N)$ are known, one could perform simulations where the solvent is treated implicitly, and configurations of the proteins and/or surfaces are sampled using traditional Monte Carlo (MC), Molecular Dynamics (MD), or Brownian Dynamics (BD) methods. While MC and MD simulations with this implicit solvent will yield correct thermodynamics, BD is needed to capture the dynamics of the surfaces in the system (Friedman,1985). Frink and van Swol, demonstrated such an implicit solvent approach using Monte Carlo simulations of hard colloidal particles interacting with a detailed implicit Lennard-Jones solvent (Frink 1994). In that case a pairwise potential of mean force between colloidal particles was computed based on detailed molecular theory calculations.

More recently, Im et.al. (Im, 1999) have described an approach for performing Langevin based Brownian Dynamics coupled with Grand Canonical Monte Carlo methods for simulation of ion permeation in ion channels with open ends. In that case, ions in the pore are treated discretely, and water is treated as a dielectric continuum with random Brownian fluctuations. A multibody potential of mean force is required to capture the effects of all of the discrete ions as well as the implicit solvent field. This PMF required the solution of the Poisson-Boltzmann equation to describe the effect of the implicit electrolyte. In this paper we do not discuss simulation with implicit solvent further. Rather we point out that a central component of these implicit solvent methods is the calculation of potentials of mean force.

The potential in Eq.4 is not the most convenient form for the implicit potential. Rather, we choose a description that adds a constant to energy (thus having no effect on the relative stability of various states) in order to insure that this mean potential approaches zero when the surfaces are far apart. Thus, we write the mean potential as

$$W(r) = U(\mathbf{R}) + \Omega[\mathbf{R}, \rho(\mathbf{r})] - \Omega[\infty, \rho(\mathbf{r})]. \quad (5)$$

We note that when studying inhomogeneous fluids near fixed surfaces, it is often more convenient to compute a *surface* excess free energy, $\Omega^s = \Omega[\mathbf{R}, \rho(\mathbf{r})] - \Omega[\rho_b]$, where the bulk contribution is calculated in the absence of any surfaces. Clearly $W(r)$ in Eq.5 can be computed based on either Ω or Ω^s since the bulk contributions cancel.

A free energy route to a PMF has also been discussed by Lagüe et.al. where the interactions between membrane bound proteins were calculated by treating the lipid bilayer with liquid state theory (Lagüe, 2000). That paper centered on the Helmholtz free energy, A , and thus utilized a closed ensemble with a fixed number of fluid atoms. This is the most common ensemble for molecular dynamics simulations, but again there is some difficulty with the fact that adsorption at a protein surface (whether from lipid or from electrolytes) is not known a priori. Therefore care should always be taken to be certain that the system is large enough that the bulk fluid densities away from the surfaces or proteins is reasonably constant.

The concept of a potential of mean force is not new and derivations can be found in classic statistical mechanics texts (e.g. Hill, 1986 and Friedman, 1985) in describing the solution theory of McMillan and Mayer (McMillan, 1945) solution theory. In this approach, the pair correlation function hierarchy, is defined by

$$\rho^N g^{(N)}(\mathbf{r}_1, \mathbf{r}_2, \dots, \mathbf{r}_N) = \frac{1}{\Xi} \sum_{n \geq N} \frac{z^n}{(n - N)!} \int \dots \int e^{-U_n/kT} d\mathbf{r}_{N+1} \dots d\mathbf{r}_n \quad (6)$$

where there are N fixed atoms and $n - N$ mobile fluid atoms in the system. For open systems, the bulk density is based on the ensemble average number of particles in the system, $\langle N \rangle$, $\rho = \langle N \rangle / V$. At the level of a pair of particles, the PMF is the familiar

$$W(r) = -kT \ln g(r) \quad (7)$$

where $g(r)$ is the pair correlation function. Friedman augments this derivation by demonstrating that if one particle is fixed, and the inhomogeneous density distribution, $\rho(\mathbf{r})$ is computed around the fixed particle, the pair correlation function is

$$g(r) = \rho(r) / \rho_b \quad (8)$$

where ρ_b is the bulk density of the fluid (Friedman, 1985). Following his derivation, and taking a mixture with one species at infinite dilution with a single particle of this dilute species at a known fixed location it is straightforward to show that the PMF experienced by a fluid atom in any arbitrary external field is given by

$$W(r) = -kT \ln \rho(\mathbf{r}) / \rho_b. \quad (9)$$

In this paper we will show that Equations 5 and 48 yield the same potentials of mean force for a variety of simple systems. These simple systems serve to facilitate a clear understanding of how the methods presented here can be applied to protein solvation. Clearly this approach hinges on computing inhomogeneous density distributions for fluids in external fields in open systems. This is precisely what Density Functional Theories (DFT) for inhomogeneous fluids are designed to do (Henderson, 1992). Before presenting results, we therefore briefly describe the basic DFT we solve.

The Density Functional Approach

Overview The basic DFT approach is to construct a grand free energy functional, $\Omega[\rho(\mathbf{r})]$ that is subject to the minimization

$$\frac{\delta \Omega}{\delta \rho(\mathbf{r})} = 0. \quad (10)$$

The grand free energy for a fluid in an external field is related to the Helmholtz free energy, F , by

$$\Omega[\rho_i(\mathbf{r})]/kT = F[\rho_i(\mathbf{r})] + \sum_i \int \rho_i(\mathbf{r}) [\mu_i - V_i(\mathbf{r})]. \quad (11)$$

where i is the species index. The Helmholtz free energy, F , may be split into ideal and excess contributions, $F = F^{id} + F^{ex}$ where the ideal contribution is

$$F^{id} = \sum_i \int \rho_i(\mathbf{r}) [\ln \Lambda \rho_i(\mathbf{r}) - 1], \quad (12)$$

and where Λ is the deBroglie wavelength.

The inhomogeneous Ornstein-Zernike equation is a direct consequence of the relationship between Ω and F in Eq.11, and common integral equation closures come from making approximations to various terms in a direct correlation function hierarchy. The various terms of this heirarcy, $c^{(1)}, c^{(2)}, c^{(3)} \dots$ are simply successive derivatives of F , $\delta F / \delta \rho(\mathbf{r})$, $\delta^2 F / \delta \rho(\mathbf{r}_2) \delta \rho(\mathbf{r}_2)$, ... Thus, the connection between DFT and integral equation theories is intimate (for more details see Henderson, 1992).

Since there are exact functionals known for only a few systems, the free energy functionals used in DFT calculations are often constructed based on truncated expansion about a uniform bulk fluid. Alternatively, they can be constructed based on perturbation of a reference fluid. We have used a second order direct correlation function expansion based approach to study polymer fluids (Frischknecht, 2002), and anticipate applying that approach to membrane bound proteins; however, for this paper, we discuss a perturbation approach to treat protein solvation in electrolytes. Since the Poisson-Boltzmann (PB) electrolyte is a well understood model electrolyte that is currently one of the most detailed and expensive implicit solvents used in the biology community, we begin by placing this model within the DFT framework.

DFT for the Poisson-Boltzmann electrolyte

Taking a strict mean field approach (Henderson,1992), the excess Helmholtz free energy for the PB electrolyte needed in Eq.11 is

$$F^{ex}[\rho(\mathbf{r})] = \frac{1}{2} \sum_i \sum_j \int d\mathbf{r} \int d\mathbf{r}' \rho_i(\mathbf{r}) \rho_j(\mathbf{r}') \frac{q_i q_j}{\kappa \epsilon_0 |\mathbf{r} - \mathbf{r}'|} \quad (13)$$

where $q_i \rho_i(\mathbf{r}) = z_i e \rho_i(\mathbf{r})$ is the charge density associated with species i .

We are interested in computing solvation of large charged bodies such as proteins, so we define the external field to be composed of two parts, $V = V^c + V^h$. The coulomb part, V^c accounts for the charge distribution on the protein. The hard-core part, V^h defines the protein geometry by excluding ions from the volume that the protein occupies. More specifically

$$V^h(\mathbf{r}) = \begin{cases} \infty & \text{if } \mathbf{r} < R_S(\mathbf{r}) \\ 0 & \text{otherwise} \end{cases} \quad (14)$$

where the location of the protein/fluid interfaces is found at $R_S(\mathbf{r})$, and

$$V_i^c(\mathbf{r}) = q_i V^c(\mathbf{r}) = q_i \int d\mathbf{r}' \frac{\rho^f(\mathbf{r}')}{\kappa \epsilon_0 |\mathbf{r} - \mathbf{r}'|} \quad (15)$$

where $\rho^f(\mathbf{r})$ is the charge density of the fixed charges on the protein.

Taking the functional derivative of Eq.10 results in an Euler-Lagrange equation

$$\mu_i^\dagger / kT = \mu_i / kT - \ln \Lambda = \ln \rho_i(\mathbf{r}) + V_i(\mathbf{r}) + \sum_j \int d\mathbf{r}' \rho_j(\mathbf{r}') \frac{q_j}{\kappa \epsilon_0 |\mathbf{r} - \mathbf{r}'|} \quad (16)$$

where the chemical potential of the ideal PB electrolyte is just $\mu_i^\dagger = kT \ln \rho_i^b$.

At this point, it is convenient to define the total electrostatic potential to be

$$\phi(\mathbf{r}) = V^c(\mathbf{r}) + \sum_i \int d\mathbf{r}' \frac{q_i \rho_i(\mathbf{r}')}{\kappa \epsilon_0 |\mathbf{r} - \mathbf{r}'|} \quad (17)$$

Combining Eq.16, Eq.17 and Eq.15 leads us directly back to the well known PB distribution with volume exclusion

$$\rho_i(\mathbf{r}) = \rho_i^b e^{-\beta(V_i^h(\mathbf{r}) + z_i e \phi(\mathbf{r}))}. \quad (18)$$

In order to solve Eq.18, we also need a governing equation for the electrostatic potential, $\phi(\mathbf{r})$, and we use Poisson's equation

$$\nabla^2 \phi(\mathbf{r}) = -\frac{4\pi}{\kappa \epsilon_o} \left(\sum_i \rho_i(\mathbf{r}) + \rho^f(\mathbf{r}) \right) \quad (19)$$

where κ is a constant dielectric constant. We have also begun to implement functionals with spatially varying polarization, but that discussion is beyond the scope of this paper.

The distribution of ions about a charged surface may be solved with either Eq.16 or Eq.18 coupled with Eq.45. In the case of Eq.16, it will be necessary to perform Ewald summations if there are periodic boundary conditions in order to compute $V^c(\mathbf{r})$ and the integral over the $1/r$ unless the domain is large enough that $\rho(\mathbf{r}) = \rho_b$ (or $\phi = 0$) at the boundaries of the computational domain.

Given the inhomogeneous density and electrostatic potential distributions, $\rho_i(\mathbf{r})$ and $\phi(\mathbf{r})$, the potential of mean force experienced by any ion near the protein can be found by substituting Eq.18 into eq.48 to get

$$w_i(\mathbf{r}) = \begin{cases} \infty & \text{if } \mathbf{r} < R_S(\mathbf{r}) \\ z_i e \phi(\mathbf{r}) & \text{otherwise} \end{cases} \quad (20)$$

Finally, using the definition of the electrostatic potential in Eq.17 it is straightforward to show that the grand potential functional becomes

$$\begin{aligned} \Omega[\rho_{\{i\}}(\mathbf{r})]/kT = & \sum_i \int \rho_i(\mathbf{r}) [\ln \rho_i(\mathbf{r}) - 1] + \sum_i \int \rho_i(\mathbf{r}) [\mu_i^\dagger - V_i^h(\mathbf{r})] \\ & + \frac{1}{2} \sum_i \int d\mathbf{r} \rho_i(\mathbf{r}) q_i \phi(\mathbf{r}) + \frac{1}{2} \int \left(\sum_i \rho_i(\mathbf{r}) q_i \right) V^c(\mathbf{r}). \end{aligned} \quad (21)$$

In order to compute the PMFs from the free energy route of Eq.5, the computational box must be large enough that the ion densities are the bulk values, $\rho_i(\mathbf{r}) = \rho_b^i$, and $\phi(\mathbf{r}) = 0$ at the boundaries. Under these circumstances, the contribution to the free energy in fluid region beyond the computational domain is zero. This is obvious for the first three terms in Eq.21. For the last term it arises as a result of charge neutrality where in a bulk fluid $\sum_i q_i \rho_b^i = 0$. As a result, while $V^c(\mathbf{r})$ may be nonzero beyond the computational boundaries, the integral will be zero provided the fluid has reached the bulk densities at the boundary. Clearly the size of the required computational domain is strongly dependent on the ionic strength of the electrolyte of interest.

bGoing beyond the Poisson-Boltzmann Electrolyte with DFT

The previous section presented the familiar Poisson-Boltzmann electrolyte in the context of a variational approach. One of the strengths of this approach is that it can be extended to more sophisticated fluid models. In this section, we present the theory for an electrolyte model that includes volume exclusion and dispersion in addition to the Coulomb effects described above. Specifically, consider a potential of the form

$$u_{ij}(\mathbf{r}) = 4\epsilon_{ij} \left[\left(\frac{\sigma_{ij}}{r} \right)^{12} - \left(\frac{\sigma_{ij}}{r} \right)^6 \right] + \frac{q_i q_j}{\kappa r} \quad (22)$$

Volume exclusion and dispersion are represented by the 12-6 Lennard-Jones (LJ) contribution to the interaction potential. Interaction potentials of this type are prevalent in molecular simulations. Here we review how the LJ potential is incorporated into the DFT approach. A great deal of work in the area has been performed in the past 20 years, and the interested reader is referred to the excellent review articles found elsewhere (Henderson, 1992)

Typically, the LJ contribution to the free energy is split into hard core and attractive contributions. The hard core part of the potential can be represented in a number of ways. In one of the first DFT treatments of electrolytes, Tang. et. al. used the very successful functionals of Tarazona et.al. (Tang 1990, Tarazona 1985). However, more recently, Rosenfeld has developed some robust functionals that are accurate and of a simpler form (Rosenfeld, 1996). These features have facilitated our 3-dimensional computational implementation of the functionals. A full 3-dimensional implementation is needed to study solvated proteins because their function is related to specific three dimensional structures and charge distributions.

Returning to the excess free energy, F^{ex} , there are now three terms that correspond to the hard core, attractive dispersion, and Coulomb interactions. Specifically, we write

$$F^{ex}[\rho(\mathbf{r})] = F^c[\rho(\mathbf{r})] + F^h[\rho(\mathbf{r})] + F^a[\rho(\mathbf{r})]. \quad (23)$$

where F^c is identical to Eq.13. The hard core part of the functional is given by Rosenfeld's description. Specifically,

$$F^h[\rho(\mathbf{r})] = \int \Phi[n(\mathbf{r}), r] dr \quad (24)$$

where the free energy density, Φ , depends on the nonlocal density functions, n . These nonlocal density functions are

$$n_\gamma(\mathbf{r}) = \sum_i \int w_i^{(\gamma)}(\mathbf{r} - \mathbf{r}') \rho_i(\mathbf{r}') dr' \quad (25)$$

and weight functions, $w^{(\gamma)}$ are based on the fundamental measures (e.g. the diameter, surface area, and volume) of the particles of interest.

$$\begin{aligned} w_i^{(3)}(r) &= \theta(r - R_i) \\ w_i^{(2)}(r) &= 4\pi R_i w_i^{(1)}(r) = 4\pi R_i^2 w_i^{(0)}(r) = \delta(r - R_i) \\ \mathbf{w}_i^{(V2)}(r) &= 4\pi R_i \mathbf{w}_i^{(V1)}(r) = (\mathbf{r}/r) \delta(r - R_i). \end{aligned} \quad (26)$$

where the bold type indicates a vector, and R_i is the radius of species i .

The hard sphere free energy density Φ is given by a sum of terms, $\Phi = \Phi_s + \Phi_v$ with

$$\Phi_s = -\bar{\rho}_0 \ln(1 - \bar{\rho}_3) + \frac{\bar{\rho}_1 \bar{\rho}_2}{1 - \bar{\rho}_3}, \quad (27)$$

$$\Phi_v = -\frac{\bar{\rho}_{V1} \cdot \bar{\rho}_{V2}}{1 - \bar{\rho}_3} + \frac{1}{24\pi(1 - \bar{\rho}_3)^2} \left(\bar{\rho}_2 - \frac{\bar{\rho}_{V2} \cdot \bar{\rho}_{V2}}{\bar{\rho}_2} \right)^3. \quad (28)$$

This functional correctly treats a crossover from a 3D to a 0D fluid (Rosenfeld, 1996). Such a crossover occurs on crystallization when fluid particles are confined to a point in a 3D volume. The nonlocal nature of these functionals makes for a significant computational challenge in the application of these functionals to the three dimensional problem of protein solvation.

The attractive contribution to the free energy is again treated in a strict mean field approximation (like Eq.13), and is

$$F^{att} = \frac{1}{2} \sum_i \sum_j \int d\mathbf{r} \int d\mathbf{r}' \rho_i(\mathbf{r}) \rho_j(\mathbf{r}') u_{ij}^{LJ:a}(|\mathbf{r} - \mathbf{r}'|), \quad (29)$$

where $u_{ij}^{LJ:a}$ is attractive part of the Lennard-Jones contribution to the interaction potential in Eq.22. We apply the Weeks, Chandler, and Anderson description for $u_{ij}^{LJ:a}$ where $u_{ij}^{LJ:a} = u_{ij}^{LJ}(r_{min})$ for $r < r_{min}$ where r_{min} is the distance at which the minimum of the Lennard-Jones potential is found (Weeks, 1971). Typically we also use a cut and shifted version of the 12-6 Lennard-Jones potential where $u^{LJ:a} = u(r) - u(r_c)$ where the cutoff distance is given by r_c . Finally, we note that we set the hard sphere diameter equal to the Lennard-Jones σ for our calculations.

The Euler-Lagrange Equations that must now be solved are given by

$$\rho_i(\mathbf{r}) = \rho_i^b e^{-\beta(V_i^{NC}(\mathbf{r}) + z_i e \phi(\mathbf{r}) + \delta F^{hs}/\delta \rho_i(\mathbf{r}) + \delta F^{att}/\delta \rho_i(\mathbf{r}))}. \quad (30)$$

Clearly the potential of mean force now deviates from the simple Poisson-Boltzmann result of Eq.20. We now find that

$$W_i(r)/kT = -\beta (V_i^{NC}(\mathbf{r}) + z_i e \phi(\mathbf{r}) + \delta F^{hs}/\delta \rho_i(\mathbf{r}) + \delta F^{att}/\delta \rho_i(\mathbf{r})) \quad (31)$$

where V^{NC} is the non-coulombic part of the external field. It may include only hard core repulsions as in the previous section or it may include dispersion interactions with soft cores as would be consistent with Eq.22. Finally we note that there have been many developments in Density Functional Theories for various kinds of fluid systems. A few examples include structureless polymers, multi-site molecular fluids, rigid non-spherical fluid particles, polymers with bond constraints, electrolytes, dipolar fluids, associating fluids. Clearly different models may be important depending of the particular system being studied (e.g. a membrane bound protein vs. a solution protein). However, the underlying analysis presented here will be essentially the same for many of these cases.

Results

Finally, in this section, we present results from a variety of calculations on simple systems, and we conclude with a demonstration of the approach for the solvation of gramicidin A. We reserve a more detailed investigation of gramicidin A to another paper, and here focus on demonstrating the inhomogeneous fluids based approach outlined above. We begin by demonstrating the equivalence of the two basic routes to computing potentials of mean force given by Equations 5 and 48.

Potentials of mean force in simple neutral systems

First consider a fluid composed of a dense liquid-like hard sphere fluid. We compute the potential of mean force, PMF, between two fluid particles via the two routes suggested above. In route I, the density distribution, $\rho(\mathbf{r})$ is computed around two explicit hard sphere atoms that are treated as fixed surfaces at known positions, with separation, r . The separation is varied, and the potential of mean force, $W(r)$ is then constructed from Eq.5. In route II, only one fluid atom is treated as a surface. It is located at the origin, and

the density distribution of the fluid around it, $\rho(\mathbf{r})$, is computed. The entire PMF, $W(r)$ is then computed from this one density distribution via Eq.48. Figure 1A compares the potentials of mean force between two hard sphere atoms as calculated using these two routes. Good agreement is found, and discrepancies are due to the staircasing effect of the underlying grid.

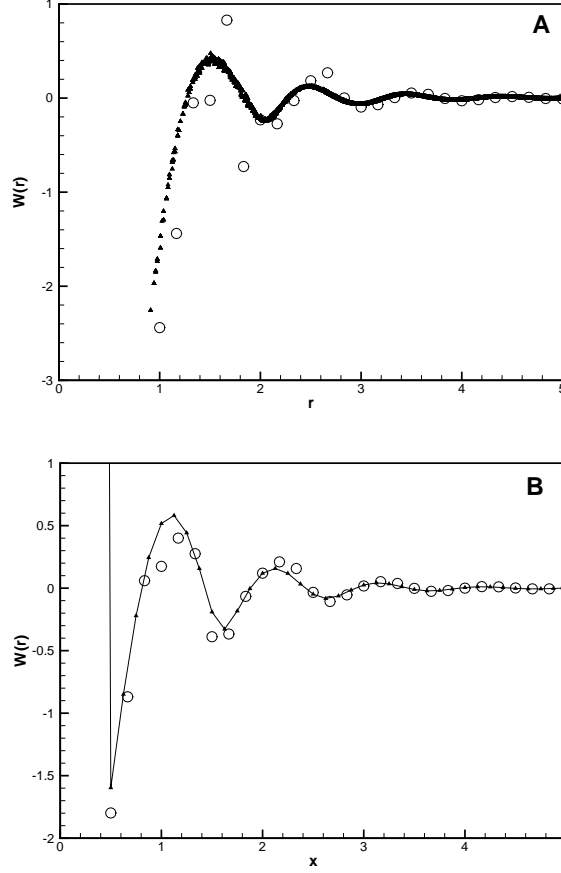


Figure 1. Potentials of mean force, $W = W/kT$ as a function of separation, $r = r/\sigma$ for two simple fluid systems. (A) is the PMF between two hard sphere atomic surfaces of diameter σ in a hard sphere fluid at a bulk density of $\rho\sigma^3 = 0.85$. (B) is the PMF between one hard sphere atom and a hard planar surface in a hard sphere fluid with a density of $\rho\sigma^3 = 0.65$. In both cases, the small filled triangles are found by computing $W(r)/kT = -\log(\rho(r)/\rho_b)$. The larger open circles are found by computing $W(r)/kT = \Omega^s(r) - \Omega^s(\infty) + U_{12}(r)$ where $U_{12}(r)$ is the interaction potential of the *surface* atoms (Note that $U_{12}(r) = 0$ for hard potentials). In (A) the open circles were computed with a mesh spacing of $\sigma/8$, all other results were computed with a mesh spacing of $\sigma/6$.

While the atomic limit is important, we are ultimately interested in understanding the behavior of fluids near proteins which are more like extended surfaces than atoms. As an intermediate example, we have therefore computed the PMF for a hard sphere fluid near a hard wall. In this case, the route I calculation treats both the hard wall and the hard sphere as explicit surfaces while in the route II calculation, only the hard wall is

treated as a surface. The latter case can be done as a single one dimensional calculation, while the former requires 3-dimensional calculations. Figure 1B shows the PMF computed via the two routes. Once again the two route show good agreement. The staircasing effect due to the cartesian grid is in fact less severe than for the case of two spherical particles most likely because the planar surface can be treated exactly on this mesh.

Dispersion interactions can also be important and we present the results for two simple Lennard-Jones systems in Fig. 2. The first case again shows two fixed Lennard-Jones atoms in an identical dense Lennard-Jones fluid (see Fig. 2)A. The agreement between the two routes to the PMF is excellent. In this case the staircasing has a negligible effect on the PMF calculations. This is because the fixed atoms now have soft core interactions with the fluid, and so there are no density discontinuities at the particle surfaces as is found for the hard systems.

The second case shows the PMF experienced by a Lennard-Jones atom as it approaches two fixed Lennard-Jones atoms. Fig. 2B shows the PMF along a single line down the middle of the domain, namely $z = 4\sigma, y = 4.5\sigma$. The two fixed atoms are both found at $z = 4\sigma$ with $y = 4.0\sigma$ and $y = 5.0\sigma$ respectively. The difference in the x-coordinate, Δx , between these fixed atoms and the third one varies. While we have specifically computed only one line of approach, this is clearly a case where a complete picture requires a 3-dimensional map of the PMF. In Figure 3A we show a 2-dimensional slice of the PMF map for the calculation of $\rho(\mathbf{r})$ with two fixed atoms (route II calculation). In Fig. 3B, we show one slice through a density distribution of the 3 sphere calculation when $\Delta x = 2.5\sigma$. In both cases, the slice shows the $z = 4\sigma$ plane. This example serves to further demonstrate that the PMF for an ion moving in an arbitrary external field (e.g. one composed of a collection of atoms) can be computed from these methods. These examples verify the derivations above and demonstrate that the DFT approach can be applied to very small atomic surfaces.

Solvation of the gramicidin A channel Finally, we demonstrate the utility of this approach by presenting the solvation of a small pore forming polypeptide dimer, namely gramicidin A. This is a simple system analogous to more complex ion channels. One advantage of studying this system is that its atomic structure is known to high resolution. We have taken the 1MAG structure from the protein data bank to define the basic properties of the channel presented here. The atom sizes and charges were assigned based on the Charmm-22 force field.

The calculations we present here compare two different fluid models for this system. In the first case, we model the electrolyte as point charges in a dielectric continuum solvent. This is the standard Poisson-Boltzmann model (PB). In the second case we also include finite size for the ions and an explicit neutral hard sphere solvent. So this is a three component system (3CM). For the purpose of this paper, we consider a very crude 3CM model where all three species have the same size. Clearly in order to perform comparative studies on ions with respect to selectivity, it will be necessary to apply more sophisticated and chemically accurate model electrolytes. In both models, volume exclusion on the gramicidin A atoms is included. Finally we note that for both models, we embed the gramicidin A atoms in an impenetrable membrane of low dielectric constant ($\kappa = 2$) that has a cylindrical pore cut out of it. The cylindrical pore has a diameter of 3σ (9\AA). The impermeable membrane had a thickness of 9σ (27\AA) For both models, the fluid has a constant dielectric constant of $\kappa = 78.5$ everywhere. Both models rely on a continuum approximation for the polarization. This is likely to be incorrect in the vicinity of the pore; however a discussion of the modifications to the DFT needed to explore spatially varying polarization is beyond the scope of this paper.

For this particular problem, we are fundamentally interested in the ability of ions to traverse the pore form-

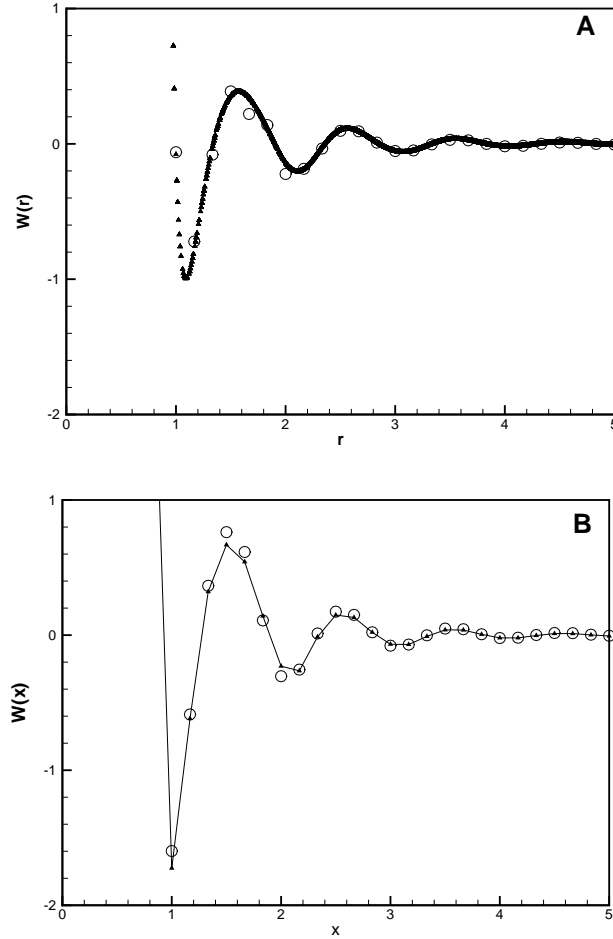


Figure 2. Potentials of mean force, $W = W/kT$ as a function of separation, $r = r/\sigma$ for two simple fluid systems that include Lennard-Jones dispersion interactions. (A) is the PMF between two Lennard-Jones atoms of diameter σ in a Lennard-Jones fluid where $kT/\epsilon = 0.8$, $\rho\sigma^3 = 0.75$, and $r_c = 2.5\sigma$, (B) shows the PMF for a single Lennard-Jones atom along one line in the field created by two additional fixed atoms. In all calculations, the mesh was $\sigma/6$. See Fig.1 for a description of the symbols.

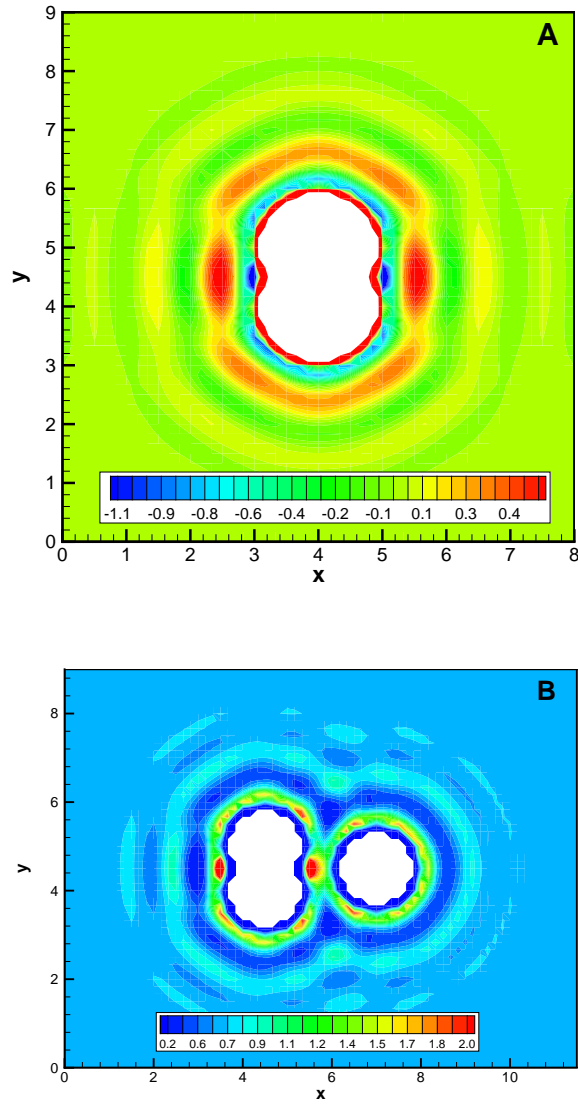


Figure 3. (A) A 2-dimensional slice of PMFs, W/kT experienced by a Lennard-Jones atom in a field created by two fixed atoms. (B) A 2-dimensional slice of a density distribution around 3 Lennard-Jones atoms. The distance between the two fixed atoms and the third approaching atom in the x-direction is $\Delta x = 2.5\sigma$.

ing gramicidin A. The simple systems shown in the previous section demonstrated that a complete potential of mean force map can be found from a single calculation where the channel is set up as an external field and Eq.48 is applied to the resulting inhomogeneous density distribution, $\rho(\mathbf{r})$. Figure 4 compares the PMF map in slices that intersect the center of the gramicidin A pore. The top two figures show the result for the PB model, the bottom three figures show the result for the 3CM model.

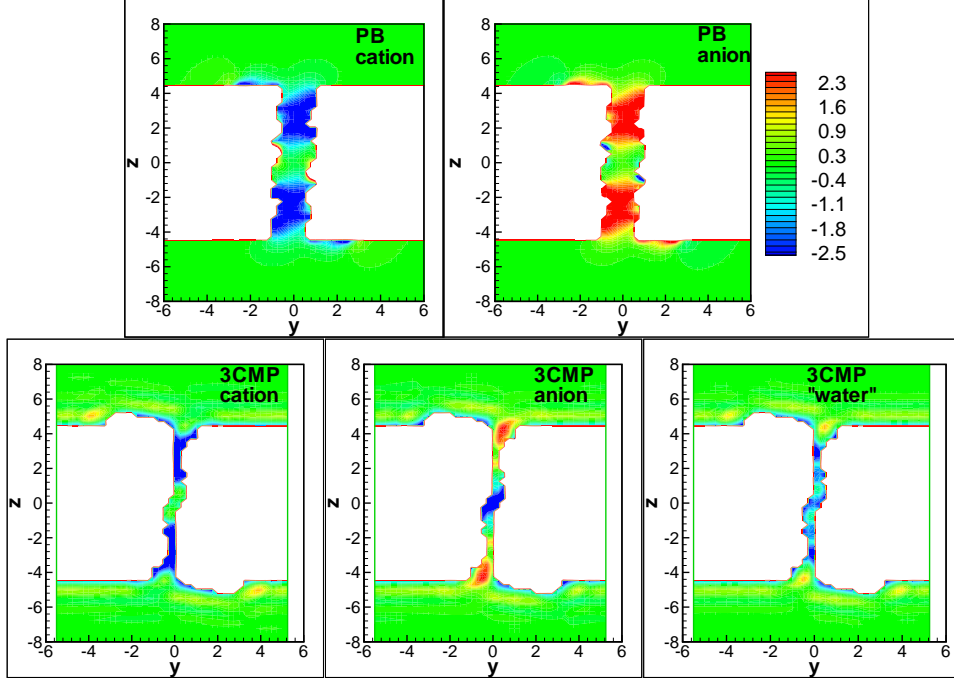


Figure 4. Slices through a PMF distribution, $W(\mathbf{r})/kT = -\ln\rho(\mathbf{r})/\rho_b$, around a static gramicidin A channel in both the PB approximation (top two figures) and the 3CM approximation (bottom three figures). The single color scale applies to all of the figures. In these examples the bulk ion densities were $\rho\sigma^3 = 0.00162$ (0.1 M where $\sigma = 3\text{\AA}$) and in the 3CM the solvent density is $\rho\sigma^3 = 0.7$. These results were generated on a mesh of $\sigma/4$, and the total domain size was $11\sigma \times 11\sigma \times 23\sigma$ ($33\text{\AA} \times 33\text{\AA} \times 75\text{\AA}$).

As expected from Eq.20, the PMF map for the cation in the Poisson-Boltzmann model of Fig.4 is just the negative of the PMF for the anion. The most important features of the PB solution for this system are the two regions of strong attraction for cations near the two entrances of the pore. In the 3CM plots there is considerably less fluid accessible volume since the fluid particles have size, and these PMF maps show only where the center of the fluid particles may be found. The cation distribution again shows two primary basins of attraction near the entrance regions of the pore. The anion distribution shows a new region of attraction towards the center of the pore. Finally, the high density neutral solvent shows considerable structure of small periodicity down the entire length of the pore.

Fig.5 provides a more quantitative picture of the PMF experienced by a fluid atom as it traverses the pore at equilibrium. As we will describe in much more detail in paper II, we find that this pore is effectively a 1-dimensional system, and so we simply present an average potential of mean force as a function of distance

down the channel, $\langle W(z) \rangle$. More specifically, this averaged PMF was computed by considering averaging all nonzero values of $W(z)$ in the pore in a given plane.

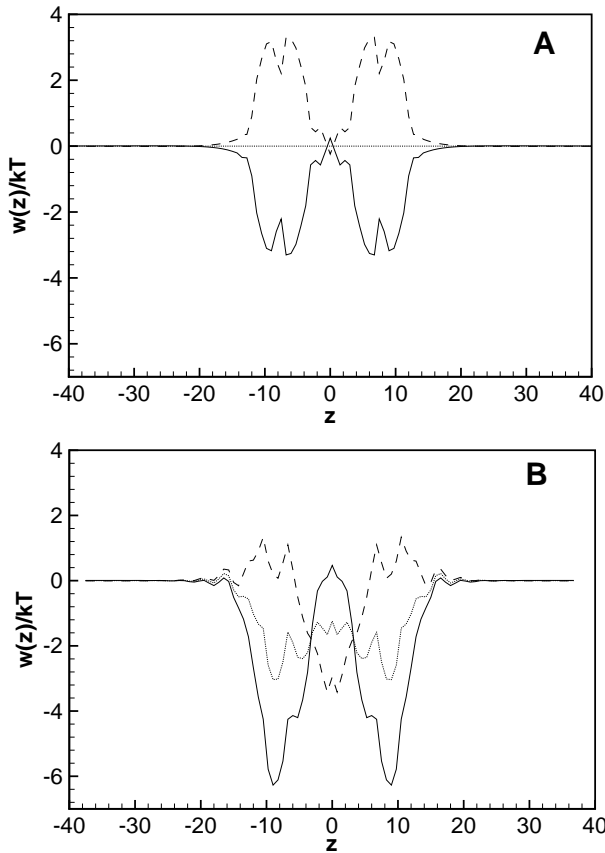


Figure 5. The average PMF experienced by fluid atoms traversing a gramicidin A channel in both the PB model (A) and the 3CM (B) presented here. The various curves are: cation PMF (solid), anion PMF (dashed), solvent PMF (dotted). The x-axis is now given in Angström units with zero at the center of the pore.

There are several differences between the PB and 3CM models as is apparent from Fig.5. The structure of the PB PMFs is dictated entirely by electrostatic effects. In the 3CM, the PMFs have some additional periodicity on a length scale similar to a particle diameter ($\sigma = 3\text{\AA}$) resulting from packing of the high density neutral fluid in the pore. This packing is also reflected in ion distributions although it is most obvious in the anion distribution. Overall, the electrostatic effects are still dominant even for the 3CM as the two deep minima at either end of the pore (cation PMF) are not compromised by the packing effects. However, the fine details of the free energy barriers do change somewhat between the models. The free energy minima for the cations are a bit deeper in the 3CM case than in the PB case. In addition the anion minima at the center of the pore has a negative PMF for the 3CM while it was always positive for the PB model.

Finally, we note that one could also represent one of the ions explicitly in the calculation. By placing it in

one of the strong adsorption site and resolving for the new density distribution, one can compute how the PMF in another adsorption site is affected by the presence of the first ion. Thus there is a clear path to studying occupancy patterns in these channels with this approach.

Conclusions

In this paper we have presented an overview of how the statistical mechanics of inhomogeneous fluids coupled with modern molecular theory and high performance computing allow for new ways to study protein solvation. We discussed how potentials of mean force computed by these methods could be used for simulation of solvated biological macromolecules as well as how they can be used to study ion adsorption and free energy barriers to transport near a protein or through a pore forming channel. This approach can be systematically improved to include more complex physical phenomena from polarization to hydrogen bonding, and provides a complementary analytical tool to molecular simulations. DFTs have become an important tool for studying inhomogeneous fluids problems in materials applications, and we expect that they could be equally important in studying inhomogeneous fluids in biology.

References

- [1] Im W., Seefeld, S., and Roux, B., 1999. A Grand Canonical Monte Carlo-Brownian Dynamics Algorithm for Simulating Ion Channels. *Biophys. J.* 79:788-801.
- [2] Friedman, H.L., 1985. A Course in Statistical Mechanics, Prentice-Hall, New Jersey.
- [27] Frink, L.J.D. and van Swol, F., 1994. Solvation Forces and Colloidal Stability: A Combined Monte-Carlo and Density Functional Theory Approach, *J. Chem. Phys.*, 100:9106-9116.
- [28] Frink L.J.D. and Salinger, A.G., 1999. Wetting of a chemically heterogeneous surface., *J. Chem. Phys.*, 110: 5969-5977.
- [6] Frink L.J.D. and Salinger, A.G., 2002. Rapid analysis of phase behavior with density functional theory, Part II: Capillary condensation in disordered porous media., *submitted to J.Chem. Phys.*
- [6] Frischknecht, A.L., Weinhold, J.D., Salinger, A.G., Curro, J.G., Frink, L.J.D., and McCoy, J.D., 2002. Density Functional Theory for Inhomogeneous Polymer Systems I: Numerical Methods and II: Application to Block Copolymer Thin Films., *in press J. Chem. Phys.*
- [9] Henderson, D., ed. 1992. Fundamentals of Inhomogeneous Fluids. Marcel Dekker, New York.
- [8] Henderson, J.R., 1999. Statistical mechanics of patterned inhomogeneous fluid phenomena., *J. Phys. Cond. Matt*, 11:629-643.

- [9] Hill, T.L., 1986. An Introduction to Statistical Thermodynamics. Dover Publications, New York.
- [10] Kierlik, E., Monson, P.A., Rosinberg, M.L., Sarkisov, L., and Tarjus, G., Capillary Condensation in Disordered Porous Materials: Hysteresis versus Equilibrium Behavior., *Phys. Rev. Lett.*, 87:5701-5704.
- [11] Lagüe, P., Zuckermann, M.J., and Roux, B., 2000. Lipid-Mediated Interactions between Intrinsic Membrane Proteins: A Theoretical Study Based on Integral Equations, *Biophys. J.*, 79:2867-2879.
- [12] McMillan, W.G. and Mayer, J.E., 1945. *J. Chem. Phys.*, 13:276.
- [19] Rosenfeld Y., Schmidt M., Lowen H. and Tarazona P., 1996., Dimensional crossover and the freezing transition in density functional theory, *J. Phys. Cond. Matt.*, 8:, L795-L801.
- [14] Roux, B. and Simonson, T. 1999. Implicit Solvent Models, *Biophysical Chemistry*, 78:1-20.
- [15] Tang Z.X., Teran L.M.-Y., Davis H.T., Scriven L.E. and White H.S., 1990., Nonlocal Free-Energy Density-Functional Theory Applied to the Electrical Double-Layer.1.Symmetrical Electrolytes *Mol. Phys.*, 71:369-392.
- [16] Tarazona P., 1985., Free-energy density functional for hard-spheres, *Phys. Rev. A*, 31:2672-2679.
- [18] Weeks JD, Chandler D and Anderson HC, 1971 *J. Chem. Phys.*, **54**, 5237.

Hydration of Krypton and Consideration of Clathrate Models of Hydrophobic Effects from the Perspective of Quasi-Chemical Theory

Henry S. Ashbaugh, D. Asthagiri, Lawrence R. Pratt¹,

and

Susan B. Rempe²

Abstract

Ab initio molecular dynamics (AIMD) results on a liquid krypton-water system are presented and compared to recent XAFS results for the radial hydration structure for a Kr atom in liquid water solution. Though these AIMD calculations have important limitations of scale, the comparisons with the liquid solution results are satisfactory and significantly different from the radial distributions extracted from the data on the solid Kr/H₂O clathrate hydrate phase. The calculations also produce the coordination number distribution that can be examined for metastable coordination structures suggesting possibilities for clathrate-like organization; none are seen in these results. Clathrate pictures of hydrophobic hydration are discussed, as is the quasi-chemical theory that should provide a basis for clathrate pictures. Outer shell contributions are discussed and accurately estimated; they are positive and larger than the positive experimental hydration free energy of Kr(aq), implying that inner shell contributions must be negative and of comparable size. Clathrate-like inner shell hydration structures on a Kr atom solute are obtained for some, but not all, of the coordination number cases observed in the simulation. The structures found have a delicate stability; inner shell coordination structures extracted from the simulation of the liquid, and then subjected to quantum chemical optimization, always decomposed. Interactions with the outer shell material are decisive in stabilizing coordination structures observed in liquid solution and in clathrate phases. The primitive quasi-chemical estimate that uses a dielectric model for the influence of the outer shell material on the inner shell equilibria gives a contribution to the hydration free energy that is positive and larger than the experimental hydration free energy. The “what are we to tell students” question about hydrophobic hydration, often answered with structural models such as clathrate pictures, is then considered; we propose an alternative answer that is consistent with successful molecular theories of hydrophobic effects and based upon distinctive observable properties of liquid water. Considerations of parsimony, for instance Ockham’s razor, then suggest that additional structural hypotheses in response to “what are we to tell students” aren’t required at this stage.

Keywords: hydrophobic hydration, clathrate hydrate, *ab initio* molecular dynamics, quasi-chemical theory, scaled particle theory, krypton.

Introduction

Kauzmann’s analysis [32] established the topic of hydrophobic effects as relevant to the structure, stability, and function of soluble proteins. Reminiscences on protein research of that period emphasize that the concept of hydrophobic stabilization of globular proteins was non-trivial [71]. Decades have passed, and the language of hydrophobic effects has become common. It is, therefore, astonishing to note that consensus on a molecular scale conceptualization of hydrophobic effects, and on molecular theories, has not been obtained. For a recent example, see reference [38]. In the present setting of competing ideas, theories, and selected results, it isn’t uncommon to hear from biophysical chemists, “What are we to tell students?” Of course, one response is to question what we tell ourselves.

In addressing the most primitive hydrophobic effects, molecular theory has achieved some surprising steps recently. A compelling molecular theory for primitive hydrophobic effects is now available [52], though a

¹Theoretical Division, Los Alamos National Laboratory, Los Alamos, NM 87545, USA

²Sandia National Laboratory, Albuquerque, NM 87185 USA

variety of more complex cases haven't been similarly resolved [58]. Still, the recent theoretical advance means that we can scrutinize conflicting theories more seriously and begin to build a more objective answer to the "what are we to tell students" question.

The recent XAFS studies of the hydration of Kr in liquid water and in a comparable solid Kr/H₂O clathrate phase [7] seem particularly helpful to the task of consolidation of molecular theories of primitive hydrophobic effects. These experiments were directed toward characterization of the 'iceberg' pictorial interpretations and conclusions of Frank & Evans [17] that were supported in part by the known structures of solid clathrate hydrates.

In the panoply of *pictures* of hydrophobic phenomena, clathrate models are especially appropriate as initial targets for modern scrutiny: it has been discovered recently how these structural models might be developed logically as a basis for molecular theory of hydrophobic effects [31, 47]. Those approaches are *quasi-chemical* theories. They hold promise for higher molecular resolution, and particularly for treating *context hydrophobicity* in which proximal hydrophilic groups affect the hydration of hydrophobic moieties.

A drawback that can be foreseen for quasi-chemical theories is one that is common to computational chemistry: several competing contributions must be evaluated at an appropriate accuracy and assembled. The net hydration free energy of Kr(aq) is an order of magnitude smaller than several of the primitive contributions to it. Every little thing counts in the assembled results and experience in evaluating the various required contributions is thin. The chemically simple case of Kr(aq) is an appropriate starting point because the various contributions that must be evaluated seem to be in hand. Nevertheless, detailed computational determination of the hydration free energy of Kr(aq) is not sought in the present effort, which instead takes the goals of testing clathrate pictures of hydrophobic hydration and of scoping molecularly detailed quasi-chemical theories.

The plan for this paper is as follows: in the next section we give some background on clathrate models of hydrophobic hydration. After that, we discuss quasi-chemical theory in order to explain the coordination number distribution that is the principal target of the following *ab initio* molecular dynamics (AIMD) calculations. AIMD results for the hydration of Kr(aq) are then compared with results from the XAFS experiments. To guide quasi-chemical descriptions of these phases, we then estimate the inner and outer shell contributions required for the most primitive approximations. The final sections discuss "what are we to tell students" and identify conclusions.

Though AIMD calculations might seem to be excessive for this chemically simple problem, this approach is available and the results aren't limited by assumptions of non-cooperativity of the interactions. Modern work [69, 70, 78] on hydrophobic hydration has suggested that attractive interactions between solute and solvent water might play a role less trivial than assumed by conventional van der Waals theories [8]. This point is consistent with the fact that clathrate phases involving inert gases as light as Ne are more exotic and are to be sought at relatively higher pressures than similar phases involving heavier inert gases [13, 34, 44, 65].

The present work is centered on the physical chemical basics of a foundational concept of molecular structural biology. We hope this focus follows the example provided by Kauzmann's wide-ranging considerations of molecular science, including topics of water and aqueous solutions [14] and molecular biophysical chemistry.

Clathrate Model Background

The status of clathrate pictures of hydrophobicity is reflected in the current literature; for example, see [9]: “Conventional views hold that the hydration shell of small hydrophobic solutes is clathrate-like, characterized by local cage-like hydrogen-bonding structures and a distinct loss in entropy.” An admirably clear and appropriately circumspect early consideration of clathrate models for solutions of hydrophobic gases in liquid water was given by Glew [22]. The data available at that time suggested “... that the nature of the water solvent surrounding weakly interacting aqueous solutes should be likened geometrically to those coordination polyhedra experimentally observed in the solid gas-hydrates.” Still, “in no sense is it considered that the water molecules adjacent to the solute are permanently immobilized or rigid as in solid structures ... ” [22]. The more recent discussion of [11] explains conventional views of hydrophobic hydration “... that the organization of water molecules in the first shell surrounding the solute is like an ‘iceberg,’ a clathrate, or a ‘flickering cluster.’” It may be disconcerting that a series of non-equivalent descriptors are used to describe the same phenomenon. This fact reflects the imprecision of these conceptualizations and we won’t distinguish them further. Another much earlier expression of such a physical view can be found in [33]; at the same time a clathrate model of liquid water *without* solutes was proposed by Pauling [49]. The review in [66] discussed again Kauzmann’s consideration [32] of clathrate models of hydrophobic hydration, which argued that the degree of ordering suggested by measured hydration entropy changes upon dissolution was too small to be conceived as crystalline ordering. Concluding, Kauzmann [32] stated: “There is no justification for using the iceberg concept as a basis for the hypothesis that protein molecules are surrounded and stabilized by regions of ordered water molecules.”

On the solution structure side of this issue, Head-Gordon [26] examined the question of whether the structure of liquid water near hydrophobic inert gas molecules was clathrate-like by exploiting computer simulation to compute the numbers of H-bonded pentagons present near those solutes compared to bulk regions of liquids. The idea was that pentagonal bonding structures are evident in clathrate crystals so pentagons might be a suitable diagnostic of clathrate-like structures in liquid solutions. Some enhancement of the populations of pentagons was observed in the first hydration shell of model CH_4 solute in liquid water, but the conclusions were ultimately mixed and included that “it is important to emphasize that no direct connection between structure and thermodynamics is made — *i.e.*, through a formal statistical mechanical theory.”

On the crystal side of this issue, clathrate phases with impressively complex guests have been discovered [75, 74]. But it can happen that, though the water molecules are ordered, the structure of the guest molecule is disordered. That is opposite to the case sought in protein crystallography. Earlier [72] analysis of crambin crystals had identified a cluster of pentagonal rings of water molecules at the surface of that protein. Those rings are extensively H-bonded to the protein and crystal packing effects are involved in principle. It has been challenged [40] whether pentagonal H-bond structures are general features of hydration of soluble proteins. Furthermore, as noted in the statement above, the thermodynamic significance of such structures hasn’t been established.

The XAFS results of Bowron, *et al.* [7], which are a motivation for this work, were directed toward an experimental test of this clathrate concept. Conditions were chosen to permit formation of a Kr clathrate from the liquid solution in the sample cell. Temperatures ranged from an initial 5 C to -5 C with pressures

of approximately 110 bar. Results taken before and after the transition permitted comparison of the radial distribution of water oxygen atoms conditional on a Kr atom. Those inferred radial distributions for the liquid solution and the clathrate phase were *qualitatively* different, as is discussed further below. This difference would be a serious problem for a literal interpretation in terms of a clathrate model of hydrophobicity. A reasonable correspondence of radial solvent density certainly should be a fundamental requirement of a successful clathrate model and it is a requirement that has received less attention than orientational distributions.

Molecular-scale simulation of aqueous solutions of hydrophobic solutes and of systems that form clathrates of common interest has been pursued many times over several decades. Much of that work on solutions is referenced in [52]. An early example of molecular simulation of a methane clathrate is [73]; a comparable more recent example can be found in [16] and a comprehensive review is given by Sloan [65]. Conclusions from that body of work are consistent with the results of the XAFS experiments discussed above. The radial layering of oxygen density conditional on the guest is much weaker in the solution case. Results from studies of liquid solutions yield a modest maximum value of oxygen radial distribution, typically slightly larger than 2, and with a weak minimum that provides little physical distinction between first and second hydration shells. In contrast, the maximum values of g_{CO} in the methane clathrate calculations are greater than 4 with an unambiguous physical definition of the first hydration shell. The important work of Owicki & Scheraga [46] compared the radial distributions of oxygen atoms neighboring a methane solute in liquid solution to an ideal clathrate possibility. In that case the mean inner shell occupancy was about 23 and the correspondence with a clathrate case seemed closest for a larger 24 vertex cage [65], which is larger than the smaller 20 vertex possibility presented by known clathrate crystals. The radial distribution was noted to be relatively diffuse in the solution case.

Distributions of orientational angles are often presented in solution simulations and sometimes compared explicitly to ideal results for clathrate crystal geometries [1]. This question of the connection between angle distributions and solution phase hydrophobicities was addressed by an information theory analysis that arranged to include systematically 2, 3, ..., n -body solvent correlations in thermodynamic predictions of solution phase hydrophobic hydration free energies. It was a surprise that inclusion of just $n=2$ and 3-body correlations *worsened* the thermodynamic predictions obtained when only $n=2$ -body correlations were used [52, 23]. That work suggested that an exclusive focus on distributions of angles, which are obtained from 3-point distributions, can be problematic for drawing conclusions about clathrate models of hydrophobicity.

It is helpful to keep in mind the observation discussed by Friedman and Krishnan [18]: The sum of the solvation entropies of K^+ and Cl^- in water is roughly the same as twice the solvation entropy of $\text{Ar}(\text{aq})$, though the case of methanol as solvent was different. These hydration entropies are negative so solvent ordering is suggested. But the specific molecular ordering of near neighbor water molecules is expected to be qualitatively different in each of these cases. So there is no simple, unique inference of molecular structuring available from the measured hydration entropy; furthermore, the observed entropies generally don't imply that H-bonding interactions among water molecules aren't substantially influenced by the solute.

Still, clathrate pictorial interpretations are widely assumed. Sloan [65] notes that "... the water scientific community refers to short-lived cavities (not unit crystals sI, sII, or sH) as clathrate-like structures in water." Indeed, it is common to describe the liquid solution results as 'clathrate-like' without extensive scrutiny of likeness or unlikeness to specific clathrate possibilities.

Perspective from *Quasi-Chemical* Theory

Quasi-chemical theories are built upon a distinction between defined inner and outer shell regions [47, 59]. The intention is to define an inner shell that can be studied at molecular resolution using tools of modern computational chemistry. For the outer shell region, in contrast, genuine statistical mechanics can't be avoided, but it ought to be simpler because complicated chemical interactions aren't a direct concern there. The inner shell is defined geometrically [31] by specification of an indicator function $b(\mathbf{j})$ that is one (1) when solution molecule \mathbf{j} occupies the intended inner shell and zero (0) otherwise. Fig. 6 shows candidates for inner shell complexes $\text{Kr}(\text{H}_2\text{O})_n$ and suggests how this approach might apply to build statistical thermodynamic models starting from 'clathrate-like' concepts.

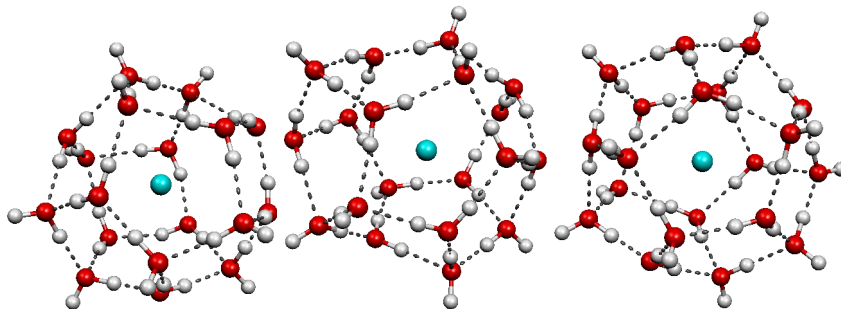


Figure 6. Structures for $\text{Kr}[\text{H}_2\text{O}]_n$. H-bonds between the water molecules are depicted by broken lines. From left to right, the structures have 18, 19, and 20 water molecules, respectively. Oxygen atoms are red, hydrogen atoms are blue, and the krypton atom is blue.

With the inner shell defined, the interaction contribution to the chemical potential of the Kr solute can be expressed as [31, 47]

$$\begin{aligned} \beta\mu_{\text{Kr}(aq)}^{ex} = & - \ln \left(1 + \sum_{m \geq 1} K_m \rho_{\text{H}_2\text{O}}^m \right) \\ & - \ln \langle \langle e^{-\beta \Delta U_{\text{Kr}}} \Pi_j (1 - b(\mathbf{j})) \rangle \rangle_0 . \end{aligned} \quad (32)$$

($\beta^{-1} = kT$, with T the temperature and k the Boltzmann constant.) This excess chemical potential is partitioned into an inner shell contribution (the first term on the right of Eq. 32) and an outer shell contribution (the remainder). The inner shell contribution is associated with equilibrium of chemical equations



for formation of inner shell complexes, as in Fig. 6, *in situ*. The coefficients K_m are equilibrium ratios for these equations.

The coefficients K_m might be obtained by observations of the population of Kr atoms coordinated to m water molecules, $m=0,1, \dots$. This directs attention to the probability that a distinguished Kr atom has m

inner shell water molecule ligands. Those fractions will be denoted by x_m and are given by

$$x_m = \frac{K_m \rho_{\text{H}_2\text{O}}^m}{1 + \sum_{n \geq 1} K_n \rho_{\text{H}_2\text{O}}^n} . \quad (34)$$

The probabilities x_m are physical observables that could be obtained, for example, from a simulation. Our first goal is to investigate these x_m to see whether they give any suggestion of coordination species present in corresponding known clathrate hydrates. We note these distributions, x_m , were conventionally considered in historical computer simulations for these problems; they were then referred to as ‘quasi-component’ distributions [69]. This discussion attempts to situate these distributions in helpful statistical thermodynamic theories.

The natural initial implementation of these quasi-chemical ideas, particularly to ion hydration, has been to treat effects of material external to the cluster by an approximation

$$K_m \approx \exp \left[-\beta \left(\mu_{\text{Kr}(\text{H}_2\text{O})_m}^{ex} - m \mu_{\text{H}_2\text{O}}^{ex} \right) \right] K_m^{(0)} \quad (35)$$

where $K_m^{(0)}$ is the equilibrium ratio for Eq. 33 in a dilute gas and the required hydration free energies are obtained standardly from a dielectric continuum model [24] and includes a contribution from the outer shell term corresponding to the bare ion. This approach will be used in the results below.

Recently it has been indicated in Ref. [47] how these inner and outer shell contributions can be naturally recombined after the most natural primitive approximations. In that sense, it isn’t necessary to consider these two terms separately. That development leads further to a revised approximation scheme in which $K_m \approx \gamma^m K_m^{(0)}$, with γ a Lagrange multiplier that plays the same role here as an activity coefficient. Further, $-kT \ln \gamma$ can also be seen as an effective external field operating on each ligand molecule, analogous to the prefactor of $K_m^{(0)}$ in Eq. 35. This leads finally to the concept of a self-consistent field treatment of quasi-chemical approximations [4].

***Ab Initio* Molecular Dynamics for Kr(aq) and Comparison with XAFS Results**

The system simulated by AIMD consisted of one Kr atom surrounded by 32 water molecules in a cubic box with sides of length 9.87 Å and periodic boundary conditions. An initial structure was obtained utilizing results from an earlier study of $\text{Li}^+(\text{aq})$ [62, 61]. A Kr atom was substituted for the Li^+ ion in a configuration from that calculation, the full system was then optimized in a much larger cell and replaced in the original simulation cube. Optimization of configurations drawn from the subsequent molecular dynamics trajectory and variations of total optimized energies with the simulation cell size suggests that this system is at a realistically low pressure. A more precise estimate of the pressure was not possible in the present effort.

The calculations based upon an electron density functional description[77] of the electronic structure and interatomic forces were carried out on the Kr(aq) system utilizing the VASP program[36, 35]. The ions were represented by ultrasoft pseudopotentials[76, 37], in the local density approximation for Kr and in the gradient-corrected approximation for O and H, and a kinetic energy cutoff of 29.10 Ry defined the plane wave basis expansions of the valence electronic wave functions. The valence electrons consisted of eight (8) electrons

for Kr (4s and 4p), six (6) electrons for O (2s and 2p), and one (1) electron for H (1s). The equations of motion were integrated in time steps of 1 fs with a thermostat set at 300 K during the first 4 ps of simulation time. The thermostat was then abandoned; the temperature rose and settled at 341 ± 24 K (see Fig. 7), higher than the experiments of interest here. The precision of temperature characterization and the corresponding awkwardness in temperature adjustment is a practical limitation of these simulations that treat small systems over short times. Subsequent work should investigate temperature effects on these simulations, but we will proceed here in considering the results.

The structural analyses presented here apply to the last 10 ps of the 18 ps trajectory. During this time, the initial structure with hydration number $n = 19$ relaxed into structures with $n = 15$ to $n = 22$ nearest neighbors within a radius of 5.1 \AA ; see Fig. 7. The resulting Kr-O radial distribution function, plotted with the solid line in Fig. 8, shows a build-up of water density to slightly more than double the bulk value, $g_{max}(r) \approx 2.4$ at a radius $r \approx 3.7 \text{ \AA}$ from the Kr atom. A comparison with the experimental XAFS data produced by [15] (Fig. 8) shows an overlap of error bars between the calculated and the experimentally determined radial distribution functions. The maximum value, $g_{max}(r) \approx 2.4$, is about the same as the value found from a force field model adjusted to give experimental solution thermodynamics [70, 78] and is slightly larger than the result found by [3] for the case of a corresponding sized hard sphere solute in SPC water, which is, as shown there, also in good agreement with the revised scaled particle model [67].

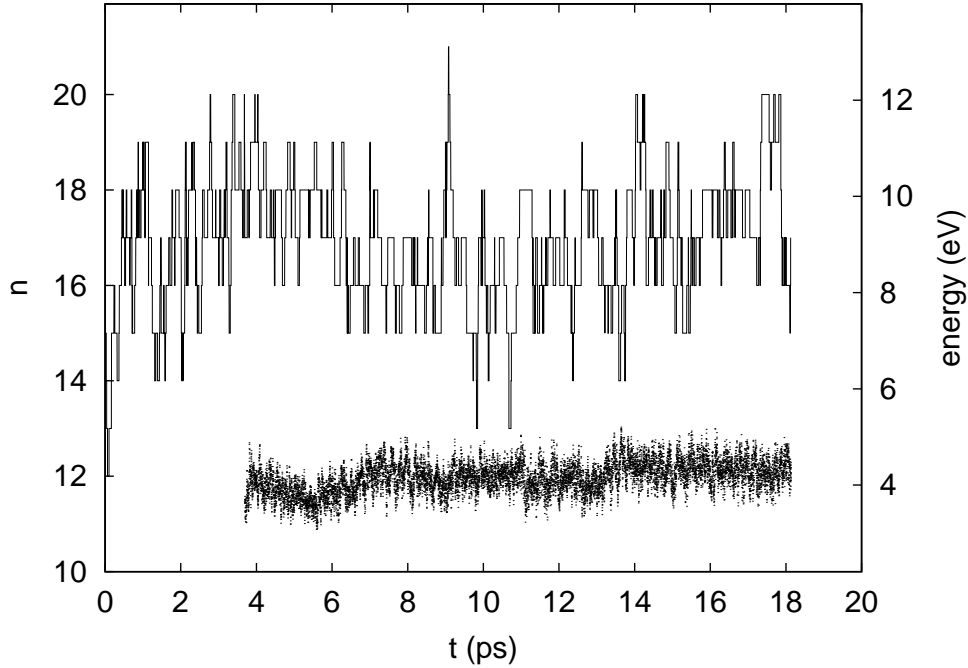


Figure 7. Oxygen coordination of the Kr atom as a function of time (upper trace and left axis). The total kinetic energy of the atomic motion shown in the lower trace demonstrates the stability of the temperature state.

The average occupancy of the inner shell defined by the radius $r \leq 5.1 \text{ \AA}$ is $\langle n \rangle = 18 \pm 1$ and $n=18$ is found

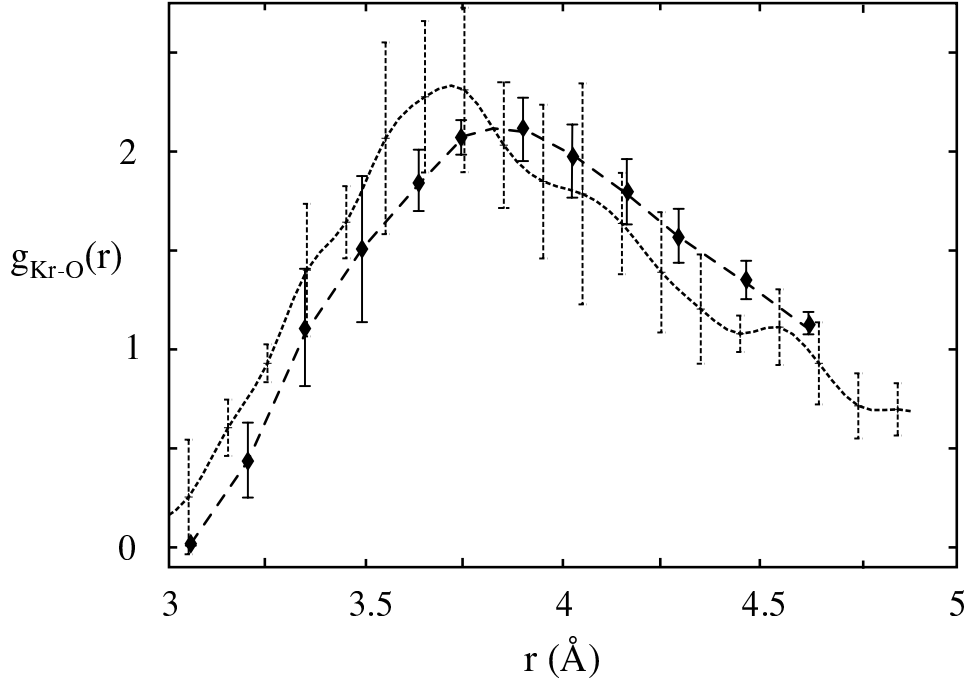


Figure 8. Pair distribution function for Kr-O measured by experiment (dashed line) and by AIMD simulation (solid line). In the latter case, indicated error bars of $\pm 2\sigma$ were estimated on the assumption that that last four 2.5 ps trajectory segments are independent. Error bars of $\pm\sigma$ are plotted with the experimental data.

also to be the most probable structure, as is shown in Fig. 9. The $n=20$ case is about half as likely as the most probable $n=18$ case and either $n=19$ or $n=17$ is more probable than $n=20$ by these results. This x_n distribution of coordination numbers is unimodal. In a limited range of thermodynamic states approaching a clathrate phase boundary, the x_n distribution might be expected to exhibit magic number features reflecting metastable coordination possibilities [41]. Those possibilities are not observed here.

Consideration of the radial Kr-H pair distribution function (Fig. 10) shows a featureless distribution. These results are not dissimilar to recent computations of radial hydrogen distributions conditional on a hard sphere solute in SPC water [3]; although those calculations have better spatial resolution and thus additional observable structure, the maximum hydrogen density is about the same here.

Although these calculations have clear limitations of scale and thus correspondence to the experiment, to within the errors of the theoretical and experimental measurements, *they do corroborate the experimentally observed local fluid structure*. They also provide the more probable features of the coordination number distribution, x_n , of physical interest from the point of view of quasi-chemical models. The coordination structures observed in the AIMD simulation should provide an appropriate starting point in considering inner shell coordination species that might found quasi-chemical models.

The following sections consider the outer and inner shell contributions to the hydration free energy of Kr

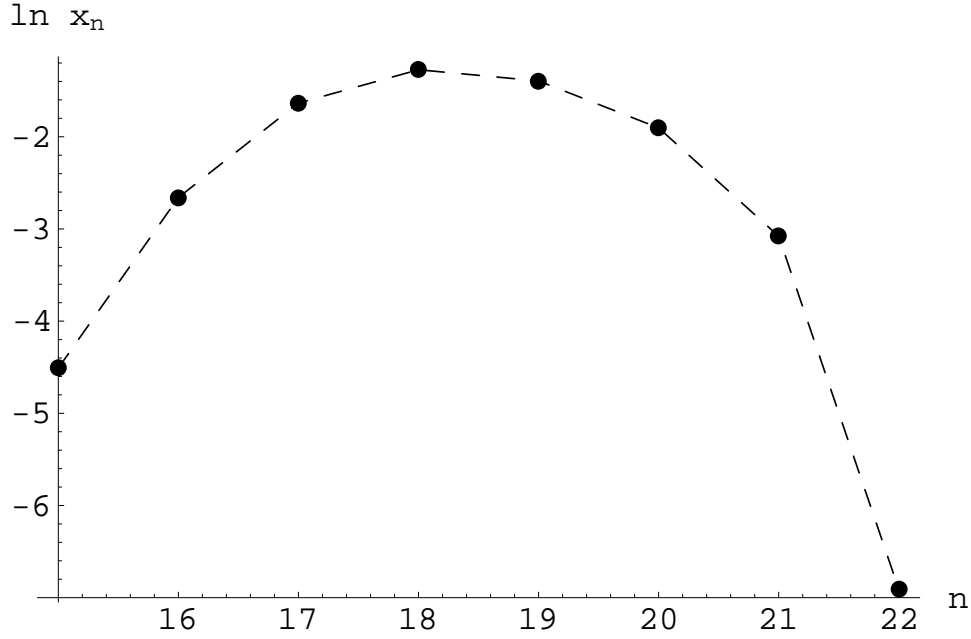


Figure 9. Probability distributions of inner-shell structures with n water molecules surrounding Kr atom where the inner-shell boundary is defined at $r=5.10$ Å.

in turn.

Outer Shell Contributions

The outer shell term would be the hydration free energy under the hypothetical constraint that inner shell occupancy be prohibited. We anticipate that an electrostatic contribution, estimated with a dielectric continuum model, will be included in the modified equilibrium ratios obtained below; see Eq. 35 and the supporting discussion. For the Kr case considered here, that leaves packing interactions associated with hard spherical exclusion volume and weaker London dispersion interactions. We will discuss those outer shell contributions here.

Scaled particle theory provides a connection between outer shell contributions to the free energy and the packing of water about an evacuated cavity. The free energy for emptying the inner sphere is given by the work of growing a hard sphere solute in aqueous solution

$$\beta\mu^{ex}(\text{outer shell}) = 4\pi\rho_{\text{H}_2\text{O}} \int_0^R G(\lambda)\lambda^2 d\lambda \quad (36)$$

where R is the inner shell radius, and $G(\lambda)$ is the contact value of the cavity-water oxygen radial distribution function as a function of the distance of closest approach λ . This expression can be thought of as the $p \cdot dV$, $\rho_{\text{H}_2\text{O}}kTG(\lambda) \cdot 4\pi\lambda^2 d\lambda$, work associated with growing an empty cavity into solution. The surface tension

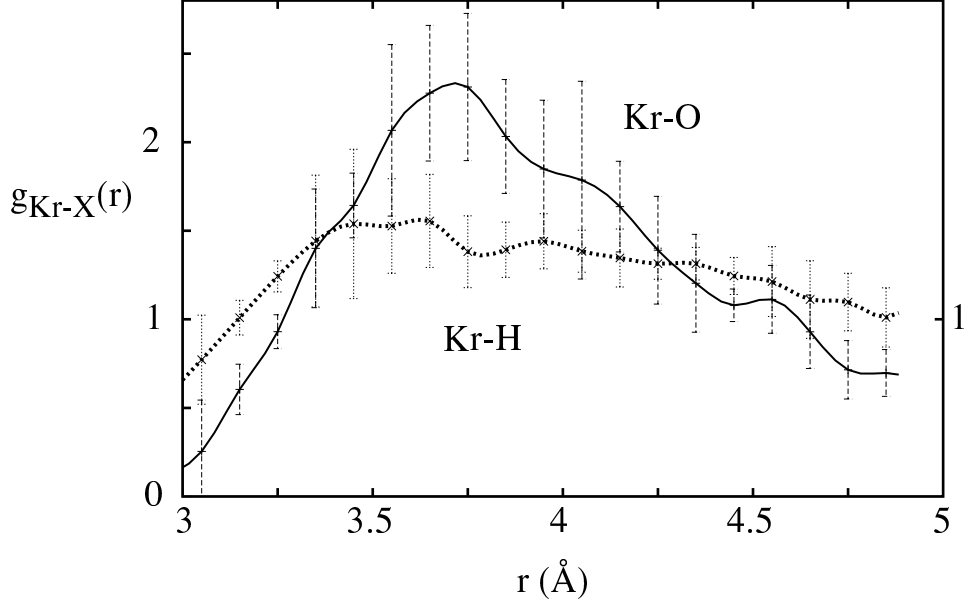


Figure 10. Pair distribution function for Kr-O and Kr-H determined by AIMD simulation. Error bars indicate the estimated 95% confidence level.

associated with differentially increasing the surface area of the outer shell cavity is given by the derivative of Eq. 36 with respect to outer shell surface area

$$\beta\gamma(R) = \left(\frac{\partial\beta\mu}{\partial R} \right) \frac{\partial R}{\partial(4\pi R^2)} = \frac{1}{2}\rho_{\text{H}_2\text{O}}G(R)R \quad (37)$$

This derivative has also been approximated simply by the ratio of the hydration free energy of exclusion volume to its surface area

$$\beta\gamma(R) \approx \rho_{\text{H}_2\text{O}} \int_0^R G(\lambda) \left(\frac{\lambda}{R} \right)^2 d\lambda \quad (38)$$

These two distinct expressions, Eq. 37 and 38, yield different values for the surface tension for submacroscopic cavities.

The contact function $G(\lambda)$ is readily obtained from molecular simulations of hard sphere hydration at discrete values of λ . Alternatively, Stillinger proposed [67] a functional form for $G(\lambda)$ that interpolates between the known microscopic and macroscopic limiting forms:

$$G(\lambda) = \begin{cases} \frac{1 + (\pi\rho/\lambda) \int_0^{2\lambda} g_{\text{OO}}(z)(z-2\lambda)z^2 dz}{1 - 4\pi\rho\lambda^3/3 + (\pi\rho)^2 \int_0^{2\lambda} g_{\text{OO}}(z)(z^3/6 - 2\lambda^2 z + 8\lambda^3/3)z^2 dz}, & \lambda < 1.75\text{\AA} \\ p_{\text{sat}}/\rho kT + \frac{(2\gamma_v/\rho kT)}{\lambda} + \frac{G_2}{\lambda^2} + \frac{G_4}{\lambda^4}, & \lambda > 1.75\text{\AA} \end{cases} \quad (39)$$

where $g_{OO}(r)$ is the water oxygen-oxygen radial distribution function, p_{sat} is the saturation pressure of water in equilibrium with its vapor, γ_v is the vapor-liquid surface tension. The coefficients G_2 and G_4 are chosen so that the contact function is seamless, matching $G(\lambda)$ and its first derivative at $\lambda=1.75\text{\AA}$, different from the originally suggested 1.95\AA [67, 3]. Extensive molecular simulations [3] have verified Stillinger’s functional form for water and give confidence for calculating outer shell contributions to the hydration of Kr.

To this end we have used simulation results for the radial distribution function of SPC/E water along the saturation line (Prof. S. Garde - personal communication) with the experimental surface tension of water and the corresponding surface hydration properties to evaluate $G(\lambda)$ using Eq. 39. The resulting surface tension as a function of cavity size at 25 C is shown in Fig. 11. While Eqs. 37 and 38 for the surface tension are zero for a cavity of zero size and converge to the same ultimate value for an infinite cavity ($\gamma = 0.411 \text{ kJ/mol-}\text{\AA}^2 = 72 \text{ dyn/cm}$) assuming the saturation pressure of water is negligible, they differ at intermediate molecular sizes. In particular, Eq. 37 nearly attains its plateau value for cavities on the order of 5 to 10 \AA in radius, while Eq. 38 more slowly approaches the large sphere limit and is still less than $0.4 \text{ kJ/mol-}\text{\AA}^2$ for the largest sizes considered. Particularly interesting is the temperature dependence of the outer shell cavity hydration free energy; Fig. 11 shows a distinct negative entropy for hydrophobic hydration for molecularly sized cavities that dominates the hydration free energy and is consistent with the known thermodynamic characteristics of small hydrophobe hydration. With increasing cavity size the entropy changes sign and becomes favorable with increasing size, approaching the surface free energy of a flat surface. Drying phenomena are, of course, not a separate issue for this revised scaled particle model[52, 43, 55].

The formula Eq. 36 gives a contribution of 9 kcal/mol, which represents the work of rearranging water to grow an empty cavity of radius $R=3.9\text{\AA}$ corresponding approximately to the distance of the inner shell water molecules in minimum energy cage structures discussed below. The first-order perturbation theory estimate [2] of the effects of dispersion interactions between the Kr solute and outer shell water molecules is $-\frac{16\pi\epsilon}{3}(\frac{\sigma}{R_0})^3\rho_W\sigma^3$; with $\epsilon=0.19 \text{ kcal/mol}$, and $\sigma=3.38\text{\AA}$, the Lennard-Jones parameters for Kr-W van der Waals interactions, this is roughly -3 kcal/mol with $R_0=3.9\text{\AA}$.

We conclude this discussion by emphasizing the important point that this treatment of the outer shell term gives a positive contribution, roughly 6 kcal/mol. The experimental value for the hydration free energy of Kr(aq) is roughly 2 kcal/mol [10]. Although these observations are straightforward, the non-trivial implication here is that inner shell contribution must be *negative* and of comparable size.

Inner Shell Structures and Contributions

The advantage of the quasi-chemical formulation is that Eq. 35 is a reasonable initial approximation to the equilibrium constants for complex formation in solution, the quantities sought for the inner shell contribution to the solute hydration free energy. The harmonic approximation to $K_m^{(0)}$ is available from electronic structure calculations.

Fig. 6 shows inner shell structures that have been obtained and we note some basic observations. Firstly, these complexes are large enough that satisfactory electronic structure calculations are non-trivial[42]. Secondly, finding mechanically stable structures for these complexes is non-trivial, particularly for values of $n<18$.

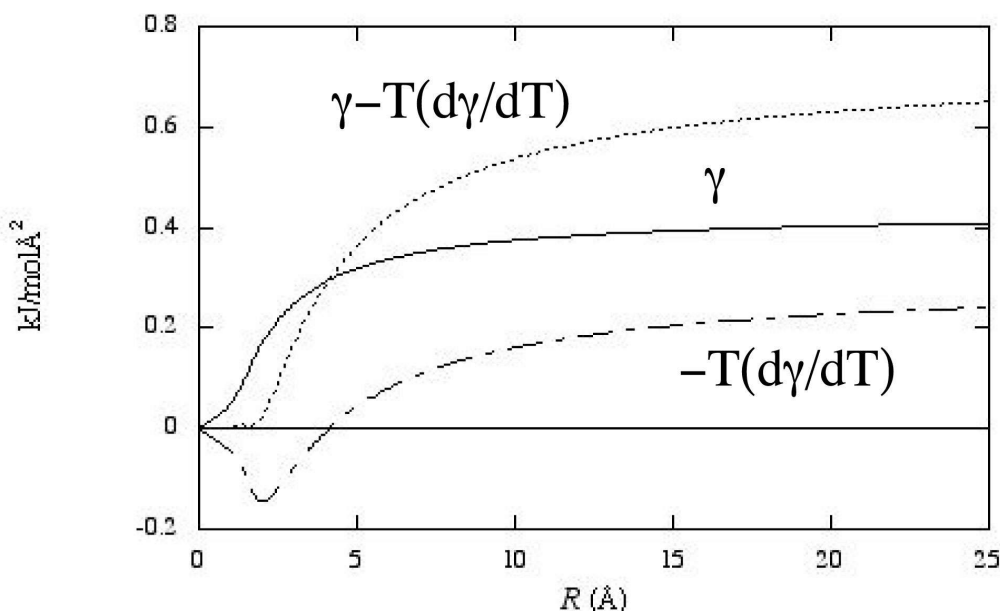


Figure 11. Apparent surface tension γ , and its temperature dependence, predicted by the revised scaled particle model Eq. 37 at 25 C, as a function of inner shell cavity radius. Where the solid curve exceeds the dotted curve, entropic contributions increase the value of this apparent surface tension.

For example, extracting inner shell structures from the AIMD trajectory and then energy optimizing always resulted in decomposition, *i.e.*, some of the water molecules were repositioned to the outer shell and then $b(\mathbf{j})=0$ for some \mathbf{j} . Finding mechanically stable complexes required some subtlety, as described below, and still only $n \geq 18$ complexes were obtained.

A 20-vertex pentagonal dodecahedron cage, present as the small cavity in all known clathrate hydrate structures [65], was built enclosing a Kr atom in several steps. First we built a carbon cage and minimized that structure with molecular mechanics. Then each vertex of this dodecahedron was replaced by oxygen atoms and hydrogen atoms were added to give a cage composed of water molecules with the Kr embedded inside it. This structure was energy minimized with a molecular mechanics potential for Kr-water interactions. The minimization occurred over multiple stages in which the force constant of a harmonic force restraining the oxygen atoms was progressively decreased. The final structure obtained with a low force constant (5 kcal/mole/Å²) was then subjected to quantum chemical optimization. The $n=19$ and $n=18$ structures were obtained by removal of water molecules from the optimized $n=20$ structure. For the $n=18$ structure, we had to once again go through the routine of employing molecular mechanics before any cage-like structure could be obtained.

Limited computational resources permitted only optimizations using HF/6-31G theory. The quantum

chemical optimizations first employed steepest descent to relax the molecular mechanics structure rapidly with the final geometry obtained using the Newton-Raphson procedure. All calculations were performed using Gaussian [19]. Frequencies (and zero-point and thermal contributions to the free energy) were computed at the HF/6-31G level of theory. Non-negative curvatures confirmed a true minimum. These structures (Fig. 6) are clearly metastable and the difficulty in finding these minima suggests that the catchment volumes are small.

For the single point energies we used the B3LYP hybrid density functional, but with two different basis sets. This functional doesn't account for Kr-H₂O interactions of London dispersion character; but it does treat electrostatic induction phenomena and is adequate for the water-water interactions. We will address this omission of Kr-H₂O dispersion interactions later. The basis sets were 6-31+G(d,p) for all atoms or the 6-31G for Kr and a much larger 6-311+G(2d,p) basis for the O and H atoms. Only the results with the latter choice are presented here (see Table 1).

Table 1. ΔE , electronic energy change upon complexation. ΔG_{corr} , zero-point and thermal corrections upon complexation. ΔG_{298} is the free energy change accounting for the actual density of water, that is the free energy change at 1 atm. pressure is adjusted by $-nRT \ln(1354)$. $\Delta\mu$ is the change in the solvation free energy. $\Delta G(aq)$ is the excess chemical potential of Kr for the assumed hydration structures. All values are in kcal/mole.

n	ΔE	ΔG_{corr}	ΔG_{298}	$\Delta\mu$	$\Delta G(aq)$
18	-195.6	220.6	-52.4	93.0	40.6
19	-204.2	226.6	-59.3	98.4	39.1
20	-218.9	245.9	-59.0	105.7	46.7

The electrostatic contributions required by Eq. 35 for the Kr[H₂O]_n cluster and the individual water molecules were computed using a continuum dielectric model. The exterior of the system was assigned the dielectric constant of liquid water and the interior had a dielectric constant of 1. The calculations were performed using a boundary integral formulation of the governing equations [79], with the surface tessellation obtained using the MSMS program [64]. The partial atomic charges needed in this calculation were ESP charges obtained using the ChelpG procedure in Gaussian [19]. For the charge fitting procedure, the Gaussian default radii for O (1.75Å) and H (1.45Å) atoms were used. For Kr a radius of 2.0Å was used. A radius of 3.0Å for Kr leads to an unphysically high positive charge on the Kr atom and, therefore, was not used. The solvation free energies are, in fact, insensitive to this choice and the values differ by only about 0.6 kcal/mole. Table 1 summarizes the inner shell results.

In the calculations above, the zero-point energies were scaled by a factor of 0.9135. This factor is suitable for the HF/6-31G(d) level and has been used for the present HF/6-31G level calculations. For the cases that we could build closed cages, we would include an approximate correction for residual entropy corresponding to conformational multiplicity. Assuming ideal tetrahedral coordination for each water, this residual entropy amounts to $S/k \approx \ln(3/2)^n$ [48], where n is the number of water molecules in the cage. Further, MP2 level calculations that do treat dispersion interactions between an isolated Kr-water pair suggest a correction that amounts to about -0.3 kcal/mole for each Kr-water pair; the excess chemical potentials would need to be adjusted by this amount also. Thus for the n=18 case, the excess free energy of Kr is 30.9 kcal/mole and

35.9 kcal/mole for the $n=20$ case. With or without these additional corrections, it is clear that the inner shell contribution is in the range of 30-50 kcal/mole, which is an order of magnitude greater than the experimental value of around 2 kcal/mole. Note that accuracies of 2 kcal/mole are barely achievable with all but the highest level of electronic structure methods.

Considering the balance of inner and outer shell contributions, we return to the fact that the accurately known outer shell contributions discussed above are positive and larger than the thermodynamical value. This implies that the inner shell contributions must be negative and about as large in magnitude as the experimental value. Here our estimates for that inner shell contributions are positive and large; this qualitative situation is unlikely to change substantially with more sophisticated electronic structure calculations. We conclude that the effects of the medium external to our clusters are decisive in stabilizing these structures. They must help to pull-open and stabilize the cage. This physical realization is consistent with Sloan’s view that these structures should be visualized as *dandelions* rather than spherical complexes [65].

More specifically, the results of Table 1 suggest that the dielectric model used here to describe the influence of the outer sphere material, though satisfactory for some corresponding ion hydration problems, is not satisfactory for the present application. It is possible that the effective fields, hinted following Eq. 35, which are self-consistent with the known fluid densities and reflect the influence of outer shell material on the K_n ’s [4, 55], should describe these effects more satisfactorily, but resolution of that possibility will remain for subsequent work.

“What are we to tell students?”

Work on the problem of hydrophobic effects has the maturity of many decades of effort; that time scale certainly reflects the difficulty of this theoretical problem. A conceptualization reflecting that maturity might be subtle, expressing the complexity of water as a material, but can be simple. An example of a surprising simple result is the formula

$$\mu_{\text{Kr}(aq)}^{ex} = -A\rho_W(T) + B T \rho_W(T)^2 + C T \quad , \quad (40)$$

with parameters A , B , and C , and $\rho_W(T)$ is the density of liquid water coexistent with its vapor at temperature T [52]. That this formula describes signature hydrophobic thermodynamic properties for small hydrophobic solutes was unanticipated [21], but it would have been unreasonable to hope for a simpler result. This simple formula points to the distinctive equation of state of liquid water as a primary feature of hydrophobicity.

A recent attempt at an answer to “what are we to tell students” appeared in [58]. That attempt tried to produce a faithful physical paraphrase of the recent molecular theories which, though non-committal on simple structural hypotheses, have identified a simple explanation of entropy convergence of hydrophobicities [21, 20, 5]. Here we refine and thus simplify that previous answer.

Several points can be made in preparation for this discussion. Firstly, we note that the revised scaled particle model [67] is the most successful theory of hydrophobicity for spherical solutes [3, 56, 57]. The widely recognized point that “... the orientational arrangement of vicinal water molecules, is absent from the theory” [25] does *not* mean that these theoretical approaches are specifically approximate because of a

neglect of orientational effects. Though the truth-content of this assertion has never changed, reappraisal of molecular theories has made this point explicit over recent years [52, 31, 54]. In fact, the revised scaled particle model along with the Pratt-Chandler theory [53], the information theory models [31, 23], and quasi-chemical treatments [52] specifically do not neglect orientational effects. What is more, because these theoretical models firmly incorporate experimental information [54], they do not assume that H-bonding among water molecules is non-cooperative, as is the case for most computer simulations of aqueous solutions.

Secondly, hydrophobicity as judged by hydration free energy is greatest at moderately elevated temperatures >100 C along the vapor saturation curve, as was emphasized by [45]. This observation may be non-canonical [12, 60, 28]; but the unfavorable hydration free energy of simple hydrophobic species is an objective property of those systems and is largest in these higher temperature thermodynamic states. What is more, the most provoking puzzle for molecular mechanisms of hydrophobic phenomena has always been the apparent increase in attractive strength of hydrophobic effects with increasing temperature for temperatures not too high. This point is experimentally clear in the phenomena of cold-denaturation wherein unfolded soluble proteins fold *upon heating*. [See, for example, [39]. Proteins *are* complex molecules, but in that elastin example no hydrophilic side chains complicated the considerations in that way. And the experimental temperature for collapse upon heating — 27 C — is in the stable range of the liquid phase of water.] This point is conceptually troublesome because the molecular structural pictures, including clathrate models, seem to point to low temperature regimes and behaviors as identifying the essence of hydrophobicity. The discussion of [68], which suggested connections between the behaviors of supercooled liquid water and hydrophobic effects, provides an example of those intuitions.

There are two characteristics of liquid water that are featured in the new answer that we propose. The first characteristic is that the liquid water matrix is stiffer on a molecular scale than are comparative organic solvents when confronted with the excluded volume of hydrophobic molecular solutes [58, 31, 57, 30]. An indication of this relative stiffness is provided by comparison of experimental compressibilities of the usual solvents [52]. We don't give a structural picture for that relative stiffness, but it is due to intermolecular interactions among solvent molecules, H-bonding in the case of liquid water [27]. This stiffness is the principal determinant of the low solubility of inert gases in liquid water. Furthermore, this stiffness is weakly temperature dependent in the case of liquid water. This temperature insensitivity is again suggested by consideration of the isothermal compressibility of water; the temperature variation of that isothermal compressibility displays a minimum at 46 C and low pressure. In theories such as Eq. 39, this stiffness and its temperature dependence is carried by the experimental $g_{OO}(r)$, which is distinctive of liquid water.

[We note in passing, that the liquid-vapor interfacial tension and its temperature dependence, $\gamma_{lv}(T)$, appears also in the model Eq. 39. In previous scaled particle models where this empirical information was not specified, the temperature dependence of the implied $\gamma_{lv}(T)$ was found to be improper [67, 6], though the magnitude of this parameter in the temperature region of most interest was reasonable. In some other important aspects that more primitive scaled particle model was satisfactory [50, 51]. Thus, a reasonable view is that the specific empirical temperature dependence of $\gamma_{lv}(T)$ better resolves the conflicting temperature dependences, but is secondary to the classic hydrophobic temperature dependences that are clearest for submacromolecular scales (see Fig. 11).]

The second characteristic in our answer is the variation of the liquid density along the liquid-vapor co-

existence curve in the temperature regimes of interest here [5]. The critical temperature of liquid water is significantly higher than is the case for the comparative organic solvents. The coefficient of thermal expansion along the coexistence curve, α_σ [63], is typically more than five times smaller for water than for common organic solvents. It is a secondary curiosity that liquid water has a small regime of density increase with increasing temperature; we are interested here in a much broader temperature region. Nevertheless, the densities of typical organic solvents decrease more steadfastly with increasing temperature than does the density of water.

These two points lead to a picture in which the aqueous medium is stiffer over a substantial temperature range and expands with temperature less significantly than the natural comparative solvents. If these structural features of the aqueous medium are thus buffered against normal changes with increasing temperatures, then at higher temperatures the solvent exerts a higher kinetic pressure through repulsive collisions with hydrophobic solutes which don't experience other interactions of comparable significance. These collisions are proportionally more energetic with increasing temperature and the aqueous environment thus becomes more unfavorable for hydrophobic solutes with increasing temperature. The rate of density decrease with increasing temperature eventually does dominate this mechanism at the highest temperatures of interest here, >100 C, and less unconventional behavior is then expected. This is our response to "what are we to tell students?"

If a balancing act minimizing the variations of the structure of the aqueous medium with temperature is possible, it should be a useful trick since it should have the consequence of expanding the temperature window over which biomolecular structures are stable and functional [58].

We emphasize again, as in Ref. [58], that hydrogen bonding, tetrahedrality of coordination, random networks and related concepts are not direct features of this answer. Nevertheless, they are relevant to understanding liquid water; they are elements in the bag of tricks that is used to achieve the engineering consequences that are discussed in the picture above.

Conclusions

The coordination number of Kr in liquid water solution is significantly different from known clathrate hydrate phases. These coordination numbers play a direct role in quasi-chemical descriptions of the hydration thermodynamics. Thus, the coordination number differences between liquid solution and clathrate phases can be expected to lead to substantial thermodynamic effects. In these respects, a clathrate picture is not supported by our current information on the molecular scale hydration of Kr(aq); the euphemism 'clathrate-like' has to be understood as 'clathrate-unlike' in these respects.

The present results for the distribution of Kr(aq) coordination numbers give no suggestion of lower probability, metastable coordination structures that might reflect the coordination possibilities in a known, lower temperature, clathrate hydrate phase; see Fig. 9.

The isolated inner shell $\text{Kr}[\text{H}_2\text{O}]_n$ complexes that have been obtained for $n=18, 19$, and 20 have a delicate stability. Inner shell complexes for $n<18$ were not found here and therefore possibilities for inner shell complexes that cover the coordination number range observed in the simulation were not found. When inner shell

coordination structures were extracted from the simulation of the liquid, and then subjected to quantum chemical optimization, they decomposed. Evidently, interactions with the outer shell material can be decisive in stabilizing coordination structures observed in liquid solution and in clathrate phases.

Although quasi-chemical approaches are formally exact and efficient in applications to the hard sphere fluid [4, 55] and to ion hydration problems [62, 61], these *ab initio* quasi-chemical theories applied to Kr(aq) will be more difficult. Several contributions have to be assembled that are an order-of-magnitude larger than the net result for the hydration free energy. Modest errors in any one of those several contributions can easily destroy any reasonable correspondence with experimental results.

We have developed a response to the “what are we to tell students” question that is based upon the known thermodynamic peculiarities of liquid water and doesn’t require specific molecular structural hypotheses. In addition, we can tell students that although the primitive concepts of hydrophobic effects based upon water-oil fluid phase separation are reasonable, the structural molecular conceptualizations of hydrophobic effects, such as clathrate models, have achieved *no* consensus.

A lack of specificity and quantitateness in the thermodynamic analyses of these molecular pictures contributes to this lack of consensus. We can tell students that there is an orthodox clathrate picture that is not literally correct. A reformed ‘clathrate-like’ picture also appears in the extant literature; this reformed picture suggests connections to the orthodox picture, and could be regarded as a poetic ‘explanation,’ borrowing Stillinger’s identification of a limiting possibility. Established quantitative connections to signature thermodynamic properties aren’t available for either the orthodox or the reformed ‘clathrate-like’ pictures of hydrophobic hydration.

Despite the fact that the various molecular scale pictures have not been proven, a role for molecular theory in this setting can follow the conventional understanding of scientific inference: approximate theories should provide clear expression of a physical idea at a molecular level and should be quantitatively testable. The degree of success in those tests then contributes to the degree of confidence in the physical pictures. Molecular mechanisms that are tested only at an impressionistic level, even after an investment in quantitative computer simulations, are less conclusive.

This discussion leads to consideration of Ockham’s razor [29]. For thermodynamics of primitive hydrophobic effects, we have simple, logical, well-tested molecular theories [52] and those theories don’t explicitly involve structural mechanisms such as clathrate models. Additional hypotheses in response to “what are we to tell students” aren’t required at this stage.

Acknowledgements

The work was supported by the US Department of Energy, contract W-7405-ENG-36, under the LDRD program at Los Alamos and Sandia.

References

- [1] G. Alagona and A. Tani. Structure of a dilute aqueous-solution of argon: Monte-Carlo simulation. *J. Chem. Phys.*, 72:580–588, 1980.
- [2] M. P. Allen and D. J. Tildesley. *Computer Simulation of Liquids*. Oxford Science Publications, Oxford, 1987.
- [3] H. S. Ashbaugh and M. E. Paulaitis. Effect of solute size and solute-water attractive interactions on hydration water structure around hydrophobic solutes. *J. Am. Chem. Soc.*, 123:10721–10728, 2001.
- [4] H. S. Ashbaugh and L. R. Pratt. A quasi-chemical self-consistent field model for the statistical thermodynamics of the hard sphere fluid. *unpublished work*, vvv:ppp–ppp, 2002.
- [5] H. S. Ashbaugh, T. M. Truskett, and P. G. Debenedetti. A simple molecular thermodynamic theory of hydrophobic hydration. *J. Chem. Phys.*, 116(7):2907–2921, February 2002.
- [6] A. Ben-Naim and H. L. Friedman. On the application of the scale particle theory of aqueous solutions of nonpolar gases. *J. Phys. Chem*, 71:448–449, 1967.
- [7] D. T. Bowron, A. Filipponi, M. A. Roberts, and J. L. Finney. Hydrophobic hydration and the formation of a clathrate hydrate. *Phys. Rev. Letts.*, 81:4164–4167, 1998.
- [8] D. Chandler, J. D. Weeks, and H. C. Andersen. Van der Waals picture of liquids, solids, and phase-transformations. *Science*, 220:787–794, 1983.
- [9] Y.K. Cheng and P. J. Rossky. Surface topography dependence of biomolecular hydrophobic hydration. *Nature*, 392:696–699, 1998.
- [10] H. L. Clever, ed., Krpton, Xenon, and Radon – Gas Solubilities, volume 2 of *Solubility Data Series*. 1 Pergamon Press, New York, 1979.
- [11] K. A. Dill. Dominant forces in protein folding. *Biochem.*, 29:7133–7155, 1990.
- [12] K. A. Dill. The meaning of hydrophobicity. *Science*, 250:297–297, 1990.
- [13] Y. A. Dyadin, E. G. Larionov, A. Y. Manakov, F. V. Zhurko, E. Y. Aladko, T. V. Mikina, and V. Y. Komarov. Clathrate hydrates of hydrogen and neon. *Mendeleev Comm.*, pages 209–210, 1999.
- [14] D. Eisenberg and W. Kauzmann. *The Structure and Properties of Water*. Oxford University Press, New York, 1969.
- [15] A. Filipponi, D. T. Bowron, C. Lobban and J. L. Finney. Structural determination of the hydrophobic hydration shell of Kr. *Phys. Rev. Lett.*, 79:1293–1296, 1997.
- [16] O. K. Forrisdahl, B. Kvamme, and A. D. J. Haymet. Methane clathrate hydrates: Melting, supercooling, and phase separation from molecular dynamics computer simulations. *Mol. Phys.*, 89:819–834, 1996.
- [17] H. S. Frank and M. W. Evans. Free volume and entropy in condensed systems. III. Entropy in binary liquid mixtures; partial molal entropy in dilute solutions; structure and thermodynamics of aqueous electrolytes. *J. Chem. Phys.*, 13:507, 1945.

- [18] H. L. Friedman and C. V. Krishnan. *Water A Comprehensive Treatise*, volume 3, 1–118. Plenum Press, New York, 1973.
- [19] M. J. Frisch. *et al.* Gaussian 98 (Revision A.2), 1998. Gaussian, Inc., Pittsburgh PA.
- [20] S. Garde and H. S. Ashbaugh. Temperature dependence of hydrophobic hydration and entropy convergence in an isotropic model of water. *J. Chem. Phys.*, 115:977–982, 2001.
- [21] S. Garde, G. Hummer, A. E. García, M. E. Paulaitis, and L. R. Pratt. Origin of entropy convergence in hydrophobic hydration and protein folding. *Phys. Rev. Lett.*, 77:4966–4968, 1996.
- [22] D. N. Glew. Aqueous solubility and the gas-hydrates. The methane-water system. *J. Phys. Chem.*, 66:605–609, 1962.
- [23] M. A. Gomez, L. R. Pratt, G. Hummer, and S. Garde. Molecular realism in default models for information theories of hydrophobic effects. *J. Phys. Chem. B*, 103:3520–3523, 1999.
- [24] P. Grabowski, D. Riccardi, M. A. Gomez, D. Asthagiri, and L. R. Pratt. Quasi-chemical theory and the standard free energy of $H^+(aq)$. *J. Phys. Chem. A*, 106:9145–9148.
- [25] B. Guillot and Y. Guissani. A computer simulation study of the temperature dependence of the hydrophobic hydration. *J. Chem. Phys.*, 99:8075–8094, 1993.
- [26] T. Head-Gordon. Is water-structure around hydrophobic groups clathrate-like? *Proc. Nat. Acad. Sci. USA*, 92:8308–8312, 1995.
- [27] T. Head-Gordon and F. H. Stillinger. An orientational perturbation-theory for pure liquid water. *J. Chem. Phys.*, 98:3313–3327, 1993.
- [28] J. Herzfeld. Understanding hydrophobic behavior. *Science*, 253:88–88, 1991.
- [29] R. Hoffman, V. I. Minkin, and B. K. Carpenter. Ockham’s razor and chemistry. *HYLE: Int. J. Phil. Chem.*, 3:3–28, 1997.
- [30] G. Hummer, S. Garde, A. E. García, M. E. Paulaitis, and L. R. Pratt. Hydrophobic effects on a molecular scale. *J. Phys. Chem. B*, 102:10469–10482, 1998.
- [31] G. Hummer, S. Garde, A. E. García, and L. R. Pratt. New perspectives on hydrophobic effects. *Chem. Phys.*, 258:349–370, 2000.
- [32] W. Kauzmann. Some factors in the interpretation of protein denaturation. *Adv. Protein Chem.*, 14:1–63, 1959.
- [33] I. M. Klotz. Protein hydration and behavior. *Science*, 128:815–822, 1958.
- [34] V. I. Kosyakov and V. A. Shestakov. Simulation of phase equilibria in the water-helium and water-neon systems. *Russ. J. Phys. Chem.*, 76:716–719, 2002.
- [35] G. Kresse and J. Furthmüller. Efficient iterative schemes for ab initio total-energy calculations using a plane-wave basis set. *Phys. Rev. B*, 54:11169, 1996.
- [36] G. Kresse and J. Hafner. Ab initio molecular-dynamics for liquid-metals. *Phys. Rev. B*, 47:RC558, 1993.

- [37] G. Kresse and J. Hafner. Norm-conserving and ultrasoft pseudopotentials for first-row and transition-elements. *J. Phys: Condens. Matter*, 6:8245, 1994.
- [38] T. Lazaridis. Solvent size vs cohesive energy as the origin of hydrophobicity. *Acc. Chem. Res.*, 34:931–937, 2001.
- [39] B. Li, D. O. V. Alonso, and V. Daggett. The molecular basis for the inverse temperature transition of elastin. *J. Mol. Bio.*, 305:581–592, 2001.
- [40] L. A. Lipscomb, F. X. Zhou, and L. D. Williams. Clathrate hydrates are poor models of biomolecule hydration. *Biopolymers*, 38:177–181, 1996.
- [41] J. P. Long and E. D. Sloan Jr. Quantized water clusters around apolar molecules. *Molec. Sim.*, 11:145–161, 1993.
- [42] R. Ludwig and F. Weinhold. Quantum cluster equilibrium theory of liquids: Freezing of QCE/3-21G water to tetrakaidecahedral “Bucky-ice”. *J. Chem. Phys.*, 110:508–515, 1999.
- [43] K. Lum, D. Chandler, and J. D. Weeks. Hydrophobicity at small and large length scales. *J. Phys. Chem. B*, 103:4570–4577, 1999.
- [44] W. L. Mao, H.-K. Mao, A. F. Goncharov, V. V. Struzhkin, Q. Guo, J. Hu, J. Shu, R. J. Hemley, M. Somayazulu, and Y. Zhao. Hydrogen clusters in clathrate hydrate. *Science*, 297:2247–2249, 2002.
- [45] K. P. Murphy, P. L. Privalov, and S. J. Gill. Common features of protein unfolding and dissolution of hydrophobic compounds. *Science*, 247:559–561, 1990.
- [46] J. C. Owicki and H. A. Scheraga. Monte Carlo calculations in isothermal-isobaric ensemble. 2. dilute aqueous-solution of methane. *J. Am. Chem. Soc.*, 99:7413–7418, 1977.
- [47] M. E. Paulaitis and L. R. Pratt. Hydration theory for molecular biophysics. *Adv. Prot. Chem.*, 62:in press, 2002.
- [48] L. Pauling. The structure and entropy of ice and of other crystals with some randomness of atomic arrangement. *J. Am. Chem. Soc.*, 57:2680–2684, 1935.
- [49] L. Pauling. The structure of water. In D. Hadži, editor, *Hydrogen Bonding*, pages 1–6, New York, 1959. Pergamon.
- [50] R. A. Pierotti. The solubility of gases in liquids. *J. Phys. Chem.*, 67:1840–1845, 1963.
- [51] R. A. Pierotti. A scaled particle theory of aqueous and nonaqueous solutions. *Chem. Rev.*, 76:717–726, 1976.
- [52] L. R. Pratt. Molecular theory of hydrophobic effects: ‘She is too mean to have her name repeated’. *Annu. Rev. Phys. Chem.*, 53:409–436, 2002.
- [53] L. R. Pratt and D. Chandler. Theory of the hydrophobic effect. *J. Chem. Phys.*, 67:3683–3704, 1977.
- [54] L. R. Pratt, G. Hummer, and S. Garde. Theories of hydrophobic effects and the description of free volume in complex liquids. In C. Caccamo, J.-P. Hansen, and G. Stell, editors, *New Approaches to Problems in Liquid State Theory*, volume 529, pages 407–420. Kluwer, Netherlands, 1999. NATO Science Series.

- [55] L. R. Pratt, R. A. LaViolette, M. A. Gomez, and M. E. Gentile. Quasi-chemical theory for the statistical thermodynamics of the hard-sphere fluid. *J. Phys. Chem. B*, 105:11662–11668, 2001.
- [56] L. R. Pratt and A. Pohorille. Theory of hydrophobicity: Transient cavities in molecular liquids. *Proc. Natl. Acad. Sci. USA*, 89:2995–2999, 1992.
- [57] L. R. Pratt and A. Pohorille. Hydrophobic effects from cavity statistics. In M. U. Palma, M. B. Palma-Vittorelli, and F. Parak, editors, *Proceedings of the EBSA 1992 International Workshop on Water-Biomolecule Interactions*, pages 261–268, Bologna, 1993. Società Italiana de Fisica.
- [58] L. R. Pratt and A. Pohorille. Hydrophobic effects and modeling of biophysical aqueous solution interfaces. *Chem. Rev.*, 102:2671–2691, 2002.
- [59] L. R. Pratt and S. B. Rempe. Quasi-chemical theory and implicit solvent models for simulations. In L. R. Pratt and G. Hummer, editors, *Simulation and Theory of Electrostatic Interactions in Solution. Computational Chemistry, Biophysics, and Aqueous Solutions*, volume 492 of *AIP Conference Proceedings*, pages 172–201. American Institute of Physics, Melville, NY, 1999.
- [60] P. L. Privalov, S. J. Gill, and K. P. Murphy. Reply to Dill. *Science*, 250:297–297, 1990.
- [61] S. B. Rempe and L. R. Pratt. The hydration number of Na^+ in liquid water. *Fluid Phase Equilibria*, 183:121–132, 2001.
- [62] S. B. Rempe, L. R. Pratt, G. Hummer, J. D. Kress, R. L. Martin, and A. Redondo. The hydration number of Li^+ in liquid water. *J. Am. Chem. Soc.*, 122:966–967, 2000.
- [63] J. S. Rowlinson and F. L. Swinton. *Liquids and Liquid Mixtures*. Butterworths, London, 1982.
- [64] M. F. Sanner, J.-C. Spohner, and A. J. Olson. Reduced surface: an efficient way to compute molecular surfaces. *Biopolymers*, 38:305–320, 1996.
- [65] E. D Sloan Jr. *Clathrate Hydrates of Natural Gases*. Marcel Dekker, Inc., New York, 2nd, revised and expanded edition, 1998.
- [66] N. T. Southall, K. A. Dill, and A. D. J. Haymet. A view of the hydrophobic effect. *J. Phys. Chem. B*, 106:521–533, 2002.
- [67] F. H. Stillinger. Structure in aqueous solutions of nonpolar solutes from the standpoint of scaled-particle theory. *J. Sol. Chem.*, 2:141–158, 1973.
- [68] F. H. Stillinger. Water revisited. *Science*, 209:451–457, 1980.
- [69] S. Swaminathan, S. W. Harrison, and D. L. Beveridge. Monte Carlo studies on structure of a dilute aqueous-solution of methane. *J. Am. Chem. Soc.*, 100:5705–5712, 1978.
- [70] W. C. Swope and H. C. Andersen. A molecular-dynamics method for calculating the solubility of gases in liquids and the hydrophobic hydration of inert-gas atoms in aqueous-solution. *J. Phys. Chem.*, 88:6548–6556, 1984.
- [71] C Tanford. How protein chemists learned about the hydrophobic factor. *Protein Science*, 6:1358–1366, 1997.

- [72] M. M. Teeter. Water-structure of a hydrophobic protein at atomic resolution: Pentagon rings of water-molecules on crystals of crambin. *Proc. Nat. Acad. Sci. USA*, 81:6014–6018, 1984.
- [73] J. S. Tse, M. L. Klein, and I. R. McDonald. Molecular-dynamics studies of ice Ic and the structure-I clathrate hydrate of methane. *J. Phys. Chem.*, 87:4198–4203, 1983.
- [74] K. A. Udachin, C. I. Ratcliffe, and J. A. Ripmeester. A dense and efficient clathrate hydrate structure with unusual cages. *Angew. Chem. Int. Ed.*, 40:1303–+, 2001.
- [75] K. A. Udachin and J. A. Ripmeester. A complex clathrate hydrate structure showing bimodal guest hydration. *Nature*, 397:420–423, 1999.
- [76] D. Vanderbilt. Soft self-consistent pseudopotentials in a generalized eigenvalue formalism. *Phys. Rev. B* 41:7892, 1990.
- [77] Y. Wang and J. P. Perdew. Correlation hole of the spin-polarized electron gas with exact small-wave-vector and high-density scaling. *Phys. Rev. B*, 44:13298, 1991. 13298.
- [78] K. Watanabe and H. C. Andersen. Molecular-dynamics study of the hydrophobic interaction in an aqueous-solution of krypton. *J. Phys. Chem.*, 90:795–802, 1986.
- [79] B. J. Yoon and A. M. Lenhoff. A boundary element method for molecular electrostatics with electrolyte effects. *J. Comp. Chem.*, 11:1080–1086, 1990.

3 Ion Transport Proteins

Applying the statistical mechanics of inhomogeneous fluids to protein solvation II: Gramicidin A as a test case

Laura J. Douglas Frink³, Andrew G. Salinger, Marcus Martin, and Martha Mitchell⁴

Abstract

In paper I of this series we presented a molecular theory based approach for treating protein solvation. In this paper we present a more detailed investigation of solvation and ion transport through the gramicidin A ion channel. This small dipeptide forms a transmembrane pore of particularly simple structure. Using the atomic coordinates from the protein data bank coupled with the Charm-22 force field to define atom sizes and partial charges, we have performed 3-dimensional density functional theory calculations to determine the equilibrium electrolyte distribution in this channel. In this paper we compare results for both a Poisson-Boltzmann electrolyte where the ions are point charges and water is a dielectric continuum and an atomic model where the ions have finite size, and the water is treated as a dense neutral hard sphere fluid.

Introduction

In paper I, we presented a molecular theory based approach for treating solvated biological macromolecules. In this paper, we apply that theory more specifically to the gramicidin A ion channel. The structure of gramicidin A is known to high resolution, and it has been thoroughly investigated with both experiments and with other molecular modeling approaches. The goal of this paper is to demonstrate how our molecular theory based approach can contribute to the understanding of gramicidin A and by extension to other problems in protein solvation. We also chose this ion channel case to facilitate discussion of the extension of our methods to systems that are not at equilibrium.

In paper I, we discussed proteins in equilibrium fluids, and demonstrated that the potential of mean force (PMF) for a fluid atom or ion near a protein can be computed via two routes. In both cases, DFT is used to compute inhomogeneous density distributions, $\rho(\mathbf{r})$, around fixed explicit surfaces. More specifically, there is a free energy route where both a fluid atom (or ion) and the protein are treated explicitly as surfaces and the PMF is computed by moving the position of the fluid particle relative to the protein, solving for the inhomogeneous density distribution, $\rho(\mathbf{r})$ around both of them. Ultimately the PMF, W is as a function of the surface excess grand potential, Ω^s as

$$W(\mathbf{r}_i) = U(\mathbf{R}_N) + \Omega^s[\rho(\mathbf{r}), \mathbf{R}_N] - \Omega^s[\rho(\mathbf{r}), \infty] \quad (41)$$

where \mathbf{R}_N represents the coordinates of the explicit surface(s) in the system. The free energies, Ω^s are surface excess grand free energies and are computed in an open ensemble where the bulk concentrations of the fluid are known, but the adsorption of fluid at the protein surface is unknown a priori. Note that when $\mathbf{R}_N = \infty$, the ion is infinitely far from the protein surface. Finally, the energy U is just the potential energy between the explicit atom (or ion) and the protein.

³corresponding author:: ljfrink@sandia.gov

⁴Chemical Engineering Department, New Mexico State University, Las Cruces, NM , USA

The alternate route is based on a classic McMillian-Mayer approach where only the protein is represented as a surface. In this case, the PMF for species, i in the field of the protein is simply

$$W_i(\mathbf{r}_i) = -kT \ln(\rho_i(\mathbf{r})/\rho_{b,i}) \quad (42)$$

where $\rho_{b,i}$ is the bulk number density of species i . While this approach is not available when computing protein-protein interactions, it is particularly useful when studying ion channel proteins. In this case the distribution of fluid species (e.g. the ions) in a channel, and the energy barriers experienced by those ions as they traverse the channel are of critical importance. These energy barriers are given by the potential of mean force, $W(r)$ above. So, in the calculations presented here, the gramicidin channel will be represented as a surface, and a single 3-dimensional DFT calculation provides $\rho(\mathbf{r})$ and $W(\mathbf{r})$ via Eq.48.

One additional complexity of the ion channel systems is that some of the relevant experiments are not performed at equilibrium. Rather, in patch-clamp experiments, a voltage is applied across a membrane, and the current passing through the channel is measured. One is generally interested in understanding the ramifications of those applied voltages on both solvation of the channels and transport through the channels. In order to model these nonequilibrium problems a few modifications to the theory presented in paper I are required.

In the remainder of this paper we detail how our molecular theory approach is modified to accommodate nonequilibrium fluids (section II), present the model we have used to compute potentials of mean force in the gramicidin A channel (section III), present DFT calculations for two simple systems of finite length nanotubes (section IV) as well as for the gramicidin A channel (section V).

Solvation in nonequilibrium fluids

As was discussed above, ion channels generally operate in nonequilibrium environments in vivo since the intracellular and extracellular fluids have different ionic contents. Furthermore in patch clamp experiments electric fields provide a driving force for transport through the channels. In either case, there is an electrochemical potential difference between the fluid on the two sides of the membrane. However, if we take the steady state limit, we can modify the DFT approach and the PMF expressions quite easily to treat the inhomogeneous electrochemical potential boundary conditions.

First, the inhomogeneous boundary conditions must provide a driving force for transport of the fluid. We have previously discussed how diffusion equations can be coupled to the DFT approach. We will not reproduce all of the arguments here except to say that the key is to recognize that the electrochemical potential, μ is not a constant, but rather an additional unknown field. The grand free energy is now

$$\Omega[\rho_{\{i\}}(\mathbf{r})]/kT = \sum_i \int \rho_i(\mathbf{r}) [\ln \Lambda \rho_i(\mathbf{r}) - 1] + F^{ex}[\rho_{\{i\}}(\mathbf{r})] + \sum_i \int \rho_i(\mathbf{r}) [\mu_i(\mathbf{r}) - V_i(\mathbf{r})]. \quad (43)$$

More specifically for an electrolyte fluid, we solve the Euler-Lagrange equations that are based on a functional minimization of the free energy defined in Eq.43. These expressions are discussed in more detail in paper I; here we simply summarize that the system of equations to solve is

$$\ln(\rho_i(\mathbf{r})) = \mu(\mathbf{r}) - \beta(V_i^{NC}(\mathbf{r}) + z_i e \phi(\mathbf{r}) + \frac{\delta F^{ex}}{\delta \rho(\mathbf{r})}). \quad (44)$$

coupled to Poisson's equation

$$\nabla^2 \phi(\mathbf{r}) = -\frac{4\pi}{\kappa\epsilon_o} \left(\sum_i \rho_i(\mathbf{r}) + \rho^f(\mathbf{r}) \right) \quad (45)$$

and in addition coupled to a diffusion equation defined by the steady state condition

$$\nabla \cdot J_i = 0. \quad (46)$$

The unknown fields are $\rho_i(\mathbf{r})$, $\phi(\mathbf{r})$, and $\mu_i(\mathbf{r})$. The noncoulombic part of the external field is given by $V_i^{NC}(\mathbf{r})$, and the excess Helmolzt free energy, F^{ex} also includes only non-Coulombic contributions.

We apply a simple diffusion equation to model transport where the diffusion of all species is assumed to be independent. Specifically,

$$J_i = -D_i \rho_i(\mathbf{r}) \nabla \mu_i(\mathbf{r}) / kT. \quad (47)$$

In the steady state limit with this independent diffusion model, the diffusion constants are not needed for calculation of the unknown fields. They are only needed for the final calculation of the flux. Since these diffusion constants are unknowns, we use experimental measures of the flux and our DFT calculations of $\rho(\mathbf{r}) \nabla \mu_i(\mathbf{r})$ to calculate and test the assumption of constant diffusion coefficients in section V this paper.

Finally, Roux has previously derived the expression for the potential of mean force when there are inhomogeneous electrochemical potential boundary conditions, and has shown that it is now

$$W_i(\mathbf{r}) = \mu_i(\mathbf{r}) - \mu_i^r - kT \ln(\rho_i(\mathbf{r}) / \rho_i^r) \quad (48)$$

where one of the bulk boundaries (intracellular or extracellular) is arbitrarily set to be the reference fluid. The potential of mean force is then measured with respect to that reference fluid.

We note that in a previous paper we demonstrated that this coupled diffusion-DFT approach can produce accurate results for density profiles, chemical potential profiles and flux predictions by direct comparison of this transport-DFT approach with grand canonical molecular dynamics (GCMD) simulations. Steady state diffusion is modeled in the GCMD method by setting up control volumes at the two ends of the computational domain, and performing particle insertions and deletions in those regions in order to maintain a constant chemical potential. Straightforward molecular dynamics is performed between the two control volumes, and the flux is measured by counting particles as they pass fixed planes perpendicular to the direction of diffusion. In our previous paper, we performed calculations on a fluid diffusing through a planar membrane that was attractive to one species and repulsive to the other. Those calculations confirmed the viability of a transport-DFT approach at the molecular level.

In the context of ion channels, several groups have effectively been performing transport-DFT calculations as outlined above for some time. In the limit of the Poisson-Boltzman (PB) electrolyte (point charge ions in a continuum dielectric solvent), this approach reduces to what is known as the Poisson-Nernst-Planck (PNP) method. If one models the electrolyte in the PB approximation, then

$$\mu_i / kT = -\ln \rho_i + z_i e \phi. \quad (49)$$

The flux expression given in Eq.47 reduces to the familiar Nernst-Planck equation,

$$J_i = -D_\alpha \frac{1}{\rho(\mathbf{r})} (\nabla \rho(\mathbf{r}) + z_i e \rho(\mathbf{r}) \phi(\mathbf{r})) . \quad (50)$$

Typically in PNP calculations, the steady state version of Eq.50 is then coupled to Poisson's equation (Eq.45) and then solved. The Euler-Lagrange (Eq.49) is not explicitly included. Several detailed studies of 1-dimensional models of ion channel transport have been performed with the PNP approach using a successive substitution iterative technique. In these studies, it is assumed that the charge distribution on the protein can be reduced to an effective Coulomb field on a single line that runs down the center of the channel pore. The diameter of the pore can be allowed to vary with distance down the pore in those models as well. In addition, a few studies have been performed using a 3-dimensional PNP code that is based on a boundary element approach. Those studies showed a remarkable agreement between PNP theory and patch clamp measurements of Sodium transport through gramicidin.

In the work presented in this paper, the DFT Euler-Lagrange equation is always explicitly included in the system of equations because we are interested in extending this approach to treat fluid models with more molecular character than the Poisson-Boltzmann electrolyte (finite size, polarization, dispersion interactions etc.). Our numerical solution is based on a parallel real space 3-dimensional implementation of the DFT. Briefly, the equations are discretized on a cartesian grid. The computational domain may be divided into different regions where mesh coarsening may be applied. A collocation approach is taken for the integral equations (the Euler-Lagrange equations) while a Galerkin finite element approach is used for partial differential equations. We use a parallel iterative solver package (Aztec) to solve these systems of equations on distributed memory parallel computers. We have also recently worked out a Fourier space based algorithm which greatly reduces the computational cost of these DFT calculations. However it is a matrix free method with only limited preconditioning options and its stability for the type of problems presented here is not yet well understood. All of the calculations presented here were done with our real space algorithms using the CPlant commodity cluster at Sandia National Laboratories. Generally, the protein solvation calculations that include finite size ions and solvent took about 2 hours to run on 100 processors of the CPlant cluster.

Description of the models

For the purposes of this work, gramicidin A is treated as a pore with complex geometry and charge distribution. The pore is constructed one atom at a time based on the known 3-dimensional crystal structure of gramicidin A. Two different model electrolyte models will be considered here. One is the Poisson-Boltzmann (PB) electrolyte (point charges in a continuum solvent of constant dielectric constant, $\epsilon = 78$). The second case is a three component (3CM) electrolyte with finite sized ions and solvent particles. The solvent (*water*) particles are neutral and not polarizable. So, the dielectric constant is again assumed to be constant ($\epsilon = 78$) in the fluid volume. The gramicidin pore is embedded in a membrane that is neutral, impermeable, and has a dielectric constant of $\epsilon = 2$. In the 3 component model electrolyte, we consider a restricted primitive model electrolyte where the ions and hard sphere solvent particles all have the same size ($0.3nm$). While this model is crude, it will serve to demonstrate the DFT based approach for studying protein solvation. It also provides an explicit example of the layering of Coulomb and volume exclusion effects, and the relative importance of each for this case. Our current work involves both implementation of better electrolyte models and more sophisticated electrostatics including solvent polarization. However, these more detailed investigations are outside the scope

of this paper.

In the particular model of gramicidin used here, we begin with the 1MAG crystal structure in the protein data bank. In the DFT calculations, the protein is defined by the external field it exerts on the fluid. for the calculations presented here, the external field has two parts. The first part is a hard core repulsion based on the sizes of each of the atoms. The second part are the Coulomb forces due to the partial charges on each of the atoms. We chose to base our atom sizes and partial charges on the Charm-22 force field. However, since our calculations are performed on a mesh, there is some staircasing of the atoms as was shown in paper I in detail. As a result, only limited precision on the atom sizes is relevant for these calculations. For the calculations presented here, the partial charges on each atom were considered to be point charges. As was described in paper I, a point charge is approximated by smearing all of the charge in one element. Provided there is an excluded volume region around the element, the underlying mesh spacing has little impact on the solutions. Clearly this treatment of charge distribution is not completely satisfying. A more precise calculation that couples electronic structure determination with the solvation calculation would be preferable, but is not yet possible.

Potentials of mean force in equilibrium systems

bf Short nanotubes

Before presenting the results for gramicidin A, we first consider a simpler model system that highlights some of the underlying physical features of these small channels. Specifically, we consider two finite length nanotubes embedded in a impermeable membrane. Specifically, the membrane is 6σ thick with a cylindrical pore inserted in it. We will consider pore diameters of $D = 2.4\sigma$ and $D = 1.4\sigma$. Figure 12 shows the fluid density and the PMF as a function of x (the axis running down the length of the pore) for all y and z for both the $D = 2.4\sigma$ and $D = 1.4\sigma$ cases.

Fig.12 shows that the density inside the pore can be much larger than the density at the surface of the membrane. In addition, while the $D = 2.4\sigma$ pore exhibits a 3-dimensional solution inside the pore, the $D = 1.4\sigma$ case exhibits a nearly 1-dimensional solution inside the pore. In the larger pore, there are many different density curves corresponding to different pathways through the pore while in the smaller pore there are only 3 distinct pathways that are nearly identical in their density distributions. This result demonstrates that there is clearly some pore size where it is no longer necessary to consider the pore to be a fully 3-dimensional system. Rather, property averaging in planes will likely be a good approximation.

To further illustrate the difference in these two solution branches, 2-dimensional slices of the PMF are plotted in Fig. 13. For the high density (liquid-like) fluid shown here, $\rho_b\sigma^3 = 0.75$, the extreme confinement of the $D = 1.6\sigma$ pore results in a fluid that is highly ordered in the pore. This packing effect is clear in both the density profile (Fig.12) and the PMF plot (Fig.13) shown above. This packing effect is important from a mechanistic point of view if one considers transport of a fluid particle through the pore. In the larger pore, there are no significant ($O(kT)$) energy barriers for a particle to overcome as it moves through the pore. However, in the small pore, the fluid acts like a 1-dimensional fluid (particles confined to a line), and significant energy barrier between adsorption sites of $O(2kT)$ are found (see Fig.12B). In the larger pore a mechanism for transport may revolve around diffusion of a particle to the pore, and the free energy needed to overcome

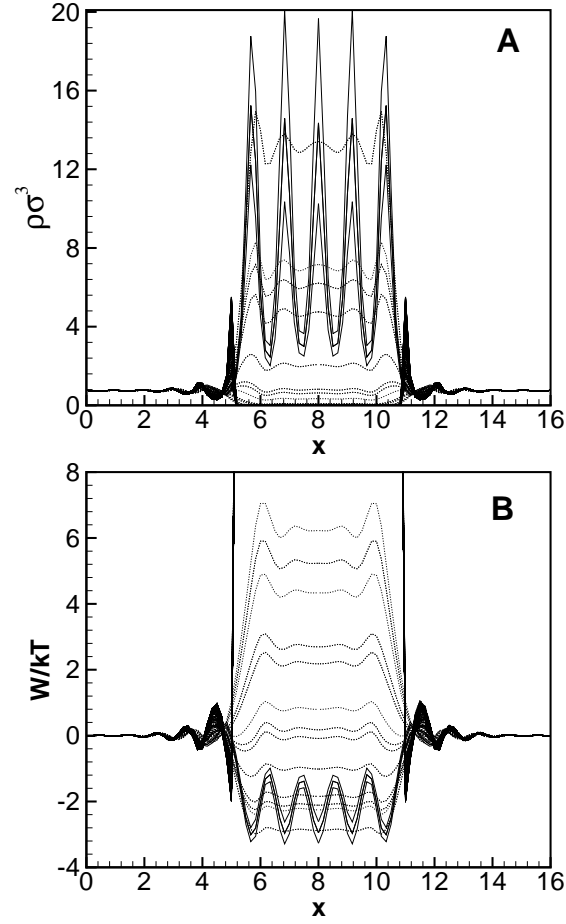


Figure 12. (A)Density, ρ and (B)potentials of mean force, W , for an atom in a dense ($\rho_b = 0.75$) hard sphere fluid adsorbed in a membrane bound pore. The solid lines show a pore with diameter $D = 1.4\sigma$, the dotted lines show a pore with diameter $D = 2.4\sigma$. The mesh density used for the calculations was $h = \sigma/6$.

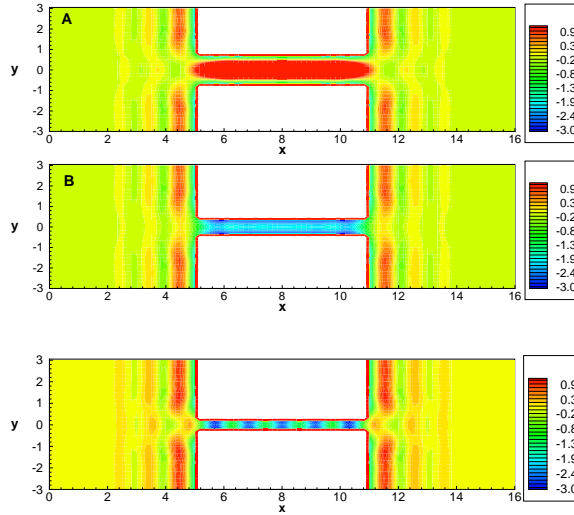


Figure 13. The potential of mean force in slices of the membrane pore domain for a pore diameters of $D = 2.4\sigma$ (top and middle) and $D = 1.4\sigma$ (bottom). The figures show a plane through the center of the $D = 2.4\sigma$ pore at $z = 0$ (top), a plane at $z = 0.6666\sigma$ of the $D = 2.4\sigma$ pore (middle), and a plane through the center of the $D = 1.4\sigma$ pore at $z = 0$ (bottom). Red regions are repulsive, blue regions are attractive.

the potential of mean force barrier on exiting the pore ($O(3kT)$). In the smaller pore, hops between all of the low free energy sites must be considered as well.

Gramicidin A

Now consider the results of DFT calculations for the gramicidin A channel at equilibrium in a system with homogeneous boundaries and no diffusion. The PMFs for both the PB and 3CM models for this case were presented in Fig.4 of paper I. As was mentioned there, the presence of the high density solvent causes significant structuring down the pore on the periodicity of the fluid particle size, σ . However, many important features of the ion distributions are not affected by the presence of the finite sized solvent. Specifically, while gA is net neutral, the charge distribution is such that there are local regions of negative charge at the pore openings with a local region of positive charge in the central region. As a result, cations adsorb strongly at the entrance regions to the pore in both cases.

To consider the nature of the confined fluid more precisely, we show all of the PMF data from the 3-dimensional solution set projected on one line in the z -direction in Figure 14. The mean PMF is also shown as a heavy solid line in these figures. Again, we compare the PB and 3CM fluid models. The first obvious difference between PB and 3CM electrolytes is that the smaller accessible pore volume results in a 1-dimensional fluid in the pore. Just as in the short nanotubes, there is significantly greater variation in the PMF through the pore in the PB case than the 3CM case which can be directly attributed to a decrease in solvent accessible volume. The 1-dimensional nature of the fluid in gA has been known for some time, so it is critical that any molecular theory be able to reproduce this result.

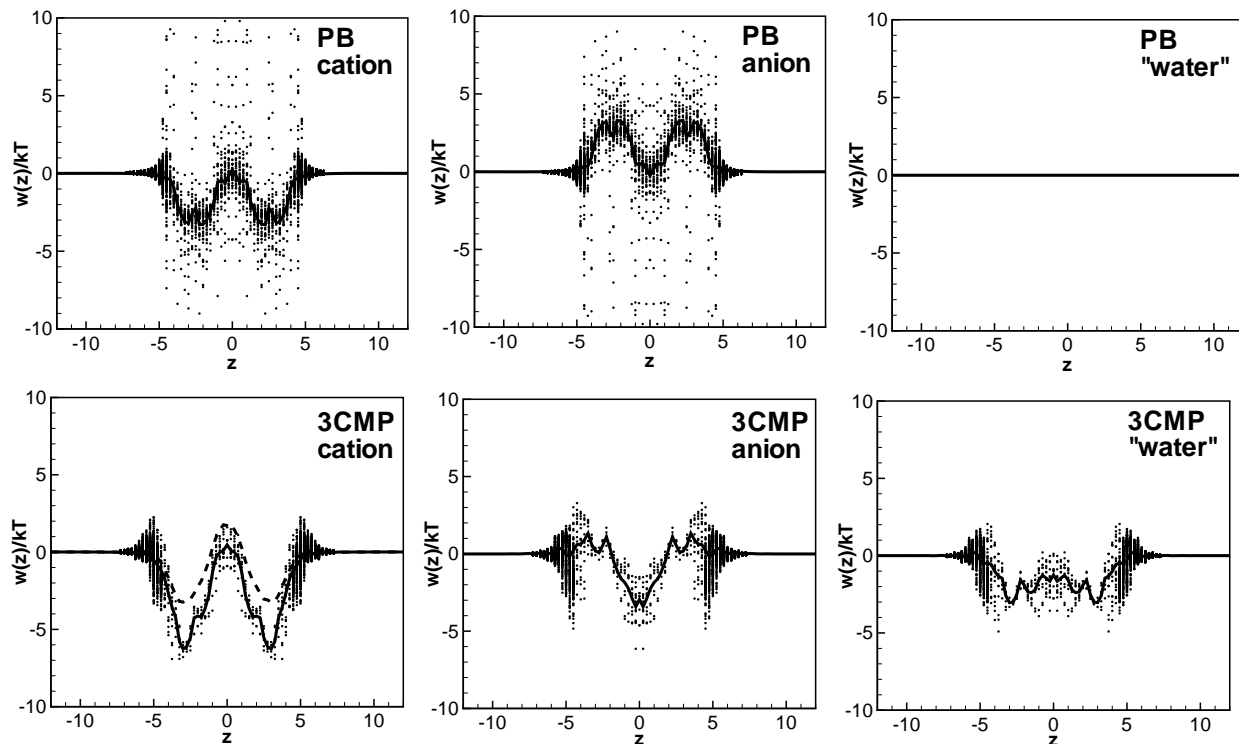


Figure 14. The potential of mean force for a PB electrolyte (top 3 figures) and a 3CM electrolyte (bottom 3 figures) in gramicidin A. In all plots the heavy solid line is an average PMF in a cylinder running through the domain that includes all of the gA pore volume. The dots show the PMF at every mesh point, and so show the spread of data around the mean curves.

The lines in Fig.14 show the mean value of the PMF in a small cylinder running through the volume and including all of the fluid accessible pore volume. Both models show two strong cation adsorption sites (large negative W) at the ends of the pore ($z/\sigma \pm 3$). The details of the average PMF also show some notable differences between the PB and 3CM models. First, the presence of the finite sized solvent introduces packing effects that are superimposed on the PMF. These are most clearly seen in the solvent and anion PMFs of the 3CM where we find characteristic packing oscillations on a period of σ the fluid particle size. Second, the depth of the PMF well for the cations is deeper when volume exclusion is included in the calculation. Third, in the 3CM case, we find negative PMFs for the anion in the center of the pore. That this could occur should not be surprising since there is a net positive charge distribution on this part of gA. However, in practice it is known that gA does not transport anions. There are therefore two possibilities. One is that the current calculations do not capture all of the essential features of the system (e.g. polarization and ion properties) or that the cation adsorption in the entry regions is simply so strong that the anion transport will be very rare.

Potentials of Mean Force in Nonequilibrium systems

Ion Transport through Gramicidin

We now turn to nonequilibrium DFT calculations for a case where the electrolytes on both sides of the membrane are identical, but a voltage is applied across the membrane. In this case we considered both a 1M and 0.1M electrolyte in order to span the complete range of experimental data presented in the literature. Figure 17 shows both the chemical potential and average PMF for the cation as a function of distance in the domain (down the axial length of the gA pore) for a system where the applied potential is nonzero on the left side of the membrane.

This figure shows that as the applied voltage is increased a linear bias is added to the PMF, and this linear bias is primarily due to the background field. There is some change in the occupancy (density distributions) of the two adsorption sites as well, but this effect is not large as can be seen in Fig.16. It is well known that as the applied voltage increases, the ion current also increases. Fig.17 shows that as the electrostatic potential increases, the height of the energy barrier for a cation to move from the left well to the right well is significantly decreased. In contrast, the energy barrier for transport in the opposite direction is increased. This variation alone can explain why an increasing flux should be measured as the electrostatic potential increases. When there is no applied voltage, the energy barriers are identical, and so ions can move either right to left or left to right and will do so with the same probability. When the left to right barrier is smaller than the right to left barrier, the ions will move preferentially to the right.

Finally, we turn to the question of predicting the flux through an ion channel protein such as gramicidin A. This is the critical question if one is interested in tailoring drugs to modify the behavior of a channel or if one is interested in making synthetic ion channels for a variety of nanotechnology applications. In the context of the present model, the distributions, $\rho(\mathbf{r})$, and $\mu(\mathbf{r})$ are computed independent of the diffusion coefficients as a result of the independent diffusion model applied. We therefore, can test this model by calculating

$$J_{exp}/(\rho(\mathbf{r})\nabla\mu(\mathbf{r})) \quad (51)$$

as a function of applied electrostatic field where J_{exp} is the ion flux measured in experiments, and the denominator is computed from the DFT calculations. Figure ?? plots the quantity in Eq.51 over the experimental

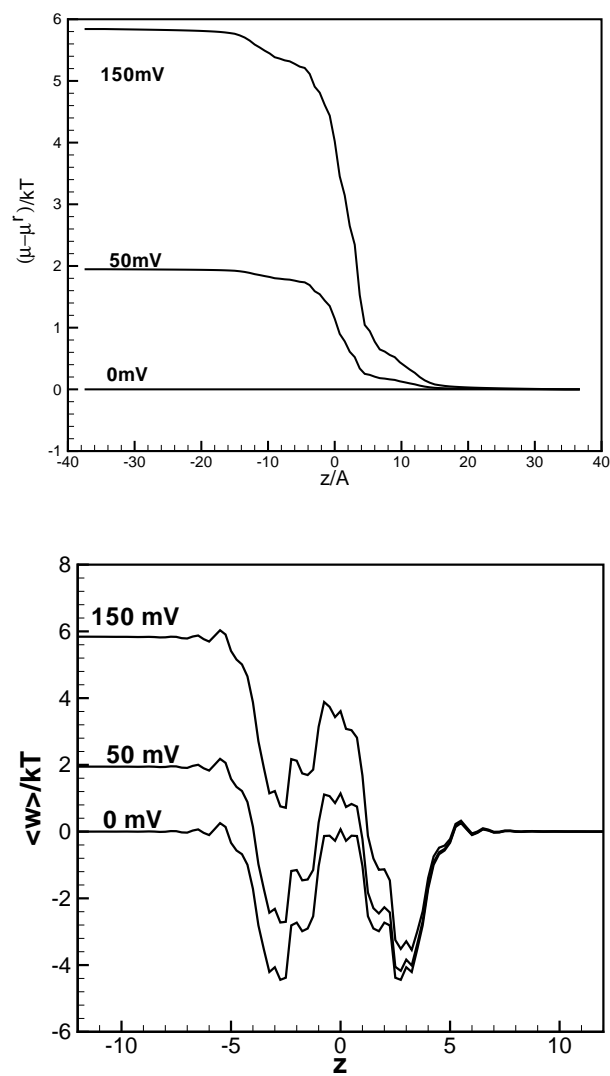


Figure 15. The electrochemical potential (top) and the average potential of mean force (bottom) as a function of distance down the pore for a cation in a 1M 3CM electrolyte moving through gramicidin A. The three curves show different values of an applied electrostatic potential across the membrane.

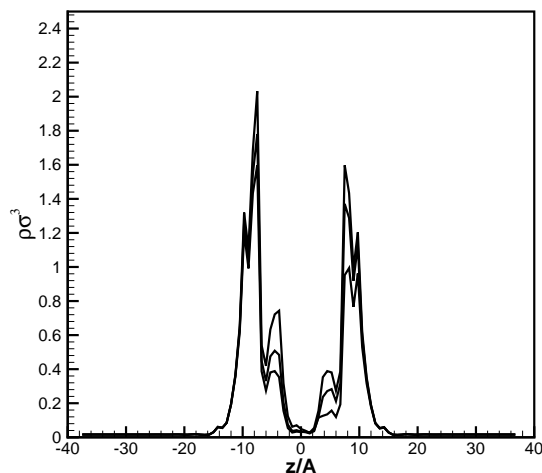


Figure 16. The mean density of the cation in the gramicin pore as a function of distance down the pore for a cation in a 1M 3CM electrolyte. The three curves show different values of an applied electrostatic potential across the membrane.

range of both applied voltage (0-200mV) and electrolyte concentration (0.1M-1M) found in the literature. For these calculations, we have assumed that the flux of the anions is zero and have attributed all of the flux to the cations. In all four cases shown, the diffusion coefficient is relatively constant with applied field. However, the diffusion coefficient is apparently dependent on the bulk concentration of the ions. Interestingly, the line in Fig.?? shows the diffusion coefficient used in [] with a 3-dimensional PB model to compute fluxes in gramicidin A where there was very good agreement with experiment.

There are clearly two approaches one could take to model transport in ion channels. Consistent the diffusive model present here, one could attempt to determine or fit diffusion coefficients and then use the density and electrochemical potential gradients to compute the flux. Alternatively, one could take the view that ion transport should be modeled as a rare event (transition state) process. The latter approach has a long history in the study of the biophysics of ion channels, the former is advocated by those who perform PNP calculations. In this paper we simply show how the DFT based approach presented here provided critical data for either approach. We note that these approaches are not necessarily at odds. Ongoing work on transport in zeolites has shown that there can (depending on the system geometry) be a simple relationship between diffusion coefficients of and the rate constants needed to predict fluxes from a transition state theory.

Conclusions

In this paper we have presented calculations on the gramicidin A channel that are based on a density functional theory approach. We have demonstrated how the Poisson-Boltzman model which leads to the Poisson-Nernst-Plank model of transport can be generalized to more realistic (from a molecular perspective) fluid models. We have demonstrated the approach for both homogeneous boundary conditions (no diffusion) and inhomogeneous

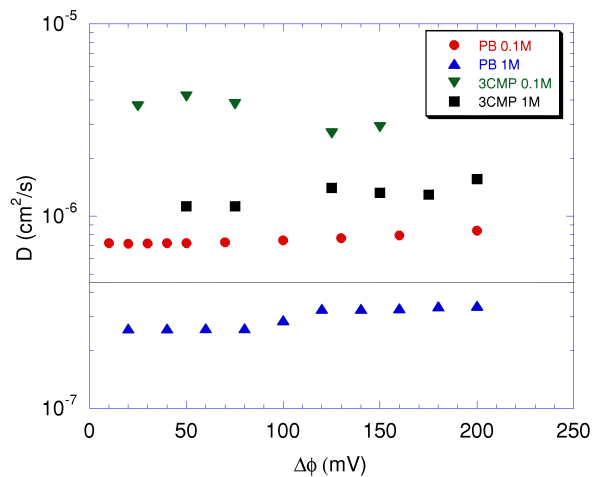


Figure 17. An estimate of diffusion coefficients calculated using the results of DFT calculations and experimentally measured fluxes through the gramicidin A channel. Results from both PB and 3CM models are included as indicated in the legend.

boundary conditions where diffusion is present. In a previous paper we also compared the approach to detailed molecular simulations to demonstrate that the transport-DFT approach could work for inhomogeneous confined fluids.

With respect to gramicidin, our results clearly show that the fluid in the channel is a 1-dimensional fluid (beads on a line) as was expected. When there is significant packing, this 1-dimensional fluid may become a 0-dimensional fluid, and a transition state based model for transport is entirely appropriate due to free energy barriers between adsorption sites. The magnitude of these barriers can be assessed with a DFT based approach. we find that for the very simple electrolyte model considered here, electrostatic effects dominate volume exclusion effects in the potential of mean force although fluid particle packing is clearly evident as a secondary effect.

Finally, we have computed diffusion coefficients by using experimental data for ion flux coupled with our detailed solutions for inhomogeneous density and chemical potential gradients in our systems. We find that these coefficients are reasonably constant as a function of applied potential, but they vary with bulk ion concentrations. Furthermore, the Poisson-Boltzman model fluid and the finite size 3-component model fluids considered here clearly must have different diffusion coefficients in order to interpret the same data set. This indicates that these diffusion coefficients are not fundamental properties of the electrolyte, but are rather the appropriate constant (in an engineering sense) needed to satisfy the continuity equation.

4 Interactions and Assembly of Solvated Macromolecules

Simulations of single grafted polyelectrolyte chains: ssDNA and dsDNA

Paul S. Crozier, pscrozi@sandia.gov Mark J. Stevens

Abstract

The structure of a single, grafted polyelectrolyte, DNA, is investigated by molecular dynamics simulations. The polyelectrolyte is treated as a bead-spring model with explicit charges using parametrizations of both flexible (ssDNA) and stiff (dsDNA) polyelectrolytes. In this single chain limit with no added salt, the flexible ssDNA is always highly extended. Counterion condensation on both molecules is found to be chain length dependent. The counterion distribution is not localized to the chain volume as in related polyelectrolyte brush states. Even at large chain lengths, where the majority of counterions are condensed, a significant fraction of counterions reside far from the chain. The distributions of positions of the non-grafted end monomer for ssDNA and dsDNA differ significantly, indicating a possibility for distinguishing the two states in DNA array technologies.

Introduction

The grafting of DNA strands to surfaces in microarrays has recently revolutionized DNA sequencing. The development of microarrays has occurred without much attention paid to the statistical conformations of the grafted DNA [19, 9]. An understanding of DNA conformations will aid further developments of DNA array-based sensors. In addition, grafted DNA is a subset of grafted polyelectrolytes, which have important applications. For instance, polyelectrolyte brushes are a key ingredient in the stabilization of colloids in aqueous solution [16]. Also, many proteins are now realized to have segments, often end segments, that are unstructured, i.e. do not fold [8]. These segments typically have amino acid sequences containing repeating motifs that generally involve charged amino acids. These unstructured tails can behave like grafted polyampholytes or polyelectrolytes depending on the charge distribution [11, 2].

Here, we extend our coarse-grained model of polyelectrolytes in solution [21, 20] to treat a single polyelectrolyte chain grafted to a solid surface. Molecular dynamics (MD) simulations are performed using this model to calculate the chain structure and ionic distributions. These simulations lay the ground work for future multiple, grafted chain systems. In particular, we treat single-stranded DNA (ssDNA) and double-stranded DNA (dsDNA) as specific examples of strong polyelectrolytes.

There has been much theoretical work on polyelectrolyte brushes [13, 15, 17, 1, 10], yet it mostly focused on weak polyelectrolytes, not strong polyelectrolytes such as DNA. Theoretical approximations (i.e. Debye-Hückel, Poisson-Boltzmann) typically used are suspect for strong polyelectrolytes, of which DNA is an archetype. These approximations assume the electrostatic interactions are weak in comparison with the thermal energy, kT , which is false by definition of a strong polyelectrolyte. Molecular simulations can avoid issues of these approximations by completely treating all the ionic interactions. Some such simulation work [6, 5, 3] has been done on polyelectrolyte brushes, while very little simulation work has been done on isolated, constrained polyelectrolyte chains such as grafted DNA [2].

Even though there is considerable interest in polyelectrolyte brushes and grafted DNA, only a small amount

of experimental data exists to test the theoretical efforts. Well controlled experimental systems have been difficult to achieve, at least until recently [14, 23, 24]. Polyelectrolyte brushes composed of poly(styrene sulfonate) have been made by initially grafting a neutral polystyrene brush and subsequently sulfonating it to obtain the polyelectrolyte [24]. DNA has been grafted onto gold surfaces using thiol chemistry [9]. Alkanethiol molecules are end-attached to DNA which will then self-assemble via thiol chemistry onto a gold substrate. These grafted DNA systems offer the potential for the development of a well-controlled model of a grafted polyelectrolyte system.

In the following section, we detail the grafted polyelectrolyte model and the coarse-grained MD simulation procedure. Then we give results of the grafted dsDNA and ssDNA simulations with and without added salt, elucidating counterion condensation behavior and chain structure as a function of chain length and salt concentration. We conclude with a general discussion and possible directions for future work on simulation of grafted DNA.

Simulation Details

Polyelectrolyte chains were modeled by a bead-spring polymer model that has been described elsewhere in the literature [21, 20, 2]. The bead-bead interaction is given by the Lennard-Jones (LJ) potential,

$$U_{\text{LJ}}(r) = \begin{cases} 4\epsilon \left[\left(\frac{d}{r} \right)^{12} - \left(\frac{d}{r} \right)^6 + \frac{1}{4} \right]; & r \leq r_c \\ 0; & r > r_c \end{cases} \quad (52)$$

where d is the bead diameter in multiples of σ , the LJ unit of length, and ϵ is the LJ unit of energy. Since water is a good solvent for polyelectrolytes, the LJ potential is cutoff at $r_c = 2^{1/6}d$, yielding a purely repulsive interaction. This same interaction is used for all pair interactions (counterion-monomer, etc.).

The bond potential is the sum of the repulsive LJ potential and the attractive FENE (finite extensible, nonlinear elastic) potential.

$$U_{\text{bond}}(r) = -1/2kR_0^2 \ln(1 - r^2/R_0^2), \quad (53)$$

with spring constant $k = 7\epsilon/\sigma^2$, and maximum extent, $R_0 = 2\sigma$. Given this bond interaction, the average bond length will be $a = 1.1\sigma$.

Molecules of ssDNA and dsDNA are also differentiated by the angle flexibility term,

$$U_{\text{angle}} = k_\theta(\theta - \theta_0)^2, \quad (54)$$

where k_θ is the angle stiffness term and θ is the bond angle in degrees. Flexible ssDNA were modeled with $k_\theta = 0$ for the angle term, whereas dsDNA chains were modeled with $k_\theta = 300\epsilon/\text{rad}^2$ and $\theta_0 = 180^\circ$ to yield the correct persistence length.

Polymer beads, coions and counterions are all monovalent. Each bead represents one DNA monomer in the N -bead polymer chain (phosphate, base, and sugar) with its corresponding charge of $-e$. Charged particles interact according to the Coulomb potential

$$u_{ij}(r) = q_i q_j k_B T \lambda / r, \quad (55)$$

Table 2. System parameters.

system	a	σ	d	ξ
ssDNA	1.7Å	3.09Å	1.29 σ	4.2
dsDNA	3.4Å	1.54Å	2.60 σ	2.1

where q_i is the charge on particle i and the Bjerrum length in water is $\lambda = 7.1\text{\AA}$. The bond length, a , that characterizes the distance between beads of the chain, has been mapped to the DNA base charge separations of 3.4Å for ssDNA and 1.7Å for dsDNA. The conversion between LJ units and Å is obtained from the value of bond length, $a = 1.1\sigma$ and is given in Table 2. In all the LJ pair interactions, d is taken to be 4 Å, which is a typical value used in primitive model electrolytes.

The solvent is treated at the primitive model level, setting the Bjerrum length to water’s characteristic value of 7.1Å. This is appropriate for most aspects of polyelectrolyte structure [21]. The focus of this work is on the electrostatic interactions in competition with entropy. We neglect the intrinsically strong H-bonds between complementary base pairs in ssDNA, because we are focusing on the polyelectrolyte nature of the structure. Furthermore, for chain lengths of interest the likelihood of self-hybridization is small. As will be seen, the electrostatic repulsion between the charged bases results in a highly extended structure without the self-contact that H-bonding would require.

The simulated systems are periodic in the x - and the y -directions. But the accessible z -direction domain is non-periodic with a wall at the grafting surface ($z = 0$) and an additional wall at $z = L_z$, where L_z is the simulated slab thickness. Walls were modeled using the same repulsive LJ interactions as given in Eq. 179 above,

$$U_{\text{wall}}(z) = U_{\text{LJ}}(z). \quad (56)$$

Long-range electrostatics were treated by the P³M mesh-Ewald method [18], with empty space left between periodically repeating slabs in the z -direction, perpendicular to the grafting surface. A slab-geometry correction term was also included in order to damp out inter-slab interactions and model an isolated slab of fluid. This method has been shown to accurately treat long-range slab-geometry electrostatic interactions [25, 4].

The total energy for the model system is

$$U_{\text{tot}} = U_{\text{LJ}} + U_{\text{bond}} + U_{\text{angle}} + U_{\text{Coulomb}} + U_{\text{wall}}. \quad (57)$$

Simulations without salt were performed at a dilute monomer density of 10^{-6} ions/ σ^3 in the particle-accessible portion of the simulation box. Beyond the cubic particle-accessible portion of the simulation box with dimensions $L_x = L_y = L_z$, an additional empty volume of $L_x \times L_y \times 2L_z$ was included between periodically-repeating images of the slabs as per the slab-geometry simulation protocol cited above, yielding a total simulation box volume of $L_x \times L_y \times 3L_z$. Three salt concentrations were explored for the ssDNA case corresponding to 5 mM, 10 mM, and 20 mM. For each simulation 10^7 time steps of 0.01τ each were performed, where τ is the LJ time. In all cases, a Langevin thermostat with damping constant $\gamma = 1$ was used to maintain a temperature of $T = 1.0\epsilon$.

Chains were grafted to the surface by tethering the first bead of the chain to a “zeroth” bead that was

uncharged and fixed in space at a distance of r_c from the left wall ($x = 0, y = 0, z = r_c$). Simulation of single isolated chains approximates the low polyelectrolyte concentration limit. Polymer chains of length $N = 16, 20, 32, 64, 128$ and 256 were simulated.

Initial configurations for each system were created by randomly placing particles within the simulation cell constrained by the requirements that 1) chains start at the grafting point, 2) neighboring beads on polymer chains were at the equilibrium bond distance, 3) chains were stretched to near full extension, 4) all particles started between the walls, at a distance of at least r_c from both walls, 5) counterions were started within 5σ of the polymer chain.

Results

The end-to-end distance, R , is a key measure of polymer structure. The calculation of R provides a check of the simulations, as well as a means to compare the two different systems. For strong polyelectrolytes such as DNA, we expect the scaling relation $R \sim N^\nu$ to have $\nu \simeq 1$. In addition, since our values of N are below the corresponding persistence length for dsDNA, ν should be 1 in this case. Figure 18 shows that this is indeed the case. For the flexible single-stranded case, the value of ν is the same, but the magnitude of R is lower due to the difference in the chain flexibility. For $N = 20$ we also include a point with added salt for ssDNA. As expected R decreases with added salt. Also, as noted in the beginning, the ssDNA structure is very extended so that intramolecular H-bonds are not likely.

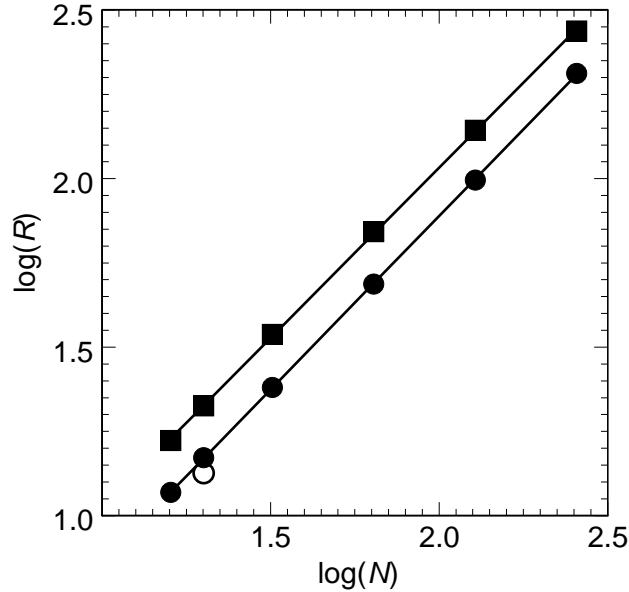


Figure 18. End-to-end distance, R , as a function of chain length, N , for both dsDNA (boxes) and ssDNA (circles). All points are for simulations of a single grafted DNA molecule with counterions sufficient to neutralize the net charge of the chain, except the empty circle point which corresponds to ssDNA with compensating counterions and 10 mM salt. In both cases, the slope, which equals ν , is 1.

The properties of grafted polyelectrolytes are intimately related to the ion distributions. Fig. 19 compares monomer, counterion, and salt density distributions in the direction perpendicular to the grafting surface (the z -direction) for the $N = 20$ case. The distributions are normalized such that $\int_0^{L_z} g(z) dz / (L_z N) = 1$, where $g(z)$ is the normalized density. Parts (a) and (b) compare results for ssDNA and dsDNA, respectively. The dsDNA monomer distribution has multiple well-resolved oscillations near the grafting surface wall. This is because dsDNA is stiff and the positions of these monomers close to the grafting site do not fluctuate much. For monomers further down the chain, pivoting about the grafting site yields significant lateral fluctuations. For this reason, $g(z)$ decreases monotonically for $z > 10\sigma$, as the lateral fluctuations increase with z . Since ssDNA is flexible, the oscillations do not appear at low z . Because R is larger for dsDNA and g is normalized, the ssDNA curve has a larger peak at low z . Otherwise, beyond the initial peak the ssDNA distribution similarly decreases with increasing z until reaching values beyond the contour length where $g = 0$.

One of the basic questions for grafted polyelectrolytes is how the counterions are arranged. Specifically, how are the counterions split between being within the ‘chain volume’ and outside of the chain volume? Here, we take the ‘chain volume’ to be defined as the volume with $z \leq a(N - 1)$. The counterion distributions in Fig. 19 show the main peak within the chain volume and a tail at larger z . For both ssDNA and dsDNA the peak height in the counterion distribution is much smaller than in the monomer distribution implying that the number of counterions within the chain volume is a small fraction of the total number. Table 3 shows the time-averaged value of the fraction of counterions within the chain volume. Both cases have values below 0.5 for this N . Thus, most of the counterions are located at values of z beyond the chain length for this N . As N increases, the fraction of counterions within the chain volume increases as shown in Table 3. This increase is related to the number of condensed counterions, as we discuss shortly.

The distributions for $N = 64$ are shown in Fig. 20. The larger N has a qualitative difference in the distributions. The maximum occurs over a plateau region instead of at a peak. This is stronger in dsDNA than in ssDNA. For dsDNA, $g(z)$ has the same oscillations at small z as seen for the $N = 20$ case, then a long plateau to about $z = 35\sigma$ and a drop thereafter to zero at about $z = 65\sigma$. The long plateau occurs because dsDNA is stiff and, on average, there is approximately one monomer per unit length in the z -direction. Different configurations for dsDNA are just different tilts about the grafting point. For a configuration at a given tilt angle θ with respect to the z -axis, there are no monomers for $z > a(N - 1) \cos \theta$. The drop-off at $z \simeq 35\sigma$ implies that the largest tilt is about 60° in this case.

Noticeable differences occur in the distribution for ssDNA due its flexibility. The value of $g(z)$ for low z is larger in ssDNA than in dsDNA, because the ssDNA can bend so that more than one monomer is at the same z . These curved configurations lead to the drop off occurring at a lower value, $z \simeq 20\sigma$.

Before discussing the counterion distributions in Fig. 20, we note that for large N the fluctuations in the monomer $g(z)$ become successively more significant. Comparing different quartiles of a 10^7 step run showed significant fluctuations about the mean. Because of the low density the counterion dynamics becomes slower as L_z increases with N . This puts a limit on accurate calculation of $g(z)$ to $N \leq 128$. Other quantities (e.g. Table 3) can be calculated accurately to $N = 256$.

The counterion distributions in Fig. 20 tend to mirror the monomer distributions. Both dsDNA and ssDNA at $N = 64$ have peaks at $g = 1$ which is larger than the corresponding value at $N = 20$. This larger value indicates the larger degree of counterion condensation (*cf.* Table 3). As the table shows by $N = 64$ the

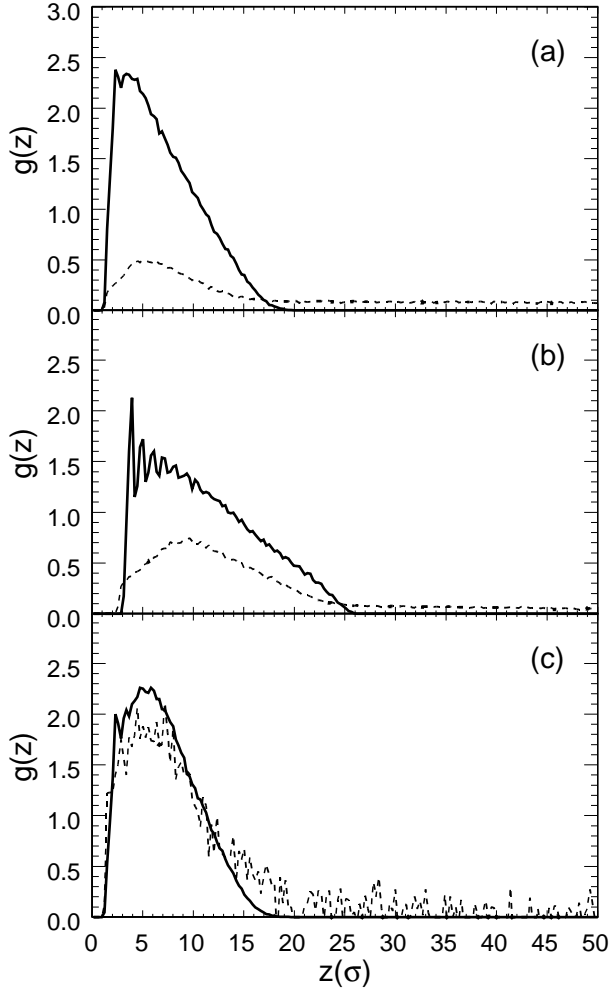


Figure 19. Monomer (thick line) and counterion (dotted line) distributions as a function of distance from the grafting surface for $N = 20$ chains of (a) ssDNA without salt, (b) dsDNA without salt, and (c) ssDNA in 5 mM salt. Net counterion (counterion – coion) density is plotted for (c). Densities have been normalized and plotted as the average number density of each species per unit length.

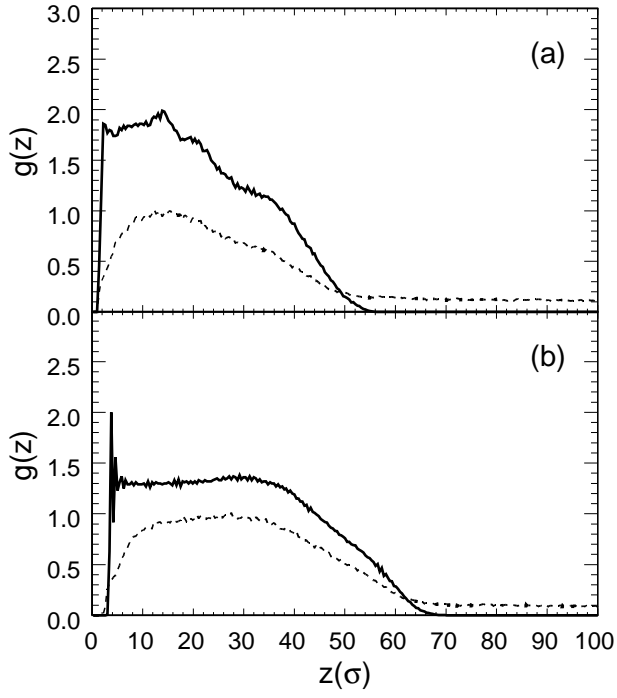


Figure 20. Monomer (thick line) and counterion (dotted line) distributions as a function of distance from the grafting surface for $N = 64$ chains of (a) ssDNA and (b) dsDNA.

Table 3. Fraction of counterions within $a(N - 1)$ of the grafting surface. Statistics for salt runs are for the net number of counterions, i.e. (counterions - coions)/ N .

N	Salt conc. (mM)	ssDNA	dsDNA
16	0	0.22	0.38
20	0	0.25	0.45
20	5	0.84	—
20	10	0.87	—
20	20	0.97	—
32	0	0.37	0.58
64	0	0.54	0.68
128	0	0.65	0.80
256	0	0.71	0.81

number of counterions within the chain volume is larger than outside the volume. Yet, there is still a long tail in the counterion distribution that accounts for a substantial amount of counterion density.

A more direct calculation of the fraction of condensed counterions is shown in Fig. 21. The distance r from a counterion to the chain is defined as the minimum of all distances from the counterion to any monomer of the chain. The time-averaged number of counterions within r is calculated and normalized by N to give $f(r)$, the fraction of counterions within a distance r . The number of condensed counterions is not a uniquely defined quantity [7]. The simple physical picture of condensed counterions has the electrostatic interactions trapping and holding these counterions within a short distance of the chain. The plots of $f(r)$ show that in salt-free solution a plateau is reached once $r > 3d$ and is maintained at least up to $r = 20\sigma$. Looking at these plateau values in Fig. 21 we see that they increase with N . For dsDNA, the largest N are identical giving a large N limit for the plateau value to be $f = 0.60$. For ssDNA, the saturation limit is apparently just above the range of the data at about $f = 0.50$. For comparison, the Manning condensation value for an infinite chain is 0.76 for dsDNA and 0.52 for ssDNA. The Manning calculation uses the Debye-Hückel equation, which breaks down for strong polyelectrolytes such as DNA and is for free, rather than grafted, polyelectrolytes. Nonetheless, it gives a good first approximation. The simulation data shows that there is a strong N dependence in the fraction of condensed counterions and that the infinite chain limit is reached for $N \simeq 100$ for dsDNA and about twice as large for ssDNA.

The effect of added salt is included in Fig. 21(a). The chain and salt counterions are identical. In the Debye-Hückel theory, added salt is excluded from the condensation regime [12]. However, we find that adding salt increases the fraction of condensed counterions. In fact, for 20 mM salt, enough counterions for complete neutralization of the chain can be found within 15σ . This result is consistent with results of simulations of free chains in salt [22]. The system prefers to achieve a more uniform charge density, and in the presence of salt does so. This can be seen in Fig. 19(c), which shows that the net counterion distribution (with coions subtracted) is almost identical to the monomer distribution.

The orientation of the DNA chain can be examined through the position of the free end monomer. Fig. 22 shows the distribution of the position of the N^{th} monomer as a function of distance from the grafting surface, $P_N(z)$, for ssDNA and dsDNA for $N = 16, 32$, and 64 . In all cases, the dsDNA peak is at larger z than the peak in the ssDNA distribution, because dsDNA is stiffer. Although it is possible for the dsDNA

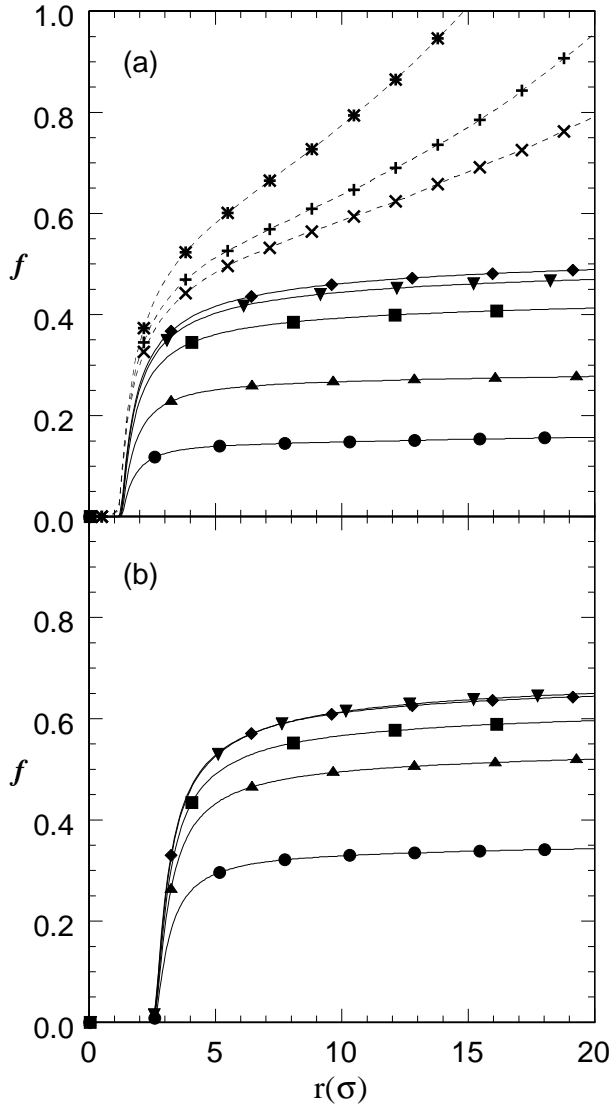


Figure 21. The solid lines are the fraction of neutralizing condensed counterions, $f(r)$, within the shortest distance to the chain, r , for both ssDNA (a) and dsDNA (b). Symbols are as follows: $N = 16$ (circles), $N = 32$ (up triangles), $N = 64$ (boxes), $N = 128$ (down triangles), $N = 256$ (diamonds). Dashed lines in Fig. 21a are for $N = 20$ chains of ssDNA with salt [5 mM salt (\times), 10 mM salt ($+$), and 20 mM salt ($*$)], where the fraction of neutralization can exceed unity due to the excess of counterions, and where coion counter-neutralization is not shown.

chains to lay flat on the grafting surface, the simulation results indicate that this rarely occurs, and that for larger N becomes more rare if it happens at all. This is in part because conformations with the grafted chain perpendicular to the wall allow larger counterion entropy than for a chain laying flat on the grafting surface with only half of the volume around the chain accessible to the counterions.

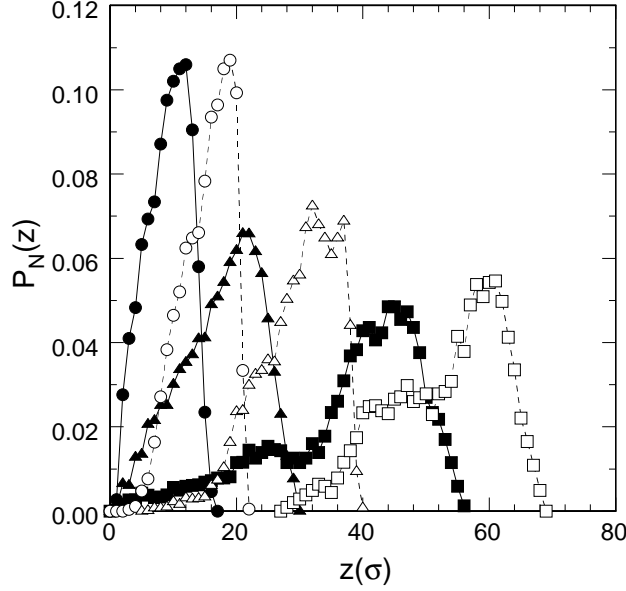


Figure 22. The distribution of distances of the N^{th} monomer from the grafting surface for ssDNA (solid lines) and dsDNA (dashed lines). The probabilities per unit length, P_N , that the end monomer will be found a given distance, z , from the surface are plotted for the $N = 16$ (circles), $N = 32$ (triangles), and $N = 64$ (boxes) chains.

Discussion

Csajka and Seidel (CS) [6] have performed simulations of polyelectrolyte brush using almost the same model with different parameters. Their parametrization has $\sigma = 9.8\text{\AA}$, which is about 3 times larger than for our ssDNA model. Their value of ξ is 0.74, which is below the Manning condensation limit in contrast to either DNA system. This value of ξ is in the region where the Coulomb and thermal interactions are about equal, which puts the system intermediate between strong and weak polyelectrolytes.

We can compare our ssDNA results to the CS brush results, since both are flexible polyelectrolytes. Our system would correspond to the low grafting density limit. However, for $N = 30$ as the grafting density decreases so does the brush height in the CS simulations. In fact, for the lowest density the average single chain structure in the brush is close to that of a neutral chain in solution, i.e., not extended like a highly charged polyelectrolyte. In contrast, we find the single, grafted ssDNA is highly extended. Since ξ is larger for ssDNA than for the CS chain, this would result in a more extended chain for ssDNA, but only by a small fraction. In solution, the polyelectrolyte chains with parameters very close to those of CS monotonically become more extended with decreasing density [21]. Calculations by Csajka et al. [5] predict a new brush

phase, the collapsed brush, in the polyelectrolyte brush phase diagram. The lowest grafting density treated by CS is much larger than our equivalent density. As the grafting density is decreased from this lowest density to our dilute limit, our results indicate that the chains must at some point become more extended. This should be true for any strong polyelectrolyte since the single, grafted chain limit is not much different from a single chain in solution limit. The main difference between the brush state and the dilute state is that the counterion distribution in the brush is contained within the brush, whereas a significant portion lies beyond the chain length in the single chain limit. It will be interesting to determine the crossover point for the ssDNA brush where the counterions become contained within the brush and to determine where the collapsed brush state exists for the ssDNA parameters. If so, this would have consequences for DNA microarray and other technologies.

Conclusion

We have examined the structure of a single, grafted polyelectrolyte, specifically ssDNA and dsDNA, using coarse-grained MD simulations. A chain length dependence to the counterion condensation is found that is relevant to many applications since rather short DNA molecules are used. The counterion distribution extends beyond the chain volume in all cases. Even for the long chains where counterion condensation is maximal, there is a significant fraction of counterions beyond the corresponding brush height. In this dilute limit the chains are highly extended; in the case of dsDNA, this is true because the chain lengths studied are less than its persistence length. The ssDNA, which has a small intrinsic persistence length, is also highly extended in the zero salt simulations. However, added salt does shrink the chain as salt ions do enter the volume near the chain.

References

- [1] O.V. Borisov, T.M. Birshtein, and E.B. Zhulina. Collapse of grafted polyelectrolyte layer. *J. Phys. II*, 1:521, 1991.
- [2] J.N. Bright, M.J. Stevens, J. Hoh, and T.B. Woolf. Characterizing the function of unstructured proteins: Simulations of charged polymers under confinement. *J. Chem. Phys.*, 115:4909–4918, 2001.
- [3] H. Chen, R. Zajac, and A. Chakrabarti. Conformational properties of polyelectrolyte brushes: A monte carlo and self-consistent-field study. *J. Chem. Phys.*, 104:1579–1588, 1996.
- [4] P.S. Crozier, R.L. Rowley, and D. Henderson. Molecular dynamics calculations of the electrochemical properties of electrolyte systems between charged electrodes. *J. Chem. Phys.*, 113:9202–9207, 2000.
- [5] F.S. Csajka, R.R. Netz, C. Seidel, and J.-F. Joanny. Collapse of polyelectrolyte brushes: Scaling theory and simulations. *Euro. Phys. J. E*, 4:505–513, 2001.
- [6] F.S. Csajka and C. Seidel. Strongly charged polyelectrolyte brushes: A molecular dynamics study. *Macromolecules*, 33:2728–2739, 2000.
- [7] M. Deserno, C. Holm, and S. May. Fraction of condensed counterions around a charged rod: comparison of poisson-boltzmann theory and computer simulations. *Macromolecules*, 33:199, 2000.

- [8] A.K. Dunker, C.J. Brown, J.D. Lawson, L.M. Iakoucheva, and Z. Obradovic. Intrinsic disorder and protein function. *Biochemistry*, 41:6573–6582, 2002.
- [9] T.M. Herne and M.J. Tarlov. Characterization of dna probes immobilized on gold surfaces. *J. Am. Chem. Soc.*, 119:8916–8920, 1997.
- [10] R. Israels, F.A.M. Leermakers, G.J. Fleer, and E.B. Zhulina. Charged polymeric brushes: structure and scaling relations. *Macromolecules*, 27:3249–3261, 1994.
- [11] S. Kumar, X. Yin, B.D. Trapp, J.H. Hoh, and M.E. Paulaitis. Relating interactions between neurofilaments to the structure of axonal neurofilament distributions through polymer brush models. *Biophys. J*, 82:2360–2372, 2002.
- [12] G. Manning. *Q. Rev. Biophys.*, 11:179, 1978.
- [13] S.J. Miklavic and S. Marcelja. Interaction of surfaces carrying grafted poly-electrolytes. *J. Phys. Chem.*, 92:6718–6722, 1988.
- [14] Y. Mir, P. Auroy, and L. Auvray. Density profile of polyelectrolyte brushes. *Phys. Rev. Lett*, 75:2863, 1995.
- [15] S. Misra, S. Varanasi, and P.P. Varanasi. A poly-electrolyte brush theory. *Macromolecules*, 22:5173–5179, 1989.
- [16] D.H. Napper. *Polymeric Stabilization of Colloidal Dispersions*. Academic, London, 1983.
- [17] P. Pincus. Colloid stabilization with grafted polyelectrolytes. *Macromolecules*, 24:2912–2919, 1991.
- [18] E. L. Pollock and J. Glosli. Comments on p3m, fnm and the ewald method for large periodic coulombic systems. *Comput. Phys. Commun.*, 95:93, 1996.
- [19] A.B. Steel, R.L. Levicky, T.M. Herne, and M.J. Tarlov. Immobilization of nucleic acids at solid surfaces: Effect of oligonucleotide length on layer assembly. *Biophys. J.*, 79:975–981, 2000.
- [20] M.J. Stevens. Simple simulations of dna condensation. *Biophys. J.*, 80:130, 2001.
- [21] M.J. Stevens and K. Kremer. Structure of of salt-free linear polyelectrolytes. *J. Chem. Phys.*, 103:1669, 1995.
- [22] M.J. Stevens and S.J. Plimpton. The effect of added salt on polyelectrolyte structure. *Euro. Phys. J. B*, 2:341, 1998.
- [23] S. A. Sukhishvili and S. Granick. Formation and characterization of covalently bound polyelectrolyte brushes. *Langmuir*, 13:4935, 1997.
- [24] Y. Tran and P. Auroy. Synthesis of poly(styrene sulfonate) brushes. *J. Am. Chem. Soc.*, 123:3644, 2001.
- [25] I.C. Yeh and M.L. Berkowitz. Ewald summation for systems with slab geometry. *J. Chem. Phys.*, 111:3155–3162, 1999.

Simple simulations of DNA condensation

Mark J. Stevens

Abstract

Molecular dynamics simulations of a simple, bead-spring model of semiflexible polyelectrolytes such as DNA are performed. All charges are explicitly treated. Starting from extended, noncondensed conformations, condensed structures form in the simulations with tetravalent or trivalent counterions. No condensates form or are stable for divalent counterions. The mechanism by which condensates form is described. Briefly, condensation occurs because electrostatic interactions dominate entropy, and the favored Coulombic structure is a charge ordered state. Condensation is a generic phenomena and occurs for a variety of polyelectrolyte parameters. Toroids and rods are the condensate structures. Toroids form preferentially when the molecular stiffness is sufficiently strong.

Introduction

The high degree of packing necessary to package DNA into cells is well known (Bloomfield, 1996). Typically, DNA is orders of magnitude longer than any dimension of the cell in which it resides. Since DNA is a highly charged polyelectrolyte, packing DNA into a small volume requires overcoming an enormous Coulomb barrier. It is only partially understood how this can occur. In this article, the interest is to treat the general case of condensing highly charged, semiflexible polyelectrolytes by multivalent ions. The prime example is fitting of DNA into a bacteriophage's capsid, since bacteriophages are simple systems which do not possess condensing proteins (histones) present in eukaryotic cells.

The purpose of this work is to demonstrate that electrostatic interactions provide a *general* mechanism to condense semiflexible, polyelectrolytes such as DNA. It is well known experimentally that multivalent ions can condense DNA into toroids and rods (Bloomfield, 1996; Bloomfield, 1991, Kleinschmidt *et al.*, 1962; Fang and Hoh, 1998). While these experiments have given many important clues to the important interactions in DNA condensation, understanding of these interactions remains incomplete. The key issue is how does the net electrostatic interaction between like charged monomers change from repulsive to attractive. For as long as the net interaction is repulsive, the polyelectrolyte cannot condense.

Condensation is directly demonstrated for semiflexible polyelectrolytes such as DNA with multivalent counterions, using molecular dynamics simulations of simple, model polyelectrolytes. Once condensation is demonstrated, the nature of the condensates and the condensation process are investigated. How multivalent ions can overcome the large Coulomb repulsion between the charged monomers is explained. The subtle competition between electrostatic interactions and entropy is noted in the failure of divalent counterions yielding condensates. The effect of molecular stiffness on the condensate structure is also treated.

Background

A net attraction between like-charged macroions is somewhat counterintuitive, but it is known to occur in certain circumstances (Lyubartsev and Nordenskiöld, 1995; Kjellander and Marčelja, 1984; Stevens and Robbins, 1990). Calculations of electrostatic interactions involving multivalent ions are difficult. The traditional

approximations such as Debye-Hückel and Poisson-Boltzmann break down in these circumstances (Kjellander and Marčelja, 1984; Stevens and Robbins, 1990). These approximations are valid primarily for Coulomb interactions weak in comparison with $k_B T$, where k_B is the Boltzmann constant and T is the temperature. This is not true for DNA and becomes even less true in the presence of multivalent ions. Both of these theories can only yield repulsive interactions between chain segments (Neu, 1999; Sader and Chan, 1999). Thus, no condensation can occur.

Treatment of the complex interactions for highly charged macroions of simple geometry (e.g. plates, cylinders) has been developed (Kjellander and Marčelja, 1984; Stevens and Robbins 1990; Ha and Liu, 1997). A short-ranged attraction between two macroions is possible and understood. DNA is often treated as a charged cylinder. Simulations have found attraction between charged cylinders (Grønbech-Jensen *et al.*, 1997; Lyubartsev and Nordenskiöld, 1995) and stiff, polyelectrolytes (Stevens, 1999) in the presence of multivalent ions. This attraction has been ascribed to correlated fluctuations of the counterions (Ha and Liu, 1997; Ray and Manning, 1994). Ha and Liu (Ha and Liu, 1997) developed a self-consistent field theory for systems of parallel, charged cylinders. Their theory shows condensed counterions induce charge fluctuations along the rods giving rise to attractive interactions. Self-attraction in flexible polyelectrolytes has also been shown to occur (Stevens and Kremer, 1995; Schiessel and Pincus, 1998; Brilliantov *et al.*, 1998). Brilliantov *et al.* (Brilliantov *et al.*, 1998) showed that *flexible* polyelectrolytes can collapse for strong Coulomb interactions using an extension to polymers of density functional theory methods (Stevens and Robbins, 1990). This is in agreement with earlier simulations (Stevens and Kremer, 1995).

A important phenomenon for highly charged polyelectrolytes such as DNA is counterion condensation (Manning, 1969; Oosawa, 1971). For a sufficiently charged polyelectrolyte some of the counterions become effectively bound. Manning's solution of the Debye-Hückel equation shows that when the ratio of the Bjerrum length, λ to the charge separation distance, a is greater than one, then enough counterions condense onto the polyelectrolyte in order to reduce the effective ratio $\xi = \lambda/a$ to be equal to 1. Counterion condensation occurs for all highly charged polyelectrolytes including DNA independent of the counterion valence. Thus, condensation of the polyelectrolyte requires more than counterion condensation.

Theory

A simple description of the physical source for the attractive interactions can be given in terms of the one component plasma (OCP) which consists of a single charged species in a uniform neutralizing background (Baus and Hansen, 1980). The OCP can be described in terms of a single parameter,

$$\Gamma = \lambda/a_p, \quad (58)$$

where a_p is the average interparticle separation, defined in terms of the density, ρ as $a_p = 3/(4\pi\rho)^{1/3}$. The OCP parameter Γ is similar to the quantity ξ ; the difference is that OCP refers to a three-dimensional system and ξ to a one dimensional system. Physically, the parameters Γ and ξ define the relative strength of the typical Coulomb pair interaction to the entropic interaction. When either quantity is greater than one such as when counterion condensation occurs, the Coulomb interactions dominate the entropic interactions. Small Γ is equivalent to low density. Figure 23 gives the normalized pressure, $P^* = \lambda^3/k_B T$ vs. Γ . The OCP pressure

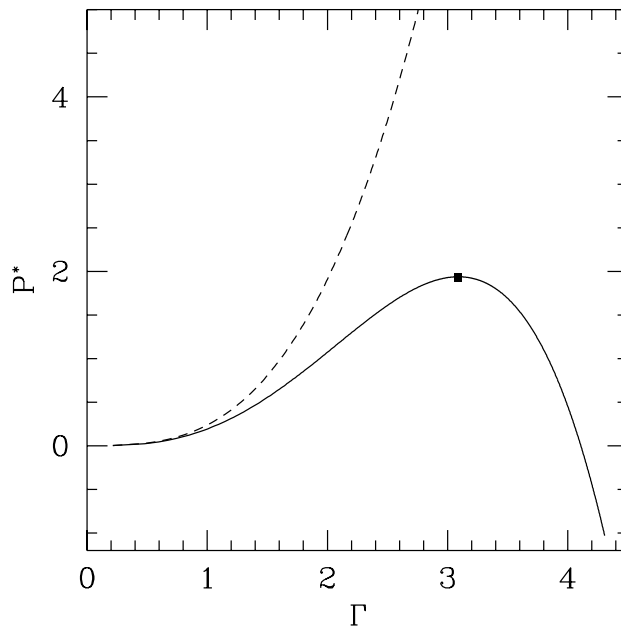


Figure 23. The pressure for the one component plasma (OCP) as a function of the parameter $\Gamma = \lambda/a_p$, where λ is the Bjerrum length and a_p is the average interparticle spacing. The dotted line gives the pressure calculated in the Poisson-Boltzmann approximation. The pressure is calculated from the free energy given in (Brami *et al.*, 1979) which was fit to a combination of Monte Carlo data and hypernetted chain calculations.

becomes the ideal gas law at small Γ ,

$$P^* \simeq \Gamma^3 \sim \rho. \quad (59)$$

In this regime the Poisson-Boltzmann approximation is valid, since entropy is the dominant interaction. As Fig. 23 shows, at $\Gamma \sim 1$, the PB approximation breaks down; the pressure calculated in the PB approximation significantly deviates from the correct value. Furthermore, the PB pressure is always positive (Neu, 1999; Sader and Chan, 1999).

As Γ increases the Coulomb interactions become more dominant until at $\Gamma = 3.09$ a mechanical instability occurs. Since the equilibrium Coulomb energy is negative and decreasing the volume brings the particles closer together, the Coulomb energy decreases with decreasing volume. Minimizing just the Coulomb interactions would collapse the system. At lower Γ sufficiently strong entropic interactions stabilize the system. However, at $\Gamma = 3.09$ entropy cannot stop the volume decreasing, and the system will shrink until steric repulsions stop the contraction. In polyelectrolytes, this instability is related to counterion condensation (Stevens and Robbins, 1990). If $\Gamma = 4.1$ can be reached without steric repulsion occurring, then the pressure is negative and the system has a global (self) attraction. For much higher Γ , the system undergoes a phase transition much like to an ionic crystal such as NaCl. A single polyelectrolyte can collapse due to this global attraction, if the equivalent Γ achieves these large values. In this picture DNA condensation is a result of the Coulomb interactions being sufficient strong (large Γ) that they dominate entropic interactions and can achieve a charged

ordered state which has the lowest Coulomb energy. In macroion systems the signature for this transition is that the equilibrium charge distribution becomes highly correlated with alternating negative and positive charges.

DNA condensation typically occurs for counterion valences 3 or larger. The importance of multivalency is that it increases the magnitude of the Coulomb interactions. In the OCP picture (Stevens and Robbins, 1990; Stevens *et al.*, 1996) the Bjerrum length is written

$$\lambda = z_c^2 e^2 / \varepsilon k_B T, \quad (60)$$

where z_c is the counterion valence and ε is the dielectric constant of water. Thus, trivalent counterions increase the Bjerrum length by a factor of 9. This enables the net attraction to occur before the steric repulsion enters. For monovalent and divalent ions, the Coulomb interactions are not strong enough to counter entropic effects. Thus, condensates do not form for low valence counterions.

A simple calculation of Γ for polyelectrolyte collapse produces rather reasonable number despite some strong simplifications (cf. Brilliantov *et al.*, 1998). In this calculation, Γ is calculated based on the condensed counterion volume. The density of condensed counterions involves just the volume near the polyelectrolyte. The volume can be estimated to be a cylinder about the polyelectrolyte with a diameter containing counterions within a single counterion diameter of the polyelectrolyte. For $z_c \geq 3$ the simulations show this is a good estimate of the volume. Writing the polyelectrolyte radius as R and the counterion diameter as d , then the volume is $V = \pi(R + d)^2 L$. The polyelectrolyte length is $L = (N - 1)a$, where N is the number of charged monomers and a is the charge monomer separation distance. Taking all counterions as condensed, then the counterion density is

$$\rho = \frac{N/z_c}{4\pi(R + d)^2(N - 1)a} \simeq (4\pi(R + d)^2 a z_c)^{-1}. \quad (61)$$

Then,

$$\Gamma = \lambda / (3(R + d)^2 a z_c)^{1/3}. \quad (62)$$

Using $\lambda = 7.1\text{\AA}$, $R = 10\text{\AA}$, $d = 4\text{\AA}$ and $a = 1.7\text{\AA}$, one obtains $\Gamma = 7.1$ for $z_c = 4$ and $\Gamma = 2.0$ for $z_c = 2$. For $z_c = 2$, the condensed counterion volume may in fact be larger, but this just reduces Γ further. Thus, tetravalent counterions are in the attractive regime, but divalent ions are just in the counterion condensation regime.

Using MD simulations, no approximations are necessary as in analytic calculations. The interactions necessary for condensation can be conclusively determined. In addition, other useful information about these interactions is obtained. Because the persistence length of DNA is large, the polymer lengths which can be studied are smaller than in DNA. The simulations will treat several model polyelectrolytes that otherwise have physical parameters in a regime similar to DNA. Three key lengths are the charge separation distance a , the intrinsic persistence length L_p and the chain length L . The important relation that holds for DNA is $a < L_p < L$. The model polyelectrolytes satisfy this relation. Condensation will occur independent of L so long as this relation holds. The condensate structure however can depend on L_p as will be seen.

Simulation Methods

A large body of work has been performed on bead-spring model polyelectrolytes (Stevens and Kremer, 1995; Stevens, 1999). Bead-spring models are necessary to treat the slow dynamics of polymers. Atomistic simulations particularly for polyethylene let alone DNA cannot treat the necessary time scales. Coarse-grained simulations have already demonstrated the aggregation of multiple stiff polyelectrolytes such as single persistence length DNA or actin (Stevens, 1999).

Molecular dynamics simulations are performed on a system composed of M bead-spring chains with N beads. In the bead-spring model, the beads represent some number of monomers. In the present case of charged polymers, each bead has a single charge and thus corresponds to the set of monomers containing a single charge. The bead is given a size by the Lennard-Jones (LJ) potential.

$$U_{\text{LJ}}(r) = \begin{cases} 4\epsilon \left[\left(\frac{\sigma}{r}\right)^{12} - \left(\frac{\sigma}{r}\right)^6 + \frac{1}{4} \right]; & r \leq r_c \\ 0; & r > r_c \end{cases} \quad (63)$$

The LJ potential is cutoff at $r_c = 2^{1/6}\sigma$ which yields a purely repulsive potential. All the units will be in terms of the LJ quantities, ϵ and σ .

The bond potential is the sum of two parts. The repulsive part is the LJ potential described above. The attractive part is the standard FENE (finite extensible, nonlinear elastic) potential

$$U_{\text{FENE}}(r) = -1/2kR_0^2 \ln(1 - r^2/R_0^2), \quad (64)$$

with spring constant $k = 7\epsilon/\text{rad}^2$, and maximum extent, $R_0 = 2\sigma$. The key aspect of the FENE bond potential is that it does not allow chains to cross. For the parameters used, the average bond length is $a = 1.1\sigma$.

The polymers are given an intrinsic stiffness by including a bond angle potential,

$$U_{\text{angle}} = k_1(\theta - \theta_0)^2 + k_2(\theta - \theta_0)^4, \quad (65)$$

where θ is the bond angle between three consecutive beads, and the equilibrium value is $\theta_0 = 180^\circ$. A few values of the spring constants k_1 and k_2 have been used. Some values of k_1 and k_2 can be found in Table 2 which lists bond angle parameter sets. When $k_2 = 0$, the intrinsic persistence length is directly proportional to k_1 . Defining the persistence length as the length of n chain segments which forms an arc of 1 radian with a bond bending energy of $k_B T$. Then, one can derive that the intrinsic persistence length is

$$L_p = \frac{k_1 a}{k_B T} \quad (66)$$

For $k_1 = 20\epsilon/\text{rad}^2$, $L_p = 19\sigma$.

In these simulations, the counterions are explicitly treated. All charged particles interact via the Coulomb potential

$$u_{ij}(r) = q_i q_j k_B T \lambda / r, \quad (67)$$

where q_i is the charge on particle i and the Bjerrum length in water is $\lambda = 7.1\text{\AA}$. Water is treated as a uniform dielectric background. For this work, no added salt is included. For these simulations we used the particle-particle mesh algorithm to calculate the long range Coulomb interactions (Hockney and Eastwood, 1988; Pollock and Glosli, 1996). Some single chain simulations used the direct sum over all pairs.

Table 4. Bond angle parameters.

Set	$k_1(\epsilon/\text{rad}^2)$	$k_2(\epsilon/\text{rad}^4)$
1	10	0
2	20	0
3	5	200

Table 5. Polyelectrolyte parameters. The lengths are in Å.

Set	σ	ξ	d
1	2.2	2.9	2.5
2	1.5	4.2	4.0

The total energy is

$$U_{\text{tot}} = U_{\text{LJ}} + U_{\text{bond}} + U_{\text{angle}} + U_{\text{Coulomb}}. \quad (68)$$

Two polyelectrolyte parameter sets have been studied. Following much work on flexible polyelectrolytes (Stevens and Kremer, 1995) $\lambda = 3.2\sigma$ has been used. This yields $a = 2.5 \text{ Å}$ which corresponds to synthetic polyelectrolytes such as sodium poly (styrene sulfonate). The parameters are listed in Table 5. Parameter set 2 matches DNA values. The value of $\lambda = 4.68\sigma$ corresponds to $a = 1.7 \text{ Å}$. The monomer diameter d is set to 4 Å as this corresponds to a typical ionic diameter including hydration shells. While DNA has a radius of about 10 Å , the key quantity is the distance of nearest approach of the monomer charge (phosphates) and the solvent ions; this distance is typically about equal to the counterion diameter.

The dynamics of the system is performed at constant temperature, $T = 1.2$, using the Langevin thermostat (Schneider and Stoll, 1978) with damping constant equal to $1/\tau$, and timestep 0.015τ , where τ is the LJ time unit. The mapping of τ to seconds has yet to be done for polyelectrolytes. For neutral polystyrene (PS) $\tau = 3.1 \cdot 10^{-8} \text{ s}$ (Kremer and Grest, 1990). Typically, stiffer polymers have larger τ . DNA is much stiffer than PS and probably has τ more than one order of magnitude larger.

In order to avoid interactions between chains, the simulations were performed at very low chain densities, typically less than or equal to $2 \cdot 10^{-5} \sigma^{-3}$. In this work only conformations of individual molecules are the focus. Figures will show individual conformations oriented with respect to the radius of gyration tensor. Each molecule is oriented with major axis to the right and the minor axis perpendicular to the page.

For most simulations the initial conformation for each molecules in the simulation cell is created by a random walk with a ‘stretch’ condition that the next nearest neighbor distance is greater than an input value, typically $2d$. The larger the value the more extended the chain is. Highly charged polyelectrolytes are typically significantly extended. The counterions are placed randomly within a volume about each molecule.

Results

Condensation

The first issue to be settled is whether toroidal structures will form in these simulations. Figure 24 shows the

conformations for parameter set 1 with bond angle set 1, $N = 64$, $z_c = 4$, $k_1 = 10\epsilon/\text{rad}^2$ and $\rho = 1 \cdot 10^{-4}\sigma^{-3}$. Not only do toroids form, but also rod structures form. The rods are more common in this simulation as well as others to be discussed. The two molecules that do not self condense have actually aggregated together; their conformations are strikingly similar because of they form a bundle pair. (In all other systems, the density was lowered to avoid pair formation.) The images are shown at time $t = 6000 \tau$. The bottom toroid is fully formed by $t = 1200 \tau$. The top toroid takes 5200τ to form. All but one of the rods forms before the first toroid forms.

The figure shows the (condensed) counterions which are within $2d$ of any monomer. In general for $z_c = 4$, all the counterions condense. While the counterions are condensed, they still move about in the volume near the polymer. In other words, the counterions are bound to the polyelectrolyte not to some monomer. As such, they do not lose all their entropy in becoming condensed. This is very important as divalent counterions typically fail to yield DNA condensation experimentally (Bloomfield, 1996). Divalent ions have relatively weaker Coulomb interactions than tetravalent ions and have more entropy costs since there are twice as many. Entropy wins in the divalent ion case.

Simulations performed with divalent ions do not form any condensed structures. This is not completely convincing since there is always the issue of whether condensation would occur if the simulation was run longer. To treat this issue, simulations have been performed starting with initial conformations near the toroid structure. The initial polyelectrolyte conformation is a spiral. The counterions are placed on a separate spiral such that they are between successive arcs of the polymer's spiral. The energy of the single conformation with counterions was calculated for varying spiral radius and pitch. The minimum energy conformation was found and used as the initial state. For parameter set 2 with bond angle set 3 and $N = 256$, one turn of the spiral has 40 beads and the pitch is $2 \cdot 2^{1/6}d$. This value of the pitch yields puts the counterions and charged monomers as close as possible without overlap of the LJ spheres. The spiral structure should be able to easily evolve into a toroidal structure which is just multiple spirals that are connected and successively surround each other.

Figure 25 shows the conformations of the 8 polyelectrolytes with divalent counterions after about $5 \cdot 10^6$ time steps ($7.4 \cdot 10^4 \tau$) starting from the spiral conformation. Clearly the toroidal structure is not stable for the divalent system. On average 116 out of 128 counterions per chain condense to within $2d$ of the polyelectrolytes. The polyelectrolyte with these counterions has a net negative charge. The simulations show that this net charge results in a net repulsion within the molecule and an extended structure. In comparison with the $z_c = 4$ system, more counterions are delocalized and are not screening the monomeric charges.

While single polyelectrolytes with divalent counterions do not self-condense, multiple polyelectrolytes with divalent counterions will form bundles (Stevens, 1999). Counterions condensed to a bundle move throughout the bundle volume. Consequently, their entropy is much larger than the entropy of counterions condensed to a single self-condensed polyelectrolyte. For this reason, divalent ions can yield multiple polyelectrolyte 'condensation,' but typically do not yield single molecule condensation.

For the same parameter set but with tetravalent counterions, toroidal structures form and are stable. Figure 26 shows the eight conformations. These conformations are not the same as the initial spiral structure. Along

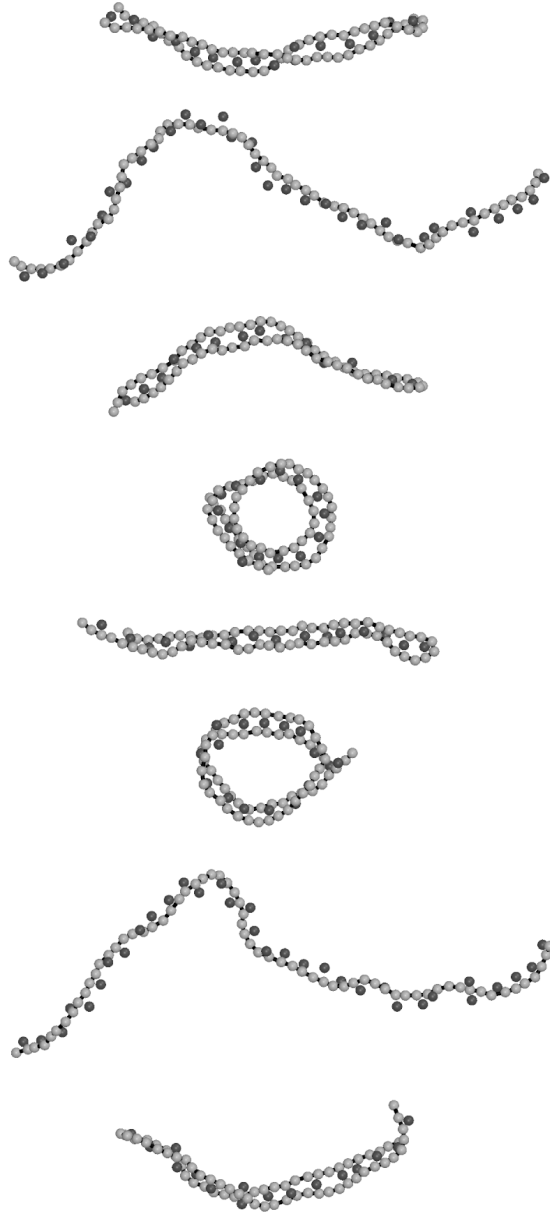


Figure 24. Images of structures for $N = 64$ molecules (light spheres) with $z_c = 4$ counterions (dark spheres). Both toroids and rods appear.



Figure 25. Equilibrated conformations of individual chains of $N = 256$ with $z_c = 2$ counterions using parameter set 2 (Table I) and bond angle set 3 (Table II). The initial conformation for each chain was a spiral.

the central axis of the spiral the polyelectrolyte has contracted, and the circular turns have more than one diameter. The connection of this structure with energetics is discussed below.

The above results demonstrate that condensation of a polyelectrolyte is due solely to electrostatic interactions. No additional interactions are involved in the simulations. It is also clear that condensation can occur for a wide range of parameters: ξ , N , d and L_p . The very long persistence lengths of DNA are not a requisite. However, multivalent ions with charge 3 or 4 are typically required (A simulation with $z_c = 3$ does find condensation). The condensed structures that form at $z_c = 4$ will now be discussed in more detail.

Condensed structure

It is not surprising that both toroidal and rod structures form. For homopolymers with varying stiffness in a poor solvent, it is known that both rod and toroidal structures form (Noguchi and Yoshikawa, 1998). When L_p is small (small k_1), the cost of a hairpin turn is relatively small and rod structures are favored over toroids. As L_p increases there is a transition to toroids. In semiflexible polyelectrolytes the competition between rods and toroids depends on whether a few sharper turns require less energy than many slight bends, or whether the rod structure has a lower Coulomb energy offsetting the additional cost of the angular term.

To examine the competition between rods and toroids, simulations similar to that of Fig. 24 were performed, but with parameter set 2 (Table I), longer chains $N = 256$ and larger L_p ($k_1 = 20\epsilon/\text{rad}^2$). Figure 27 shows all eight molecules condense into twisted rod structures. Close examination of the ‘hairpin’ turns in Fig. 27 shows that the turns are not true hairpins, rather each bend is several monomers long. The innermost turns

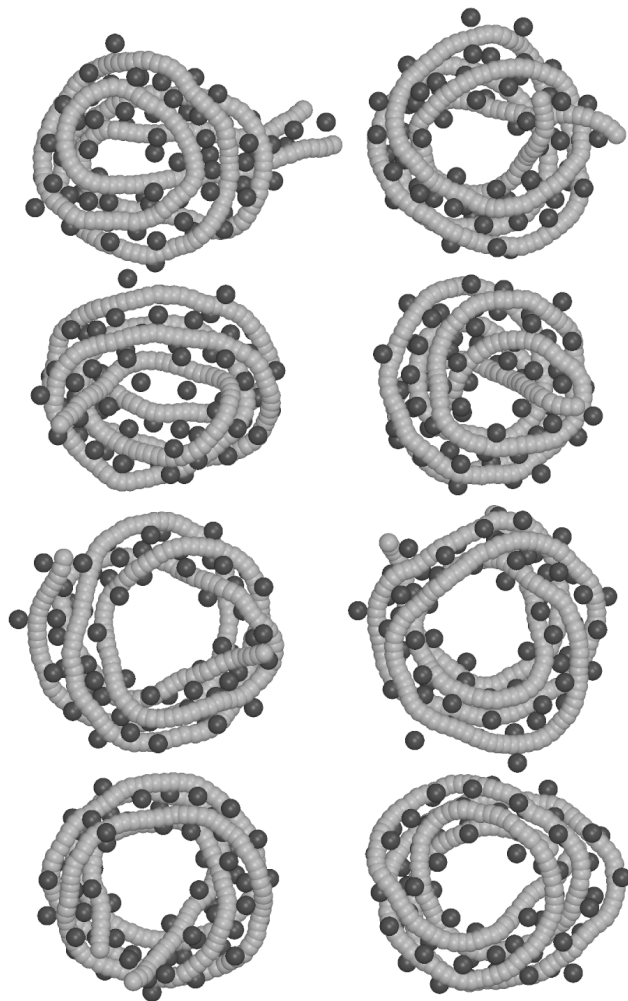


Figure 26. Images of toroidal structures for $N = 256$ molecules (light spheres) with $z_c = 4$ counterions (dark spheres) using parameter set 2 (Table I) and bond angle set 3 (Table II). The initial conformation for each chain was a spiral.

are the sharpest and the differential bond angle, $\Delta\theta = \theta - \theta_0$ is typically less than 40° . Other bends in the structure wrap around the inner segments, and consequently are much less sharp. Thus, the angular energy in the rod's turns is not as expensive as might initially be expected.

There also appears to be a kinetic preference for hairpin turns in these cases with k_1 not prohibitively large. The structures in Fig. 27 start with the formation of single hairpin turn typically near the polymer end. The kinetic preference for the hairpin is due to relatively few monomers needed in the initial formation. When two segments of the polymer are parallel with counterions in between them, the Coulomb energy is significantly reduced. Once the hairpin turn has occurred, the energy is further decreased as the position of the hairpin turn progressively moves so that the parallel segments comprise more and more of the polyelectrolyte. In contrast, for toroid formation a complete circle must occur within the polymer before the Coulomb energy is lowered. This requires a larger number of monomers to be involved in the initial transition. The transition time is then longer for toroids, or, equivalently, the formation rate is lower for toroids. In the system of Fig. 27 the first hairpin turn occurs at about $t = 4500\tau$. The first complete rod structure occurs by 6000τ . It takes $33,000\tau$ for all the chains to achieve their final rod structure.

While rod structures have been observed for DNA (Bloomfield, 1996; Fang and Hoh, 1999), toroids are the typical condensate structure. While the model system has a large bond bending stiffness relatively to the bond length, L_p is small compared to that in DNA. For DNA the total persistence length is 240 base pairs (Calladine and Drew, 1997) or 480 charged monomers. For such a large persistence length, the maximum bend per monomer is at most a few degrees precluding hairpins. In addition, for DNA it is not likely that the bending potential is harmonic at large bends. In the bead-spring model the bond bending corresponds not to the bending of individual bond bending within a DNA molecule, but to bending of the whole molecule.

The large angle bends can be made prohibitively expensive by including a quartic term in the bond bending potential as is given in Eq. 99. The bond angle parameters in set 3 (Table II) yield a potential similar to that of set 2 at small angles while making large angle bends more expensive. As already shown in Fig. 26, the toroid structure is stable for this parameter set. While the hairpins appear kinetically favored in these simulations, the lowest energy state has not been determined. Between the toroidal and hairpin structures, the energies can be compared to determine the state with the lower energy.

To compare the energies of the toroid and rod states, simulations with identical parameters (i.e. bond angle potentials) must be performed, but for the two different conformations. Using the conformations in Figs. 26 and 27 as the starting configurations enables the calculations of their respective energy. In addition, the effect of increased molecular stiffness on the rod structures has been investigated. As the stiffness is increased, the toroidal structure will become more favorable. If the polymer length is long enough, the toroidal structure will in fact become the thermodynamic state (Noguchi and Yoshikawa, 1998).

To change the polymer stiffness, the quartic term in the bond angle potential (Eq. 99) is varied. As discussed above, increasing this term reduces the likelihood of large angle bends. Starting from parameter set 2 (Table I) and bond angle set 2 (Table II) for which the hairpins formed, the value of k_2 is increased. Figure 28 shows how specific k_2 values are chosen. The solid line is for the bond angle potential set 2. The dotted lines are for the harmonic version ($k_2 = 0$) with $k_1 = 100$ and $200\epsilon/\text{rad}^2$. For the dotted curves there would

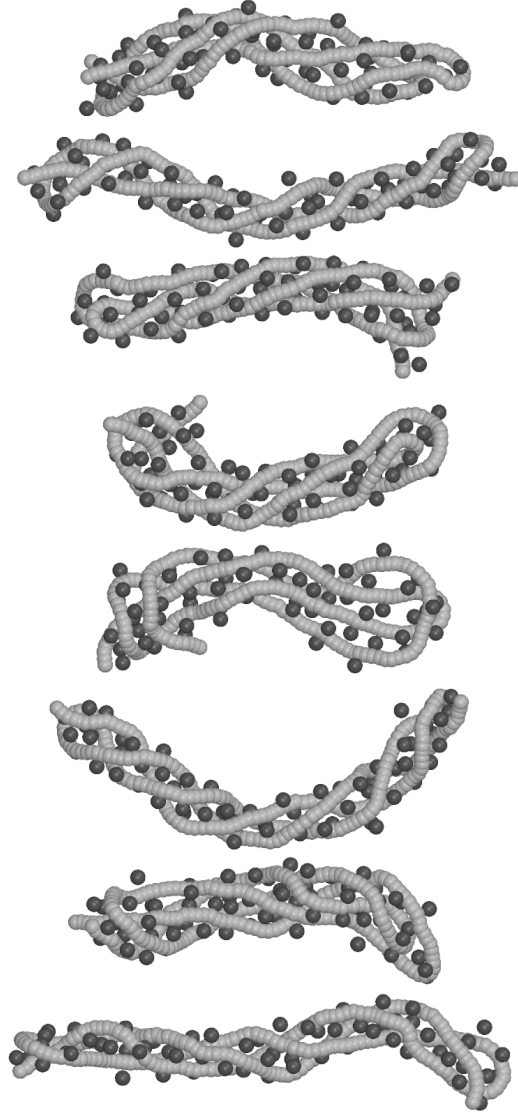


Figure 27. Images of rod structures for $N = 256$ molecule (light spheres) with $z_c = 4$ counterions (dark spheres). This is system 2 in Table III.

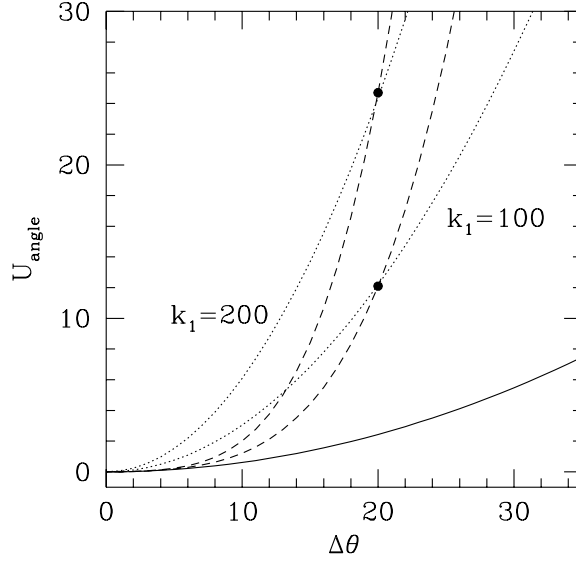


Figure 28. The bond angle potential for various parameters is shown. The solid line and the two dotted lines are harmonic ($k_2 = 0$). The solid line represents bond angle set 2 ($k_1 = 20\epsilon/\text{rad}^2$), and the dotted lines are labeled. The dashed lines have the same k_1 as the solid line, and k_2 is chosen to fit the dotted lines at $\Delta\theta = 20^\circ$ (marked by dots).

be no condensates at $N = 256$ since L_p is too large; these potentials are thus not used. By adding a quartic term to the bond angle set 2, the large angle bends can be progressively removed as it would be for the large k_1 potentials while the small angle bends will have the same energy. The value of k_2 is chosen so that U_{angle} is equal to the harmonic potential at $\Delta\theta = 20^\circ$. To fit the $k_1 = 100\epsilon/\text{rad}^2$ line at $\Delta\theta = 20^\circ$, the value of k_2 must be $650 \epsilon/\text{rad}^4$ with $k_1 = 20\epsilon/\text{rad}^2$. Similarly, to fit the $k_1 = 200\epsilon/\text{rad}^2$ line, $k_2 = 1500\epsilon/\text{rad}^4$. These potentials should alter the hairpin structure of Fig. 27. The simulations will determine whether these bond angle parameters are strong enough to cause the transition to toroids.

Table 6 gives the energies per particle for the different starting states and different bond angle parameters. System 1 is for the toroidal structure. The potential energy for the toroid structure is the lowest of all the structures. Compared to the rod system of Fig. 27 (System 2), the toroidal structure of Fig. 26 has a higher Coulomb energy but a lower bond angle energy; the net effect is that the toroid potential energy is lower. Table III gives the energies for the rod structures as k_2 increases. As k_2 increases the bond angle potential energy decreases which was not expected. However, this energy decrease occurs because the conformations change. The diameter of the turns in the structure increases such that the turns are no longer hairpins, but have a diameter smaller than the toroid loops. The structures in systems 3 and 4 do not evolve into toroids. Instead, they remain elongated but now with large loops at the ends wider than the more compact middle sections of parallel segments. The twisted nature of the rod disappears in system 4.

For system 5 (Fig. 29), the final structure depends on the initial rod structure. Some molecules become toroids; some remain rods; some look like tennis rackets with a large loop at one end and a rod at the other

Table 6. Energy comparison. Energy in units of ϵ .

System	Total PE	Coulomb	Angle	Bond	LJ	k_1	k_2
1	-2.84	-8.27	0.80	4.38	0.26	20	650
2	-2.73	-8.47	1.09	4.37	0.26	20	0
3	-2.73	-8.21	0.86	4.37	0.25	20	300
4	-2.65	-8.11	0.84	4.37	0.25	20	650
5	-2.62	-7.97	0.78	4.35	0.25	20	1500

end (cf. Schurr *et al.*, 1999). In the starting rod structures (Fig. 27) there are two structural subsets. One set has the molecule ends at different rod ends and 3 middle ‘parallel’ segments; the other has the molecule ends at the same rod end and 4 middle ‘parallel’ segments. The rods with 3 segments remains rods as k_2 is increased, but the rods with 4 segments become toroids or ‘tennis rackets.’ With 4 segments the transition to a toroid can occur continuously by having the center open up with two segments going to the left and two going to the right. The rods with 3 segments cannot continuously transform into a toroidal structure. Two segments going to the left would leave only one segment going to right and an unbalanced situation. The 3 segment rod would have to first become an extended chain and the recondense into a toroid. In this case, the kinetic barrier is too high. The configurations are shown at about $t = 80,000\tau$. In a similar manner, the tennis racket structures occur for the 4 segment molecule in which the free ends have paired up and not gone to separate sides of the loop. This makes the rod structure more stable; there is effectively an ‘entanglement’ at the racket handle. Presumably if the simulation was run long enough these molecules would transform to a complete toroid.

Overall, the clear trend in increasing k_2 for the systems with the rod starting states is that the Coulomb energy decreases monotonically. The bond angle energy also decreases, but the majority of this decrease occurs once $k_2 > 0$. The decrease in the Coulomb energy is related to the larger separation of the charges particularly at the turns in the rod. The toroid structure has the lowest energy of all states, and by increasing k_2 a transition to toroids does occur. There are clear kinetic barriers associated with specific initial structures so that rod structures can be strong metastable states.

Charge ordering of polyelectrolyte condensation

The ordering of charged monomers and counterions involved in toroidal structures compared to extended, noncondensed polyelectrolyte structure can be seen in radial distribution functions (rdf). Figure 30 shows both the monomer-counterion $g_{mc}(r)$ rdf and the counterion-counterion rdf, $g_{cc}(r)$ for both structures. Because of the strong counterion condensation due to tetravalent counterions, the peaks are very large in the figure. Because the molecular condensation process is rather slow on the simulation time scale, simulations that start with extended structures easily remain extended long enough for calculation of $g(r)$ in this state. The rdfs for the noncondensed state are rather structureless and the only feature is due to counterion condensation. The single, large peak at contact in $g_{mc}(r)$ is due to the condensed counterions which spend most of the time right next to the polymer. Because there are so many counterions on the polymer, the counterion-counterion rdf exhibits a peak at about 5.7σ corresponding to the average separation along the polymer between neighboring counterions. For $z_c = 4$, all the counterions condense yielding a counterion for every z_c monomers. The separation of charged monomers is 1.1σ giving a distance of 4.4σ between neighboring condensed counterions,

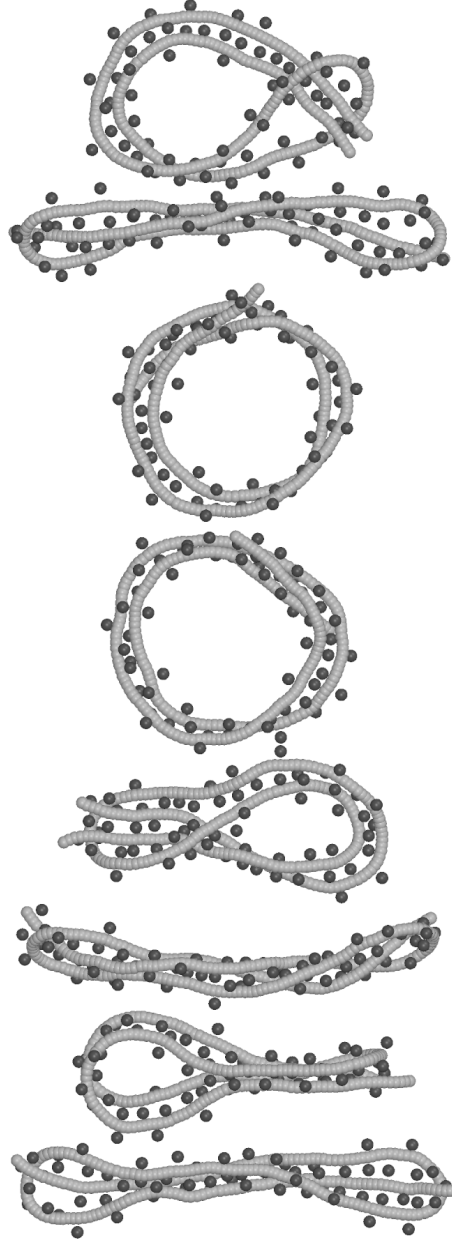


Figure 29. Images of structures for $N = 256$ molecule (light spheres) with $z_c = 4$ counterions (dark spheres). This is for system 5 in Table III which had Fig. 27 as starting state.

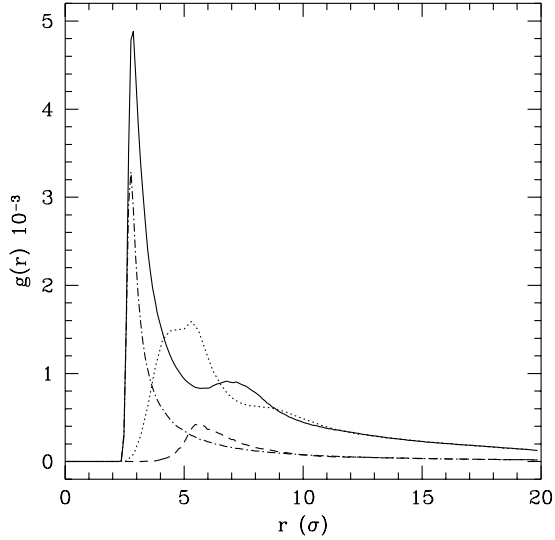


Figure 30. The monomer-counterion and the counterion-counterion radial distribution functions (rdf) for the toroid structure (Fig. 26) and for the extended, noncondensed structure. Both systems have tetravalent counterions. The solid line is the monomer-counterion rdf for the toroids; the dot-dashed line is for the noncondensed structure. The dotted line is the counterion-counterion rdf for the toroids; the dashed line is for the noncondensed structure.

if they were on the same side of the polyelectrolyte. This is not a very favorable position due to the Coulomb repulsion between counterions and $g_{cc}(4.4\sigma) \simeq 0$ confirms this point. If the counterions were on opposite sides of the polyelectrolyte, then the separation distance is 6.2σ which is slightly larger than the peak position. The smaller value of the peak position corresponds to the distribution of positions with the most probable being close to that of counterion on opposite sides.

For toroids (and rods), both distribution functions exhibit structure beyond just counterion condensation. Moreover, this structure is a result of charge ordering due to condensate structure. For example, in $g_{mc}(r)$ for the toroids, a second peak appears at about 7.2σ . This peak is due to counterions condensed on a neighboring loop in the toroid. To simplify the notation, let c stand for counterion and m for monomer. Then, the peak at 7.2σ corresponds to the sequence m-c-m-c, where the first m is the central monomer, the first c is its condensed counterion, the second m is a monomer of a neighboring loop and the last c is a condensed counterion to this neighboring loop. The straight line separation between the central monomer and the last counterion is $3d = 7.9\sigma$. The peak position is smaller than $3d$ implying that the m-c-m-c sequence tends not to be straight, but zig-zagged as in a triangular lattice. This more compact structure lowers the Coulomb energy.

The $g_{cc}(r)$ for the toroids is the most interesting of all the distributions. Besides the peak at 5.7σ which occurs in the noncondensed state, there are two additional peaks. There is now a peak at 4.4σ as well as

a discernable, but relatively weak peak at about 9.5σ . The peak at 4.4σ was noted above to be just the separation distance between counterions on the same side of the polymer. In the noncondensed state, this ordering is unfavorable. In the toroid structure, this ordering becomes favorable, because the counterion is shared among multiple loops of the toroid. The peak at large $r = 9.5\sigma$ is the correlation between counterions with *two* loops in between. In the notation above, the sequence is c-m-c-m-c. A straight arrangement would give the peak at $4d = 10.5\sigma$. Again, the peak position implies that the arrangement is more compact.

From Fig. 30 the charge ordered, sequence c-m-c-m-c is clearly resolvable. Such charge ordering is the favored structure by the Coulomb interactions, since the Coulomb energy is lowered. Such structure can form when the Coulomb interactions dominate entropic interactions. DNA condensates form because these charge ordered states are more stable and have lower energy than extended structures when the Coulomb interactions are sufficiently strong (i.e. $z_c \geq 3$).

The charge ordered state corresponds to the collapsed state at large Γ in the OCP picture. Condensation occurs when the Coulomb interactions are strong enough to stabilize charge ordered structures such as toroids or rods. For $z_c \geq 3$ and typical diameters, the Coulomb interactions are strong enough for condensation. However, for $z_c \leq 2$, entropy is dominant, and condensates are not stable.

Conclusions

Molecular dynamics simulations of a simple, bead-spring model of semiflexible polyelectrolytes such as DNA have been performed to study condensation. Starting from extended polymer conformations, condensation into toroids and rods occurs in the MD simulations. Condensates form for tetravalent and trivalent counterions, but not divalent counterions. Besides treating the charge density of DNA, various polymer lengths, polymer stiffnesses, charge densities, and monomer sizes were simulated and produced condensates. Condensation is a generic phenomenon of semiflexible polyelectrolytes. Furthermore, condensation is primarily an electrostatic phenomenon. For condensation to occur the Coulomb interactions must be stronger than the entropic interactions to overcome the entropic loss of condensation. For this reason, multivalent ions of valence at least 3 are typically required. When the Coulomb interactions are strong enough to dominate the entropic interactions, the polyelectrolyte along with its counterions forms a charge ordered structure. This structure is either a toroid or a rod depending on the stiffness of the polymer (assuming $L_p \ll L$). Toroidal structures are favored by the large persistence lengths found in molecules like DNA.

It is very important biologically that the condensation mechanism is independent of the base pair sequence and more generally the chemistry of DNA. Fitting DNA into small packages must be done independent of the genetic code it contains. Otherwise, some genetic sequences could not exist. The mechanism described here depends solely on electrostatic interactions of the DNA phosphates and the counterions.

References

- Baus, M and J.P. Hansen. 1980. Statistical Mechanics of Simple Coulomb Systems. *Phys. Rep.*, 59:1.
- Brami, B, J.P. Jansen and F. Joly. 1979. Phase separation of highly disymmetric binary ionic mixtures.

- Binder, K, editor. 1995. Monte Carlo and Molecular Dynamics Simulations in Polymer Science. Oxford, New York.
- Bloomfield, V.A. 1991. Condensation of DNA by multivalent cations: consideration on mechanism. *Biopolymers*, 31:1471.
- Bloomfield, V.A. 1996. DNA condensation. *Curr. Op. in Str. Biol.*, 6:334.
- Brilliantov, N.V., D.V. Kuznetsov, and R. Klein. 1998. Chain collapse and counterion condensation in dilute polyelectrolyte solutions. *Phys. Rev. Lett.*, 1433:81.
- Calladine, C.R. and H.R. Drew. 1997. Understanding DNA. Academic Press, San Diego, CA.
- Grønbech-Jensen, N., R.J. Mashl, R.F. Bruinsma, and W.M. Gelbart. 1997. *Phys. Rev. Lett.*, 78:2477.
- Ha, B.-Y. and A.J. Liu. 1997. Counterion-mediated attraction between two like-charged rods. *Phys. Rev. Lett.*, 79:1289.
- Hockney, R.W. and J.W. Eastwood. 1988. Computer Simulation using Particles. Adam Hilger, New York.
- Fang, Y. and J. Hoh. 1998. Early intermediates in spermidine-induced DNA condensation on the surface of mica. *J. Am. Chem. Soc.*, 120:8904.
- Fang, Y. and J.H. Hoh, 1999. Cationic silanes stabilize intermediates in DNA condensation. *FEBS Lett.*, 459:173.
- Kjellander, R. and S. Marčelja. 1984. *Chem. Phys. Lett.*, 112:49.
- Kleinschmidt, A. K. D. Land, D. Jacherts, and R.K. Zahn. 1962. Darstellung und Längenmessungen des gesamten desoxyribonucleinsäure-inhaltes von t_2 -bakteriophagen. *Biochimica et Biophysica Acta*, 61:857.
- Lyubartsev, A.P. and L. Nordenskiöld. 1995. Monte Carlo simulation study of polyelectrolyte properties in the presence of multivalent polyamine ions. *J. Poly. Chem. B*, 101:4335.
- Kremer K. and G.S. Grest. 1990. Dynamics of entangled linear polymer melts: A molecular-dynamics simulation. *J. Chem. Phys.*, 92:5057.
- Manning, G. 1969. Limiting laws and counterion condensation in polyelectrolyte solutions i. colligative properties. *J. Chem. Phys.*, 51:924.
- Neu, J.C., 1999. Wall-mediated forces between like-charged bodies in an electrolyte. *Phys. Rev. Lett*, 82:1072.
- Noguchi H. and K. Yoshikawa. 1998. Morphological variation in a collapsed single homopolymer chain. *J. Chem. Phys.*, 109:5070.
- Oosawa, F. 1971. Polyelectrolytes. Marcel Dekker, New York.
- Pollock, E. L. and J. Glosli. 1996. Comments on p3m, fmm and the ewald method for large periodic coulombic systems. *Computer Physics Comm.*, 95:93.
- Ray, J. and G.S. Manning. 1994. Fluctuations of counterions condensed on charged polymers. *Langmuir*, 10:2450.
- Sader, J.E. and D.Y.C. Chan. 1999. Long-Range Electrostatic Attractions between Identically Charged Particles in Confined Geometries: An Unresolved Problem. *J. Coll. Int. Sci*, 213:268.
- Scheissel, H. and P. Pincus. 1998. Counterion-condensation-induced collapse of highly charged polyelectrolytes. *Macromolecules*, 31:7953.

- Schneider T. and E. Stoll. 1978. Molecular-dynamics study of a 3-dimensional one-component model for distortive phase-transitions. *Phys. Rev. B* 17:1302.
- Schurr, B., F. Gittes, F.C. MacKintosh, and D.R. M. Williams. 1999 Collapse dynamics of biopolymers with attractive interactions: The transition to toroids via tennis racquets. *Biophys. J.*, 76:245.
- Stevens, M.J. 1999. Bundle binding in polyelectrolyte solutions. *Phys. Rev. Lett.*, 82:101.
- Stevens, M.J. and K. Kremer. 1995. Structure of of salt-free linear polyelectrolytes. *J. Chem. Phys.*, 103:1669.
- Stevens, M.J. and M.O. Robbins. 1990. Density functional theory of ionic screening : when do like charges attract. *Europhys. Lett.*, 12:81.
- Stevens, M.J., M.L. Falk and M.O. Robbins. 1996. Interactions between charged spherical macroions. *J. Chem. Phys.*, 104:5209.

Towards understanding the function of unstructured proteins: simulations of charged polymers under confinement

Joanne N. Bright,⁵ Mark. J. Stevens, Jan Hoh⁶, Thomas B. Woolf⁷

Abstract

Experimental findings that some polypeptides may be unstructured and behave as entropically driven polymeric spacers in biological systems motivates a study of confined polymers. Here we examine the confinement of neutral, polyampholyte and polyelectrolyte polymers between two parallel surfaces using course grained models and molecular dynamics. Forces between the confining surfaces are determined for different polymer classes and as a function of chain length, charge sequence (pattern) and degree of confinement. Changes in chain properties are also evaluated under these conditions. The results reinforce the significance of length and net charge for predicting chain properties. In addition the clustering of charge along the chain appears to be critical, and changes in cluster size and distribution produce dramatic changes in chain behavior.

Introduction

It is becoming increasingly clear that many proteins or regions of proteins are intrinsically unstructured, and that their function is directly related to being unstructured. A number of potential functions for unstructured polypeptides have been proposed.[50, 14, 20] One of these functions is based on the thermally driven motion of a polypeptide acting as a molecular spacer through primarily entropic forces. This type of entropic exclusion is common in non-biological systems.[48] In biological systems there is evidence to suggest that unstructured polypeptides play an important role in stabilizing of casein micelles,[47, 7] maintaining interfilament spacing between neurofilaments,[5] and possibly a range of other functions.[20] Sequence analysis of unstructured polypeptides shows that these chains often have low sequence complexity and have an abundance of charged or hydrophilic amino acids.[46, 14] This suggests that the extensive body of models and theory that have been developed to predict the behavior of non-biological polymers might be productively applied to understand functional properties of unstructured polypeptides. In particular, the practice within the polymer community of using course grain (mesoscopic) models offers significant computational advantages over the detailed all atom representations commonly used in the protein simulation community. Within the course grain framework one can begin by categorizing polypeptides into one of three general polymer types, neutral, polyampholyte or polyelectrolyte. Here neutral polymers have no charged monomers, polyampholytes have charged monomers but a near net zero charge and polyelectrolytes have charged monomers and a net charge. It should be noted that polymer theory has been extensively applied to biopolymers in other contexts, such as protein folding issues (e.g. [43, 25]), and polyelectrolyte systems such as DNA (e.g. [45, 3]). However, here our long-term aim is to obtain functionally relevant properties of intrinsically polypeptides.

Polymer theory provides clear predictions for general chain behavior under certain limits. There is a substantial body of literature describing the properties of neutral polymers under a range of conditions.[9] Polyampholytes and polyelectrolytes have also been studied, but are less well understood.[39, 35, 1, 31, 22, 37] However, making more detailed analytical predictions for charged polymer systems is challenging. This reflects

⁵Department of Physiology, Johns Hopkins University, School of Medicine, Baltimore, MD 21205

⁶Department of Physiology, Johns Hopkins University, School of Medicine, Baltimore, MD 21205

⁷Department of Physiology, Johns Hopkins University, School of Medicine, Baltimore, MD 21205

the difficulties in approximating the interplay between long-range electrostatic effects and entropic effects. Some of these difficulties can overcome using simulations.

Most studies on charged polymers have used either random or regularly alternating charge sequences, and have focused on average properties (e.g. radius of gyration or the shape of chains). From such analysis there is an understanding of chain behavior as a function of total charge, [1, 44, 30] and changes in solvent quality,[1, 51] or in the presence of an external field.[12, 11] There has been much less work on the effect of a particular charge sequence[13, 24, 29, 35] or on constrained (e.g. surface attached, adsorbed) chains or chains in confined geometries. Here we present molecular dynamics simulations of neutral, polyampholyte and polyelectrolyte polymers under varying degrees of confinement, performed using the Large-scale Atomic/Molecular Massively Parallel Simulator (LAMMPS) molecular dynamics code.[36] In addition to confinement, we vary chain length, charge sequence and net charge of the charged polymers. In these simulations we use coarse grained bead representations of the polymer chain. Non-bonded interactions are treated by a strictly repulsive Lennard-Jones (LJ) potential. Bonds are simulated by a sum of the repulsive LJ potential and the finitely extensible, nonlinear elastic (FENE) potential. The solvent is treated implicitly using a continuum dielectric, and LJ parameters yield good solvent conditions for each chain. In addition, for charged polymers the simulations include explicit counterions. For these systems we compute full Coulombic interactions via the particle mesh Ewald algorithm. In all simulations, polymer chains are end-attached to a flat surface. For confinement, a second flat "probe" surface is moved to variable distances above the first. Both flat surfaces are purely repulsive, except for the anchoring bead. By examining the force on the probe surface as a function of distance between the two surfaces, force-distance curves similar to those obtained experimentally by atomic force microscopy are produced. We also examine the confined polymer's structure.

We first present a brief background section discussing initial expectations for polymer chains in the neutral, polyelectrolyte and polyampholyte categories. Section one then describes simulations with confinement of neutral chains. We present the calculated confining force on the walls and chain properties for chains of varying length. Section two presents simulations of charged systems—i.e. simulations of polyelectrolytes and polyampholytes with a variations in their charge sequence. This second section used simulations with fixed chain length and varying degrees of confinement. We conclude with a general discussion and possible future directions for these studies.

Theoretical Background and Expectations

Polymer theory has been successfully applied to macromolecules with many individual bead components. The general approach is to compute properties as averages over the full statistical mechanical phase space of accessible conformations. For example, the average end-to-end distance of the chain is calculated by balancing entropic and excluded-volume effects to exhibit the classic scaling behavior: $R_F = \langle R^2 \rangle^{1/2} \sim aN^\nu$, where a is the segment or monomer size, N the number of monomers and ν is the Flory exponent, equal to $1/3$, $1/2$ and $\sim 3/5$ in poor, θ and good solvents in $3D$ respectively.

For chains end-attached (grafted) to a surface the configurational space is reduced from bulk, due to the additional constraint on the tether point of the chain. For high grafting densities interactions with other chains leads to strong stretching away from the surface (the polymer brush state). For sparse grafting (and sufficiently long) chains the surface is characterized by individual polymer occupying half "mushroom" spheres

with radial dimensions following the same scaling behavior as dilute chains in bulk. The density profile of segments normal to the surface is predicted [34] to exhibit a maximum several monomer lengths from the surface and spread more in the radial direction parallel to the attachment plane than normal to it.

The presence of an additional confining surface will alter the unperturbed behavior of the chain. The simplest system to consider is the case of confinement between two parallel plates separated by a distance D in good solvent [6, 26, 10] (Figure 31). For $D > R_F$ the chain is weakly confined and interacts with the surfaces through fluctuations in the chain beyond its average dimensions. For $R_F > D$ may be described as a string of “blobs” [9], with radius $D/2$, containing $(D/a)^{5/3}$ monomers exhibiting similar statistics to an unperturbed coil. The chain adopts a two dimensional pancake of radius $R_{F2} \sim aN^{3/4}(\frac{a}{D})^{1/4}$. The total free energy of this type of system is determined by summing the contributions of the blobs $\sim kT$:

$$F = kTN\left(\frac{a}{D}\right)^{5/3}, \quad (69)$$

for $a \ll R_F < D$ and the chain resists further compression by exerting a force scaling as:

$$f = kTNa^{-1}\left(\frac{a}{D}\right)^{8/3}, \quad (70)$$

on the confining plane. The force required to compress the polymer is predicted to increase linearly with the chain length and with a power law exponent of $-8/3$ with D . For separation distances $D > R_F$ the force loses its dependence on chain length and scales inversely with the surface separation. For finite size compressing objects there is a possible escape transition by chains stretching to unconfined regions of space [17] or by arbitrary shape/misalignment [21], however this is precluded by the geometry adopted in this paper.

The predictions of scaling approaches have been tested by numerical SCF [4], and MC and MD [26, 10, 23] studies for chains of varying finite length. Most studies find an exponent in excess of that predicted by Eq.70 while retaining the predicted scaling behavior with chain length N . Analysis of the monomer distribution profiles via SCF confirms the “mushroom” configuration of the chain at large separations and the gradual transition to a two dimensional pancake with increasing confinement.

The properties of polymers bearing charged groups are less easily accessible to either simple theory or simulation. Analytic theory is complicated by the additional length scales of the system. Simulation is complicated by the difficulty in accounting accurately for the full electrostatic interactions of the system while retaining computational efficiency.

The average properties of a polyampholyte (of which a polyelectrolyte may be considered a limiting case), will be controlled by the balance of electrostatic interactions and entropic degrees of freedom. For example, the electrostatic interactions in overall neutral chain promote collapse, while in the case of charge imbalance they promote swelling. In contrast, entropy promotes Gaussian like configurations. Different regimes of behavior are dependent on the relative importance of these effects. Thus at high temperatures thermal effects dominate chain behavior and chain dimensions and shape are relatively unperturbed by the presence of charged groups. At intermediate temperatures and significant charge asymmetry (net overall charge) the chain behavior is dominated by electrostatic repulsion between uncompensated charged groups. Thus the chain is predicted to extend beyond its unperturbed dimension, reaching in the limit of infinite dilution and a strongly charged polyelectrolyte, a rodlike configuration. For intermediate temperatures and net neutrality the behavior is dominated by fluctuation induced attractions between unlike charges and the PA collapses to a globular

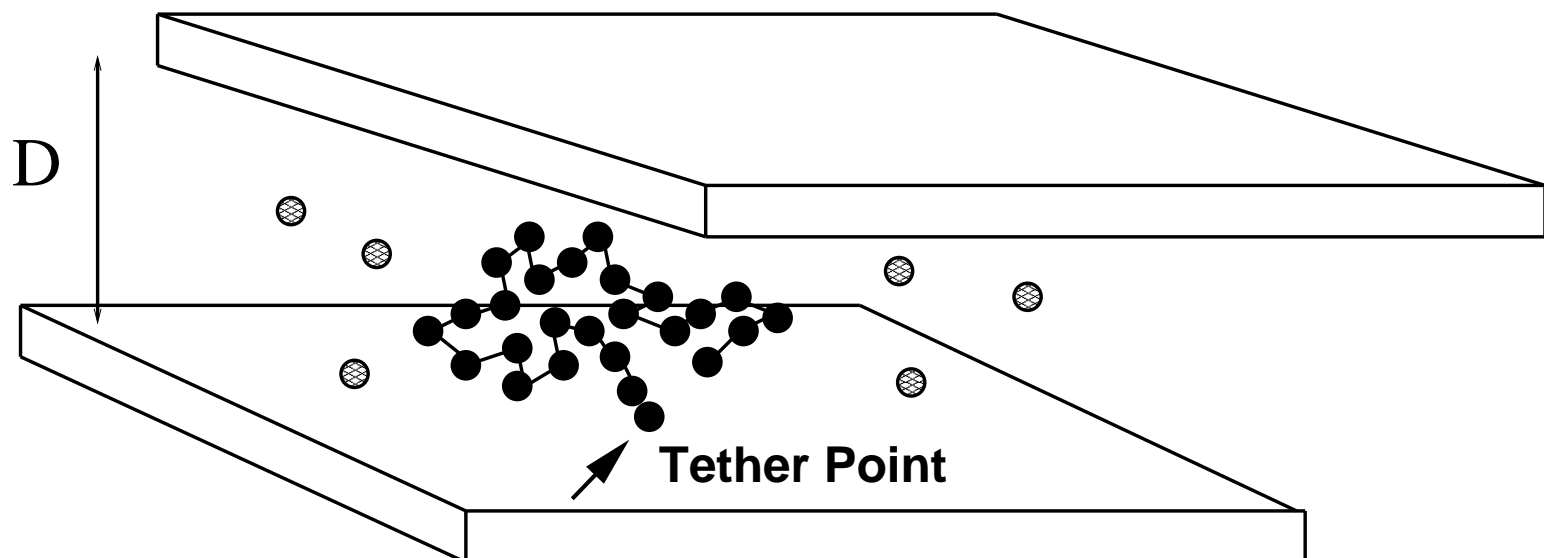


Figure 31. Geometry of the simulations. The chain is permanently attached via the first neutral segment to the bottom surface. The top surface, modelling a probe or similar confining object is held parallel to the bottom surface at a separation D . D is varied in the simulations to individually collect force curves and chain properties for each simulation once equilibration has been obtained.

configuration with dimensions less than that of the unperturbed chain. That is the charges screen each other in a Debye-Huckel like fashion. At very low temperatures or very poor solvents the configuration may be frozen, resulting in “pearl-necklace” configurations of the chain.

External fields, added salt, charge sequence variation and excess charge may significantly influence the behavior of polyampholyte chains. An external field, for example, can lead to further frustration of the chain, due to an additional pull or repulsion on the charged groups. A similar situation is predicted for chains with a net overall charge $> \sim q\sqrt{fN^{1/2}}$, where frustration may result in chains exhibiting both collapsed neutral and stretched highly charged portions [41]. The charge sequence may also play an important role in the balance of thermal and electrostatic effects producing variation in the chain dimensions for chains with similar total composition [13]. Chains with strictly alternating sequences of charge are not well described by Debye-Huckel theory since charge fluctuations over distances of the order of the screening length are generally not possible. They are predicted [24] to collapse in the same manner as neutral polymers in a poor solvent and may be described by an effective, negative second virial coefficient. Such chains are more soluble than polyampholytes with random sequences of charges, with decreasing solubility as randomness or size of charged blocks along the chain increases.

Three important length scales can be identified for the description of polyampholyte chains. All our simulations are performed with charge separation along the backbone b equal to the monomer size a and we work with this later parameter. The Bjerrum length, $\lambda_B = \frac{e^2}{4\pi\epsilon\epsilon_0 kT}$ is a measure of the distance over which charge groups interact. Under physiological conditions it has a value of $\sim 7\text{\AA}$. The relative importance of thermal and electrostatic interactions is characterized by the dimensionless coupling constant $\Gamma = \lambda_B/a$. For polyampholytes with charge fraction $f = 1$ (all segments charged) in good solvents and $\Gamma < N^{2/5}$ the thermal effects dominate while for $\Gamma > N^{2/5}$ the electrostatic interactions dominate behavior. For values of $\Gamma > 1$ condensation of counterions may occur [16] making theoretical analysis difficult. Finally the Debye screening length $\kappa^{-1} = (4\pi\lambda_B\rho)^{-1/2}$ where ρ is the ionic concentration (in our simulations \sim monomer concentration) measures the length scale over which electrostatic interactions are screened. For very dilute solutions this screening effect is negligible.

Simulation Details

Simulations are performed using the LAMMPS [36] code designed for the study of neutral and charged polymer systems. The code was modified to model the system of interest – end-grafted chains in the low density limit confined by impenetrable surfaces in an infinite 2-dimensional geometry. As in many applications of polymer theory, we are interested in a general class of polymers–polypeptides. Thus we look for common trends across our set of simulations. Towards this end, we employ the representation of the system as a set of coarse grained bead-springs. In this representation each bead-spring/monomer represents several chemical bonds. Water molecules are not represented explicitly, however their stochastic effect is captured by coupling to a heat bath producing random thermal forces through the friction constant γ . At the length and timescales of interest that we consider, the precise nature of this coupling should not play a role. Additionally screening effects of water on electrostatics are captured with a continuum dielectric. Ions are included explicitly and the full Coulomb interactions are calculated with particle-particle-particle mesh Ewald. Use of this code to treat electrostatics is central is critical, since cutoff methods have been shown to lead to artifacts and several recent

theoretical, numerical and experimental works [27, 38, 2] have indicated that ion fluctuations may significantly alter the electrostatic interactions of polyelectrolyte and polyampholyte chains. The two confining surfaces are modelled as homogeneous, flat, parallel surfaces exerting a short-range repulsive force on all monomers but the tether monomer. These surfaces are periodic with the periodic boundaries of the simulation cell. That is, the simulation is seen as approximating an infinite x - y periodic system with the z periodicity present, but adjusted to have a small effect on the planar energies and forces. We should also note that the x - y dimensions were chosen to enable a polymeric chain to remain confined with the central cell. The exact fraction of the cell confining the chains and ions is varied in different simulations, however the chains are always in the dilute limit. That is, there are no LJ interaction between the polymer in the central cell and its periodic images.

The behavior and properties of any one given chain is determined by (i) excluded-volume type interactions with bead monomers, with explicit ions and with the two wall surfaces, (ii) the constraint of connectivity along the backbone, (iii) random thermal agitation and frictional drag due to the solvent (modelled through the Langevin equation), and (iv) long-range Coulombic interactions between charged groups. The net potential is thus given by the summation:

$$U_{TOT} = U_{LJ} + U_{CH} + U_{WALL} + U_{COUL}, \quad (71)$$

and the motion of any given bead i , with mass m and position \mathbf{r}_i is described by the Langevin equation:

$$m \frac{d^2 \mathbf{r}_i}{dt^2} = -\Delta_i U - m\gamma \frac{d\mathbf{r}_i}{dt} + \mathbf{W}_i(t), \quad (72)$$

where γ is the friction constant and $\mathbf{W}_i(t)$ represents the random forces coupled to γ through the fluctuation-dissipation theorem.

We take into account excluded volume interactions for the monomers and ions via a standard Lennard-Jones potential:

$$U_{LJ} = 4\epsilon \left(\left(\frac{\sigma}{r} \right)^{12} - \left(\frac{\sigma}{r} \right)^6 - \left(\frac{\sigma}{r_c} \right)^{12} + \left(\frac{\sigma}{r_c} \right)^6 \right) \quad r \leq r_c, \quad (73)$$

truncated at $r_c = 2^{1/6}\sigma$ so that the interactions are strictly repulsive and athermal good solvent conditions are reproduced. Since this work is the initial part of a general treatment, the size of ions in the system are identical. The effect of differing ion size will be treated later.

To model the effects of connectivity we employ a finite extensible nonlinear elastic (FENE) spring potential:

$$U_{CH}(r) = -\frac{1}{2}kR_0^2 \ln\left(1 - \left(\frac{r}{R_0}\right)^2\right), \quad (74)$$

which produces the required restoring force counterbalancing the excluded volume interactions of the chain. A spring constant of $k = 30\epsilon/\sigma^2$ and a maximum bond extension $R_0 = 1.5\sigma$ are adopted in all our simulations, following previous studies indicating this parameter set to be a good choice for tethered systems. For uncharged chains this leads to an average bond length $l_{av} = 0.97\sigma$ [28] while for charged chains this is stretched slightly to $l_{av} = 0.98\sigma$ [15].

In the uncharged simulations each monomer in the chain is neutral and no ions are present in the system. For the charged simulations each monomer of the chain is charged either positively or negatively to produce a polyampholyte with zero net charge, or a progressively greater net charge ending with the limiting case of

a polyelectrolyte. The charge separation b along the chain backbone is given by the average bond length l_{av} . All charged chains have 32 charged monomers and one neutral tether monomer and are simulated at a fixed monomer density of $10^{-5}\sigma^{-3}$ (for the unconfined system) with 32 explicit counterions balancing the charge on the chain and 12 additional ions with net charge zero. The monomers and ions are always confined by the boundaries of the surfaces so that the effective density varies, depending on the surface-surface separation.

For all calculations with charges present (net neutral systems) we used particle-particle-particle mesh Ewald methods [19] within the LAMMPS code. This method is similar to the particle mesh Ewald method [42] in providing $N\log N$ performance. For our, 2-D periodic system, we also considered using 2-D Ewald methods [32, 33, 18, 8], but these are known to be an order of magnitude (or worse) slower than 3-D methods. We used the “parallel plate capacitor” approximation developed by Spohr [40]. In this approximation, a large amount of empty space is allowed in the z direction within the primary simulation cell. Spohr found that at least 5-times more distance in the z dimension should be used than present in the “matter-filled” regions. That is, with sufficient “empty-space” present, the coupling between the lattice spacing in the z -direction to the rest of the periodic images in the x - y plane is reduced to nearly zero. In our case the empty space varied with the polymeric system, but generally was on the order of from five to fifty times larger than the primary “matter-filled” region of interest. The variability in this ratio reflects the position of the probe surface relative to the simulation box dimensions. With this choice of simulation conditions we have created a 2-D periodic system that represents the electrostatics of confinement.

The strength of the Coulomb interactions is set by the Bjerrum length λ_B . All our simulations adopted the value $\lambda_B = 0.833\sigma$, giving $\Gamma = 0.85$ and placing our simulations within the counterion condensation regime. We are thus modeling strongly charged polyelectrolyte and polyampholyte chains. The charge sequence variations along the chain backbone are systematically varied either by increasing the size of repeating blocks of charged monomers (for the net neutral chains) or by varying the net charge on a random sequence of charges (for the $Q_{TOT} > 0$ chains).

In all our simulations the first bead is neutral and fixed permanently to the bottom of two confining surfaces (see Figure 31). These surface interact with all other monomers and ions in the system via the repulsive potential:

$$U_{WALL} = z^{-6}, \quad (75)$$

cut off at 2.2σ from the walls. The potential of mean force is calculated as a function of distance from the top surface. The bottom surface is maintained at a fixed position throughout all the simulations. Results for each D separation are collected individually and the potential of mean force reported as a function of D . The top surface is first rapidly brought from large distance to the confinement distance and then held fixed while the chain is allowed to equilibrate. We monitored the approach to equilibrium of the chain with running averages of the potential of mean force and chain properties e.g. R , R_g with a typical run time of $5 \cdot 10^7$ timesteps.

For the neutral chains, full force curves for four different chain lengths $N = 16, 32, 64, 128$ (excluding the tether monomer) were collected in this manner. For lengths varying between $N = 16$ and $N = 256$ the potential of mean force and chain properties were studied for several different separations. With charged chains the length was kept fixed and the charge sequence of the backbone varied – the potential of mean force and chain properties were then calculated for fixed separations of confinement for the chain.

The average end-to-distance R and radius of gyration R_g were calculated from:

$$\langle R^2 \rangle = \langle (r_0 - r_{N-1})^2 \rangle, \quad (76)$$

and:

$$\langle R_g^2 \rangle = \frac{1}{N} \langle \sum_{j=0}^{N-1} (r_j - r_{CM})^2 \rangle, \quad (77)$$

where 0 denotes the first monomer after the tether and $N - 1$ the last i.e. there are N “chain monomers” and the tether point is excluded from the calculation. The ratio $r = R^2/R_g^2$, indicative of the chain asymmetry and the average position of the center of mass were also monitored, and density profiles $n(r)$ of the chain segments calculated at different compression distances. For the charged systems the counterion distributions were monitored, as were the radial distribution functions of oppositely charge segments within the chain. The configurations of the chains over time were followed through visualisation in gnuplot and typical snapshots collected and plotted using RASMOL.

In all simulations the timestep is $\Delta t = 0.0015\tau$, where $\tau = \sigma(m/\epsilon)^{1/2}$ is the LJ time and is set to 1. The temperature is maintained at $T = 1.2\epsilon$ and coupled to the heat bath via the friction constant $\gamma = 1\tau^{-1}$. This choice leads to good sampling while ensuring the motion of the chains is not overdamped.

The force was calculated in a push-hold-equilibrate approach where the probe surface was shifted to a new position and the polymer system allowed to relax and equilibrate before data was collected on the average force exerted on the probe wall. The net force on the wall at a given position was then used to determine a relative free energy for motion of the probe wall by integration (potential of mean force).

A map of our system onto an experimental system is as follows: If we map $\lambda_B = 0.833\sigma$ onto the Bjerrum length of NaPSS in water, or alternatively physiological conditions we have $\lambda_B = 7.14A$, so that $\sigma = 8.57A$. Since our average bond length is 0.98σ this implies that a charge fraction $f = 0.3$. Alternatively, for an unstructured polypeptide with average residue size $3.6A$ our 32 monomers would correspond to approximately 75 residues of which approximately a fraction 0.4 bear a net charge.

The systems simulated are summarized in Table 1.

Results and Discussion

We first present results for neutral chains and then for polyampholyte (and polyelectrolyte) chains. Because the set of polyampholyte simulations used a fixed chain of 32 beads, we will first present the results for a neutral chain of 32 beads. This is followed by analysis, in the neutral chain case, for the effects of chain length.

1. Neutral Chains In the absence of a confining surface the conformation of our individual end-grafted chains is determined entirely by the monomer-solvent, the solvent-solvent interactions and the interactions of monomers of the chain with the attachment surface. Polymer theory predicts this to take the form of a “mushroom” occupying a pear shaped half sphere of radius $R \sim aN^{3/5}$, [34], with a distribution of R due to thermal fluctuations. For sufficiently long chains a maximal occupancy of monomers should occur several monomers from the vicinity of the surface and spread more in the x - y plane than the z dimension. In Figure 32

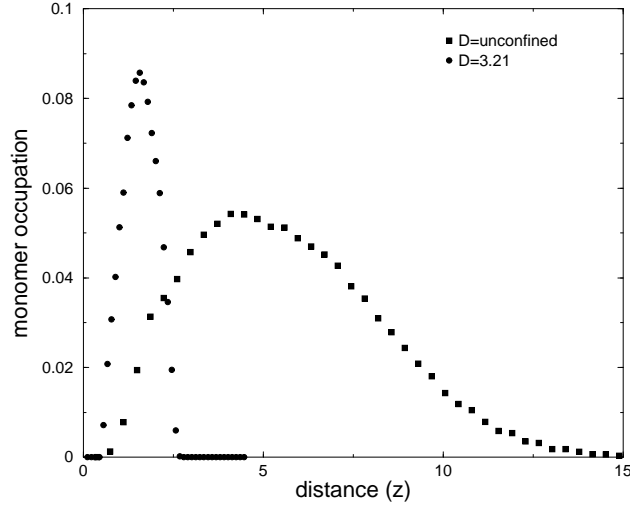


Figure 32. Plot of the distribution of chain segments of a neutral chain of length $N = 32$ as a function of distance from the bottom surface z for both an unconfined system (probe surface absent) and strong compression (surface separation $D = 3.21$). The chain preferentially occupies space in the proximity of the tether surface in the unconfined case, but is sharply peaked and exhibits a symmetric segment distribution in the case of strong confinement.

we plot the monomer distribution in the direction normal to the surface for a chain of $N = 32$ monomers. The distribution exhibits a gradual increase in occupancy peaking at $\sim 5\sigma$ from the surface for the $N = 32$ chain and spreading significantly to a distance $\sim 15\sigma$ with greatest occupancy closer to the tether surface. The strongest compression $D = 3.21$ is also shown to illustrate how the configurational space of the confined chains is sharply reduced. The average end-to-end distance R distribution (not plotted) peaks at an average value 9.89 and has $rms(= R_g)$ of 3.68. The ratio $r = R^2/R_g^2$ is thus just over 7 in both cases. For a neutral chain in a good solvent and in the absence of other constraints theory predicts $r \simeq 6.3$. The chains are thus perturbed by the presence of the wall and the grafting constraint, exhibiting on average larger dimensions than unconstrained chains consistent with the predicted asymmetric shape of the chain. The average dimensions of the unconfined $N = 16$, $N = 64$ and $N = 128$ chains were measured to be: $R = 6.20, R_g = 2.33$ ($N = 16$), $R = 14.48$ and $R_g = 5.57$ ($N = 64$) $R = 23.74, R_g = 8.70$ ($N = 128$).

These values and figures are important for determining the onset and extent of confinement of the polymer chains in the presence of a second parallel probe surface. When the separation distance is $D > R$ the chain interacts with the probe surface through relatively infrequent thermal fluctuations. Since the conformational space of the chain is not greatly reduced, the potential of mean force between polymer and surface is negligible, and the average dimensions of the chain are not significantly perturbed. Note that given that the chains are more spread in the direction parallel to the tethering plane, this range of weakly confined separations is likely to be larger than this estimate. For $D < R$ however the conformational space begins to be progressively reduced. Figure 32 illustrates this effect in the monomer distribution profile perpendicular to the surface. The confined polymer exerts a repulsive entropic force on the confining surface or object. Full force-distance curves that extend from unconfined to $D = 3.21$ for chains of $N = 16, 32, 64$ and 128 are presented in Figure 33. In

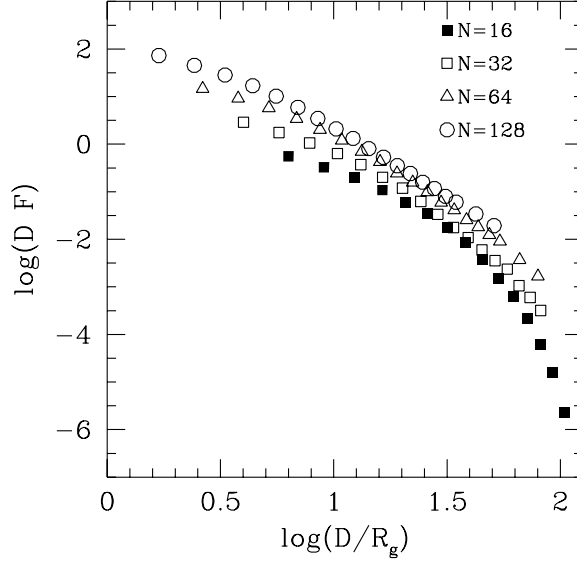


Figure 33. The average force exerted by the tethered chains on the probe surface as a function of surface-surface separation D . Chain lengths of $N = 16, 32, 64$ and 128 are depicted.

this case the force is a function of surface-surface separation D . We find good agreement with the predicted power law of $-8/3$ at close separations for all four chain lengths with a crossover to -3 at greater separations for the longest chains and a more rapid falloff for shorter chains. We are far from the limit of asymptotic chains and the $> -8/3$ power law is likely to be an effect of the finite length of our polymers. The rapid fall off for the shorter chains is similarly due to separations $D > R$ for these chains. Comparison of the average end-to-end distance spread of the $N = 32$ chain for the unconfined system and for the smallest separation $D = 3.21$ indicates the progressive shift of R with increasingly smaller separation. At $D = 3.21$ it peaked at 12.32 and skewed to higher values. The average center of mass of the chain in the z direction is measured to be ~ 1.5 i.e. at approximately midway between the surfaces and the segment distribution more sharply peaked and symmetric around this value than for the unconfined chain. The chain is thus squashed into a pancake geometry constrained by the tethered monomer to a finite range of x - y exploration and constrained by the surfaces to a narrow slit in the z dimension. Similar behavior was exhibited by the other chains.

To test our understanding of the chain length dependence of both the potential of mean force upon compression and the variation in the average dimensions of the chains, we analyzed data for chains of length $N = 16$ to $N = 256$ confined at 4 different separation lengths $D = 3.21, 5.39, 7.57$ and 9.75 . The force exerted by the chains on the top surface is plotted as a function of chain length in Figure 34. The figure indicates linear behavior over all separations with minor deviations for the larger separations and very short chains. The results are thus in good agreement with both theory and simulation. As the chains are more strongly confined the chain dimensions are predicted to crossover to 2-dimensional behavior. In Figure 35. we show how this is reflected in the average end-to-end distance of the chains. At the smallest separation the chains are pancakes with size increasing with a power law $\sim 3/4$ in agreement with the scaling of the average dimensions

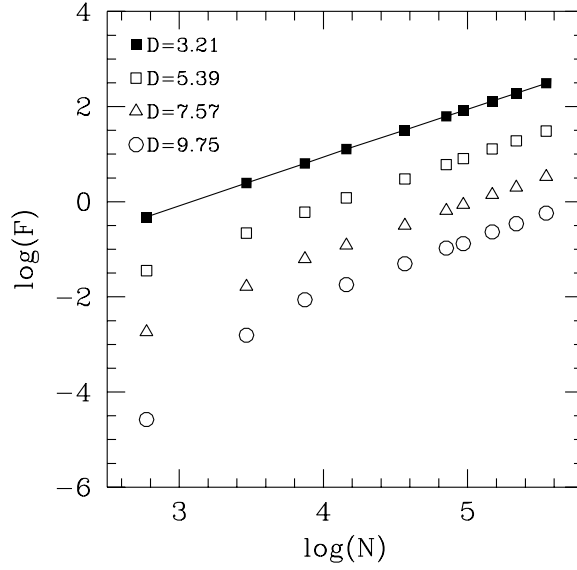


Figure 34. Average force exerted by chains of length between $N = 16$ and 256 on a probe surface at four different separations. The curves are plotted on a log scale to make the power law more visible.

of a two-dimensional self-avoiding walk $bN^{3/4}$. As the separation distance increases the exponent becomes progressively weaker, indicative of the gradual crossover to 3 dimensional scaling.

2. Polyampholyte Chains In order to determine the effects of charge distribution and charge imbalance on the end-attached polyampholyte chains, we first studied the chain properties ($N = 32$) in the absence of the confining surface. In Figure 36 we plot the average end-to-end distance spread of the net neutral chains with varying block size (listed in Table 1). The sequences possessing the smallest repeat unit (1 – 1, 2 – 2) are negligibly perturbed from their neutral behavior, peaking at roughly the same value and demonstrating similar spread. This is to be expected given that we are in a regime in which thermal effects dominate the electrostatic interactions along the chain at distances of the order of the charge separation. As the size of the charged blocks is increased, however, both the polyampholyte effect (promoting collapse) and the polyelectrolyte effect (promoting portions of chain stretching) are enhanced. Figure 36 depicts the resulting effects on the behavior of the chain. As the block size is increased the average end-to-end distance of the chain is shifted to smaller values and the distribution becomes less broad. This is indicative of the substantially reduced configurational space of the chain i.e. it adopts configurations maximizing block-block interactions, while being frustrated from complete collapse by thermal agitation. The behavior is further illustrated by the asymmetry parameter r , which is substantially reduced for the largest block sizes ($= 3.23$ for the 16 – 16 sequence).

The effect of a charge imbalance on a random sequence under similar conditions is presented in Figure 37. A small excess charge of +4 produces little deviation from neutral behavior. As the excess charge is increased, however, the average end-to-end distance is shifted to larger values and the distribution narrows. This is due to the increased tendency of segments to repel each other as a result of mainly repulsive electrostatic interactions.

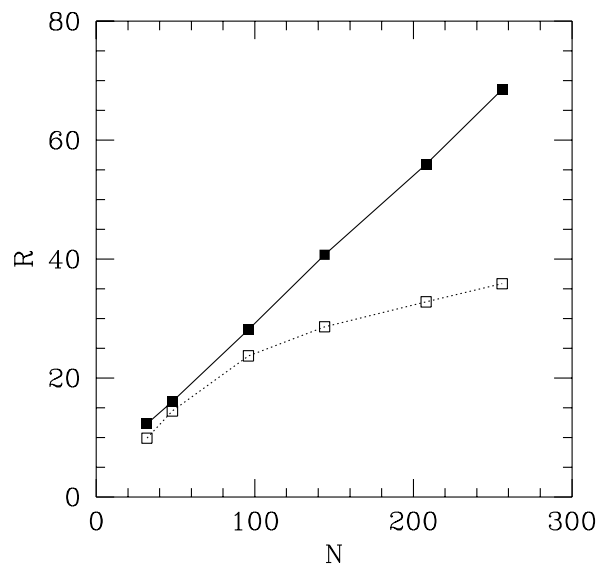


Figure 35. Average end-to-end distance of chains of length $N = 16$ to 256 at compression $D = 3.21$ (open points) and in the absence of a confining surface (solid points). In the strongly confined case the chains are effectively two dimensional and the radius increases as for two dimensional chains. A crossover to three dimensional behavior occurs at larger separations.

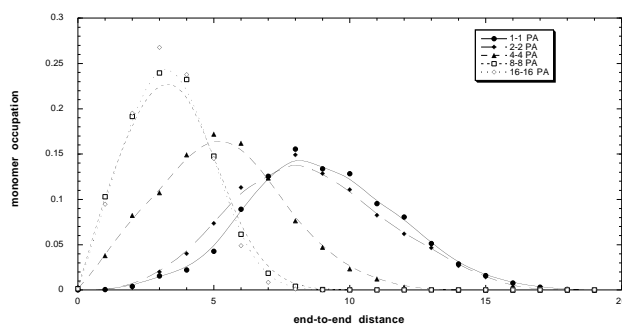


Figure 36. End-to-end distance spread as a function of charge block size for $N = 32$ in the polyampholyte sequence for chains of overall net neutrality. The top surface is absent in this system and the curves thus depict the unconfined dimensions of the chains. The curves peak sharply at small values for large charge blocks and approach the results of the equivalent neutral system for small repeating units.

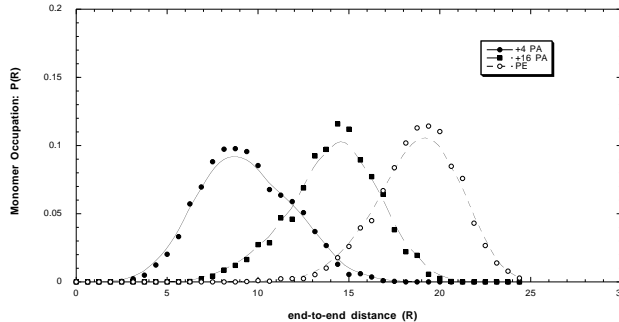


Figure 37. End-to-end distance spread as a function of net charge on polyampholytes with random charge sequences. Similar to Fig.(6a) the chains are unconfined in this system. As the net charge on the chains is increased the curves are progressively shifted to larger values indicative of chain expansion.

In the limit of a polyelectrolyte the chain is highly stretched with asymmetry parameter $r = 9.28$. These results are in qualitative agreement with the prediction of stretching from theory for chains with a charge imbalance ($\sim q\sqrt{fN^{1/2}}$).

In contrast to the neutral chains, confinement alters the behavior of the polyampholyte systems in several ways. First, in the same manner as in the neutral system, separations $D < R$ reduces the conformational space of the chain with a resultant loss in entropy and a potential of mean force between chain and surface. However in the polyampholyte systems, confinement may additionally enhance the polyampholyte (or alternatively polyelectrolyte effect) by increasing the electrostatic interactions. In our systems a decrease in the separation distance also leads to an increase in the effective density of ionic species. Screening effects will thus be enhanced, particularly in the polyelectrolyte (and polyelectrolyte-like) chains.

We first study the influence of confinement on the end-to-end distance of different net neutral sequences and for different net charge. Figure 38 plots the average value of R_g at 3 different separations as a function of sequence block size for the net neutral polyampholyte chains. A plot of the end-to-end distance produced similar results. R_g may in this case be a better gauge of the average dimensions of the chains since each PA has the first and last segments with charges of opposite sign. Over all separations the 1 – 1 and 2 – 2 repeating chains exhibits behavior very close to that of their neutral counterparts. The reduction in chain dimensions with separation distance is most pronounced for the smaller repeats (1 – 1, 2 – 2, 4 – 4) than for the 8 – 8 and 16 – 16 chains. This is in agreement with our earlier finding that even with the absence of a confining surface the polyampholyte effect is sufficient to cause the PA to adopt collapsed dimensions.

Further evidence for a behavior change for polyampholytes with difference charge sequence distributions is shown by Figure 39. In this figure the end-to-end distance spread is plotted for the strongest compression $D = 3.21$. This can be compared with Figure 36 (unconfined). While the average value of R and its spread are similar for the 8 – 8 and 16 – 16 chains, a substantial shift occurs for the smaller repeats to larger values and wider spread in a similar manner as for the neutral system. Similar results were found for PAs with charge imbalance although the shift in this case was less pronounced.

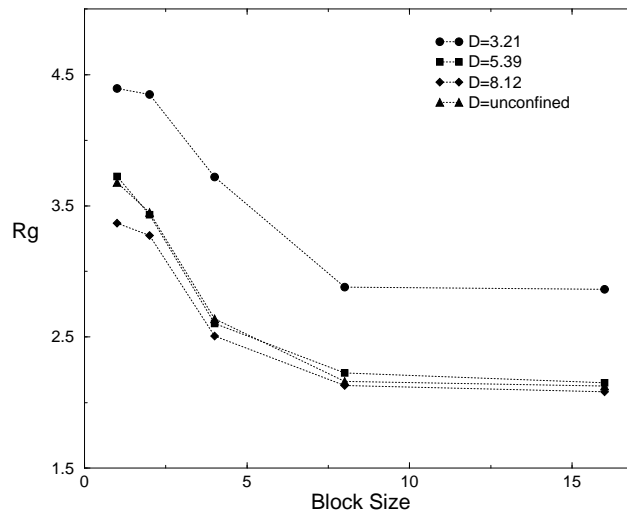


Figure 38. Average radius of gyration of net neutral polyampholytes at different surface separations versus the block size of repeating charge units. As the block size is increased departures from the behavior of the neutral system become more apparent indicative of the tendency of collapse of the chains.

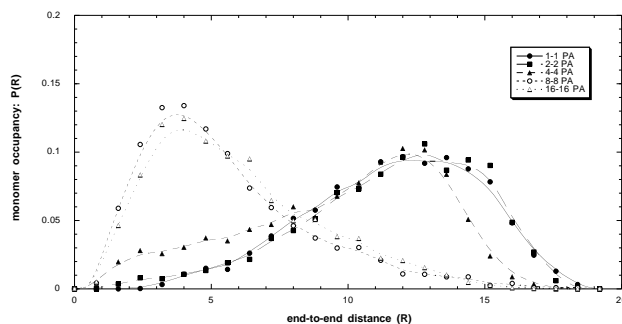


Figure 39. End-to-end distance spread as a function of block size for the strongest compression $D = 3.21$. The results are similar to those of unconfined chains for the chains with largest repeating units while for the chains with smaller repeats the curves are shifted to higher values in the same manner as for the identical neutral system. Note that only a block size of 8 is necessary for significant pairing and collapse.

These results are in qualitative agreement with the MC simulations of Ref.[13] in which the average dimensions of polyampholytes with varying degrees of blockiness (measured in terms of the intrachain energies) were found to be sequence dependent. It is also consistent with theoretical studies on the effects of correlations in PA sequences [35], in which it has been shown that sequence correlations become important when the correlation is sufficiently large to produce polyelectrolyte behavior within the chain. This may be important in some unstructured protein sequences in which the charge sequence is predetermined and may exhibit such low complexity [49].

The potential of mean force differs very little from that of the neutral chain at the two smaller separation distances but shows a marked drop for the larger block repeat sequences at weaker separation, indicative of the decreased tendency of the chain to thermally explore conformations resulting in interaction with the surface. This suggests that while the smallest block chains may map well onto the neutral force curve, substantial deviations are to be expected at moderate to weak separations for chains with polyelectrolyte portions. Further confirmation of this finding was seen in the distributions $n(z)$ for the different sequences which peaked at larger values for the smaller repeat chains.

Figure 40 depict typical snapshots of different repeat chains and different chains with net charge at a surface separation of $D = 3.21$. The smallest repeat unit chains behaved in a manner very similar to uncharged chains, consistent with our chain property results and a thermally dominated system. For the larger repeating unit chains, however, typical configurations located oppositely charged portions of the chain in proximity and involved stretched portions of chain involving the same charge type. The 4 – 4 repeat chain was most frustrated in its attempts to balance thermal and polyelectrolyte/polyampholyte effects and exhibited more diverse configurations than the larger repeat chains. A net charge of +4 resulted in behavior not dissimilar from a neutral chain, while larger excess charge resulted in predominantly stretched configurations.

We studied the typical configuration space of the different repeating chains more explicitly by calculating the radial distribution function of oppositely charged segments of the chains. Bonded segments were excluded from the calculation. Figure 41 plots the distributions of three of the repeating chains at the surface separation $D = 3.21$ corresponding to the snap shots in Figure 10. The 2 – 2 and 8 – 8 repeating chains (not shown) exhibited behavior very close to the 1 – 1 and 16 – 16 respectively. All sequences peak at small distance at about $2-3 \sigma$, however the distribution broadens for the smaller repeat chains. The 4 – 4 sequence exhibits two maxima, one at $\sim 2.5\sigma$ and the other at about 6σ . The secondary peak is absent for the weakly confined case $D = 8.12$ shown in Figure 42, in which its available configurational space is increased and may be a result of two energetically favourable configurations for the chain under strong confinement.

Conclusions

We have performed MD simulations of neutral, charged and polyampholyte polymers within a confined geometry. Our neutral polymer simulations provide a good test of polymer predictions for finite length chains. Our polyampholyte simulations suggest a previously unexplored dependence of the properties of a tethered, confined polyampholyte on the charge sequence of the chain.

To summarize, the simulations varied the length of the polymers, the charge distribution along the polymer chain, and the distance between a tethered wall and a probe wall. For neutral chains of varying length we

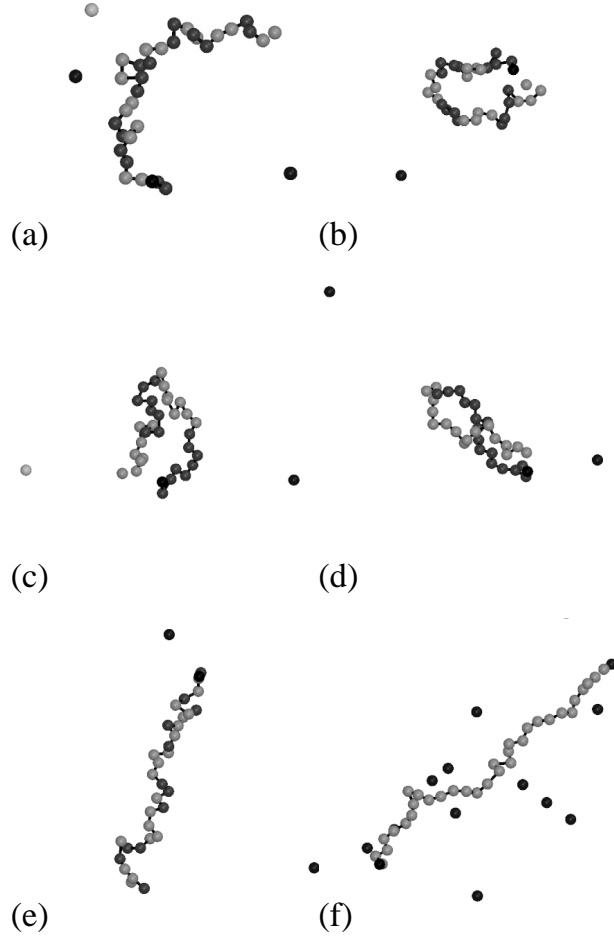


Figure 40. Snapshots typical of polyampholyte configurations at the strongest compression distance $D = 3.21$ for different charge sequences. (a) corresponds to a 2-2 repeating chain, while (b), (c), (d) correspond to 4-4, 8-8, 16-16 repeats and (e) and (f) to chains with a net charge of +8 and +32 (polyelectrolyte). Different segment charge types are depicted with different shades. In all cases the tether point is artificially enlarged, as are the additional ions, for clear distinction from the chain segments.

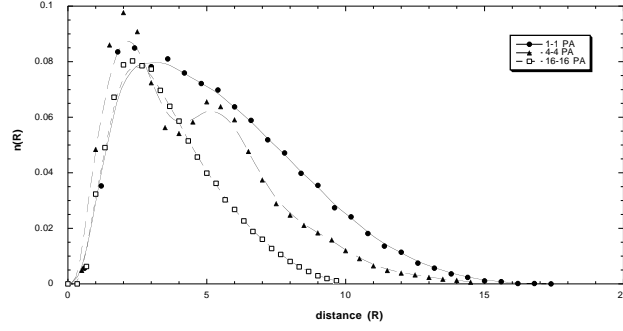


Figure 41. Radial distribution function of segments of opposite charge in repeating polyampholyte chains at a surface separation of $D = 3.21$ i.e. strong compression. Large repeat block chains exhibit the sharpest distributions while the smaller repeats produce typically broader distributions. An interesting double peak is found for the 4 – 4 repeating chain.

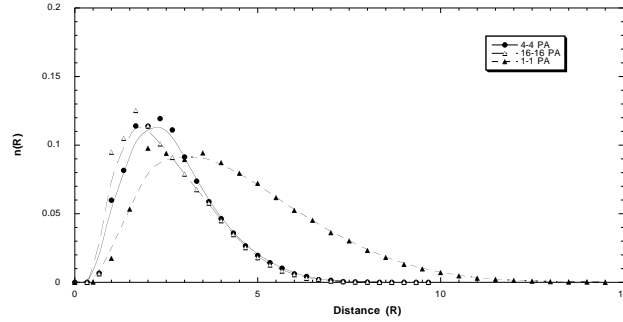


Figure 42. Radial distribution function of segments of opposite charge in repeating polyampholyte chains at a surface separation $D = 8.12$ i.e. weakly confined. The double peak in Figure 10A for the 4 – 4 repeating chain is absent.

obtained force curves in good agreement with theoretical predictions for compressed neutral polymer chains, with some deviations for the smallest chain lengths simulated. The chain properties such as the average end-to-end distance and radius of gyration and segment distribution functions were also in good agreement with theory and MC simulation. Our study is one of few MD simulations of compressed end-attached neutral chains. The agreement with similar MC studies is thus encouraging.

For chains bearing charged groups we found an interesting dependence of chain properties on the charge sequence of the chain. For polyampholytes bearing an excess charge our results are in agreement with predictions for similar chains in bulk: for excess charge above a critical value, the chains expand beyond their neutral dimensions and in the limit of a polyelectrolyte result in an almost fully extended chain. For polyampholytes with equal numbers of positive and negative charged segments (net neutral) our results indicate that while thermal dominance was sufficient to maintain near neutral dimensions and chain properties for small repeating block chains, the enhancement of both the polyelectrolyte (promoting chain expansion) and polyampholyte (promoting chain collapse) effects was sufficient to promote local stretching and overall collapsed configurations of the chains. The extent to which the chain was frustrated in balancing the different constraints and interactions was sequence dependent, being determined by the size of the repeating blocks. Further studies employing longer chain lengths and further systematic sequence variation would be interesting to pursue this point. Given that exclusion properties of unstructured polypeptide domains [20] may be closely related to their biological function, and the possibility of exploring such a mechanism via experimental techniques such as atomic force microscopy, an understanding of the properties of polyampholyte systems such as we have studied here is highly desirable. We have here taken the first steps toward this end.

Table 7. The number of monomers is N , and the wall separation is D .

Class	N	Net Charge	Repeat	D
neutral	16	0		3.21-14.11, ∞
neutral	32	0		3.21-14.11, ∞
neutral	64	0		3.21-14.11, ∞
neutral	128	0		3.21-14.11, ∞
neutral	256	0		3.21-9.75, ∞
polyampholyte	32	0	1-1, 2-2, 4-4, 8-8, 16-16	3.21, 5.39, 8.20, ∞
polyampholyte	32	4	random	3.21, 5.39, 8.20, ∞
polyampholyte	32	8	random	3.21, 5.39, 8.20, ∞
polyampholyte	32	12	random	3.21, 5.39, 8.20, ∞
polyampholyte	32	16	random	3.21, 5.39, 8.20, ∞
polyelectrolyte	32	32		3.21, 5.39, 8.20, ∞

References

- [1] A.V.Dobrynin and M.Rubinstein. *J. Phys. II*, 5:677, 1995.
- [2] B.-Y.Ha and A.J.Liu. *Phys. Rev. Lett.*, 79:1289, 1997.
- [3] V. A. Bloomfield. *Biopolymers*, 31:1471, 1991.
- [4] B.M.Steels, J.Koska, and C.A.Haynes. Analysis of compression of polymer mushrooms using self consistent field theory. *J. Chromatogr. B.*, 743:41, 2000.
- [5] H. G. Brown, J. C. Joncroso, and J. H. Hoh. *Cell Vision*, 3:225, 1996.
- [6] M. Daoud and P. G. deGennes. *J. Phys. (France)*, 38:85, 1977.
- [7] C. G. de Kruif. Skim milk acidification. *J. Coll. Int. Sci.*, 185:19–25, 1997.
- [8] S.W. de Leeuw and J.W. Perram. *Mol. Phys.*, 37:1313, 1979.
- [9] P.-G. deGennes. Scaling concepts in polymer physics. *Cornell Univ.Press and NY*, 1971.
- [10] J. deJoannis, J. Jiminez, R. Rajagopalan, and I. Bitsanis. *Europhys. Lett.*, 51:41–47, 2000.
- [11] D.Long, A.V.Dobrynin, M.Rubinstein, and A.Ajdari. *J. Chem. Phys.*, 108:1234, 1998.
- [12] D.Loomans, H.Schiessel, and A.Blumen. *J. Chem. Phys.*, 107:2636, 1997.
- [13] D.Srivastava and M.Muthukumar. *Macromolecules*, 29:2324, 1996.
- [14] A. Keith Dunker, J. David Lawson, Celeste J. Brown, Pedro Romero, Jeong S. Oh, Christopher J. Oldfield, Andrew M. Campen, Catherine M. Ratliff, Kerry W. Hipps, Juan Ausio, Mark S. Nissen, Raymond Reeves, ChulHee Kang, Charles R. Kissinger, Robert W. Bailey, Michael D. Griswold, Wah Chiu, Ethan C. Garner, , and Zoran Obradovic. Intrinsically disordered proteins. *J. Mol. Graphics.*, 0:0, 2001. in press.
- [15] F.S.Csajka and C.Seidel. *Macromolecules*, 33:2728–2739, 2000.

- [16] G.S.Manning. *Quarterly Rev. Biophysics*, 11:179, 1978.
- [17] G.Subramanian, D.R.M.Williams, and P.A.Pincus. *Macromolecules*, 29:4045, 1996.
- [18] D.M. Heyes, M.Barber, and J.H.R. Clarke. *J. Chem. Soc. Faraday Trans. II*, 73:1485, 1977.
- [19] R.W. Hockney and J.W. Eastwood. *Computer Simulation using Particles*. McGraw-Hill and NY and NY, 1981.
- [20] J. Hoh. *Proteins: Structure and Function and Genetics*, 32:223, 1998.
- [21] I.Szleifer and M.Carignano. Tethered polymer layers: phase transitions and reduction of protein adsorption. *Macromol. Rapid Commun.*, 21:423–448, 2000.
- [22] J.C.Barrat and J.-F.Joanny. *Adv. Chem. Phys.*, 44:1–66, 1996.
- [23] J.Jiminez and R.Rajagpolan. *Langmuir*, 14:2598–2601, 1996.
- [24] J.Wittmer, A.Johner, and J.F.Joanny. *Europhys. Lett.*, 24:263–268, 1993.
- [25] K.A.Dill. *Biochemistry*, 29:7133, 1990.
- [26] A. Milchev and K. Binder. *Euro. Phys. B*, 3:477–484, 1998.
- [27] M.J.Stevens and K.Kremer. *J. Chem. Phys.*, 103:1669, 1995.
- [28] M.Murat and G.S.Grest. *Phys. Rev. Lett.*, 63:1074, 1989.
- [29] M.Tanaka, A.Y.Grosberg, and T.Tanaka. *J. Chem. Phys.*, 110:8176–8191, 1999.
- [30] M.Tanaka, A.Y.Grosberg, V.S.Pande, and T.Tanaka. *Phys. Rev. E.*, 56:5798–5808, 1997.
- [31] P.-G.deGennes, P.Pincus, R.M.Velasco, and F.Brochard. *J. de Physique*, 37:1461, 1976.
- [32] D.E. Parry. *Surf. Sci.*, 49:433, 1975.
- [33] D.E. Parry. *Surf. Sci.*, 54:195, 1976.
- [34] P.G.deGennes. *Macromolecules*, 13:1069–1075, 1980.
- [35] P.G.Higgs and J.-F.Joanny. *J. Chem. Phys.*, 94, 1991.
- [36] S. Plimpton. *J. Comp. Phys.*, 117:1–19, 1995.
- [37] P.Pfeuty. *J. Phys. Colloq.*, page 149, 1978.
- [38] R.Podgornik and V.A.Parsegian. *Phys. Rev. Lett.*, 80:1560, 1998.
- [39] S.Edwards, P.R.King, and P.A.Pincus. *Ferroelectrics*, 30:3, 1980.
- [40] E. Spohr. Effect of electrostatic boundary conditions and system size on the interfacial properties of water and aqueous solutions. *J. Chem. Phys.*, 107:6342–6348, 1997.
- [41] S.Wolfling and Y.Kantor. *Phys. Rev. E.*, 57:5719–5726, 1998.

- [42] T.Darden, D. York, and L. Pedersen. Particle mesh ewald: An $n \log(n)$ method for ewald sums in large systems. *J. Chem. Phys.*, 98:10089–10092, 1993.
- [43] E. G. Timoshenko, Yu. A. Kuznetsov, and K. A. Dawson. *Phys. Rev. E*, 53:3886, 1996.
- [44] T.Soddemann, H.Schiessel, and A.Blumen. *Phys. Rev. E.*, 57:2081–2090, 1998.
- [45] J. Ubbink and T. Odijk. *Biophysical J.*, 68:54, 1995.
- [46] V.N. Uversky, J.R. Gillespie, and A.L. Fink. Why are "natively unfolded" proteins unstructured under physiologic conditions? *Proteins-Structure Function and Genetics.*, 41:415–427, 2000.
- [47] P. Walstra, V.A.Bloomfield, G.J. Wei, and R. Jenness. Effect of chymosin action on the hydrodynamic diameter of casein micelles. *Biochim Biophys Acta*, 669:258–9, 1981.
- [48] W.B.Russel, D.Saville, and W.R.Schowalter. *Colloid Dispersions*. Cambridge Uni. Press, New York, 1989.
- [49] J. C. Wooton. *Current Opinion in Structural Biology*, 4:413, 1994.
- [50] P. E. Wright and H. J. Dyson. *J. Mol. Biol.*, 293:321, 1999.
- [51] Y.Kantor and M.Kardar. *Europhys. Lett.*, 27:643, 1994.

Association of two semiflexible polyelectrolytes by interchain linkers: Theory and simulations

Itamar Borukhov, Department of Chemistry and Biochemistry, Department of Physics, University of California at Los Angeles, Los Angeles, California 90095 Kun-Chun Lee, Department of Chemistry and Biochemistry, University of California at Los Angeles, Los Angeles, California 90095 Robijn F. Bruinsma, Department of Physics, University of California at Los Angeles, Los Angeles, California 90095 William M. Gelbart and Andrea J. Liu, Department of Chemistry and Biochemistry, University of California at Los Angeles, Los Angeles, California 90095 Mark J. Stevens, Sandia National Laboratories, P.O. Box 5800, MS 0316, Albuquerque, NM 87185-0316

Abstract

The aggregation of two highly charged semiflexible polyelectrolytes in the presence of generalized linkers is studied theoretically. This model provides insight into biological processes such as DNA condensation and F-actin self-assembly induced by either multivalent counterions or bundling proteins. The interplay between the bending rigidity of the chains and their electrostatic interactions leads to an effective interlinker interaction that is repulsive at large distances and attractive at short ones. Here, the results of molecular dynamics simulations of two semiflexible charged chains in a mixture of monovalent and polyvalent counterions are presented. These simulations were performed in part to test the analytic theory as well as to probe the stability of two-chain complexes at different counterion mixtures. We found that below a certain threshold number of trivalent counterions the chains do not hold together and separate from each other. Above it, the chains remain paired in a very special way; along some fraction of their total length they are essentially parallel and share some of the trivalent counterions serving as interchain linkers. Upon further increase in the number of trivalent counterions the parallel region increases up to finally a complete pair bundle.

Introduction

Biomolecules, notably nucleic acids and proteins, are invariably charged because of their need to be soluble over a broad range of concentrations in aqueous solution. Furthermore, their charge provides a powerful yet subtle basis for control of their aggregation and condensation, both with themselves and each other. Of particular importance is the condensation of DNA in the presence of multivalent counterions.¹⁻⁴ In vitro studies of highly dilute DNA solutions have established that DNA can be condensed in this way into hexagonally-packed, circumferentially-wound, toroids whose interaxial spacings are as small as those in crystalline DNA. In vivo analogies of these structures have been studied most thoroughly in bacterial viral capsids, where the high density of DNA is necessary for storage purposes. Indeed, the genes carried by the condensed viral genome are not accessible for transcription or replication until the DNA is freed by injection into the bacterial cell.

Polymerized actin (F-actin), a ubiquitous and important structural protein, is comparably strongly condensed by the addition of either multivalent counterions or “bundling” (“linker”) proteins.⁵⁻⁹ Because the actin filaments are stiff, i.e. not long compared to their persistence lengths, their condensates consist in general of straight bundles of close-packed filaments. Synthetic stiff polyelectrolytes such as poly(p-phenylene benzobisthiazole) (PBZT) can also be induced to form bundles.¹⁰ In all the above cases, when the concentration of condensing agents is not sufficiently high, it is expected that some sort of intermediate structure will arise, involving a network of junctions at which individual or small numbers of counterions or linker proteins are shared between pairs of polyelectrolyte molecules.¹¹

The effect of multivalent counterions on the interaction between highly-charged polyelectrolytes has been the focus of a great deal of attention in the past decade, both experimentally¹³ and theoretically.^{14–23} Of special interest is the attractive force that can arise between such chains, which necessarily implies the qualitative breakdown of the mean-field (Poisson Boltzmann) theory of electrostatic interactions. Two main mechanisms have been proposed for the origin of this attraction. In both mechanisms, the condensed counterions in a narrow layer surrounding the chains give rise to charge distributions that are highly correlated along the axes of the chains; the attraction arises from anticorrelations between these charge distributions. At low temperatures/high fixed-charge densities the attraction is due to short-ranged correlations in the charge distributions, reminiscent of a Wigner crystal;^{18,20–22,24–26} at high temperatures/low fixed-charge densities, on the other hand, the attraction is due to long-wavelength fluctuations in the charge distributions.^{14,17,19,26,27} An additional contribution to the attraction arises from the nonisotropic distribution of counterions in the plane perpendicular the chain axes.^{15,23}

In this standard view of aggregation of highly-charged chains, one focuses on how multivalent counterions mediate attractive effective interactions between the chains. By contrast, in this paper we take the opposite view we consider how the chains mediate effective interactions between the multivalent ions.^{28,29} We then consider the consequences of these effective interactions on chain aggregation. Indeed, we sidestep the question of the origin of the attraction by treating the multivalent counterions explicitly as interchain linkers, i.e. particles that hold the two chains together by a short-ranged attraction. By keeping the discrete nature of the multivalent counterions instead of replacing them with a continuous distribution surrounding the chains we manage to keep the most important effect of ion correlations. On the other hand, since the correlations between monovalent ions are not expected to play an important role, we treat them as a continuous background, which leads to the standard exponential screening of electrostatic interactions. It should thus be emphasized that in our approach, multivalent counterions are treated qualitatively differently from monovalent ones.

One advantage of treating the multivalent counterions as linkers is that our approach can be generalized to include other forms of linkers, as well. In particular, we consider how chains mediate effective interactions between binding proteins that connect the chains together. Thus, we treat both multivalent counterions and bundling proteins as generalized linkers that adsorb onto the polyelectrolytes and result in the formation of interchain junctions. To gain insight into the phenomenon of chain aggregation, we focus on a simplified system, namely a pair of semiflexible polyelectrolytes in the presence of generalized linkers. We note that a strong similarity can be seen between the theory treated here and that of DNA melting,^{30–35} where a double-stranded DNA molecule denatures separates into two single-stranded chains. In this latter case the role of linkers is played by the hydrogen bonds connecting complementary base pairs.

The analytic linker theory is tested in a series of molecular dynamics simulations. The simulations are described in the next section, where we treat a pair of semiflexible charged chains in the presence of neutralizing counterions. The counterion fluid is composed of a mixture of monovalent and trivalent counterions. The simulations are aimed at determining the stability of two-chain complexes for different counterion mixtures, varying between purely monovalent and (almost) purely trivalent. We found that below a certain threshold number of trivalent counterions $N_{z=3} = N^*$ the chains do not hold together and separate from each other. Above it, the chains remain paired in a very special way; along some fraction, f_2 , of their total length they are essentially parallel and share some of the trivalent counterions serving as interchain linkers. Upon further increase in $N_{z=3}$, f_2 increases (linearly with $N_{z=3}$) up to its maximum value (unity) at N^{**} . Throughout this

regime ($N^* < N_{z=3} < N^{**}$) the density of linkers remains constant, corresponding to the condensed state predicted by our theory, and consistent with the specific prediction that the onset of pair stability occurs within the two-phase coexistence region, i.e., as soon as chains are paired they are in a parallel configuration with a high-density of linkers. Above N^{**} further addition of multivalent counterions leads to an increase in the density of linkers and to a saturation of the strength of binding (pair association).

Molecular dynamics simulations

Introduction

We have performed molecular dynamics simulations of an overall neutral system consisting of two charged semiflexible chains and a mixture of monovalent ($z = 1$) and trivalent ($z = 3$) counterions with no co-ions (see Fig. 1). Each chain consists of 64 charged monomers carrying one unit charge per monomer. All particles in the system (monomers and free ions as well) repel each other through a repulsive Lennard-Jones (LJ) potential,

$$U_{\text{LJ}}(r) = \begin{cases} 4\epsilon_{\text{LJ}} \left[\left(\frac{\sigma}{r}\right)^{12} - \left(\frac{\sigma}{r}\right)^6 + \frac{1}{4} \right]; & r \leq r_c \\ 0; & r > r_c \end{cases} \quad (78)$$

where ϵ_{LJ} and σ are the LJ energy and length scales, respectively. The chain bond potential is the standard finite extensible nonlinear elastic (FENE) potential,

$$U_{\text{FENE}}(r) = -1/2 k_0 r_0^2 \ln(1 - r^2/R_0^2), \quad (79)$$

with a spring constant $k_0 = 7\epsilon_{\text{LJ}}/\sigma^2$ and maximal extension $r_0 = 2\sigma$. The simulations are performed at a fixed temperature $k_B T = 1.2\epsilon_{\text{LJ}}$, where the average bond size is $\langle r \rangle = 1.1\sigma$. Chain rigidity is introduced by the sum of angle dependent harmonic potentials,

$$U_{\text{bend}}(\theta) = k_1(\theta - \pi)^2 \quad (80)$$

Here θ is the angle between neighboring bonds and $k_1 = 20\epsilon_{\text{LJ}}/\text{rad}^2$, which corresponds in our simulations to an intrinsic persistence length $l_p \simeq 18\sigma$. Finally, the Coulomb interaction between pairs of charged particles of valency z_i, z_j is given by

$$U_{\text{Coulomb}}(r)/k_B T = z_i z_j l_B / r, \quad (81)$$

and is calculated with periodic boundary conditions using the particle-particle particle-mesh (PPPM) algorithm³⁶ with a mesh consisting of 16^3 points. The Bjerrum length is $l_B = 3.2\sigma$ and the Manning-Oosawa parameter characterizing the linear charge density along the chains is $\xi = l_B/\langle r \rangle \simeq 2.9$. The simulations were performed in a cubic cell of dimensions $(109\sigma)^3$.

The dynamics of the system are performed with a Langevin thermostat.³⁷ system is advanced in time steps $\Delta t = 0.015\tau$ with τ being the basic Lennard-Jones time unit, while the damping constant is taken as $\gamma = 1/\tau$.

Results

The main aim of the simulations was to probe the stability of two-chain complexes at different counterion mixtures. The initial configurations consisted of two chains next to each other and the counterions (monovalent

and trivalent) closely near by. Since the total number of charged monomers is 128 the number of trivalent counterions can vary between 0 and 42. When the two chains are initially separated from each other they do not form a two-chain complex even at counterion mixtures where the complex appears to be stable. This can be attributed to a high kinetic barrier for aggregated similar to the one suggested for the bundling of rigid rods.³⁸ Due to this limitation we can only interpret our results in terms of the stability of the two-chain complex and we can not determine whether the complex is indeed the global minimum of the system or just a local one.

Another limitation of the simulation resides in the choice of the simulation box size, which corresponds to the concentration of chains in solution. The results of the simulation do depend on the box size since translational entropy of the chains depends logarithmically on the box size. In fact, at very low concentrations (large box size) the low osmotic pressure of the chains will pull them apart. On the other hand at large concentrations many chain effects become important. We have chosen an intermediate box size for which both these effects are minimal. Our choice is somewhat arbitrary and affects the results presented here quantitatively but not qualitatively.

Typical snapshots from the simulations are shown in Fig. 1, while a quantitative analysis is presented in Fig. 2. The fraction of chain charge (128) neutralized by trivalent counterions is given in each case by

$$f_{z=3} = \frac{3N_{z=3}}{3N_{z=3} + N_{z=1}} = \frac{3N_{z=3}}{128}. \quad (82)$$

Four different regimes can be distinguished depending on the number of trivalent counterions in the system. At low trivalent counterion numbers, $N_{z=3} < N^* = 14$, the chains are not complex (remain together) and are basically isolated [see Fig. 1b]. In this first regime (I) less than one third of the monomer charges are balanced by the trivalent counterions ($f_{z=3} < f^* = 33\%$).

At intermediate trivalent counterion numbers $N^* < N_{z=3} < N^{**} \simeq 24$ ($f^* < f_{z=3} < f^{**} = 60\%$) the chains start to form a paired complex [see Fig. 1b]. Pairing is partial with the two chains being shifted with respect to each other (regime II). We note that some meta-stable structures such as the “fork” shown in Fig. 1b appear occasionally during the simulation. Such a structure is less favorable energetically as compared to the “shifted” structure [see, e.g., Fig. 1a] due to the electrostatic energy associated with the branching point.

In Fig. 2 the length of the shared segment l_2 and the density ρ_2 of trivalent counterions in this segment are plotted as functions of the total number of trivalent counterions in the system. The length of the shared section l_2 calculated by first identifying the left and right neighbors of each shared multivalent counterion, and then summing up the interlinker separations. The density is simply the inverse of the average interlinker separation. First, note that the structure of the shared segment confirms that the trivalent counterions can be viewed as interchain linkers connecting the two chains. In the shared segment the two chains are as close to each other as they can be while accommodating trivalent counterions (“linkers”) in between. Although some monovalent counterions are in close proximity to the two chains they only rarely squeeze in between the two chains.

Second, it is clear from Fig. 2 that in this regime the density of interchain linkers remains more or less constant even as the total number of multivalent counterions is increased. Furthermore, the trivalent-trivalent

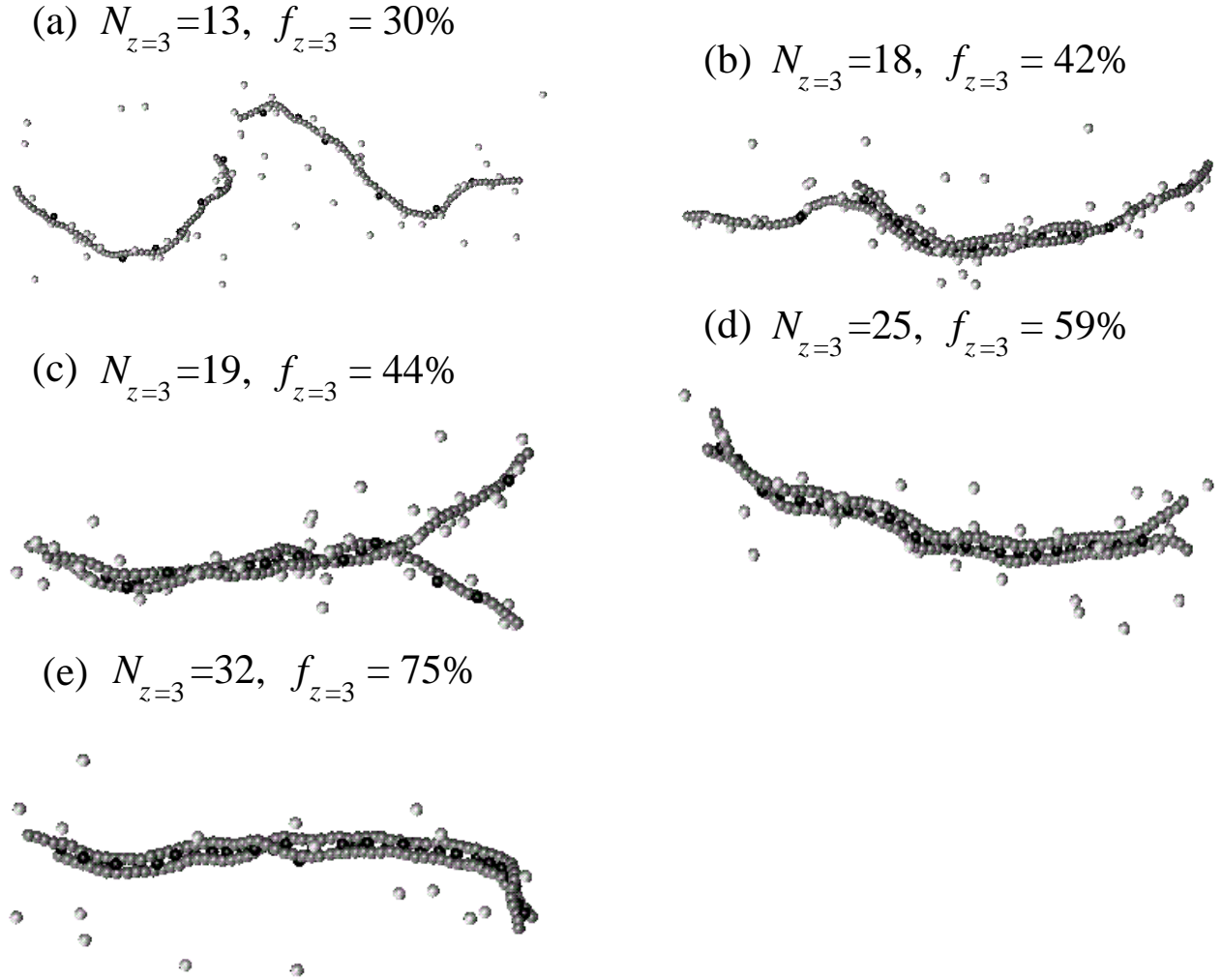


Figure 43. Typical snapshots of the molecular dynamics simulations at different compositions: (a) isolated chains at $N_{z=3} = 13$; (b) partial chain overlap at $N_{z=3} = 18$; (c) metastable “fork” structure at $N_{z=3} = 19$; (d) fully zippered structure at $N_{z=3} = 25$; and (e) saturated structure at $N_{z=3} = 32$. The black spheres are trivalent counterions, the white spheres are monovalent ones, and the gray spheres are the monomers.

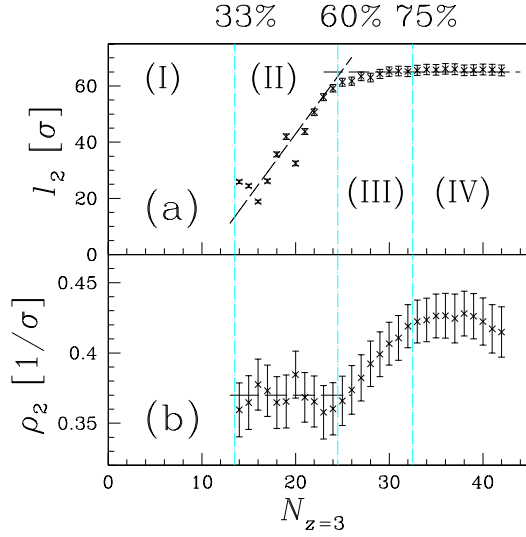


Figure 44. The length of the segment shared by the two chains $l_2(a)$ and the density of trivalent counterions ρ_2 in this segment (b) as functions of the total number of trivalent counterions in the system $N_{z=3}$. See text for discussion of the four different regimes.

correlation function $g_{3:3}(r)$ defined as

$$g_{3:3}(r) = \frac{V}{4\pi r^2 N_{z=3}^2} \sum_{i \neq j} \langle \delta[r - |\mathbf{r}_i - \mathbf{r}_j|] \rangle \quad (83)$$

does not change drastically as the total number of trivalent counterions varies. A typical correlation function (corresponding to $N_{z=3} = 25$) is plotted in Fig. 3. The principal features are the main peak around $r \simeq 2.5\sigma$ and the secondary peak around $r \simeq 4.5\sigma$. The presence of these two peaks is a signature of short range liquidlike ordering of the trivalent counterions in between the two chains.

Constant linker density with increasing number of linkers in the system is a typical signature of phase coexistence. In our case the two phases are (i) trivalent counterions adsorbing at density ρ_1 onto unpaired chain sections of total length $2l_1$ and (ii) trivalent counterions serving as linkers at density ρ_2 in the shared chain section of length l_2 . At coexistence, both phases must share the same chemical potential and osmotic pressure,

$$\mu_1(\rho_1) = \mu_2(\rho_2), \quad (84)$$

$$2P_1(\rho_1) = P_2(\rho_2). \quad (85)$$

The solution of these two equations gives the optimal densities ρ_1^* , ρ_2^* which must remain constant in the coexistence regime. The number of trivalent counterion in each of the phases N_1, N_2 as well as the lengths the unpaired sections (l_1) and the shared section (l_2) can be extracted from the following set of equations:

$$\rho_1^* = N_1/l_1, \quad (86)$$

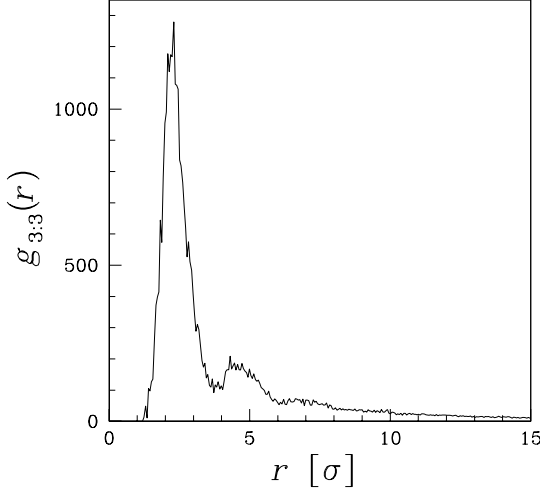


Figure 45. Trivalent ion correlation function $g_{3:3}(r)$ for $N_{z=3} = 25$.

$$\rho_2^* = N_2/l_2, \quad (87)$$

$$N_{z=3} = 2N_1 + N_2, \quad (88)$$

$$l_{tot} = l_1 + l_2. \quad (89)$$

The solution yields a linear dependence of the shared length on the number of polyvalent counterions (the “lever rule”),

$$l_2 = \frac{N_{z=3} - 2l_{tot}\rho_1^*}{\rho_2^* - 2\rho_1^*}. \quad (90)$$

As can be seen in Fig.2a, l_2 is indeed a linear function of $N_{z=3}$ in regime II. The dashed line is drawn using the above equation with the following estimates: $\rho_1^* = 0.075\sigma^{-1}$, $\rho_2^* = 0.37\sigma^{-1}$, and $l_{tot} = 70.4\sigma$.

It is interesting to compare this regime with the results of the theoretical model where we had two different transitions: (i) the crossover of the one-dimensional linker fluid from a dilute to a dense phase, and (ii) the chain pairing transition. Due to computational constraints we are limited in the simulations to relatively short chains. As a result, we cannot observe the large loops that should accompany the transition from the dilute linker fluid to the dense phase since the loops are expected to be longer than the chains themselves. The unpaired sections observed in the simulation are therefore reminiscent of two different features of the theoretical model: (i) the large loops characteristic of the intermediate linker phase; and (ii) unpaired chains coexisting with paired chains at the pairing point.

The coexistence regime ends around $N_{z=3} \simeq N^{**}$ when about 60% of the monomer charges are balanced by trivalent counterions. At this point the two chains are almost fully paired and the unpaired sections

disappear [Fig. 1c and regime III in Fig. 2]. The shared length saturates quickly and any addition of trivalent counterion is accompanied by an increase in the linker density. Finally, when $N_{z=3} > N^{**} \simeq .32$ (75% charge neutralization) the interlinker Coulomb repulsion makes it unfavorable to further squeeze trivalent counterions between the two chains and the extra counterions are excluded from the region between the two chains. In this regime the linker density saturates to its maximal value and does not increase further. The extra counterions do not diffuse far away from the chains but remain in the close vicinity of the two chain complex.

Conclusions

In this work we have studied the association of two charged semiflexible chains due to the presence of multivalent counterions as interchain linkers. The results of the analytic theory compare favorably with molecular dynamics simulations of two charged chains in a mixture of monovalent and multivalent counterions at varying compositions. We find in both cases that chain pairing can only occur if the number of linkers is high enough.

References

1. L. C. Gosule and J. A. Schellman, *Nature (London)* 259, 333 (1976).
2. J. Widom and R. L. Baldwin, *J. Mol. Biol.* 144, 431 (1980); *Biopolymers* 22, 1595 (1983).
3. V. A. Bloomfield, *Biopolymers* 31, 1471 (1991); H. Deng and V. A. Bloomfield, *Biophys. J.* 77, 1556 (1999).
4. J. Pelta, F. Livolant, and J.-L. Sikorav, *J. Biol. Chem.* 271, 5656 (1996); E. Raspaud, M. Olvera de la Cruz, J.-L. Sikorav, and F. Livolant, *Biophys. J.* 74, 381 (1998); E. Raspaud, I. Chaperon, A. Leforestier, and F. Livolant, *ibid.* 77, 1547 (1999).
5. M. Kawamura and K. Maruyama, *J. Biochem. (Tokyo)* 68, 899 (1970).
6. T. D. Pollard and J. A. Cooper, *Annu. Rev. Biochem.* 55, 987 (1986).
7. J. X. Tang and P. A. Janmey, *J. Biol. Chem.* 271, 8556 (1996); J. X. Tang, Sh. Wong, Ph. T. Tran, and P. A. Janmey, *Ber. Bunsenges. Phys. Chem.* 100, 796 (1996).
8. Z. Shao, D. Shi, and A. V. Somlyo, *Biophys. J.* 78, 950 (2000).
9. C. Safinya and G. Wong (private communication).
10. Y. Cohen and E. Cohen, *Macromolecules* 28, 3631 (1995).
11. At the other extreme are charged linear polymers such as poly(styrene sulfonate) (PSS) that are so flexible that they condense into globular aggregates in the presence of multivalent counterions (Ref. 12).
12. M. Olvera de la Cruz, L. Belloni, M. Delsanti, J. P. Dalbiez, O. Spalla, and M. Drifford, *J. Chem. Phys.* 103, 5781 (1995). Even for flexible chains one might expect a loose network at low enough multivalent counterion concentrations.
13. D. C. Rau and V. A. Parsegian, *Biophys. J.* 260, 260 (1992).
14. F. Oosawa, *Polyelectrolytes* (Marcel Dekker, New York, 1971).
15. J. Ray and G. S. Manning, *Langmuir* 10, 2450 (1994).
16. A. P. Lyubartsev and L. Nordenskiöld, *J. Phys. Chem.* 99, 10373 (1995).

17. J. L. Barrat and J. F. Joanny, *Adv. Chem. Phys.* 94,1(1996).
18. N. Grnbech-Jensen, R. J. Mashl, R. F. Bruinsma, and W. M. Gelbart, *Phys. Rev. Lett.* 78, 2477 (1997).
19. B.-Y. Ha and A. J. Liu, *Phys. Rev. Lett.* 79, 1289 (1997); 81,1011(1998).
20. *Phys. Rev. E* 58, 6281 (1998); 60,803(1999).
21. M. Stevens, *Phys. Rev. Lett.* 82, 101 (1999); *Biophys. J.* 80, 130 (2001).
22. B. I. Shklovskii, *Phys. Rev. Lett.* 82, 3268 (1999).
23. F. J. Solis and M. Olvera de la Cruz, *Phys. Rev. E* 60,4496(1999).
24. R. Kjellander, T. A. kesson, B. Jo nsson, and S. Marcelja, *J. Chem. Phys.* 97, 1424 (1992); P. Kekicheff, S. Marcelja, T. J. Senden, and V. E. Shubin, *ibid.* 99, 6098 (1993).
25. I. Rouzina and V. A. Bloomfield, *J. Phys. Chem.* 100, 9977 (1996).
26. A. W. C. Lau, D. Levine, and P. Pincus, *Phys. Rev. Lett.* 84,4116(2000); A. W. C. Lau, P. Pincus, D. Levine, and H. A. Fertig, *Phys. Rev. E* 6305, 1604 (2001).
27. P. A. Pincus and S. A. Safran, *Europhys. Lett.* 42, 103 (1998).
28. I. Borukhov, R. F. Bruinsma, W. M. Gelbart, and A. J. Liu, *Phys. Rev. Lett.* 86, 2182 (2001).
29. I. Borukhov and R. F. Bruinsma, *Phys. Rev. Lett.* 87, 158 101 (2001).
30. D. Poland and H. A. Scheraga, *Theory of Helix Coil Transitions in Biopolymers*, (Academic, New York, 1970).
31. M. Ya, *Phys. Rev. A* 20, 1671 (1979).
32. J. H. Shibata and J. M. Schurr, *Biopolymers* 20, 525 (1981).
33. R. M. Wartell and A. S. Benight, *Phys. Rep.* 126, 67 (1985).
34. M. Peyrard and A. R. Bishop, *Phys. Rev. Lett.* 62, 2755 (1989).
35. A. Yu. Grosberg and A. R. Khokhlov, *Statistical Physics of Macromolecules* (American Institute of Physics, New York, 1994).
36. R. W. Hockney and J. W. Eastwood, *Computer Simulations Using Particles* (Adam Hilger, Bristol, 1988).
37. See, e.g., J. M. Thijssen, *Computational Physics* (Cambridge University Press, Cambridge, 1999); D. Frenkel and B. Smit, *Understanding Molecu-lar Simulations* (Academic, San Diego, 1996).
38. B.-Y. Ha and A. J. Liu, *Europhys. Lett.* 46, 624 (1999).

Interactions and assembly of simple solvated polymers models

Laura J. Douglas Frink and Andrew G. Salinger

Abstract

In this letter we discuss the application of a 3-dimensional implementation of a geometry-based nonlocal density functional theory to the interactions between rigid polymers in solution. Deoxyribonucleic Acid (DNA) provides inspiration for the three simple model polymers (cylindrical, bead-chain, and periodic) we consider; however the results are more generally applicable to rigid polymers such as liquid crystals. The calculations show that fine details of polymer surface structure play a critical role in determining the solvation energy landscape. This solvation energy landscape in turn controls routes for assembly of bundles of macromolecules. This approach provides a new level of molecular insight into interactions in solvated polymer systems with wide applications to both industrial and biological polymers.

Introduction

Polymer solutions are critical to the processing of a wide range of materials (from thin films for optical applications [1] to paper[2]). They are also critical to biological function as proteins are nearly always solvated in physiological conditions[3]. In fact, recent simulations of peptide folding have confirmed the importance of including explicit solvent in the calculations[4].

Theories for solvated polymers usually begin from a solution point of view, and focus on capturing polymer physics (polymer configurations, radius of gyration, etc.) while treating the solvent of the system with a single parameter that defines the strength of polymer-solvent interactions[5]. In this paper we take an alternate approach that treats the polymers as surfaces that generate an external field in which the fluid molecules equilibrate. Polymers then interact through a solvent mediated potential of mean force. We have calculated potentials of mean force between three model polymers with a novel 3-dimensional (3D) nonlocal density functional theory code[6]. This approach allows for detailed free energy calculations of the solvated interactions of locally rigid interacting polymers. The calculations presented here show how polymer geometry can affect the solvation energy landscape, and more specifically how assembly of polymer bundles can occur via minor adjustments in the alignment of two polymer strands with respect to one another.

Theoretical approach

The statistical mechanics behind our approach has been detailed elsewhere[7, 27]. Briefly, the semi-grand ensemble for a solution of N macromolecules in a solvent with known chemical potential, μ at a temperature, T and volume, V is

$$Z_{NV\mu T} = \int_V d\mathbf{R}^N e^{-\beta U_N(\mathbf{R}^N)} \times \left\{ \sum_{n=0}^{\infty} \frac{z^n}{n!} \int_V d\mathbf{r}^n e^{-\beta U_n(\mathbf{R}^N, \mathbf{r}^n)} \right\} \quad (91)$$

where $z = e^{\beta\mu}/\Lambda^3$ is the solvent activity, $\beta = 1/k_B T$, k_B is the Boltzmann constant, and Λ is the DeBroglie wavelength. Integrals are taken over all possible configurations of the N surfaces (denoted \mathbf{R}^N) and the n solvent molecules (denoted \mathbf{r}^n).

The potential energy of direct surface-surface interactions is given by U_N while the energy of both solvent-solvent and solvent-surface interactions are summed in U_n . Identifying the inner integral in Eq.91 as the grand partition function, $\Xi_{\mu VT}$ of a fluid in an external field of N fixed surfaces, the mixture partition function may then be written in terms of the grand potential,

$$\Omega(\mathbf{R}^N; \mu, T) = -\beta^{-1} \ln \Xi_{\mu VT}. \quad (92)$$

Substituting for $\Xi_{\mu VT}$, Eq.91 becomes

$$Z_{NV\mu T} = \int_V d\mathbf{R}^N e^{-\beta U_N(\mathbf{R}^N)} e^{-\beta \Omega(\mathbf{R}^N; \mu, T)}. \quad (93)$$

Taking two hard rigid macromolecules ($U_N = \infty$ if overlapping, otherwise, $U_N = 0$), the potential of mean force (PMF) acting between the macromolecules is

$$W(\mathbf{R}) = \Omega(R; \mu, T) - \Omega(\infty; \mu, T) \quad (94)$$

in the limit of two surfaces separated by R in an otherwise infinitely dilute solution of the macromolecules (ie. $\rho_M \rightarrow 0$).

Providing that the Gibbs dividing surface is chosen to be identical at all surface separations, the PMF may also be written in terms of the surface free energy, $W(\mathbf{R}) = \Omega^s(R; \mu, T) - \Omega^s(\infty; \mu, T)$ where $\Omega^s = \Omega(R; \{\rho(\mathbf{r})\}, T) - \Omega(R; \{\rho_b\}, T)$, ρ_b is the bulk fluid density associated with the known μ , and $\rho(\mathbf{r})$ is the equilibrium nonuniform density distribution of fluid particles in the external field of the N macromolecules.

The surface free energy is directly related to the solvent mediated (or solvation) force acting on the polymer strands. Given hard impenetrable surfaces, this solvation force may be calculated from the sum rule[9]

$$f = -\frac{\partial \Omega^s}{\partial R} = \int \rho(\mathbf{r}_s) n_x d\mathbf{r}_s \quad (95)$$

where $\int d\mathbf{r}_s$ indicates a integral over the surface of the macromolecule, and \mathbf{n} is the unit normal to the surface.

The inhomogeneous solvent density distribution, $\rho(\mathbf{r})$ and the surface free energies, Ω^s , and consequently the potential of mean force, W , can be calculated with molecular simulation or density functional theory (DFT). DFTs are based on the functional minimization of the grand free energy, $\Omega[\rho(\mathbf{r})]$ with respect to the density distributions, $\rho(\mathbf{r})$ at constant temperature, T , and fluid chemical potential, μ .

$$\left(\frac{\delta \Omega}{\delta \rho(\mathbf{r})} \right)_{T, \mu} = 0. \quad (96)$$

The particular functional formulation we apply here is very accurate for inhomogeneous hard sphere fluids, and was originally developed by Rosenfeld[19]. While most DFT calculations have considered geometries with considerable symmetry (slit-pores, cylindrical pores, spherical cavities etc); the polymer calculations here will require a full 3D DFT solution. Götzmann et.al. have shown that when an accurate equation of state is known for the macromolecule-solvent mixture, PMFs can be found by taking the explicit limit of $\rho_M \rightarrow 0$ [11]. While their approach shows great promise for certain geometries (e.g. spherical colloids near flat surfaces), it cannot be easily extended to the polymer-solvent mixtures considered here because reliable free energy functionals for the binary polymer-solvent mixtures are not available. In addition while the sphere-plate geometry has

the advantage of one surface with simple symmetries (the plate), that results in a 1D calculation of solvent in its fixed external field, there are no simple surfaces in the interaction of two polymer strands. Treating one polymer strand as the fixed surface would still require a 3D calculation.

Our 3-dimensional numerical implementation is based on a Newton's method solve of the system of equations, and convergence is usually obtained in less than 20 Newton iterations[6]. Each of the 3D polymer solutions presented here was obtained in approximately 3 minutes of CPU time on 50 processors of the ASCI-Red (Intel pentium 333 MHz chips) computer at Sandia National Laboratories.

Discussion of Results

We restrict the current discussion to hard sphere fluids in contact with hard rigid polymers. While other physical effects such as van der Waals, polarization, or Coulomb forces may be critical in many systems, we consider only volume exclusion in order to demonstrate our approach, the benefit of having a 3D numerical method for arbitrary surfaces, and the richness of the physics that arises even from volume exclusion alone.

The stiffness of the polymer models discussed here is not a realistic representation of all polymers; however there are some important exceptions. One example is deoxyribonucleic acid (DNA) which is rigid over long persistence lengths, λ_p , due to the double helix that composes its backbone. Due to this rigidity, DNA is in fact often treated as a rigid cylindrical polymer in molecular investigations[12, 13, 14]. More generally, every polymer is rigid on length scales smaller than its characteristic persistence length[5]. Thus part of our discussion here involves identifying the λ_p associated with strong ($> kT$) solvation energy barriers.

Using DNA as a trial system (see Fig.1), we consider three possible coarse models based on the overall topology of the chains. They include cylindrical, bead-chain, and periodic models. Sketches of the three models can be found in Fig. 2). Taking the z -axis down the long axis of a polymer chain, the cylindrical polymer is described by $R_p(z) = 1.5\sigma$ where R_p is the radius of the polymer chain and σ is the diameter of the solvent particle. The bead chain polymer is composed of spheres with radius $R_p = 1.5\sigma$ where the centers of the spheres along the z -axis are separated by 3σ . The periodic polymer has a radius, $R_p(z) = r_o + A\cos(2\pi z/\lambda)$ where the reference radius, $r_o = 0.75\sigma$, the amplitude, $A = 0.75\sigma$, and the period, $\lambda = 3\sigma$.

While all three polymer models exhibit surface curvature perpendicular to the long axis of the polymer, the bead-chain and periodic polymers also exhibit structure parallel to the polymer axes. Thus, we have calculated potentials of mean force as a function of both relative alignment and surface separation for these two cases.

Potentials of mean force for the three solvated polymer models are shown in Fig.2. In all cases, solvent packing leads to oscillatory potentials as a function of the interaxial separation of the polymers. The magnitude of the oscillations is largest for the parallel cylinders in Fig.2A where densities are uniform along the long axis of the polymer strands. However, in all cases, the free energy peaks are substantial in comparison with kT . Consider the peak at $R/\sigma = 3.6$ in the case of the aligned bead-chain polymer. It's magnitude per unit length is $W\sigma/L \approx 0.25kT$. The persistence length needed for this energy barrier to be $W \approx kT$ is $\lambda_p \approx 4\sigma$ (or $\lambda_p \approx 2nm$ for a $\sigma = 0.5nm$ solvent molecule). Since this requisite persistence length is quite short, these results should be applicable to many polymer systems.

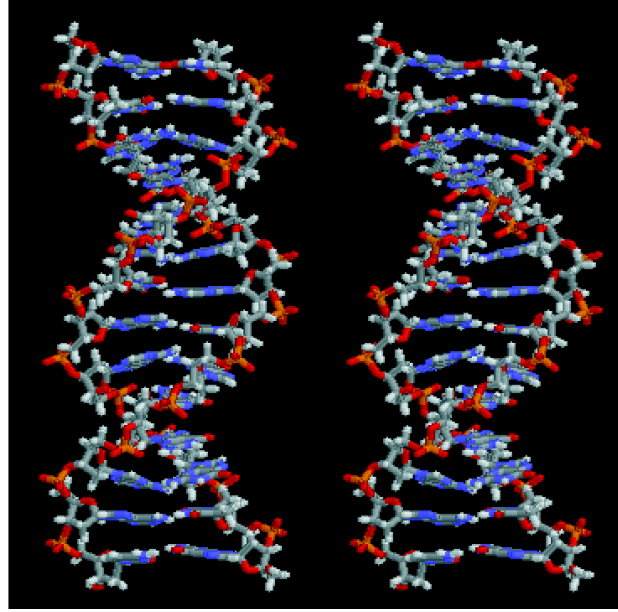


Figure 46. Two interacting DNA strands with atomic coordinates taken from the protein data bank.

The bead-chain case in Fig.2B demonstrates that the details of the surface structure of the polymer play an important role in assembly of the strands. Consider the energy barriers experienced by two polymer strands as they come together from infinite separation. If the strands remain in a perfectly aligned state (solid curve in Fig. 2B), they will need to overcome the substantial solvation barriers mentioned above. However by shifting their relative alignment (dashed curve in Fig. 2B) at the appropriate separations, the solvation barriers can be avoided altogether since the maxima in the aligned state very nearly correspond to the minima for the unaligned state. As a corollary, the forces experienced by the bead-chain polymers may be always attractive from infinite separation to contact provided that the polymers can freely change their relative alignment. The only way for the cylindrical polymers to avoid the large solvation barriers would be for the cylinders to rotate away from the parallel position. Such a rotation would be kinetically unfavorable in comparison with the small adjustments needed when surface structure is present.

While the surface structure on the bead-chain polymers provides a low-energy route to assembly by avoiding solvation energy barriers, this is not the case for the periodic polymer as shown in Fig.2C. Here, the unaligned and aligned cases have minima and maxima at similar separations. Nevertheless, the solvation energy landscape is significantly affected by the surface structure on the periodic polymers. Specifically, the period of solvation oscillations increases from 1σ (Fig.2A,B) to approximately 1.5σ (Fig.2C). In addition, the global free energy minimum is now found at $R/\sigma = 2.75$ where there is a layer of fluid between the polymer strands.

This solvated assembly predicted for the periodic polymers is in contrast to both cylindrical and bead-chain cases (Fig.2A,B) where the global free energy minimum is found at contact. In these two cases, osmotic exclusion of the hard-sphere solvent results in the strong attractive forces at contact[11]. Thus while solutions composed of any of the three polymers would self-assemble in to tightly ordered arrays, the periodic polymer

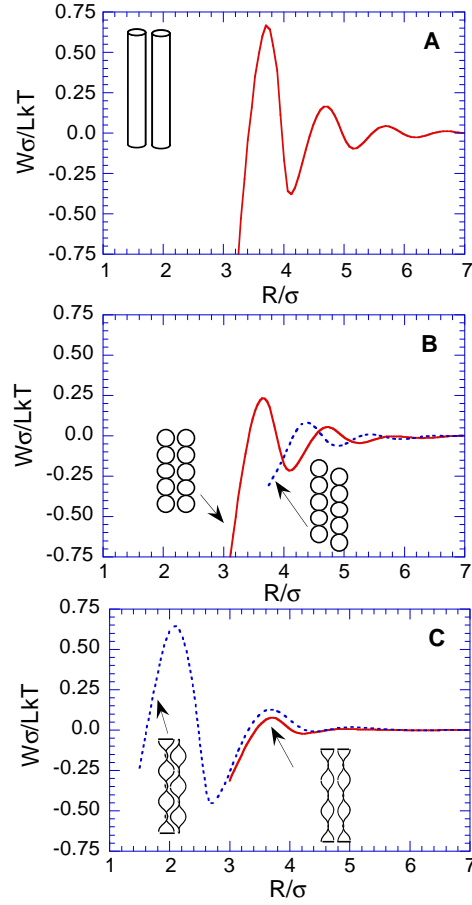


Figure 47. The potential of mean force as a function of the interaxial separation, R , of two cylindrical (A), bead-chain (B), and periodic polymers (C). In B and C, the solid lines show the cases where the polymers are perfectly aligned while the dashed lines show cases where the polymers are misaligned as shown in the sketches. The bulk fluid density away from the polymers was $\rho_b \sigma^3 = 0.63$ for all cases.

assembly will be the most highly solvated. Predicting the existence of solvated assemblies from the theory is important for further studies of swelling of ordered phases and investigations of the forces that stabilize highly solvated crystals. For example, swollen DNA assemblies have been observed in experiments[15, 16], and protein crystals may contain 50% water by volume[17, 18].

For all of the cases in Fig.2 except the unaligned bead-chain polymer, the potential curves are drawn to the point of closest approach of the polymer strands. However, it was not possible to obtain solutions for the case of the unaligned bead-chain polymer when $R/\sigma \leq 3.5$. The physical origin of the numerical instability is local crystallization (or physical *binding*) of solvent in the annuli around the points where two beads on one chain meet (see Fig.3). In this case, narrow steep density peaks must be resolved. This becomes impossible for a direct solve on a fixed mesh grid using linear basis functions to represent the density profiles. This problem may be exasperated in our calculations by using Rosenfeld's original functional that is known to exhibit incorrect zero-dimensional crossover behavior[19]. Due to the numerical limitations of the collocation

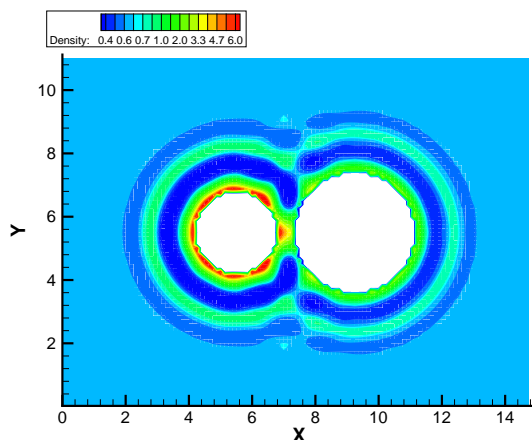


Figure 48. The density distribution as a function of position (x, y in units of σ) in a slice of constant z from a 3-dimensional calculation on the misaligned bead-chain model (See sketch in Fig. 2B). The z slice was taken at the point where two beads on the left chain come together. The white regions include both the polymer volume and solvent exclusion zones due to the hard interactions between the polymer and solvent particles. The maximum density in the 3-dimensional solution, $\rho\sigma^3 = 10.7$, is found in the plane of this figure at $x/\sigma = 6.375$, $y/\sigma = 4.5, 6.5$.

approach, a gaussian basis approach used in DFT calculations of crystals[20] may be needed for cases where strong solvent localization is important.

Summary

To summarize, this paper presents detailed 3-dimensional density functional theory calculations of the solvation energy landscape between interacting solvated polymers. This approach is quite different from most treatments of polymer solutions where the solvent is a continuum. For each of the three polymer surface topologies considered, the theory predicts that solvent packing can be an important effect even for polymers with rather small (e.g. $\lambda_p \approx 20nm$) persistence lengths. Furthermore, it was shown how the fine details of surface topology may affect the solvation energy landscape through which the polymers interact. This solvation energy landscape in turn controls both the available pathways to assembly of bundled arrays of polymer strands, and the degree of solvation in the self-assembled state that ultimately forms. While the link between polymer topology, solvent properties, and assembly is clearly complex, these calculations show that it is possible to assess these fine molecular details using a DFT based approach. Our current work involves replacing the rather crude polymer models discussed here with models based on known atomic configurations of complicated polymers such as DNA and proteins.

ACKNOWLEDGEMENTS The authors would like to thank Mark Stevens and Jeff Weinhold for many helpful discussions.

Sandia is a multiprogram laboratory operated by Sandia Corporation, a Lockheed Martin Company, for the United States Department of Energy under Contract DE-AC04-94AL85000.

References

- [1] Lee, J.W.; Wang, C.S.; Price, G.E.; Husband, D.M. *Polymer*, **1997**, *38*, 1403.
- [2] Nada, A.M.A.; Abdelhakim, A.A.; Mohamed, E.S.; Badran, A.S. *J. Elastomers and Plastics*, **1998**, *30*, 29.
- [3] Cheng, Y.K.; Rossky, P.J. *Nature*, **1998**, *392*, 696.
- [4] Daura, X.; Mark, A.E.; van Gunsteren, W.F. *Computer Physics Communications*, **1999**, *123*, 97.
- [5] de Gennes, P.-G. *Scaling Concepts in Polymer Physics*, Cornell Univ. Press, New York, 1979.
- [6] Frink, L.J.D.; Salinger, A.G. *J. Comp. Phys.*, **2000**, *159*, 407.
- [7] Douglas, L.J.; Lupkowski, M.; Dodd, T.L.; van Swol, F. *Langmuir*, **1993**, *9*, 1442.
- [27] Frink, L.J.D.; van Swol, F. *J. Chem. Phys.*, **1994**, *100*, 9106.
- [9] D. Henderson, ed., *Fundamentals of Inhomogeneous Fluids*, Marcel Dekker, New York, 1992.
- [19] Rosenfeld, Y. *Phys. Rev. Lett.*, **1989**, *63*, 980.
- [11] Götzelmann, B.; Roth, R.; Dietrich, S.; Dijkstra, M.; Evans, R. *Europhys. Lett.*, **1999**, *47*, 398.
- [12] Lyubartsev, A.P.; Nordenskiöld, L. *J. Phys. Chem.*, **1995**, *99*, 10373.
- [13] Gröbech; Jensen, N. Mashl, R.J.; Bruinsma, R.F.; Gelbart, W.M. *Phys. Rev. Lett.*, **1997**, *78*, 2477.
- [14] Allison, S.A.; Mazur, S. *Biopolymers*, **1998**, *46* 359.
- [15] Rau, D.C.; Parsegian, V.A. *Biophys. J.*, **1992**, *61*, 260.
- [16] Frink, L.J.D.; van Swol, F. *Colloids and Surfaces A*, **2000**, *162*, 25.
- [17] Smith, P.E.; Pettitt, B.M. *J. Phys. Chem.*, **1994**, *98*, 9700.
- [18] Schoenborn, B.P. *J. Mol. Biol.*, **1988**, *201*, 741.
- [19] Rosenfeld, Y.; Schmidt, M.; Löwen, H.; Tarazona, P. *J. Phys.: Condens. Matter*, **1996**, *8*, L577.
- [20] Ohnesorge, R.; Löwen, H.; Wagner, H. *Phys. Rev. E*, **1994**, *50*, 4801.

5 Biological Membranes

Coarse-grained models and simulations of bilayer membranes

Mark J. Stevens Jan Hoh and Thomas Woolf, Department of Physiology, Johns Hopkins University, School of Medicine, Baltimore, Maryland 21205

Abstract

We develop coarse-grained models and methodology to treat bilayer biomembranes. One phenomena of interest is membrane fusion. The large length and time scales for fusion events are a significant barrier to atomistic molecular simulations of fusion. To overcome these problems we apply coarse-grained models of lipid molecules. In our models the lipids are treated as bead-spring molecules (10-12 beads) and water as a single bead.* The force-field includes Lennard-Jones, bond stretching, and angle bending interactions. With this model several intriguing results have already been determined from molecular dynamics simulations using different boundary conditions and starting configurations. For example, starting with random configurations the lipids/water self-assemble to form planar bilayer membranes. By varying the lipid concentration and cell geometry, other structures can be created. In particular, we can stabilize two parallel bilayers and two bilayers with a perpendicular connecting stalk (similar to models of fusion intermediates). With constant pressure simulations following constant volume simulations we further show that a frustrated lipid system, one not able to form a bilayer in the cell-volume, can form a stable bilayer structure when the cell dimensions change. These results suggest that this simple bead-spring model can be used to study the mesoscopic behavior of membrane systems. *R. Goetz and R. Lipowsky, J. Chem. Phys. 108, 7397 (1998).

Introduction

Understanding the properties and behavior of biomembranes is fundamental to many biological processes and technologies. Microdomains in biomembranes or ‘lipid rafts’ are now known to be an integral part of cell signaling, vesicle formation, fusion processes, protein trafficking, and viral and toxin infection processes. Understanding how microdomains form, how they depend on membrane constituents, and how they act not only has biological implications, but also will impact Sandia’s effort in development of membranes that structurally adapt to their environment in a controlled manner.

Because lipid dynamics and self-organization in membranes occur on length and time scales beyond atomistic MD, we develop and use coarse-grained models of double tail lipid molecules that automatically self-assemble into bilayers. Using such a model we demonstrate that the time scales of lipid diffusion and fusion intermediates are accessible to MD simulations. This model enables the study of a whole set of membrane dynamics such as microdomain formation, membrane fusion, pattern formation, and protein insertion.

Molecular dynamics simulations

Model

Our coarse-grained model for the lipid molecules consists of a double tail bead-spring molecule composed of two types of beads (tail and head). The simulations presented here have 11 beads per lipid with 3 in the head group and 4 each in the tails (Fig. 49).

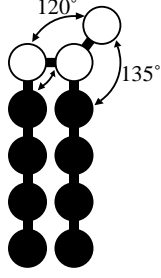


Figure 49. A diagram of the model lipid molecule with 3 bead in the head (open circles) and two tails each with four beads (filled circles). The special angle terms are denoted with the unlabeled angle having $\theta_0 = 105^\circ$.

The model including the interactions are similar to that of Goetz and Lipowsky [1, 2], but include some features from coarse-grained polymer simulations [3]. The basic idea of self-assembly is that the interaction between two head beads or between two tail beads is attractive, but interaction between a head and a tail bead is repulsive. The solvent bead is equivalent to a head bead in the nonbond interaction. Specifically, the nonbond interaction is a Lennard-Jones (LJ) potential,

$$U_{\text{LJ}}(r) = \begin{cases} 4\epsilon \left[\left(\frac{\sigma}{r} \right)^{12} - \left(\frac{\sigma}{r} \right)^6 + \frac{1}{4} \right]; & r \leq r_c \\ 0; & r > r_c \end{cases} \quad (97)$$

where ϵ and σ are the LJ energy and length scales, respectively. The cutoff, r_c is used to define the different interaction types. Let H denote a head bead, T a tail bead and S a solvent bead. Then $r_c = 2.5\sigma$ yielding the full attractive tail is used for H-H, T-T, S-S and H-S interactions. For the H-T and S-T interactions the cutoff is set to $r_c = 2^{1/6}\sigma$ which gives a purely repulsive potential.

The bond potential a combination of the purely repulsive LJ potential and the standard finite extensible nonlinear elastic (FENE) potential (the attractive term),

$$U_{\text{FENE}}(r) = -1/2k_0r_0^2 \ln(1 - r^2/R_0^2), \quad (98)$$

with a spring constant $k_0 = 30\epsilon/\sigma^2$ and maximal extension $r_0 = 7\sigma$. This potential can be integrated with same time step as the LJ potential (i.e. much longer than the potential for a C-C bond, for example).

Chain stiffness is introduced by an angle potential,

$$U_{\text{bend}}(\theta) = k_1(\theta - \theta_0)^2 \quad (99)$$

Here θ is the angle between neighboring bonds and $k_1 = 2\epsilon/\text{rad}^2$. For the tails the equilibrium angle is 180° . Figure 49 shows the other equilibrium angles.

The MD time step is 0.005τ and a Verlet algorithm was used to integrate the equations of motion. All simulations are performed at a fixed temperature $k_B T = 1.35\epsilon$. The NVT simulations use the Langevin thermostat with a damping constant $\Gamma = 1.0\tau^{-1}$ [6]. Simulations in the NPT ensemble use the Nose-Hoover thermostat and barostat. The relaxation period for the thermostat is 10.0τ and for the barostat is 0.1τ .

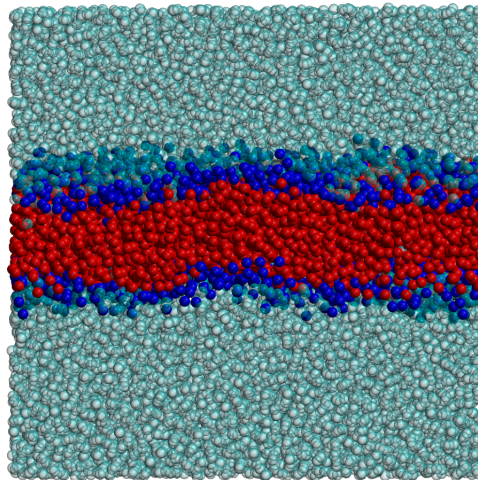


Figure 50. Image of system with $N_{\text{lip}} = 488$ lipids and an area per lipid of $3.7 \sigma^2$. The tail beads are red; the head beads are blue; and the solvent beads are transparent and cyan.

Results

Self-Assembly

We first demonstrate that our modified interactions and our specific molecule self-assembles into a bilayer. Figure 50 shows a bilayer formed starting from a random initial configuration of lipids and solvent. In this simulation there are $N_{\text{lip}} = 488$ lipid molecules and an initial bead density of $0.67 \sigma^{-3}$. Overlap was initially allowed and removed by push off with a cosine potential. Afterward the LJ potentials were turned on. After about 1 million time steps, the bilayer formed. For this system, the area per lipid is $A = 3.7\sigma^2$. In NVT simulations single bilayers have been formed for $A = 3.5 - 4.1\sigma^2$. For larger A pores occurs or a capped bilayer forms.

The NVT ensemble constrains the possible structures a system can form. For example, we simulated a system with enough lipids to form 1.5 bilayers across the system. In the NVT simulation the system was not able to self assemble with 1 million time steps. Continuing the simulation in the NPT ensemble allowing the cell shape to vary, a single bilayer forms spanning the system within 2 million time steps. In general, NPT simulations are required to determine the value of A for the given input pressure.

Density Profile and Diffusion

To confirm that the bilayer structure has the appropriate statistical distribution, we calculated the average density profile for a bilayer system. Figure 51 shows the density profile (single beads) is color coded the same way as the images. The basic features are what you would expect. The solvent has low probability of being found in the central region containing the solvophobic tails. In fact the probability is zero in a region about the center. The head profile forms two peaks just outside the tail distribution. Interestingly the head distribution extends further into the tail distribution than the solvent does. The peak-peak separation for the heads is 8

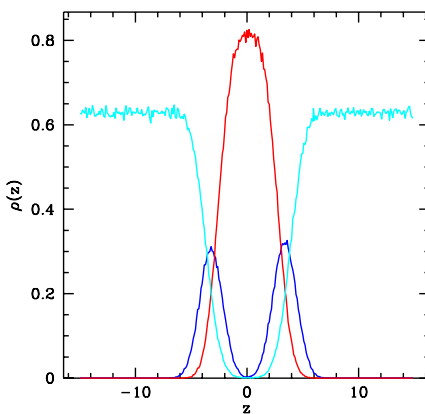


Figure 51. Density profiles of system in Fig. 1 for H, T and S beads. Colors correspond to that of Fig. 1.

σ which is slightly shorter than the maximum value.

The mean square displacement for the head, tail and solvent beads is shown in Fig. 52. The tail and head data overlap as they should. Over the 1 million time step run, the solvent beads travel on average about 17σ . The lipid beads start off at the same diffusion rate, but their connectivity reduces the rate so that they travel 14σ . These distances are quite respectable value. The lipid molecules travel well beyond their nearest neighbors. This data shows that the the bilayer is a fluid bilayer. Thus, these coarse-grained models can clearly study dynamical processes of the bilayers.

Membrane Fluctuations

One of the well known characteristics of membranes is their lateral fluctuations. These fluctuations can be important for a variety of phenomena. We performed a simulation on a large system to show that we can observe such fluctuation. Figure 53 is for a 103,100 particle system of 2100 lipid molecules in a simulation cell of dimensions $125\sigma \times 31\sigma \times 40\sigma$ giving $A = 3.7\sigma^2$. By performing simulations on such a large system, we can see the membranes spatial fluctuations. This will enable us to treat system with Helfrich forces, for example, and to examine issues of how molecular architecture affects these fluctuations. Another area of interest is inclusions and how they affect and are affected by these fluctuations. This will involve further work to model inclusions using either bead-spring models or large single particles.

Controlling Structure of Self-Assembled System

Since we are interested in modeling AFM fusion experiments, we simulate systems confined between two solid surfaces, where the bottom surface will be a substrate and the top surface the AFM tip. Periodic boundary conditions are applied in the x and y directions. In these simulations the solvent preferentially adsorbs to the surface; the solvent-surface LJ cutoff is 2.5σ . The lipids including the head beads are repelled by the surface; their LJ interaction with the surface is cutoff at $2^{1/6}\sigma$. All such simulations were performed in

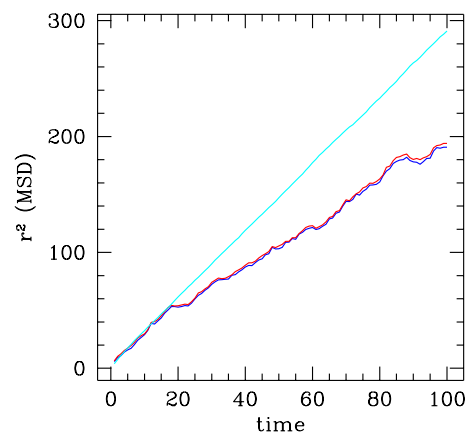


Figure 52. Mean square displacement of solvent (cyan), head beads (blue) and tail beads (red) for system of Fig. 1.

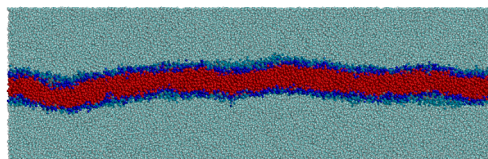


Figure 53. Image of wide system showing fluctuations with $N_{\text{lip}} = 2100$ lipids and an area per lipid of $3.7 \sigma^2$. Coloring is same as Fig. 1.

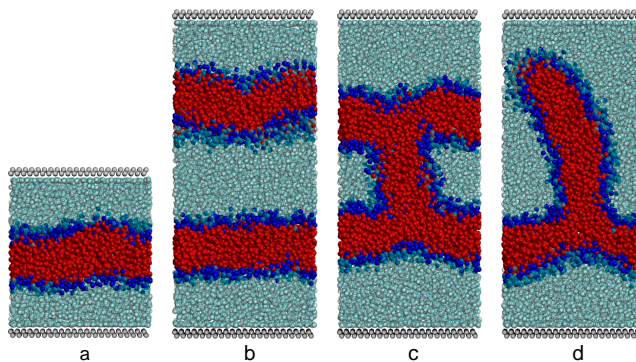


Figure 54. Images of system between solid surfaces with varying number of lipids and surface separation. (a) $N_{\text{lip}} = 220$, $A = 3.5\sigma^2$ and L_z is half the value of the rest of the cases. (b) $N_{\text{lip}} = 440$, $A = 1.75\sigma^2$. (c) $N_{\text{lip}} = 500$, $A = 1.5\sigma^2$ and $s = 5\sigma$. (d) $N_{\text{lip}} = 451$, $A = 1.68\sigma^2$ and $s = 2\sigma$.

the NVT ensemble.

Knowing the area/lipid and given the area of the solid surfaces, the number of lipids N_{lip} can be chosen to yield a single bilayer as in above Fig. 54(a). Doubling the surface separation ($L_z \rightarrow 2L_z$) and doubling N_{lip} yields a system with two bilayers (Fig. 54(b)). In (c) and (d) we consider what happens when the N_{lip} is not an integral multiple of the number of lipids to make a single bilayer. In (c) an excess of lipid is present that could and does make a connector between two bilayers of length $s = 5\sigma$. In (d) the connector length is $s = 2\sigma$, but the system in this case does not form two bilayers with a connector. Instead, similar to villi a capped bilayer forms perpendicular to a bilayer. Simulations with the same setup as in (d) but with different starting connections, do yield two bilayers with a connector. This simply shows that metastable states can form.

Vesicle Simulations

We have just begun to perform simulations of vesicles. We start the system with a preformed spherical vesicle. For a chosen inner radius of the spherical bilayer, the lipid molecules are oriented radially with the areal density found in lamellar simulations. The outer layer is built similarly. Solvent particles are inserted inside and outside at the total bead density ($0.67 \sigma^{-3}$). The images in Fig. 55 are for a system of 180,000 total beads, $N_{\text{lip}} = 1235$ and a 10σ inner radius from the origin to the center of the lipid molecule. Vesicles are metastable states and presumably, this small radius yields a vesicle with a large curvature relative to the models preferred curvature. After 1.6 million time steps a bud forms on the vesicle. The value of A is small compared to the preferred bilayer value. Thus, the vesicle forms a bud in order to release the stress and reduce the area per lipid closer to the preferred value.

Conclusions

We have laid most of a framework to use bead-spring models to study bilayer membranes. By changing the bond potential we have increased the speed of the simulations by a factor of 10. By performing molecular

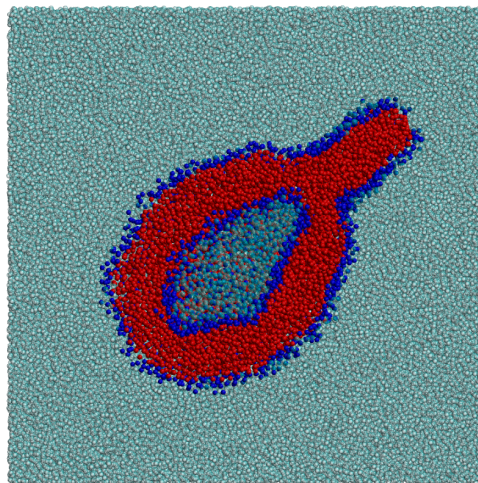


Figure 55. Image of vesicle system at $6 \cdot 10^6$ time steps showing bud formed. System has $N_{\text{lip}} = 1235$ and $A = 3.0\sigma^2$.

dynamics simulations on parallel computers, we can treat the large systems ($10^5 - 10^6$ beads) necessary to treat membrane fusion. With rather small systems, we have demonstrated that we can form intermediate fusion structures and can control the self-assembly to produce a variety of intermediate structures. These bilayer membranes are fluid as demonstrated by the diffusion rate of the lipids. Thus, we have demonstrated the capability to treat several important aspect of biomembranes.

References

- [1] R. Goetz and R. Lipowsky. Computer simulations of bilayer membranes: Self-assembly and interfacial tension. *J. Chem. Phys.*, 108:7397–7409, 1998.
- [2] R. Goetz and R. Lipowsky. Mobility and elasticity of self-assembled membranes. *Phys. Rev. Lett.*, 82:221–224, 1999.
- [3] K. Kremer and G.S. Grest. *Entanglement effects in Polymer Melts and Networks*, chapter 4, pages 194–271. Oxford, New York, 1995.
- [4] G. Manning. *Q. Rev. Biophys.*, 11:179, 1978.
- [5] E. L. Pollock and J. Glosli. Comments on p3m, fmm and the ewald method for large periodic coulombic systems. *Computer Physics Comm.*, 95:93, 1996.
- [6] J. Schneider, W. Hess, and R. Klein. The static structure factor of a dilute system of charged rods in solution. *J. Phys. A*, 18:1221, 1985.
- [7] M.J. Stevens and K. Kremer. Structure of of salt-free linear polyelectrolytes. *J. Chem. Phys.*, 103:1669, 1995.

- [8] M.J. Stevens and S.J. Plimpton. The effect of added salt on polyelectrolyte structure. *Euro. Phys. J. B*, 2:341, 1998.

Electroporation

Electroporation is a well-known physical process in biological cells [1, 2, 3]. It involves rapid structural rearrangement of the membrane, in response to an externally applied electric field. The most prominent observable effect is a rapid increase in the electrical conductivity by several orders of magnitude [4]. This is attributed to the formation of aqueous pathways, or pores, in the lipid bilayer of the membrane. The opening of such channels, or more appropriately, transient aqueous pores, enables the transport of ions and water-soluble species both into and out of individual cells. Electroporation can, therefore, be used to initiate large molecular fluxes for purposes of introducing genetic material into cells. Numerous related applications in molecular biology, biotechnology, and medicine are beginning to emerge [5, 6].

Electroporation has also been linked to the nonthermal killing of micro-organisms subjected to strong electric fields [7, 8]. For this reason, it offers great potential for decontamination and the elimination of harmful micro-organisms and biohazards. Traditionally, most electroporation studies have focused on relatively low external electric fields less than a kilovolt per centimeter, applied over extended time periods ranging from several tens of microseconds to millisecond [8]. In a very recent development, work has focused on the use of much shorter, high-voltage pulses for initiating electroporation. [9, 10]. Electric fields as high as 100 kV/cm were used with pulse durations ranging from nanoseconds to several microseconds. There appear to be several fundamental advantages in using short electric pulses for cellular manipulation. First, negligible thermal heating of the biological matter can be expected to occur due to the short time duration. Also, much lower energies are required for pulsed inputs, and yet large values of the electric fields and peak powers can be obtained. Next, pulsed fields afford a way by which the time scales can easily be manipulated. For example, by turning off the applied fields relatively quickly, the slower processes, for example, biochemical events, could effectively be inhibited, while intracellular mechanisms would be active. In order to fully utilize its potential of ultrashort pulses for cellular manipulation, it is important to develop a good understanding of the electroporation physics and membrane electroporomeabilization.

Our work on this problem is described in a series of publications in which we extended the previous theoretical work and compared the results with a series of experiments using ultrashort electrical pulses [11, 12, 13]. In these studies, the temporal dynamics of electroporation of cells subjected to ultrashort voltage pulses are studied based on a coupled scheme involving the Laplace, Nernst-Planck, and Smoluchowski equations. The results show that there is an effective time window for destruction by a second pulse, and this time-window is demonstrated by experimental data for *E. coli* cells [11]. In further work, the model of the cell was refined to examine the mechanical effects of the electric field and the interactions of the pores [12, 13].

References

- [1] R. Stampfli, *Z. Chem.*, vol. 30, pp. 57, 1958.
- [2] Tan Y. Tsong, "Electroporation of cell membranes," *Biophysics*, vol. 10, pp. 297–308, 1991.
- [3] James C. Weaver and Yu. A. Chizmadzhev, "Theory of electroporation: A review," *Bioelectrochemistry and Bioenergetics*, vol. 41, pp. 135–160, 1996.
- [4] I. G. Abidor, V. B. Arakelyan, L. V. Chernomordik, Yu. A. Chizmadzhev, V. F. Pastushenk, and M. R.

- Tarsevich, "Electric breakdown of bilayer lipid membranes i. the main experimental facts and their qualitative discussion," *Electrochemistry and Bioenergetics*, vol. 6, pp. 37–52, 1979.
- [5] G. A. Hofmann, S. B. Dev., S. Dimmer, and G. S. Nanda, "Electroporation therapy: A new approach for the treatment of head and neck cancer," *IEEE Trans. Biomedical Engineering*, vol. 46, pp. 752–759, 1999.
 - [6] D. C. Chang, B. M. Chassy, J. A. Saunders, and A. E. Sowers, *Guide to Electroporation and Electrofusion*, Academic Press, New York, NY, 1992.
 - [7] A. J. H. Sale and W. A. Hamilton, *Biochim. Biophys. Acta*, vol. 148, pp. 781, 1967.
 - [8] H. Huelshager, J. Potel, and E. G. Niemann, *Radiat. Environ. Biophys.*, vol. 20, pp. 53, 1981.
 - [9] K. H. Schoenbach, F. E. Peterkin, R. W. Alden, and S. J. Beebe, *IEEE Trans. Plasma Sci.*, vol. 25, pp. 284, 1997.
 - [10] A. Ghazala and K. H. Schoenbach, *IEEE. Trans. Plasma Sci.*, vol. 28, pp. 115, 2000.
 - [11] R. P. Joshi, Q. Hu, R. Aly, K. H. Schoenbach, and H. P. Hjalmarson, "Self-consistent simulations of electroporation dynamics in biological cells subjected to ultrashort electrical pulses," *Phys. Rev. E*, vol. 64, pp. 11913, 2001.
 - [12] R. P. Joshi, Q. Hu, K. H. Schoenbach, and H. P. Hjalmarson, "Theoretical predictions of electromechanical deformation of cells subjected to high voltages for membrane electroporation," *Phys. Rev. E*, vol. 65, pp. 21913, 2002.
 - [13] R. P. Joshi, Q. Hu, K. H. Schoenbach, and H. P. Hjalmarson, "Improved energy model for membrane electroporation in biological cells subjected to electrical pulses," *Phys. Rev. E*, vol. 65, pp. 41920, 2002.

6 Cell Modeling

Intracellular Calcium Dynamics Modeling with Unstructured Finite Element Solution Methods

Shawn Means

Calcium is exploited in a variety of biological cell systems for signalling mechanisms. Typically biological cells maintain a low intracellular concentration on the order of 100 nM in contrast with extracellular concentrations in the 10 μ M range, and intracellular organelles (i.e., mitochondria, sarcoplasmic reticulum) maintaining concentrations even higher in the 100 μ M range. Such concentration gradients are established via pumping mechanisms at the cell's plasma membrane and its intracellular organelle membranes as well. When a signal in the form of either a membrane depolarization or a ligand such as a neurotransmitter binds to the cell's receptors, calcium channels may open and allow calcium to flow down its concentration gradient, in turn initiating some cellular response.

We present the preliminary results obtained for three calcium dynamics cell modeling projects funded this year under the LDRD. 1) Calcium sparks in atrial cardiac cells; 2) calcium concentrations in a neuron terminus during depolarization events; and 3) calcium dynamics in the endoplasmic reticulum as determined by varying calcium channel distributions. These results were obtained with continuum, reaction-diffusion models, where we constructed the systems of equations based upon the relevant species in the cell to each model. Such models were solved numerically via the finite-element method with the Sandia developed package MPSalsa for solution on parallel platforms. We provide details and commentary on these solution methods below.

Unstructured Finite Element Solution Methods

In a continuum model of a cell, the species of interest are modeled not as individual objects but as a concentration varying over space and time. The objects' behavior is handled by means of partial differential equation systems known as reaction-diffusion equations. Advantageous to this model is the handling of large numbers of objects (here molecules) as a continuous distribution throughout a region. Further, this class of equations is readily applicable to multiple problems of interest in cellular biology, specifically here, intracellular calcium dynamics.

However, continuum cell models are computationally challenging. The systems of partial differential equations are typically strongly coupled with complex varieties of boundary flux mechanisms, in addition to the geometric complexities of cellular structures and multiple time and spatial scales inherent in the system.

Other cellular modeling programmes exist, namely the Virtual Cell at the University of Connecticut Health Center and MCell, or Monte-Carlo Cell, at the Salk Institute. The Virtual Cell is however somewhat limited. It utilizes regular meshing techniques and an assumed steady-state for fast time scales, which makes multiple spatial scales intractable and introduces errors in certain systems over long timespan solutions. The MCell project is a large-scale, parallel platform solution package which utilizes a probabilistic depiction of molecule reaction / transport. Such a depiction is excellent for small numbers of species; however, the larger

concentration values encountered for some diffusive species is more appropriately described with a continuum model.

The unstructured finite element method allows a reasonable computational effort in depicting multiple spatial scaling in a continuum model. This in turn also allows increased complexity in the number of reacting species, and management of multiple time scales as well. Further, with the relatively parsimonious spatial representations of unstructured grids, fully three-dimensional models are more computationally feasible. This is a notable improvement over two-dimensional models (some systems presented here were represented in prior works as 2D models) which suffer the criticisms of assumed symmetries or unrealistic representations. Since Sandia has contributed significant effort to development of unstructured finite-element solution methods of continuum reaction-diffusion equations, we employ them as described below.

MPSalsa - A Reacting Fluid Flows Solver

This section briefly overviews the numerical solution methodology that is currently used in Sandia's MPSalsa to approximate the solution of the multi-species diffusion/reaction equations that are used in the continuum biological cell simulations. MPSalsa is a general parallel transport/reaction solver that is used to solve the governing transport/reaction PDEs describing fluid flow, thermal energy transfer, mass transfer and non-equilibrium chemical reactions in complex engineering domains. In the current study we take advantage of the general framework and limit the transport mechanisms that are included to only a multi-species diffusion transport by mass fraction gradients as described by Ficks law.

The governing PDEs for multi-component diffusion mass transfer and non-equilibrium chemical reactions are presented in equation (100) in residual form. This residual definition is used in the subsequent brief discussion of the Galerkin FE formulation. The continuous problem, defined by the transport / reaction equations, is approximated by a Galerkin FE formulation. The resulting weak form of the equations are shown in equation (101).

$$R_{Y_k} = \frac{\partial Y_k}{\partial t} - \nabla \cdot D_k \nabla Y_k - W_k \dot{\omega}_k \quad k = 1, 2, \dots, N \quad (100)$$

$$F_{Y_k} = \int_{\Omega} \Phi \left[\frac{\partial Y_k}{\partial t} - \nabla \cdot D_k \nabla Y_k - W_k \dot{\omega}_k \right] d\Omega \quad (101)$$

The transient time integration methods used in MPSalsa follow closely the development of Gartling in the NACHOS II [6] code and the work of Gresho [7]. Two types of implicit predictor/corrector integrators are used in MPSalsa: Forward/Backward Euler and Adams-Bashforth/Trapezoidal Rule. Though computationally expensive, implicit methods are desirable because of their stability and ability to integrate efficiently to steady state solutions for problems where the diffusion operator is important. The implicit time integrators in MPSalsa are based on predictor/corrector methods to improve their accuracy and efficiency. Both integrators may be used with either a constant or dynamic time step selection algorithm.

The particular implementation of the Newton's method for nonlinear solution differs somewhat from the

typical Newton’s method. Following the work of Eisenstat and Walker [5], we use an inexact scheme based on iterative solution techniques instead of direct matrix inversion.

The linear subproblems generated from the inexact Newton method are solved by preconditioned Krylov methods as implemented in our Aztec solver library [9]. The parallel Krylov algorithms implemented in Aztec include techniques such as the conjugate gradient methods (CG), the restarted generalized minimal residual [GMRES(k)] and transpose-free quasi-minimal residual techniques for nonsymmetric systems. All Krylov methods rely on a small, well defined set of basic kernel routines. These kernel routines consist of parallel matrix-vector, vector-vector, vector inner-product, and preconditioning operations [15], [16], [17].

MPSalsa is run on a multitude of platforms, but is primarily designed for Massively Parallel architectures, hence the ‘MP’ prefix. Results presented here were from solutions computed on workstations up to large scale parallel platforms. The unstructured spatial discretizations allowed for efficient representations of multiple spatial scales, and hence allowed for the usage of workstations instead of the large scale architectures on some problems.

Cardiac cell calcium sparks

Atrial cardiac cells in the heart exploit calcium concentration gradients across intracellular structure membranes (sarcoplasmic reticulum) for signalling the contractions necessary for the heart’s function. The exact mechanism of calcium release from the intracellular structures remains unclear. Calcium release units (CRU) on the membrane of the sarcoplasmic reticulum are sensitive to the ambient calcium levels within the cardiac cell. When a signal arrives in the form of a membrane depolarization at the cardiac cell’s surface, calcium influxes into the cell and raises the ambient calcium and in turn initiates release of more calcium via the CRU and then causes contraction.

Details of this CRU sensitivity and the modulations between the neighboring CRU’s as well as the precise fluxes of CRU’s await explanation. Experimentally, a range of possible flux, or current, strengths of CRU’s is posited, but precise measurements are unobtainable. Hence, cell modeling is employed to assess the impact of variations of CRU current strengths on observed behavior in the cardiac cell.

A particular phenomenon of interest regarding these CRU release current strengths are the so-called calcium ‘sparks,’ [4] or spontaneous release of calcium - see figure 56. When enough CRU’s spontaneously release calcium in close proximity, a calcium wave emerges [3] [4] (see figure 56). This wave and the corresponding sparks in turn impact the contractile behavior of the cell. By substantially increasing the intracellular calcium concentrations, this alters the responsiveness of the cardiac cell to control by the heart contraction mechanism, which may result in heart arrhythmias.

A reaction-diffusion model of the calcium dynamics in this atrial cardiac cell was constructed. In collaboration with Leighton Izu, University of Maryland, we applied the parameters for a previously constructed two-dimensional model [10], [11] into a fully three dimensional model. Additional parameters were provided by the their laboratory as needed. The aim is testing of various CRU current strengths with stochastic dependence on ambient calcium levels and evaluation of what currents are necessary to initiate the experimentally observed calcium waves.

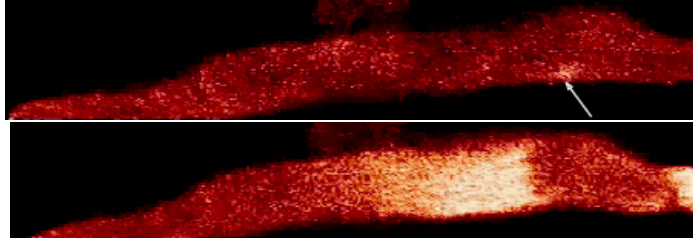


Figure 56. Calcium activity in a cardiac cell. Experimental images of an atrial cardiac cell, injected with fluorescent dye indicator showing the concentration of calcium. (Top) A single spark is indicated in the image (arrow). The overall calcium levels are higher than normally found in a physiological cell (greater than 100 nM), hence there is a high degree of background fluorescence. (Bottom) A pair of calcium waves after spark aggregation. Two waves are converging on the region surrounding the spark in the previous image. After enough sparks occur within proximity of each other, a wave of CRU calcium release occurs.

We are still in the construction phase; reactions with calcium buffers are still being installed and the remarkably complex interaction between calcium concentration and membrane surface potential remains to be elucidated and mathematically expressed. However, we have overcome significant spatial discretization difficulties for optimal solutions over the multiple spatial scales inherent in the geometry of interest, in addition to exhaustive testing of the model in comparative, two-dimensional simulations.

Provided here are images depicting the mesh of a cylindrical section of an atrial cell, and a preliminary simulation of stochastically firing CRU's. In figure 57, we show the surface and interior mesh of a cylindrical representation of the atrial cell. The vertical banding is the result of representing a physiological aggregation of the CRUs in the atrial cell along so-called 'z-lines' [2]. Each z-line contains 115 CRUs, each of which are represented by a cubic geometry, with side length of 200 nm. This particular geometry is a small subsection of the entire model yet to be constructed which will contain 50 z-lines (this section contains only five).

The reaction-diffusion equations for the model are given below, where C , F_B and F_D are the primary species representing calcium, free protein buffer and free dye concentrations respectively.

$$\frac{\partial C}{\partial t} = D_C \nabla^2 C + \sum_j R_j(C, F_j) \quad (102)$$

$$- J_p + J_{leak} + \sum_i S(u_i, t; T_{open}) \quad (103)$$

where the buffering reaction is represented with

$$R_j(C, F_j) = -k_j^+ C \cdot F_j + k_j^- (H_j - F_j); \quad j = D, B$$

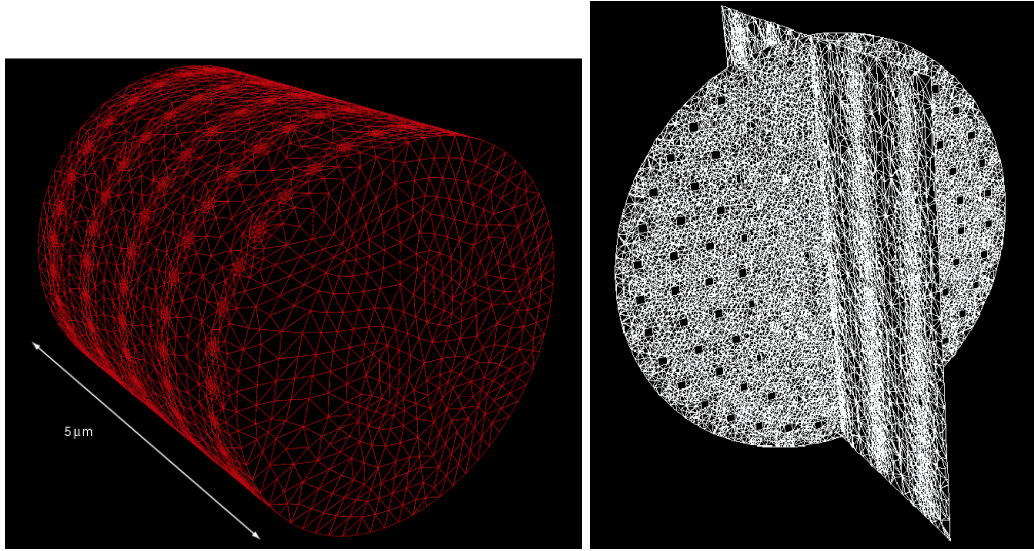


Figure 57. Cylindrical cardiac cell representation spatial discretization. (Right) Surface mesh of cylinder. Again note the banding of finer elements along the 'z-line' representation. Mesh resulted in approximately 900,000 tetrahedrons and 110,000 nodes. (Left) Slice planes of the cylinder's mesh. The square 'holes' are the omitted cubic representations of the CRU's (scale: 200 nm). Vertical banding on the plane orthogonal to the circle of CRU's result of finer mesh size along the so-called 'z-lines,' or collections of CRUs on the sarcoplasmic reticulum, as observed in the physiological system.

with H_j the total concentration of bound and unbound buffer. The flux terms depict the sarcoplasmic reticulum pumping mechanism, J_p and its membrane leakage, J_{leak} . Activation of CRUs is determined via the source term summation of S over the number of CRUs. S is a stochastic function taking values of 0 or 1, depending upon the probability P of the CRU firing, and remains 1 for the timespan of T_{open} . J_p and P are listed below, except for J_{leak} which is constant:

$$J_p = V_p \frac{C^{n_p}}{K^{n_p} + C^{n_p}} \quad (104)$$

$$P(C, K, n) = P_{max} \frac{C^n}{K^n + C^n} \quad (105)$$

Parameter values such as P_{max} , T_{span} , V_p and binding coefficients K^n are determined either experimentally in the University of Maryland laboratory or via published literature.

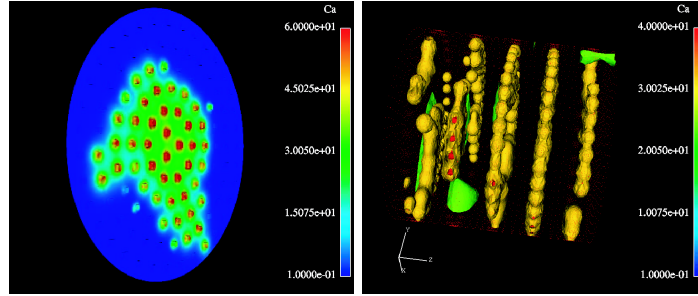


Figure 58. Calcium concentrations in cylindrical sections of cardiac cell. (Left) Calcium levels in a single z-line simulation. Note the irregular wave front of calcium levels due to stochastic behavior of CRUs. (Right) Calcium levels in multiple z-line simulation. Time of simulation at point where most of CRUs are activated, and wave essentially propagated throughout cylinder.

In figure 58 we present images of simulation results for trial runs of a single z-line and a multiple z-line domain construction. A calcium wave is generated in both the single and multiple simulations by initially elevating the calcium concentrations in a region surrounding a single CRU. With this increased probability of firing, the CRU activates and initiates a cascade of CRU activation and calcium elevations.

These preliminary results are the first fully three-dimensional simulations of either a section or a whole cardiac cell. A full 50 z-line geometry including membrane potential depictions is under construction, and will provide the first full model of calcium dynamics in a cardiac cell for exploration of various CRU current impact on contractile activity leading to heart arrhythmias.

The University of Maryland is engaged in contractual negotiations to provide funding for this work, in order to complete the full model and exploration of this issue of CRU current strength. In addition, Leighton Izu and the University of Maryland will pursue in collaboration with Shawn Means and Sandia National Laboratory,

funding from the National Institute of Health to continue this work as initially funded by the Biotechnology LDRD.

Neuron terminus calcium dynamics

Neurons establish concentration gradients across their cellular membrane, or plasma membrane, for a variety of ionic species. Of special importance are sodium and calcium ions. Sodium ion fluxes across the neural membrane propagate signals from a source (another neuron or sensor) to the neuron terminus, where calcium ion influxes initiate a sequence of events known as neurotransmitter release. This release transfers the information signal to, for example, another neuron for further transmission or a muscle for contraction. Both of these ions are typically maintained at low intracellular concentrations, while the extracellular space concentration is orders of magnitude higher.

Experiment has established a modulatory role for sodium on the affect of calcium's initiation of neurotransmitter release [1], [14]. The precise mechanism for this modulation is elusive; however, multiple hypotheses exist. One such hypothesis is that sodium's impact on calcium is through a mechanism known as the sodium-calcium exchanger [14], which typically exploits sodium gradients to eject calcium from the neuron, but under certain conditions reverses operation and uptakes calcium. It is not currently possible, however, to determine experimentally the precise impact of this exchanger upon calcium levels at the neurotransmitter release sites. In addition, research has shown the spatial locations of the exchangers raise some doubt as to whether they impact calcium levels at the neurotransmitter release sites: the exchangers are on the opposite site of the neuron terminus from the release mechanisms [12]. Hence, we turn to a spatial cell model to explore the impact of this exchanger on intracellular calcium concentrations.

Again we employ a reaction-diffusion model of the calcium and sodium dynamics in the neuron terminus. Based on a two-dimensional model utilized previously [13], a fully three-dimensional geometry was constructed, with the specific aim of representing the exchanger site's spatial location and impact on calcium levels at the release sites. This includes the difficulty of resolving multiple spatial scales for the exchangers, ion channels (for ionic influx) and pumping mechanisms (for ionic extrusion), at 10 nm length up to the 2 μ m length scale of the terminus.

The reaction-diffusion system of equations is given below, for the multiple species involved: sodium (N), calcium (C), mobile (B, S1, S2, S3, S4), and immobile protein calcium buffers (I, IC):

$$\frac{\partial N}{\partial t} = D_N \nabla^2 N \quad (106)$$

$$\frac{\partial C}{\partial t} = D_C \nabla^2 C + \Phi_C(C, B, S1, S2, S3, S4, I, IC) \quad (107)$$

$$\frac{\partial B}{\partial t} = D_B \nabla^2 B + \Phi_B(C, B, S1) \quad (108)$$

$$\frac{\partial S1}{\partial t} = D_{S1} \nabla^2 S1 + \Phi_{S1}(C, B, S1, S2) \quad (109)$$

$$\frac{\partial S2}{\partial t} = D_{S2} \nabla^2 S2 + \Phi_{S2}(C, S1, S2, S3) \quad (110)$$

$$\frac{\partial S3}{\partial t} = D_{S3} \nabla^2 S3 + \Phi_{S3}(C, S2, S3, S4) \quad (111)$$

$$\frac{\partial S4}{\partial t} = D_{S4} \nabla^2 S4 + \Phi_{S4}(C, S3, S4) \quad (112)$$

$$\frac{\partial I}{\partial t} = \Phi_I(C, I, IC) \quad (113)$$

$$\frac{\partial IC}{\partial t} = -\Phi_I(C, I, IC) \quad (114)$$

The buffering mechanisms are crucial for control of and dampening the large calcium influxes into the neuron, which otherwise would result in toxic levels of calcium. Each source term, Φ_{C-S4} , represents the mass-action reaction kinetics scheme for the binding of calcium to the mobile and immobile protein buffers naturally found in the neuron(not shown). No buffering mechanism is included for sodium, and the only source of coupling between the sodium and calcium dynamics are via the boundary flux mechanism, the sodium-calcium exchanger, which is one of the following Neumann boundary conditions:

$$-D_N \frac{\partial N}{\partial \mathbf{n}} \Big|_{\mathbf{x} \in \partial \Omega} = \frac{1}{F} (q_G^N + q_P^N + q_e + q_L^N) \quad (115)$$

$$-D_C \frac{\partial C}{\partial \mathbf{n}} \Big|_{\mathbf{x} \in \partial \Omega} = \frac{1}{F} (q_G^C + q_P^C + q_e + q_L^C) \quad (116)$$

$$(117)$$

Each ‘ q ’ term represents a flux mechanism: a voltage-gated ion channel, ion pump, the exchanger, and a membrane leakage respectively.

We focus only on describing the mechanism of interest, the sodium calcium exchanger. A hyperbolic sine depiction as found in the literature [8] is utilized, which is given by:

$$q_e = \sum_{\mathbf{x}_e \in \mathcal{E}} \phi_e(N, C, t) \delta^\epsilon(\mathbf{x} - \mathbf{x}_e) \quad (118)$$

$$\phi_e(N, C, t) = K_e [N^3 C_o \kappa(t) - N_o^3 C \kappa(t)^{-1}] \quad (119)$$

$$\kappa(t) = e^{V_m(t) \frac{F}{2RT}} \quad (120)$$

where the notation $\mathbf{x}_e \in \mathcal{E}$ indicates the spatial localization of the exchanger, and activates these exchangers with the delta function. A parameter, K_e is used to scale the activity of the hyperbolic sine function such that the exchanger's maximal current corresponds to the physiologically observed value. F , R , and T are the standard valued parameters for Faraday's, the Ideal Gas constant, and temperature for the cellular system (in Kelvins). The $V_m(t)$ term in the exponential function is the membrane voltage which exhibits a characteristic temporal profile during the stimulation of a neuron, where the membrane potentials vary as a so-called 'action potential.' It is during the maximal activation of the neuron that the exchanger may reverse operation, depending upon the concentrations of both sodium and calcium available to the mechanism.

This reversal behavior naturally is amenable to investigation only if the ionic concentrations are suitably represented, and are physiologically realistic during the neural stimulation event. A fully three-dimensional representation of the neuron terminus has been constructed and tested; however, we are now cultivating a working relationship with the University of New Mexico Calcium Signalling Group regarding obtaining experimental data directly related to the simulated conditions for comparison and verification of the model. Further expansion of the three-dimensional geometry beyond the primitive representation into a realistic reconstruction of the terminus from confocal microscopy images is an additional goal of this relationship.

Meanwhile, we present the preliminary three-dimensional simulation results for the neuron terminus model. This particular iteration of the model is a straightforward cubic representation of the terminus, with subdomains distributed along the surface for application of the appropriate Neumann flux conditions as related above. In figure 59, we illustrate the surface mesh of the cubic neuron terminus with the subdomains described on each surface, as well as a surface plot of calcium concentrations during a stimulation. The calcium levels qualitatively match experimental observation (maximal concentrations at the ion channel mouths are $400 \mu\text{M}$) as well as the time decay of calcium removal by pumping mechanisms. Sodium levels are more problematic; little experimental work has been performed on intracellular sodium dynamics. Hence, we anticipate coordination with the University of New Mexico for such measurements.

A level P-20 Center Grant for Cellular Modeling was awarded by the National Institutes of Health for collaborative work between the University of New Mexico and Sandia National Laboratory. This money is primarily for initialization of the center for cell modeling between these organizations, and was crucially enabled by the Biotechnology LDRD funding. Ultimately, the aim is production of tangible research results for a following application for a full P-50 Center Grant. This effort is coordinated as well with the next project described, the endoplasmic reticulum simulations in collaboration with Alex Smith at the University of New Mexico Cancer Research Center.

Endoplasmic Reticulum calcium dynamics

Another issue regarding the intracellular dynamics of calcium centers around the variable distributions of calcium channels on the surface of the cellular organelle, the endoplasmic reticulum. Upon variations of the intracellular calcium levels and another molecule, called Inositol Triphosphate, or IP3, these calcium channels which bind IP3 change their spatial distribution and aggregate on the surface of the endoplasmic reticulum, according to work at the University of New Mexico. Such clustering of the calcium channels is puzzling to these experimental researchers; the precise impact of these clusters on a myriad of interdependent signalling mechanisms is unclear. Furthermore, only observations under these conditions of the intracellular

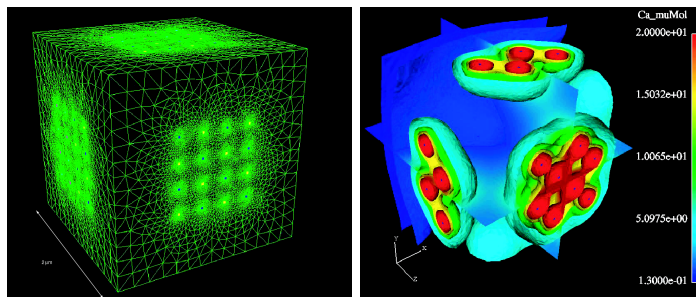


Figure 59. Cubic neuron terminus model. (Left) Surface mesh of cubical representation of a neuron terminus. The cube is $2\ \mu\text{m}$ per side with 64 boundary subdomains, each of which are 10 nm per side. Membrane pumping mechanisms and ion channels are represented on these subdomains as Neumann flux conditions. The mesh contains 770,000 tetrahedrons and 140,000 nodes. This resulted in over 1 million unknowns per time step for solution, which required a parallel computational platform. (Right) Isosurface plot of calcium concentrations at maximal activation of the terminus. The ion channel boundary terms are all fully activated, and calcium is flooding into the terminal representation. Notice the influxes are contained in a relatively small volume surrounding the channel mouths, similarly to experimental observation, demonstrating the impact of calcium buffering. Qualitatively, the simulation corresponds to experimental observations; the maximal calcium concentration at the channel mouth peaks at about $400\ \mu\text{M}$. Sodium concentration measurements are simply not as available in the literature as calcium; hence, collaborations with experimentalists are underway.

concentrations of calcium are possible and not the endoplasmic reticulum calcium. Hence, cell modeling is engaged to explore these various spatial distributions of calcium channels.

Although a reaction-diffusion model is constructed for this system, we are only now completing the surface reconstruction of the endoplasmic reticulum and we limit the discussion to the model's geometry. Alex Smith at the University of New Mexico Cancer Research Center utilized confocal microscopy imaging to reconstruct a three-dimensional representation of a section of an endoplasmic reticulum (see figure 60). Via tedious tracing of slice plane images, a surface representation was obtained, but a viable meshing surface required further refinement.

We engaged the efforts of Sandia's CUBIT meshing team, and John Fowler (developer of surface regeneration software) in the surface reconstruction. The surface images required that they be connected together in a topologically continuous manner, and the software provided by John Fowler (ddv) performs this function, albeit imperfectly. This problem provided opportunities for modifications to the surface reconstruction code. Unfortunately, a smooth surface proved inadequate for the meshing capabilities of CUBIT. Iterations of surface alterations and meshing attempts eventually provided a reasonable, computationally feasible mesh. We provide images illustrating the original confocal microscopy of an endoplasmic reticulum, the surface reconstruction and resultant mesh in figure 61.

Currently, a simple model of the calcium dynamics for various channel clusterings is being applied to the

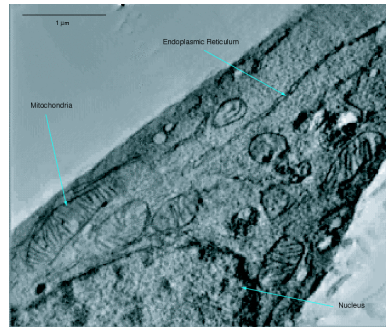


Figure 60. Confocal light microscopy image of cell. This image is one 'slice' plane image of a stack of images through the z-plane taken of a cell. The endoplasmic reticulum outline was traced per stack and the collection of stacks utilized to reconstruct a full three-dimensional representation of the structure's surface.

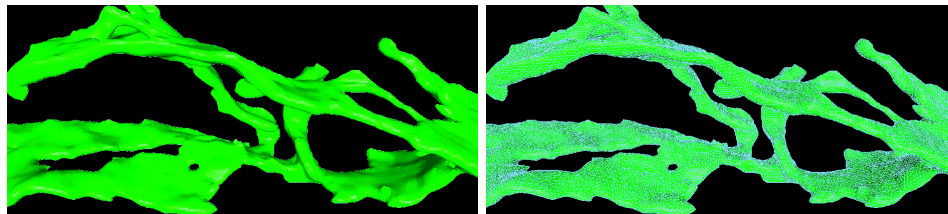


Figure 61. Endoplasmic reticulum surface reconstruction and mesh. (Top) Faceted face representation of the endoplasmic reticulum tracing. Initially, the faceted surface was inundated with inviable surface projections and perforations. The result of multiple iterations of retracing the original confocal microscopy images and surface smoothings, the facet representation shown still contains some perforations (note hole in surface, lower left of center), but the surface is topologically continuous and viable for meshing. (Bottom) The tetrahedral mesh shown on the surface of the facet representation. This mesh resulted in a total of 460,000 tetrahedrons and 100,000 nodes. Upon construction of the calcium channel cluster subdomains, the numbers of nodes should increase to represent this aggregation of mechanisms which dramatically increase calcium concentrations in a relatively small area.

mesh finally obtained. No simulation results are available at this time.

In concert with the neuron terminus model, we are collaborating with the University of New Mexico on the P-20 NIH center grant for cell modeling on this endoplasmic reticulum project. This particular project highlights the potential for a collaborative center for cellular modeling with the University of New Mexico. With the image processing and realistic geometry reconstruction capabilities at the university and the computational capabilities at Sandia, significant cellular modeling progress is possible. This effort was moreover made possible in part due to the Biotechnology LDRD funding.

Concluding Remarks

We established the ability of Sandia to apply its expertise in finite element solution methods as well as mesh generations to relevant biological cell modeling problems. The geometric primitive representations of a cardiac cell and a neuron terminus provided opportunities to directly approach systems of reaction-diffusion equations depicting intracellular dynamics of ion concentrations as well as reacting buffer mechanisms. Determination of the relevant mechanisms for the model are based upon a history of cellular modeling focusing on dynamics of species of interest; no model will ever capture every detail of cellular function. Meanwhile, however, we coordinate modeling efforts with experimental work in this determination, as well as providing the parameter data required for the model. Additionally, the exhaustive reconstruction of realistic geometric representations of cellular structures will provide further confidence in the results, and Sandia has shown its capability in this arena.

Based upon this preliminary work, we are engaged in efforts to systematize and streamline to some degree the reconstruction of geometry, mesh generation, and numerical solution of the reaction-diffusion systems accomplished with Sandia developed software. We plan on coordination of our effort with the software developers regarding each of these three crucial phases. This includes John Fowler's surface reconstruction toolkit for extraction of surfaces from the confocal microscopy images, CUBIT mesh generation on these surfaces and the volumes contained, and the modification and refinement of MPSalsa specifically for more efficient solution of the types of equations utilized in cell modeling. Such adaptations of the codes utilized provides an opportunity for Sandia software engineers to engage in a novel and challenging sphere of research.

Given modifications to the primary software tools, we aim to expand the complexity of models as shown in these three examples. Examples include: increased complexity in geometric representations as illustrated by the endoplasmic reticulum model; increased numbers of diffusive species possible due to more efficient solution methods; inclusion of multiple domains in the cell models since biological cells contain multiple diffusive and reacting domains; and expansion of the numerical solver's boundary condition capabilities to include complex systems of nonlinear reactions at domain surfaces.

Further establishing Sandia's capabilities for biological cell modeling, these projects are already receiving funding. The cardiac cell model is of particular interest to the University of Maryland Cardiology Department, and hence contractual negotiations for direct support of the cell modeling effort at Sandia is underway and will initiate in fiscal year 2003. The P-20 Center Grant from NIH also supports the neuron terminus and endoplasmic reticulum projects, and will, contingent upon successful publication of results, probably result in the more significant funding available in the P-50 Center Grant.

References

- [1] H.L. Atwood, Milton P. Charlton, and C.S. Thompson. Neuromuscular Transmission in Crustaceans is Enhanced by a Sodium Ionophore, Monensin, and by Prolonged Stimulation. *Journal of Physiology*, 335:179–195, 1983.
- [2] L.S. Carl, K. Felix, A.H. Caswell, N.R. Brandt, Jr. W.J. Ball, P.L. Vaghy, G. Meissner, and D.G. Fe-

- gusun. Immunolocalization of sarcolemmal dihydropyridine receptor and sarcoplasmic reticular triadin and ryanodine receptor in rabbit ventricle and atrium. *J. Cell Biol.*, 129:673–682, 1995.
- [3] H. Cheng, , M.R. Lederer, W.J. Lederer, and M.B. Cannell. Calcium sparks and $[Ca^{2+}]_i$ waves in cardiac myocytes. *Am. J. Physiol. Cell Physiology*, 270:C148–C159, 1996.
- [4] H. Cheng, W.J. Lederer, and M.B. Cannell. Calcium sparks: elementary events underlying excitation-contraction coupling in heart muscle. *Science*, 262:740–744, 1993.
- [5] S.C. Eisenstat and H.F. Walker. Globally convergent inexact Newton methods. *SIAM J. Optimization*, 4:393–422, 1994.
- [6] D.K. Gartling. NACHOS II: A Finite Element Computer Program for Incompressible Flow Problems. Part 1 Theoretical Background. *Sandia National Laboratories Technical Report*, SAND86:1816, 1986.
- [7] P.M. Gresho, R.L. Lee, and R.L. Sani. The time dependent solution of the incompressible Navier-Stokes equations in two and three dimensions. *Recent Advances in Numerical Methods in Fluids*, 1:22681, 1980.
- [8] Donald W. Hilgemann. Numerical Approximation of Sodium-Calcium Exchange. *Progress in biophysics and molecular biology*, 51:1–45, 1988.
- [9] S. A. Hutchinson, L. Prevost, J. N. Shadid, C. Tong, and R. S. Tuminaro. Aztec Users Guide Version 2.0. *Sandia National Laboratories Technical Report*, SAND99:8801, 1999.
- [10] Leighton T. Izu, C.W. Balke, and W. Gil Wier. Evolution of Cardiac Calcium Waves from Stochastic Calcium Sparks. *Biophysical Journal*, 80:103–120, 2001.
- [11] Leighton T. Izu, Joseph R. H. Mauban, C.W. Balke, and W. Gil Wier. Large Currents Generate Cardiac Ca^{2+} Sparks. *Biophysical Journal*, 80:88–102, 2001.
- [12] Magdalena Juhaszova, Paul Church, Mordecai P. Blaustein, and Elis F. Stanley. Location of Calcium Transporters at Presynaptic Terminals. *European Journal of Neuroscience*, 12:839–846, 2000.
- [13] Shawn A. Means. *Impact of Sodium on Intracellular Calcium and its Implications in Neurotransmitter Release*. University of New Mexico Master’s Thesis, Albuquerque, New Mexico, 2001.
- [14] Rosel M. Mulkey and Robert S. Zucker. Posttetanic Potentiation at the Crayfish Neuromuscular Junction is Dependent on Both Intracellular Calcium and Sodium Ion Accumulation. *Journal of Neuroscience*, 12(11):4327–4336, 1992.
- [15] J.N. Shadid, S.A. Hutchinson, G.L. Hennigan, H.K. Moffat, K.D. Devine, and A.G. Salinger. Efficient Parallel Computation of Unstructured Finite Element Reacting Flow Solutions. *Parallel Computing*, 23:1307–1325, 1997.
- [16] J.N. Shadid and R.S. Tuminaro. Comparison of Preconditioned Nonsymmetric Krylov Methods on a Large-Scale MIMD Machine. *SIAM J. Sci. Comput.*, 15(2):440–459, 1994.
- [17] R.S. Tuminaro, J.N. Shadid, and S.A. Hutchinson. Parallel Sparse Matrix-Vector Multiply Software for Matrices with Data Locality. *Concurrency: Practice and Experience*, 10(3):229–247, 1998.

7 Development of Computational Tools

Applying molecular theory to steady-state diffusing systems

Laura J. Douglas Frink, Aidan Thompson, Andrew G. Salinger

Abstract

Predicting the properties of nonequilibrium systems from molecular simulations is a growing area of interest. One important class of problems involves steady state diffusion. To study these cases, a grand canonical molecular dynamics approach has been developed by Heffelfinger and van Swol [J. Chem. Phys., **101**, 5274 (1994)]. With this method, the flux of particles, the chemical potential gradients, and density gradients can all be measured in the simulation. In this paper, we present a complementary approach that couples a nonlocal density functional theory (DFT) with a transport equation describing steady-state flux of the particles. We compare transport-DFT predictions to GCMD results for a variety of ideal (color diffusion), and nonideal (uphill diffusion and convective transport) systems. In all cases excellent agreement between transport-DFT and GCMD calculations is obtained with diffusion coefficients that are invariant with respect to density and external fields.

Introduction

Molecular scale diffusion plays an important role in a wide variety of systems including polymer degradation, catalysis, membrane separations, and ion transport through biological membranes. In all of these cases, understanding diffusive processes on a molecular scale will provide the ability to engineer these systems as desired.

The primary computational approaches that have been applied to molecular diffusion are molecular dynamics (MD) simulation[1, 3, 4, 5, 2] and transition state theory (TST)[6, 7]. TST has been most often applied to rare event diffusion where the diffusing species is dilute, and the potential energy barriers between different states are high. A few recent efforts are focusing on the calculation of diffusive free energy barriers in the presence of a solution or multiple diffusing particles[8]. MD approaches include both linear response theory as coupled with equilibrium MD calculations[1, 2], and non-equilibrium molecular dynamics (NEMD) methods[9]. MD has been applied to a wide range of diffusion problems including diffusion in zeolites[10, 11], amorphous membranes[4, 12], nanoporous carbon materials[13], and polymers[14, 15].

The particular NEMD method we have applied is grand canonical molecular dynamics (GCMD)[3, 4, 5, 16]. In GCMD, an overall chemical potential driving force is maintained and particle flux is measured. A transport law with some assumed functional form is then used to estimate diffusion coefficients. Typically Fick's law[3, 5, 11, 16, 17],

$$J_{\alpha} = -D_{\alpha}\nabla\rho_{\alpha}, \quad (121)$$

is applied where J is the flux of species α , D is the diffusion coefficient, and ρ is a number density.

While GCMD provides an exact computer experiment for studying diffusion, the calculations (as with most molecular simulations) are quite expensive to perform. It is therefore desirable to develop complementary approaches for steady state non-equilibrium systems that are based on molecular theories. In this paper we

present the results of coupling a nonlocal density functional theory (DFT) to a transport equation, and solving the system of equations under steady state conditions.

In section II, the transport-DFT approach is presented, in section III, DFT and GCMD calculations are compared for a variety of model systems, and in section IV a summary of our conclusions is presented. In general, good agreement is found between transport-DFT and GCMD approaches; however, transport-DFT calculations are $O(10^5)$ times faster than the GCMD calculations. Therefore, this new transport-DFT approach may provide a new route for studying molecular steady state transport.

Model and Theory

For the GCMD calculations presented here, the underlying molecular model describing fluid-fluid interactions is the Weeks-Chandler-Anderson (WCA) fluid which is based on a cut and shifted 12-6 Lennard-Jones (LJ) potential[18], $u(r) = u_{LJ}(r) - u_{LJ}(r_c)$, where

$$u_{LJ}(r) = 4\epsilon \left[\left(\frac{\sigma}{r} \right)^{12} - \left(\frac{\sigma}{r} \right)^6 \right], \quad (122)$$

σ is the diameter of the solvent molecule, ϵ is the energy parameter controlling the strength of fluid-fluid interactions, and r_c is the cutoff distance for the potential. For a WCA fluid, the LJ potential is reduced to only the repulsive part of the LJ potential since the cut-off is taken at the potential minimum, $r_c/\sigma \approx 1.122$.

DFT approaches are generally based on the assumption of chemical equilibrium, and a free energy functional, Ω is minimized with respect to the density distribution, $\rho(\mathbf{r})$ at constant chemical potential, μ . We relax this condition, and assume instead that steady state is equivalent to a condition of *local* equilibrium where the chemical potential varies spatially. In this case, the energy minimization we perform is

$$\left(\frac{\delta \Omega}{\delta \rho(\mathbf{r})} \right)_{\mu(\mathbf{r}), T} = 0. \quad (123)$$

Fluid density distributions in the cases considered here are inhomogeneous spatially due to nonuniform boundary conditions. In the cases discussed in section IIID, external fields lead to more pronounced inhomogeneities in the fluid. Thus, the grand canonical free energy is

$$\Omega = F_{id} + F_{hs} - \sum_{\alpha} \int d\mathbf{r} \rho_{\alpha}(\mathbf{r}) [\mu_{\alpha}(\mathbf{r}) - V_{\alpha}^{ext}(\mathbf{r})]. \quad (124)$$

where the sum is taken over all the species in the system, V^{ext} is the external field (zero in all cases except section IIID), the ideal and excess hard sphere free energy contributions are

$$F_{id} = kT \sum_{\alpha} \int d\mathbf{r} \rho_{\alpha}(\mathbf{r}) \{ \ln (\Lambda^3 \rho_{\alpha}(\mathbf{r})) - 1 \}, \quad (125)$$

and

$$F_{hs} = \int d\mathbf{r} \Phi \{ \bar{\rho}_{\gamma}(\mathbf{r}) \} \quad (126)$$

respectively, Λ is the de Broglie wavelength, Φ is the free energy density of the hard sphere fluid, and $\bar{\rho}_{\gamma}$ are nonlocal densities. In calculating the hard sphere contribution, we have applied the nonlocal formulation of Rosenfeld that is detailed in the appendix[19].

The functional minimization of Eq.123 produces the Euler-Lagrange equations

$$\mu_\alpha(\mathbf{r}) = kT \ln \rho_\alpha(\mathbf{r}) + \int d\mathbf{r}' \sum_\gamma \frac{\partial \Phi}{\partial \bar{\rho}_\gamma} w^{(\gamma)}(|\mathbf{r} - \mathbf{r}'|) + V_\alpha^{ext} \quad (127)$$

which can be solved at each point in the domain for the steady state density distributions, $\rho_\alpha(\mathbf{r})$ for a given $\mu_\alpha(\mathbf{r})$.

We are interested in steady state diffusion where $\mu(\mathbf{r})$ is not known a priori, but rather satisfies a known diffusion equation. Steady state is defined by a time independent mass balance consisting only of the divergence-free condition on the total flux,

$$\nabla \cdot J = 0. \quad (128)$$

The total flux may be attributed to a variety of physical effects as is discussed in detail by Mason and Lonsdale[20] in the context of membrane transport. For diffusion in binary solutions in the absence of both a membrane and pressure gradients, we can write a diffusion model using the Stefan-Maxwell form[21]

$$\frac{\rho_2}{\rho D_{12}}(\mathbf{u}_1 - \mathbf{u}_2) = -\frac{1}{RT} \nabla \mu_1 \quad (129)$$

and

$$\frac{\rho_1}{\rho D_{21}}(\mathbf{u}_2 - \mathbf{u}_1) = -\frac{1}{RT} \nabla \mu_2 \quad (130)$$

where \mathbf{u} is the particle velocity, and $\rho = \rho_1 + \rho_2$. It follows from either the Gibbs-Duhem relation and Onsager's reciprocal relation that $D_{12} = D_{21} = D$. In solving the transport-DFT problem, we additionally assume that the diffusion coefficient is independent of concentration. This assumption is exact in the case of pure color diffusion in the absence of a field. We have found that it also may be a good approximation for cases of uphill diffusion (non-ideal ternary mixtures) and diffusion in the presence of an external field. It is well known that the alternative generalized Fickian diffusion coefficients are much more sensitive to changes in concentration, and can even become negative in the case of uphill diffusion[22, 23].

Any center of mass motion in the system, J_{CM} is defined by

$$J_{CM} = J_1 + J_2 = \rho_1 \mathbf{u}_1 + \rho_2 \mathbf{u}_2 \quad (131)$$

and combining Eqs.131 with 129 or 130 it is straightforward to show that the flux may be defined as

$$J_\alpha = -D \rho_\alpha \nabla \mu_\alpha + \bar{v} \rho_\alpha \quad (132)$$

where \bar{v} is the mean velocity per particle in the fluid. Note that the diffusive contribution to the flux is not Fick's law (Eq.121).

The chemical potential of a given species can be written as a sum of ideal, excess hard sphere, and external field contributions,

$$\mu = \mu_{id} + \mu_{hs} + V^{ext}, \quad (133)$$

as shown in Eq.127. If $V^{ext} = 0$, and there are no nonideal contributions to the flux, (e.g. $\mu_{hs} = 0$ or $\nabla \mu_{hs} = 0$), then only the ideal contribution ($\nabla \mu_{id} = kT \nabla \rho / \rho$) is present, and Fick's law

$$J_\alpha = -D \nabla \rho_\alpha, \quad (134)$$

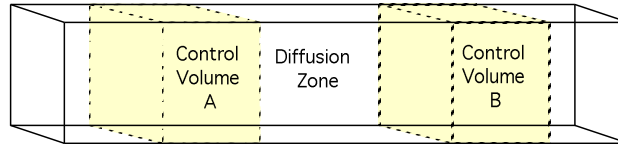


Figure 62. A sketch of the computational domain for GCMD simulations. Periodic boundary conditions are applied in all dimensions, and chemical potential control is maintained in the two control volumes in the shaded regions.

is recovered.

The two contributions to the flux in Eq.132 are diffusive and convective fluxes respectively. The convective term is written in terms of a mean velocity implying that we are considering cases of plug flow where the velocity field is homogeneous. For more complex flows, velocity distributions must be solved simultaneously with the transport-DFT described here. Such calculations have been previously performed (without diffusive transport) for cases of Couette flow and Poiseuille flow[24].

In the following sections we test the transport-DFT approach outlined above by explicit comparison with GCMD simulations in a variety of situations. We discuss the magnitude and type of errors that can develop when Fick's law (Eq.134) is used to analyze data from GCMD simulations. We also show that the transport-DFT approach can be applied in cases where pressure gradients and external fields are present.

Results

In this section, we will compare GCMD calculations to the predictions of the steady-state DFT described above. We begin with a brief description of the GCMD method.

In GCMD calculations, the simulation volume is split into two control volumes and two diffusion zones as sketched in Fig.62. One of the diffusion zones is split between the ends of the box (in the x -direction) where there are periodic boundary conditions. The total system size for calculations presented here is $60\sigma \times 10\sigma \times 10\sigma$.

The GCMD calculations were done on the massively parallel ASCI-Red Tflops computer (composed of 200 MHz Pentium Processors) at Sandia National Laboratories using the parallel code LADERA. The LADERA code is parallelized using a spatial decomposition, and has been discussed elsewhere[14, 25]. All the calculations presented here were performed on 48 processors with each processor owning a cube that is 5σ on edge (ie. the processors have a spatial decomposition of $12 \times 2 \times 2$). Every processor that owns pieces of the control volumes split their volumes into eight sub-domains. One insertion/deletion cycle involves an attempted insertion or deletion in each of the eight subdomains on all of the processors. Hence for the chosen geometry and processor array, one grand-canonical (GC) cycle is composed of 128 insertions/deletions total[26].

The geometry in Fig.62 allows for variations in the equilibrium properties (e.g. $\langle \rho \rangle$) only in the x -direction. Therefore the DFT calculations are reduced to solving for density and chemical potential profiles in

only one dimension (1D). Our numerical solution (discussed elsewhere in the context of equilibrium 2D and 3D problems[27, 28]) combines a collocation approach to the Euler-Lagrange equations with a Galerkin finite element approach for the transport equation. Linear basis functions were used for the discretization, and a fully coupled Newton method was used to solve for the steady-state solution. The DFT calculations were run in serial on a 433 MHz DEC Alpha workstation.

A: Color Counter-Diffusion

We begin with color counter-diffusion where there are two species with identical properties. Each particle is labeled (or colored) by its assigned species number (1,2). To set up equal counter-diffusion, we set $\mu_1^L = \mu_2^R$ and $\mu_2^L = \mu_1^R$ where the superscripts R and L refer to the right and left control volumes respectively.

The case of color diffusion is unique in that Eq.134 and Eq.132 are identical regardless of the fluid density. This result stems from the fact that $\bar{v} = 0$ and the total density is constant everywhere in the simulation volume. As a result, $\nabla\mu_{hs} = 0$, and only the ideal term contributes to the flux.

We considered two cases of color diffusion. Both are WCA fluids with a temperature of $kT/\epsilon = 1$, but the two cases have different total densities. The chemical potential set points in the control volumes for the first case were $\beta\mu_1^L = 1.54$ and $\beta\mu_2^L = 2.34$, while they were $\beta\mu_1^L = 3.0$ and $\beta\mu_2 = 6.0$ for the second case ($\beta = 1/kT$ where k is the Boltzmann constant).

The GCMD simulations were composed of 100,000 MD time-steps for equilibration and 400,000 MD time-steps for accumulating averages. The time increment for the integration of Newton's equations of motion was $\Delta t = 0.01\sigma(m/\epsilon)^{1/2}$, and 10 GC cycles were attempted at every 10th MD time-step. The total run time on the parallel computer was approximately 3 hours. For comparison, the DFT results converged in less than 10 Newton iterations in about 5 seconds on a workstation.

Figures 63 and 64 compare GCMD and transport-DFT density and chemical potential profiles for the two cases described above. The boundary conditions on the DFT calculations were chosen to match the densities observed in control volumes of the GCMD calculations ($-15 < x/\sigma < -10$ and $10 < x/\sigma < 15$). The chemical potentials from DFT calculations do not match GCMD set points, but rather are shifted down in both cases. This shift arises because the DFT assumes the WCA fluid can be treated as a hard sphere fluid, and because the equation of state (Percus-Yevik) is not exact. Considering the diffusion zone in each case, it is apparent that DFT predictions of the density profiles and chemical potential *gradient* profiles reproduce GCMD simulations very well.

The success of the transport-DFT in reproducing $\rho(x)$ and $\nabla(\beta\mu(x))$ is significant because it demonstrates that the DFT and GCMD approaches will yield consistent flux predictions. Thus if one wants to predict the variation of the flux through a range of parameters, it is possible to perform only a few GCMD calculations to establish the bounds for the diffusion coefficient. DFT calculations may then be performed to determine the flux through a wider range of system parameters.

To illustrate the equivalence of Eq.132 and Eq.134 for color counter diffusion, Fig.65 compares GCMD $\rho d(\beta\mu)/dx$ and $d\rho/dx$ profiles to the DFT prediction of $\rho d(\beta\mu)/dx$. The GCMD estimates of $d\rho/dx$ were found both from an overall fit to the density profile, and by applying central finite differences (CFD) performed on

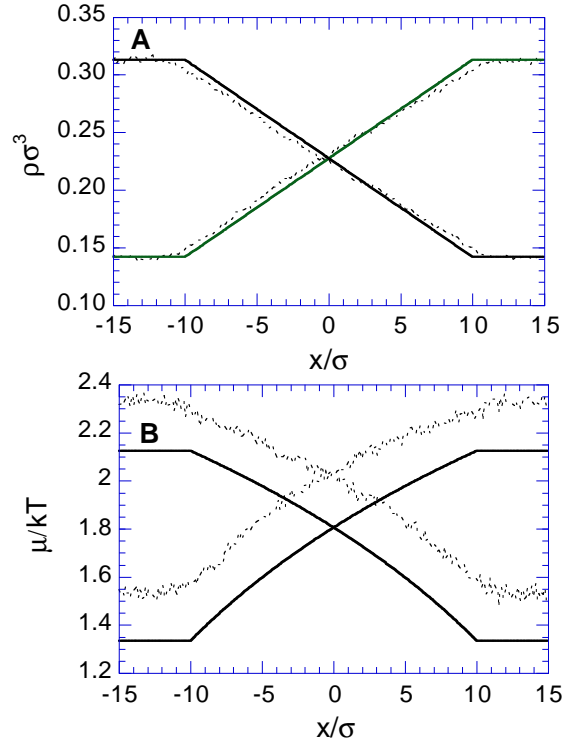


Figure 63. Density ($\rho\sigma^3$) profiles (A) and chemical potential ($\beta\mu$) profiles (B) in a diffusion zone. The total density is $\rho_{tot}\sigma^3 \approx 0.45$. Solid lines are transport-DFT results; dotted lines are GCMD results.

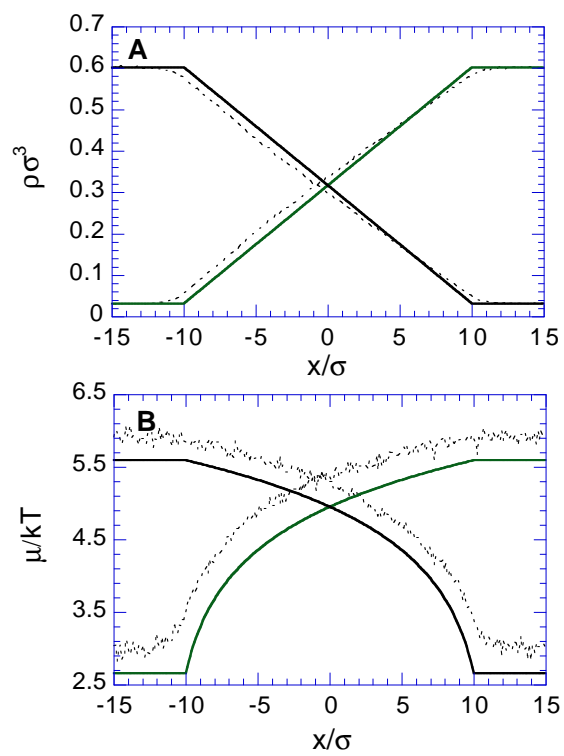


Figure 64. Same as Fig.2 except that the total density is $\rho_{tot}\sigma^3 \approx 0.64$

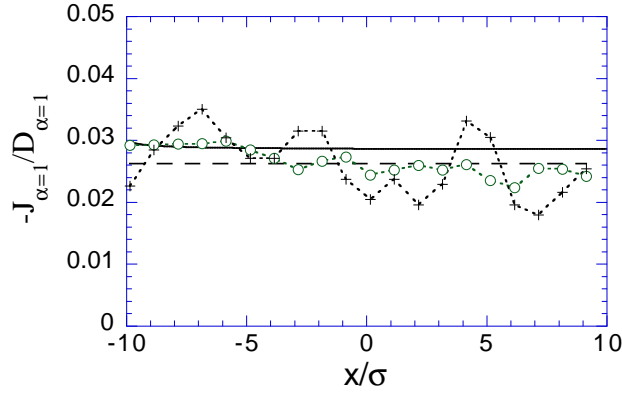


Figure 65. The flux divided by the diffusion coefficient in the central diffusion zone of Fig.3. The various curves are: DFT prediction of $\rho d(\beta\mu)/dx$ (solid line), GCMD calculation of $d\rho/dx$ based overall slope of density profiles (dashed line), GCMD CFD calculation of $\rho d(\beta\mu)/dx$ (+), GCMD CFD calculation of $d\rho/dx$ (\circ).

1σ increments of the $\rho(x)$ data. The GCMD estimates of $\rho d(\beta\mu)/dx$ are based on CFDs performed on 1σ increments of *smoothed* chemical potential profiles.

All the estimates of J/D in Fig.65 are consistent with one another, but the GCMD/CFD estimations of $\rho d(\beta\mu)/dx$ and $d\rho/dx$ have the largest uncertainties due to statistical noise in the data. Therefore, the highest precision GCMD estimates of diffusion coefficient come from taking the overall slope of the density profile, and applying Fick's law. However, as we will show in the following sections there are many cases where either the nonideal contributions to the chemical potential will contribute to the flux (section IIIB) or where external fields will cause the density profile to have a complex structure (section IIID). These cases will make application of Fick's law difficult.

B: Uphill Diffusion

One case where Fickian diffusion is clearly incorrect may be found in studies of *uphill* diffusion. It has been observed in GCMD studies of ternary systems, that chemical potential and density gradients can have slopes with opposite sign[17]. In these cases, the measured particle flux always goes in the direction of decreasing chemical potential. So from a Fickian point of reference, the diffusion appears to be uphill. Several experimental observations of uphill diffusion have been reported as well[29, 30, 31].

In this section we consider application of the transport-DFT approach to non-ideal ternary systems. We assume that there is no center of mass motion in this system. We further assume that the transport law given in Eq.132 is valid for this ternary system. This formulation of the flux may not be optimal for the non-ideal ternary systems discussed here. However, for the purposes of this discussion we only seek to demonstrate that nonideal behaviors such as uphill diffusion can be found using the transport-DFT approach, and estimate how such nonidealities may affect estimates of the driving force.

Both the mixing rules for interaction diameters, σ_{ij} and our control volume densities were chosen based

Species	$d\rho/dx$	$\rho d(\beta\mu)/dx$	% difference
1	-0.0015	-0.0012	25%
2	-0.00044	0.00067	166%
3	0.0013	0.0021	38%

Table 8. A comparison of proposed driving forces for transport for each of the three species in the transport-DFT calculations of the ternary system detailed in Fig.5.

on previous GCMD studies of uphill diffusion[17]. More specifically the interaction diameters were, $\sigma_{ij} = \sigma_k$ where $k = \text{Min}(i, j)$. In the particular case we present here, the matrix of interaction diameters was

$$\begin{matrix} & \sigma_1 & \sigma_2 & \sigma_3 \\ \sigma_1 & \begin{pmatrix} 1.0 & 1.0 & 1.0 \end{pmatrix} \\ \sigma_2 & \begin{pmatrix} 1.0 & 1.3 & 1.3 \end{pmatrix} \\ \sigma_3 & \begin{pmatrix} 1.0 & 1.3 & 1.5 \end{pmatrix} \end{matrix} \cdot \quad (135)$$

Transport-DFT results in Fig.66 show similar behavior as was observed in GCMD simulations [17] where the slope of the density and chemical potential profiles of component 2 have opposite sign. This uphill diffusion result shows that the transport-DFT approach may be useful in analyzing transport in complex multicomponent mixtures as well as the simple binary systems of the previous section.

The nonidealities in these mixtures lead to nonzero contributions to the flux from $\nabla(\beta\mu_{hs})$. The result is that the density profiles are not linear. Thus, a local application of Fick's law would predict a spatially varying diffusion coefficient while a more global analysis based on the overall slope between the control volumes would not have the precision of the color counter diffusion case in Fig.4.

Table 8 details the difference between $\rho\nabla(\beta\mu)$ and the global approach to $\nabla\rho$ based on the results in Fig.66. The nonidealities in the system now contribute to a 20-40% difference between these two estimations of diffusive driving forces even for components 1 and 3 where downhill diffusion is observed.

C: Pressure Driven Diffusion

We now turn to cases where convective transport occurs simultaneously with diffusive transport, and we begin with pressure driven diffusion. Once again binary color mixtures are used for the calculations.

GCMD calculations were performed by setting the chemical potential of both species in the left control volume to $\beta\mu_1^L = \beta\mu_2^L = 3.0$ and the chemical potential of species 1 in the right control volume to $\beta\mu_1^R = 2.0$. The chemical potential of species 2 in the right control volume varied from $\beta\mu_2^R = 4$ (case A) to $\beta\mu_2^R = 3.5$ (case B), to $\beta\mu_2^R = 3$ (case C). In case A, the pressure in the right control volume is higher than the left; in case C, the pressure imbalance is reversed; and in case B, there is almost no pressure drop.

100,000 MD time-steps were performed for equilibration, and 600,000 MD time-steps were used for accumulating averages. The time increment for the integration of Newton's equations of motion was $\Delta t = 0.01$, and 20 GC cycles were attempted at every 5th MD time-step. The total run time per solution was approximately

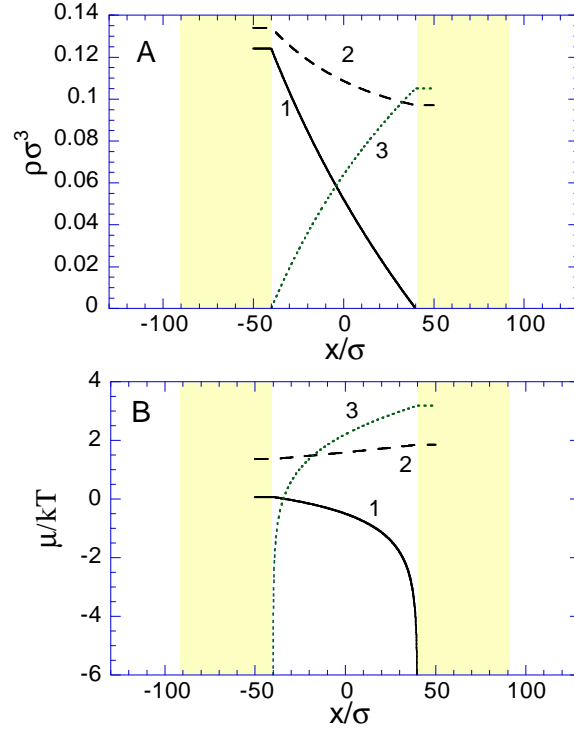


Figure 66. Density (A) and chemical potential (B) profiles for a case of uphill diffusion. The curves are labeled by the component number, and the x-axis is scaled for ease of comparison with Figs. 2 and 3 of Thompson *et.al*[21]. The grey regions indicate where the control volumes were located in GCMD calculations. In locating this particular case, σ_2 and σ_3 were varied in the range $\sigma_{2,3}/\sigma_1 = 1.0 - 1.6$. For all values of σ_2 , a transition in component 2 from downhill diffusion to uphill diffusion occurred at $\sigma_3/\sigma_1 \approx 1.45$.

14 hours.

Equilibration of GCMD profiles is more difficult in these cases than the previous color diffusion example due to the particle acceleration that accompanies the pressure gradient. Steady-state is achieved as a result of the effective friction in the control volumes that arises from the insertions and deletions of particles. These particle insertions are accompanied by velocity randomization that provides the needed friction.

Figures 67 and 68 show the density and chemical potential profiles from GCMD and transport-DFT calculations where both diffusive and convective terms are included in DFT calculations. For comparison, DFT calculations without the convective flux term are also included in the figures. Inclusion of the center of mass motion (or convective terms) is crucial to reproducing GCMD results with the transport-DFT approach.

The small discontinuities in $\beta\mu(x)$ in the GCMD calculations, seen at $x/\sigma = 10$ in Fig.68A and $x/\sigma = -10$ in Fig.68C show that the pressure drop, and therefore the acceleration, occur almost instantaneously and not over the whole domain. This feature justifies the use of a constant velocity convective flux, and is supported by the excellent agreement with transport-DFT calculations.

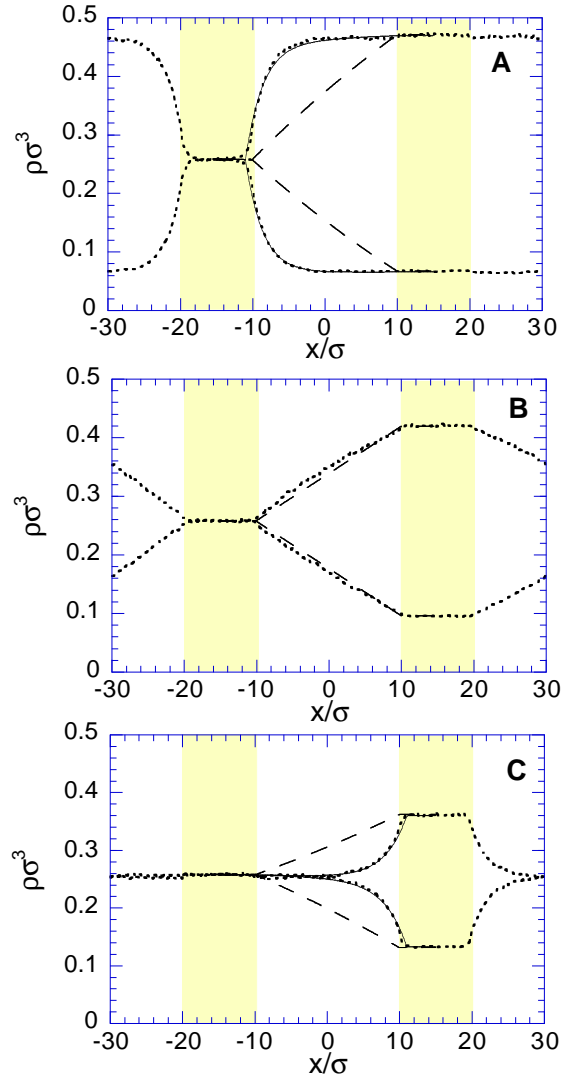


Figure 67. Density profiles for both GCMD (dotted lines) and steady state DFT (solid and dashed lines) calculations. DFT results in dashed lines include only the diffusive flux while solid lines include the convective term as well. The three cases have $\beta\mu^R = 4.0$ (A), $\beta\mu^R = 3.5$, and $\beta\mu^R = 3.0$ (C). In all cases, the densities in the left control volume for both species are $\rho_i\sigma^3 = 0.258 \pm 0.001$ ($\rho\sigma^3 = 0.516$). The densities on the right hand side vary from $\rho_1\sigma^3 = 0.471$, $\rho_2\sigma^3 = 0.067$, and $\rho\sigma^3 = 0.538$ (A); to $\rho_1\sigma^3 = 0.419$, $\rho_2\sigma^3 = 0.096$, and $\rho\sigma^3 = 0.515$ (B); to $\rho_1\sigma^3 = 0.362$, $\rho_2\sigma^3 = 0.131$, and $\rho\sigma^3 = 0.493$ (C).

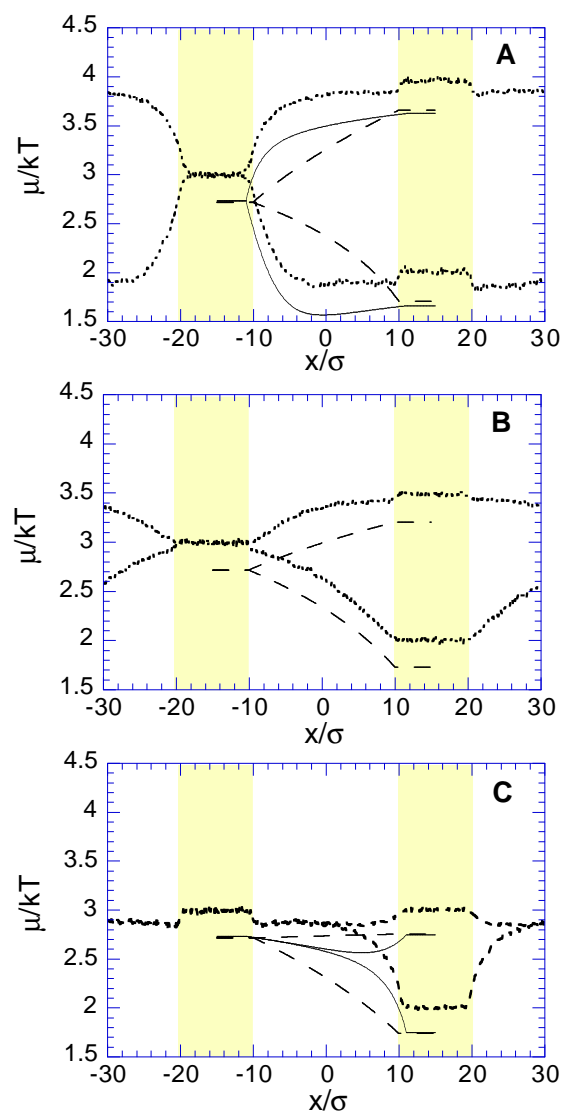


Figure 68. Chemical potential profiles corresponding to the density profiles results in Fig.6.

D: External Fields

Finally we consider transport of the binary tagged by color particles in the presence of external fields. This is a particularly important case since transport through any porous media involves an external field composed of the interactions of the fluid particles with the porous media. We consider an external field representative of a simple porous membrane with the form $V^{ext}(x) = v(|x|) - v(x_{cut})$ when $|x| > x_{min}$ and $V^{ext}(x) = v(x_{min}) - v(x_{cut})$ when $|x| \leq x_{min}$ where

$$v(x)/kT = \epsilon_{wf} \left[\frac{2}{15} \left(\frac{\sigma}{x} \right)^9 - \left(\frac{\sigma}{x} \right)^3 \right], \quad (136)$$

$x_{cut} = 2.5\sigma$, and $x_{min} = (2/5)^{1/6}\sigma$ is the distance where the potential is a minimum.

We consider two cases. In the first, $\beta\epsilon_1^{wf} = \beta\epsilon_2^{wf} = 1.0$ so both species (1,2) are equally attracted to a potential energy well at $x = 0$. In the second case, $\beta\epsilon_1^{wf} = 1.0$ and $\beta\epsilon_2^{wf} = -1.0$. In this case species 2 must overcome a potential energy barrier that inhibits its transport. In the first case, the symmetric nature of the problem leads once again to zero net motion of the center of mass of the system, while in the second case, species α can be expected to dominate the transport creating a net center of mass motion.

Figure 69 shows density and chemical potential profiles respectively for the case where both species experience the same external field. Only one species is shown in 69A for clarity of presentation. As expected, adsorption is observed in the center region due to the external field, and density oscillations are due to packing constraints on the fluid. Clearly application of Fick's law in the vicinity of these density oscillations cannot yield sensible results.

The chemical potential profiles in Fig.69B appear to be very similar to those in Fig.1B. However, transport-DFT calculations were based on Eq.132 so the density oscillations in Fig.69A must be balanced by oscillations in $\nabla(\beta\mu)$. In fact, when $\nabla(\beta\mu(x))$ is plotted (see Fig.70) the oscillations are apparent. The statistical noise on the GCMD calculations will likely prevent accurate computation of $\nabla(\beta\mu)$ in many cases where external fields are present. Thus, in some cases it may be useful to combine the transport-DFT and GCMD approaches for an estimation of diffusion coefficient. The DFT provides an estimate of the driving force while the GCMD provides a measure of the flux. Together a prediction of diffusion coefficient can be obtained.

When the external field is attractive to one species and repulsive to the other, both diffusive and convective transport are important. In transport-DFT calculations, the ratio, \bar{v}/D was adjusted for the best match of GCMD and DFT calculations. Fig.71 shows density and chemical potential profiles for our example of this situation. The density of the one adsorbed species in the center region is now significantly higher than it was even in Fig.69A. The other species shows significant exclusion from the central region. Again, there is good agreement between GCMD and transport-DFT calculations of both $\rho(x)$ and $\nabla(\beta\mu(x))$.

The excellent agreement between transport-DFT and GCMD calculations for the cases in this section are particularly remarkable as transport-DFT calculations are based on spatially invariant diffusion coefficients. Calculations of diffusion through pores have shown that surface effects can alter (usually decrease) the magnitude of the diffusion coefficient[32]. Clearly, the application of the transport-DFT approach to porous systems will require a more thorough investigation.

E: Diffusion Coefficients

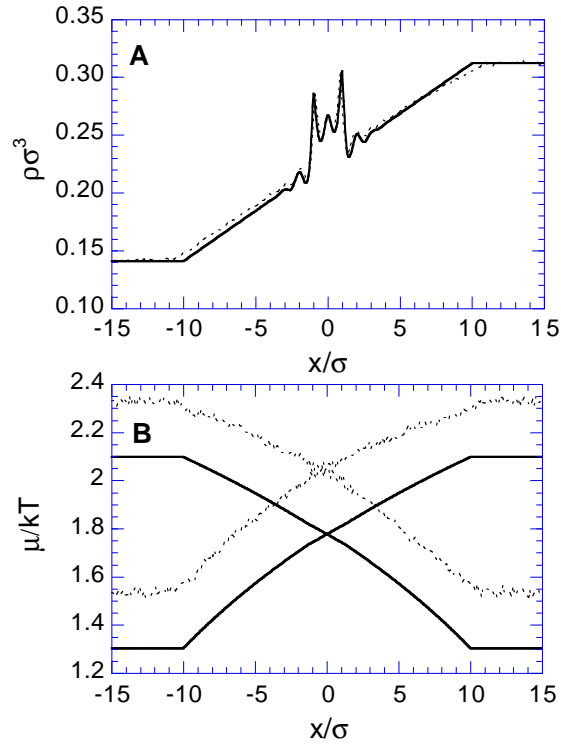


Figure 69. Density ($\rho\sigma^3$) profiles (A) and chemical potential ($\beta\mu$) profiles (B) in a diffusion zone where there is an external field centered at $x = 0$ that is attractive to both species. Solid lines are transport-DFT results, dotted lines are the results of GCMC simulations.

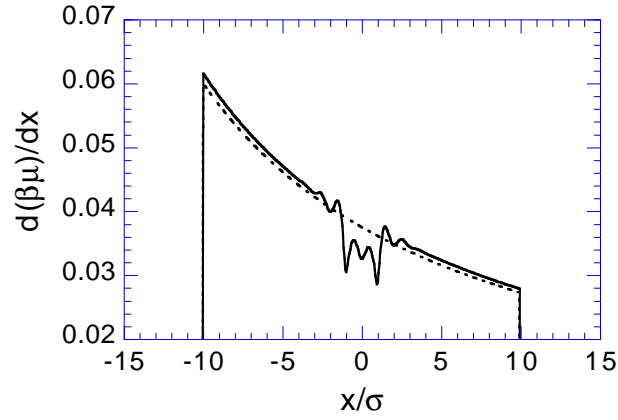


Figure 70. Chemical potential gradient, $\nabla(\beta\mu)$ profiles corresponding to transport-DFT profiles in Fig.8B (solid lines) and Fig.2B (dashed lines).

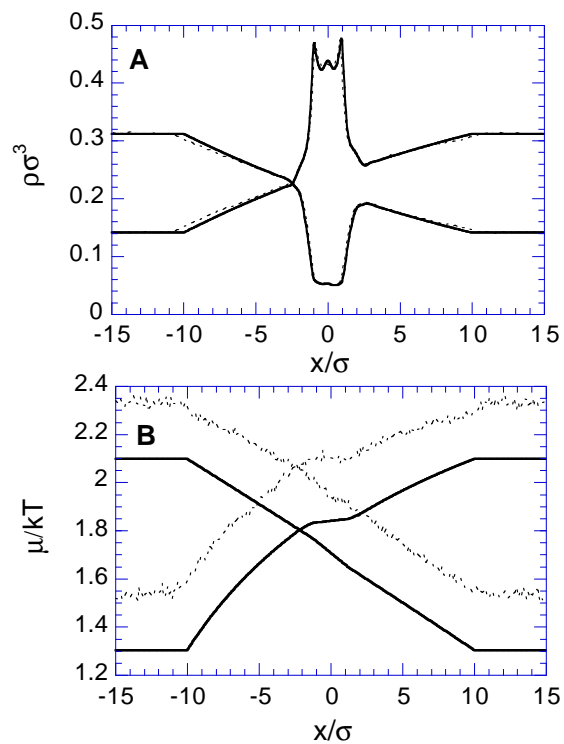


Figure 71. Density ($\rho\sigma^3$) profiles (A) and chemical potential ($\beta\mu$) profiles (B) in a diffusion zone where there is an external field centered at $x = 0$ that is attractive to only one species and repulsive to the other. Solid lines are transport-DFT results, dotted lines are results of GCMD simulations.

Figure	J_1	J_2	$D_{(1)}$	$D_{(2)}$
2	-0.0024	0.0025	0.28	0.29
8	-0.0026	0.0024	0.30	0.28
10	-0.0054	-0.00016	0.30	0.27

Table 9. A comparison of diffusion coefficients for several of the cases investigated in this paper (as indicated by the figure number). The parameters are all given in reduced Lennard-Jones units with $J = J\sigma^3(m/\epsilon)^{1/2}$ and $D = D\sigma^{-1}(m/\epsilon)^{1/2}$

Finally, we present calculations of diffusion coefficients that combine flux measurements from GCMD simulations with driving forces from transport-DFT. Results for the cases that were presented in Figs.2, 8, and 10 are shown in Table II. These cases all have the same overall chemical potential driving forces, but the fluid particles experience very different external fields in the diffusion zone. The predicted diffusion coefficient is found to be constant within the errors associated with flux measurements among all the cases.

Conclusions

To summarize, we have presented a novel approach to studying molecular steady-state transport. This approach couples a molecular theory, DFT, with a diffusive (and in some cases convective) transport law in order to predict density and chemical potential gradients in nonequilibrium steady-state systems for several simple mixtures.

The results of transport-DFT calculations were compared explicitly with grand canonical molecular dynamics simulations(GCMD) for a variety of systems. We found that the two methods were in agreement for predictions of both chemical potential and density profiles given the assumption of a spatially invariant diffusion coefficient provided that the center of mass motion of the system was known. Thus given a diffusion coefficient, both methods will yield the same flux. In order to compute the flux as a function of system parameters efficiently, only a few GCMD calculations are needed to determine the bounds on diffusion coefficients. The transport-DFT approach may then be used for exploring a complete range of the parameters of interest.

The agreement we found was based on the application of a local transport law. The diffusion contribution to the transport was $J = -D\rho(x)\nabla(\beta\mu(x))$. Fick's law, $J = -D\nabla\rho(x)$ was demonstrated to be incorrect locally for cases where an external field is present and globally for a case of nonideal *uphill* diffusion.

Given the efficiency of transport-DFT calculations, this new transport-DFT approach may provide a new route for studying molecular steady state transport and its effects on complex surface phenomena such as capillary condensation and wetting.

appendix

In the nonlocal DFT of Rosenfeld[19], the hard sphere free energy density, Φ , was derived from scaled particle theory in terms of the nonlocal densities, $\bar{\rho}_\gamma$. These nonlocal densities are

$$\bar{\rho}_\gamma(\mathbf{r}) = \sum_\alpha \int d\mathbf{r}' \rho_\alpha(\mathbf{r}') w_\alpha^{(\gamma)}(|\mathbf{r} - \mathbf{r}'|). \quad (137)$$

where the summation is taken over the species, α . The weight functions, $w_\alpha^{(\gamma)}$, are

$$\begin{aligned} w_\alpha^{(3)}(r) &= \Theta(r - R_\alpha) \\ w_\alpha^{(2)}(r) &= 4\pi R_\alpha w_\alpha^{(1)}(r) = 4\pi R_\alpha^2 w_\alpha^{(0)}(r) = \delta(r - R_\alpha) \\ w_\alpha^{(V2)}(r) &= 4\pi R_\alpha w_\alpha^{(V1)}(r) = (\mathbf{r}/r)\delta(r - R_\alpha) \end{aligned} \quad (138)$$

where the \mathbf{r} indicates a vector. These weight functions are based on the geometry of the fluid particles as Θ is the step function, δ is the Dirac delta function, and R is the radius of a particle. Thus the integrals over weight functions are related to the volume, surface area, and radius of the particle. Note that w^{V1} and w^{V2} are vectors, and so the hard sphere free energy density is a sum of scalar and vector contributions, $\Phi = \Phi_s + \Phi_v$, with

$$\begin{aligned} \Phi_s &= -\bar{\rho}_0 \ln(1 - \bar{\rho}_3) + \frac{\bar{\rho}_1 \bar{\rho}_2}{1 - \bar{\rho}_3} + \frac{1}{24\pi} \frac{\bar{\rho}_2^3}{(1 - \bar{\rho}_3)^2} \\ \Phi_v &= -\frac{\bar{\rho}_{V1} \cdot \bar{\rho}_{V2}}{1 - \bar{\rho}_3} - \frac{1}{8\pi} \frac{\bar{\rho}_2(\bar{\rho}_{V2} \cdot \bar{\rho}_{V2})}{(1 - \bar{\rho}_3)^2}. \end{aligned} \quad (139)$$

References

- [1] E.J. Maginn, A.T. Bell, and D.N. Theodorou, J. Phys. Chem., **97**, 4173 (1993).
- [2] D. Nicholson, J. Membrane Sci., **129**, 209 (1997).
- [3] G.S. Heffelfinger and F. van Swol, J. Chem. Phys., **101**, 5274 (1994).
- [4] J.M.D. MacElroy, J. Chem. Phys., **101**, 5274 (1994).
- [5] D. Nicholson and R. Cracknell, Langmuir, **12**, 4050 (1996).
- [6] R.L. June, A.T. Bell, and D.N. Theodorou, J. Phys. Chem., **95**, 8866 (1991).
- [7] A.A. Gusev and U.W. Suter, J. Chem. Phys., **99**, 2228 (1993).
- [8] C. Tunca and D.M. Ford, J.Chem.Phys., in press.
- [9] P.T. Cummings and D.J. Evans, Ind. Eng. Chem. Res., **31**, 1237 (1992).
- [10] J.M.D. MacElroy and S.-H. Suh, in *Progress in Zeolite and Microporous Materials*, ed. H. Chon, S.-K. Ihm, and Y.S. Uh, Elsevier (1997).
- [11] S. Fritzsche, R. Haberlandt, and J. Kärger, Zeitschrift für Physikalische Chemie, **189** 211 (1995).
- [12] S.-J. Marrink and H.J.C. Berendsen, J. Phys. Chem., **98**, 4155 (1994).

- [13] L. Xu, M.G. Sedigh, M. Sahimi, and T.T. Tsotsis, Phys. Rev. Lett., **80**, 3511 (1998).
- [14] D.M. Ford and G.S. Heffelfinger, Mol. Phys., **94**, 673 (1998).
- [15] S. Sunderrajan, C.K. Hall, and B.D. Freeman, J.Chem.Phys., **105**, 1621 (1996).
- [16] W. Dong and H.Luo, Phys. Rev. E, **52** 801 (1995).
- [17] A.P. Thompson, D.M. Ford, and G.S. Heffelfinger, J. Chem. Phys., **109**, 6406 (1998).
- [18] J.D. Weeks, D. Chandler, and H.C. Anderson, J. Chem. Phys., **54**, 5237, (1971).
- [19] Y. Rosenfeld, Phys. Rev. Lett., **63**, 980 (1989).
- [20] E.A. Mason and H.K. Lonsdale, J. Membrane Science, **51**, 1 (1990).
- [21] E.A. Mason and L.A. Viehland, J.Chem.Phys., **68**, 3562 (1978).
- [22] R. Taylor and R. Krishna, *Multicomponent Mass Transfer*, Wiley, New York, 1993.
- [23] A.P. Thompson and G.S. Heffelfinger, J. Chem. Phys., **110**, 10693 (1998).
- [24] I. Bitsanis, T.K. Vanderlick, M. Tirrell, H.T. Davis, J. Chem. Phys., **89**, 3152 (1988).
- [25] G.S. Heffelfinger and D.M. Ford, Mol. Phys., **94**, 659 (1998).
- [26] G.S. Heffelfinger and M.E. Lewitt, J. Comp. Chem., **17**, 250 (1996).
- [27] L.J. Douglas Frink and A.G. Salinger, J.Chem.Phys., **110**, 5969 (1999).
- [28] L.J. Douglas Frink and A.G. Salinger, submitted to J. Comp. Phys. (1999).
- [29] J.B. Duncan and H.L. Toor, A.I.Ch.E. J., **8** 38 (1962).
- [30] S. Tsuchiya and M. Senō, J. Phys. Chem., **98**, 13680 (1994).
- [31] V. Vitagliano, R. Sartorio, S. Scala, and D. Spaduzzi, J. Solution Chem., **7**, 605 (1978).
- [32] M. Schoen, J.H. Cushman, D.J. Diestler, and C.L. Rhykerd, Jr., J. Chem. Phys., **88**, 1394 (1988).

Comparison of the Amber, Charmm, Compass, Gromos, OPLS-aa, and TraPPE-UA force fields for the prediction of liquid densities and vapor-liquid coexistence for small organics

Marcus G. Martin ³

Abstract

Configurational-bias Monte Carlo simulations are performed to compute liquid densities and vapor-liquid coexistence curves for a series of small organic molecules for the Amber-96, Charmm22, Compass, Gromos-43A1, OPLS-aa, and TraPPE-UA force fields. The simulation results are compared with experimental measurements in order to provide an assessment of the accuracy one could expect when using these force fields to study unknown molecules. The similarity of the test molecules to the side chains of the neutral amino acids also provides information about the validity of the force fields for representing the nonbonded interactions in proteins.

Introduction

The accuracy of a molecular simulation is determined by how well the parameters and equations describing the atomic interactions (force field) reproduces reality. There are several large efforts world-wide to produce general force fields for organic molecules, with particular attention paid to the functional groups in proteins and DNA. Users of molecular simulation tools are faced with an important choice of which force field is best suited for their particular problem.

Of the six force fields studied in this paper, four were parameterized with primary interest in protein simulation, while the other two were parameterized for other specific chemical systems. The biological force fields often go to great lengths to describe the fitting procedure for the intramolecular interactions, while only mentioning the fitting of the nonbonded parameters in passing. Thus, it is not clear from the literature how well one could expect these force fields to perform in situations where the interactions are dominated by the nonbonded terms. Drug docking calculations are one example of a biological application where the nonbonded interactions are important. Most drug docking programs are only able to provide qualitative agreement with experiment, but it is not clear whether this poor agreement is due to the force fields, or to other fundamental limitations such as the lack of solvation or flexibility.

In recent years there have been several studies in the chemical engineering community to determine how well new and existing force fields reproduce experimental liquid densities and vapor-liquid coexistence curves. To the author's knowledge, none of these studies have considered using the biological force fields in these chemical applications despite the fact that proteins and petroleum share many functional groups. This study was designed to answer two questions. First, is the poor agreement observed in docking studies due to inadequate force fields? Second, how well do the biological force field perform in traditionally chemical engineering applications? Metrics of performance for several of the major force fields are reported to enable simulation users to make an informed force field selection for their problems.

³Electronic address: marmart@sandia.gov

Models

Amber param96

The Amber param96 [1] force field was parameterized for use in protein simulations and has functional groups for all 20 standard amino acids. It utilizes a 12-6 Lennard-Jones plus point charges for atoms that are not bonded, or are separated by more than three bonds. Lennard-Jones terms between unlike atoms are computed using the Lorentz-Berthelot mixing rules. Intramolecular interactions represent bond stretch with a harmonic potential, bending angles with a harmonic potential, and dihedral angles with a cosine series plus 12-6 Lennard-Jones scaled by 0.5 and coulombic scaled by 5/6. A single improper torsion, represented by a cosine series, is centered on each *sp*² center in order to enforce planarity.

Amber param96 suggests the use of the RESP methodology for fitting the point charge distribution for each molecule. This method was not used in this work and instead the point charge distributions were inferred from the amino acid examples in their paper. The actual point charge distributions used here are listed in the supporting information.

Charmm 22

The Charmm22 [2] force field was parameterized for use in protein simulations and has functional groups for all 20 standard amino acids. Charmm utilizes a 12-6 Lennard-Jones plus point charges for atoms that are not bonded, or are separated by more than three bonds. Lennard-Jones terms between unlike atoms are computed using the Lorentz-Berthelot mixing rules. Intramolecular interactions represent bond stretch with a harmonic potential, bending angles with a harmonic potential plus a distance dependent harmonic potential, and dihedral angles with a cosine series plus a special set of 12-6 Lennard-Jones parameters and unscaled coulombic terms. Improper torsions are used in special cases to enforce planarity with a harmonic term.

Charmm22 contains a set of example charge distributions and these examples were used to infer charge distributions on the molecules used in this study. The actual point charge distributions used here are shown in the supplementary information.

Compass

Compass [6, 7, 8, 9] is a semi-proprietary force field which utilizes complex intramolecular interactions. The Compass force field was parameterized for use on various systems of interest to customers of Accelrys. Only a portion of the Compass force field has been published in the open literature and that portion only contains functional groups for about half of the standard amino acids. Compass utilizes a 9-6 Lennard-Jones plus point charges for atoms that are not bonded, or are separated by more than three bonds. Lennard-Jones terms between unlike atoms are computed using special sixth-power mixing rules. Intramolecular interactions in this force field are quite complex compared to the other force fields in this study. Compass represents bond stretch with a polynomial of power two, three and four; bending angles with a polynomial of power two, three, and four; and dihedral angles with a cosine series. There are also cross terms between the bond stretches, bending angles, and dihedral angles.

Compass contains a rule set for determining the partial charge on any atom given its atom type and the

atom types of its neighbors. This rule set was used to compute the partial charge distribution shown in the supplementary information.

Gromos 43A1

Gromos 43A1 [10] is a united-atom force field which lumps most hydrogens onto their neighboring carbon atoms. This force field was parameterized for protein simulations and has parameters for all 20 standard amino acids. Gromos uses the 12-6 Lennard-Jones plus point charges for atoms that are not bonded, or are separated by more than three bonds. Lennard-Jones terms between unlike atoms are computed using special mixing rules, along with some special cases. Intramolecular interactions represent bond stretch with a quartic potential, bending angles with a harmonic cosine potential, and dihedral angles with a cosine series unscaled 12-6 Lennard-Jones parameters and unscaled coulombic terms. Unlike the other five force fields, Gromos only applies a single cosine series across any two central atoms. Thus, for a molecule like 2-methylbutane only one of the two symmetric $CH_3 - CH - CH_2 - CH_3$ torsions has the cosine series plus 1-4 nonbond while the other one only has the 1-4 nonbond.

Gromos-43A1 contains a set of example charge distributions and these examples were used to infer charge distributions on the molecules used in this study. The actual point charge distributions used here are shown in the supplementary information.

OPLS-aa

The OPLS-aa [3, 4, 5] force field was parameterized for use in protein simulations, and also for small organic molecules, and has functional groups for all 20 standard amino acids. It utilizes a 12-6 Lennard-Jones plus point charges for atoms that are not bonded, or are separated by more than three bonds. Lennard-Jones terms between unlike atoms are computed using the geometric mixing rules. Intramolecular interactions represent bond stretch with a harmonic potential, bending angles with a harmonic potential, and dihedral angles with a cosine series plus 12-6 Lennard-Jones scaled by 0.5 and coulombic scaled by 0.5. A single improper torsion, represented by a cosine series, is centered on certain sp^2 centers in order to enforce planarity.

The OPLS-aa force field papers provide a list of example functional groups and charge distributions. Charges for the molecules in this study were inferred from this information. The actual point charge distributions used here are listed in the supporting information.

TraPPE-UA

TraPPE-UA [11, 12, 13, 14] is a united-atom potential which represents CH_x groups as a single interaction site placed upon the carbon. This force field was fitted to reproduce vapor-liquid coexistence curves of small organic molecules so one would expect it to do well in this study, but it currently has a limited number of functional groups and cannot be used for protein simulation. It utilizes a 12-6 Lennard-Jones plus point charges for atoms that are not bonded, or are separated by more than three bonds. Lennard-Jones terms between unlike atoms are computed using the Lorentz-Berthelot mixing rules. Intramolecular interactions represent bond stretch with fixed bond lengths, bending angles with a harmonic potential, and dihedral angles with a cosine series. Unlike the other force fields, there are no 1-4 nonbonded interactions and no improper torsions.

The TraPPE-UA force field provides a list of example charge distributions, although for alkanes there is no

charge to distribute. The point charge distributions used here are shown in the supplementary information.

Simulation Methods

All simulations used the freely available MCCCSTowhee simulation program [15]. Coupled-decoupled configurational-bias [12] simulations were performed in either the NVT-Gibbs ensemble [16, 17, 18] (vapor-liquid coexistence), or in the isobaric-isothermal ensemble [19] (liquid densities). In all cases an Ewald summation was used to handle the coulombic interactions. The Gromos 43A1 force field was parameterized for use with a cut and shift potential so this was used in all simulations for Gromos 43A1 with a 14 Å cutoff. All of the all-atom force fields (Amber, Charmm, Compass, OPLS-aa) were run with a 10 Å nonbond cutoff with analytical tail corrections applied. TraPPE-UA was run with a 14 Å cutoff plus analytical tail corrections.

Liquid density simulations performed Monte Carlo moves with the following probabilities; volume change (0.01); configurational bias regrowths (0.32); translation of the molecule center of mass (0.34); rotation about the center of mass (0.33). Vapor-liquid coexistence curve calculations require a 2-box molecule transfer move whose probability was set in order to achieve roughly one accepted move every 5 to 10 cycles. The remaining probability was divided up between volume changes (0.002), type 1 aggregation volume bias moves [20] (0.01), and the rest equally divided between configurational bias regrowths, translation of the center of mass, and rotation about the center of mass.

The coupled-decoupled configurational bias algorithm used in this work is an extension of the one presented in previous work [12]. As many of the force fields tested here employ flexible bond lengths an additional decoupled selection of bond lengths was added to the old algorithm. Bond trials were generated according to the following probability

$$P_{\text{gen}} = l_{\text{equil}} \times [low^3 + random[0, 1] \times (high^3 - low^3)]^{\frac{1}{3}} \quad [1]$$

where l_{equil} is the equilibrium bond length, $random[0, 1]$ is a random number generated uniformly on the range $[0, 1]$, low and $high$ are variables set by the user. This algorithm generates bond lengths between $low \times l_{\text{equil}}$ and $high \times l_{\text{equil}}$ with the appropriate probability from the phase space terms. Simulation were performed using a low value of 0.85 and a $high$ value of 1.15. All configurational bias moves used 1000 trials for bond length selection, 1000 trials for each part of the bending angle selection, 360 trials for the dihedral selection, and 10 trials for the nonbonded selection. All cross terms in the Compass force field were computed as soon as all of the terms were known. Thus, any cross terms involving torsions were computed in the dihedral selection; cross terms with bending angles (but not torsions) were computed in the angle selection, and the bond-bond cross terms were computed in the bond length selection. Improper torsions were included as soon as all of the atoms were in position and this occurs either in the bending angle portion, or in the dihedral portion, depending on the growth pattern.

Simulations were equilibrated for at least 20,000 Monte Carlo cycles (a cycle is N moves where N is the number of molecules in the system) and production runs were 10,000 cycles and were broken into 5 blocks to estimate error bars.

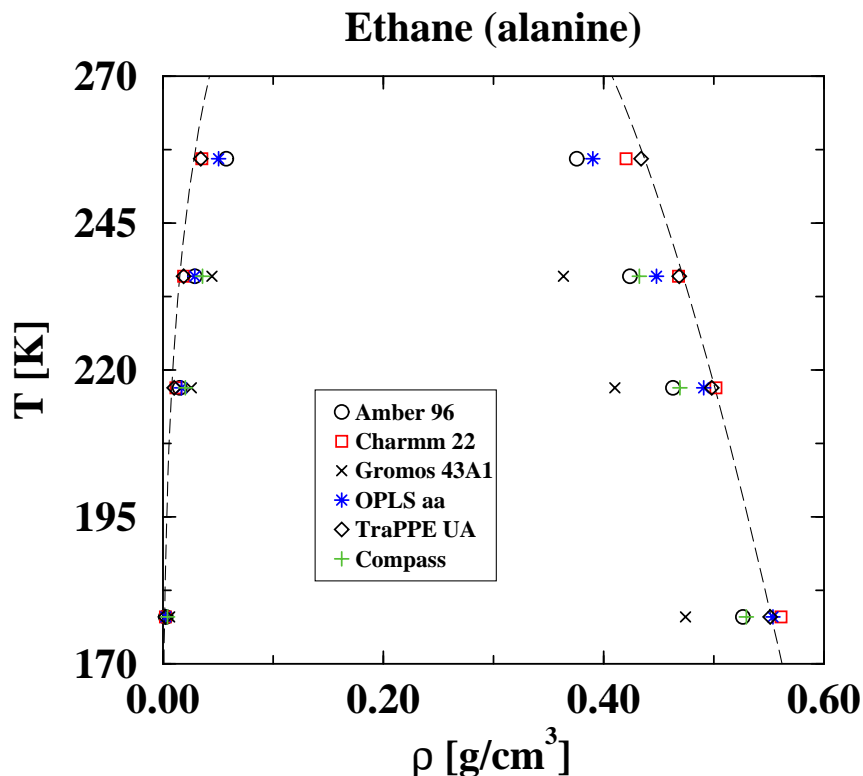


Figure 72. Vapor-Liquid equilibria for ethane.

Results and Discussion

The vapor-liquid coexistence curve (VLCC) for ethane (methyl capped side chain of alanine) shows Gromos does a poor job for the methyl groups. TraPPE has the best agreement, but this is no surprise as their methyl parameters were fitted to the VLCC of ethane. Charmm has the next best agreement while other force fields give reasonable results, but generally several percent too low in the liquid densities.

The VLCC for 2-methylbutane (leucine and isoleucine) provides another test for the hydrocarbon parameters. The agreement for all force fields is very good for this molecule and generally better than the agreement for ethane. The excellent agreement for Gromos is surprising given the problems with the methyl groups from ethane. Clearly the Gromos parameters work better for branched alkanes than for pure ethane. OPLS has the largest deviations, but only at the highest temperatures.

Isobutane (valine) is another test of the hydrocarbon parameters for a small branched alkane, but here we see gromos overestimating the density so perhaps the excellent agreement for 2-methylbutane was fortuitous. Interestingly, all force fields except Charmm (which is substantially too low) overpredict the liquid densities slightly. This is a departure from the trends observed in the other hydrocarbon molecules.

Ethanol (serine) provides a test of the alcohol parameters (OH) and again the agreement is good for the force fields. OPLS again does well at reproducing liquid densities at the lower temperatures, but severely

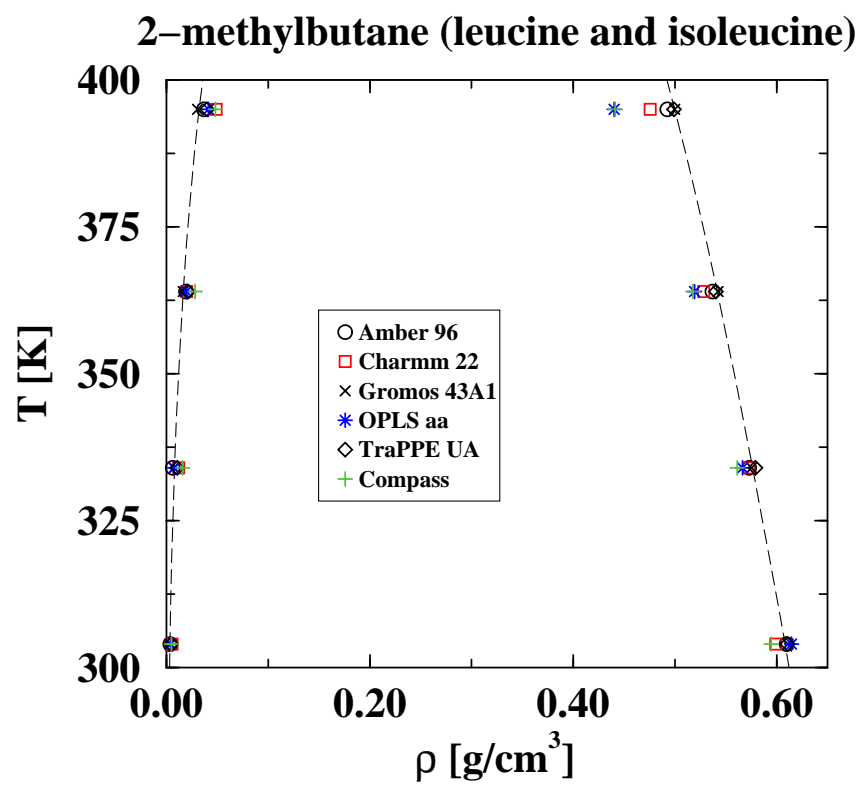


Figure 73. Vapor-Liquid equilibria for 2-methylbutane.

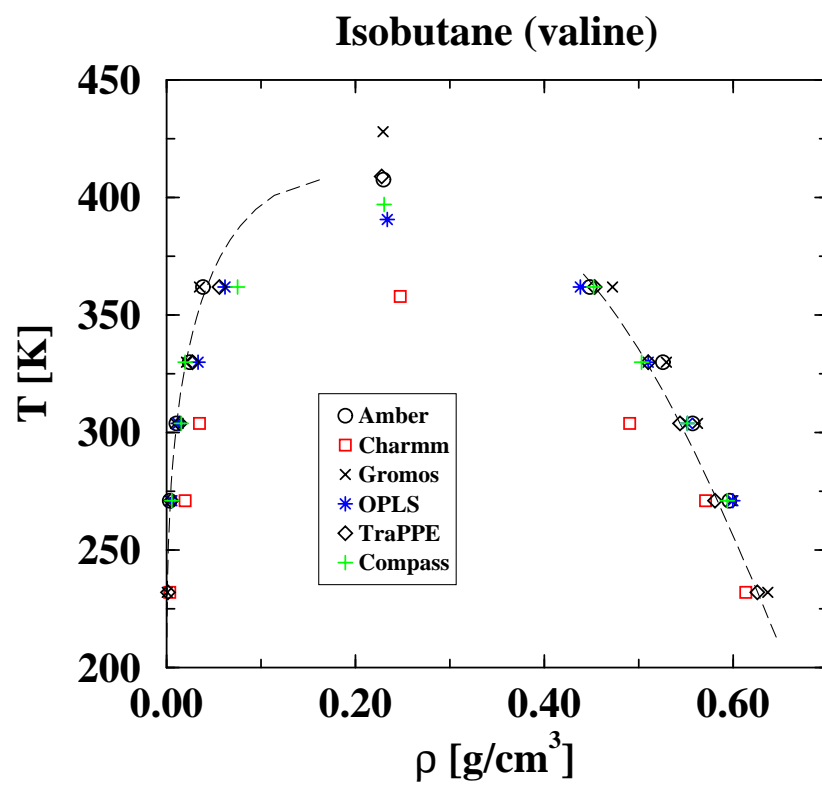


Figure 74. Vapor-Liquid equilibria for isobutane.

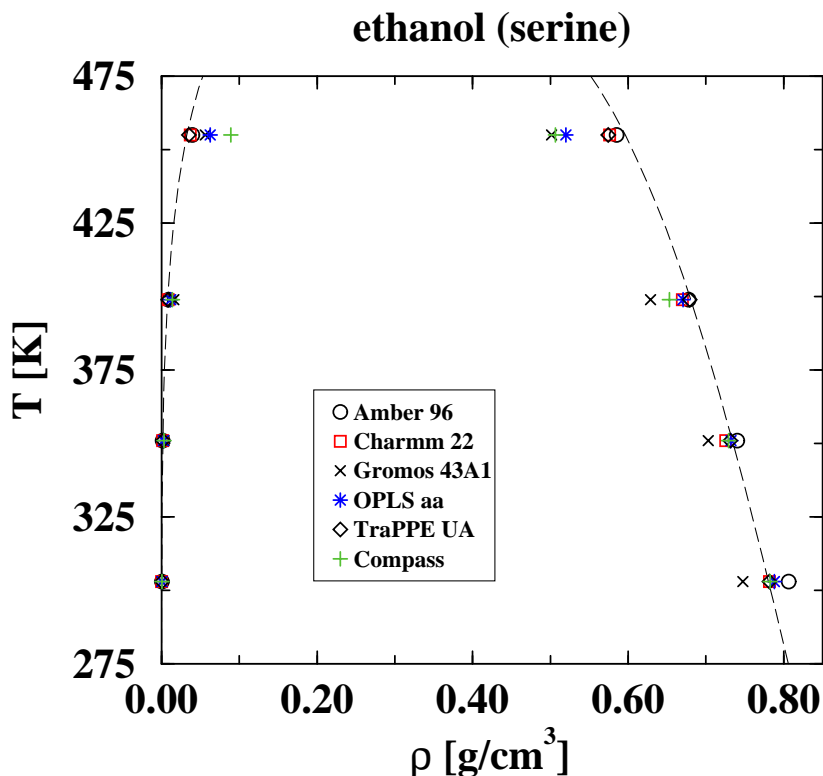


Figure 75. Vapor-Liquid equilibria for ethanol.

underestimates the high temperature densities. Gromos shows a similar pattern, but does less well even at the low temperatures. Charmm has the best agreement of the biological force fields.

Isopropanol (threonine) provides another test of the alcohols and roughly the same level of agreement is seen as was seen for ethanol. All the force fields overestimate the liquid density at the lowest temperature, and then scatter around the correct densities at the higher temperatures.

Finally, the liquid densities were computed for ethanethiol (cysteine), methylpropylsulfide (methionine), propanamide (asparagine), and butanamide (glutamine). TraPPE and Compass did not have the Sulfur and Nitrogen parameters needed for these molecules and no experimental VLCC were available. The predicted liquid densities for the rest are within 5 percent of experiment.

References

- [1] Cornell, W. D.; Cieplak, P.; Bayly, C. I.; Gould, I. R.; Merz Jr., K. M.; Ferguson, D. M.; Spellmeyer, D. C.; Fox, T.; Caldwell, J. W.; Kollman, P. A.; *J. Am. Chem. Soc.* **1995**, 117, 5179.
- [2] MacKerell Jr., A. D.; Bashford, D.; Bellott, M.; Dunbrack Jr., R. L.; Evanseck, J. D.; Field, M. J.; Fischer, S.; Gao, J.; Guo, H.; Ha, S.; Joseph-McCarthy, D.; Kuchnir, L.; Kuczera, K.; Lau, F. T. K.; Mattos, C.; Michnick, S.; Ngo, T.; Nguyen, D. T.; Prodhom, B.; Reiher III, W. E.; Roux, B.; Schlenkrich,

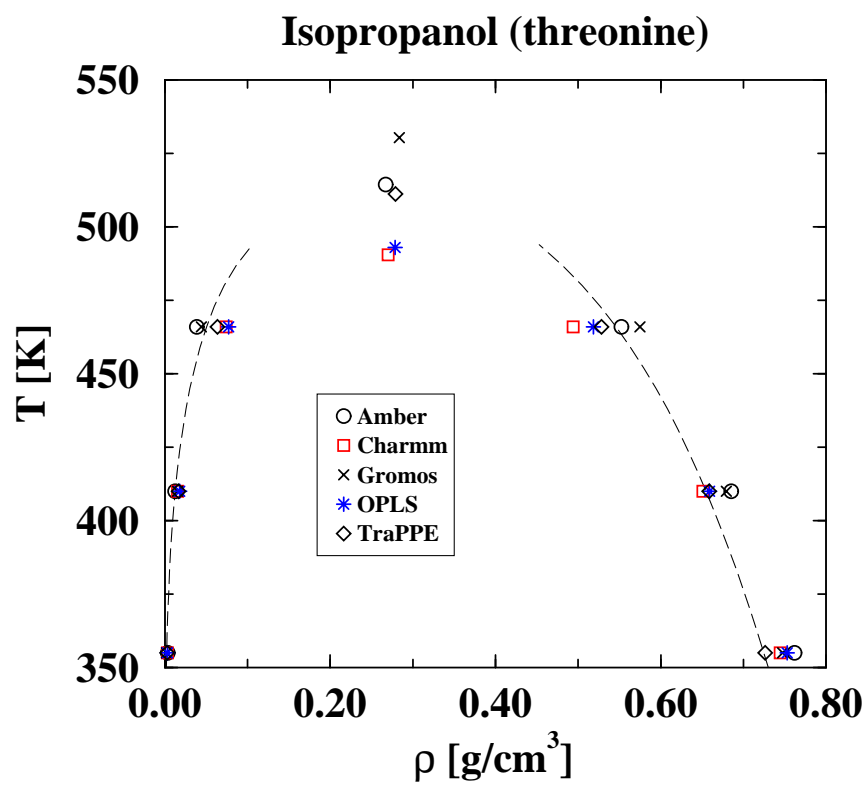


Figure 76. Vapor-Liquid equilibria for isopropanol.

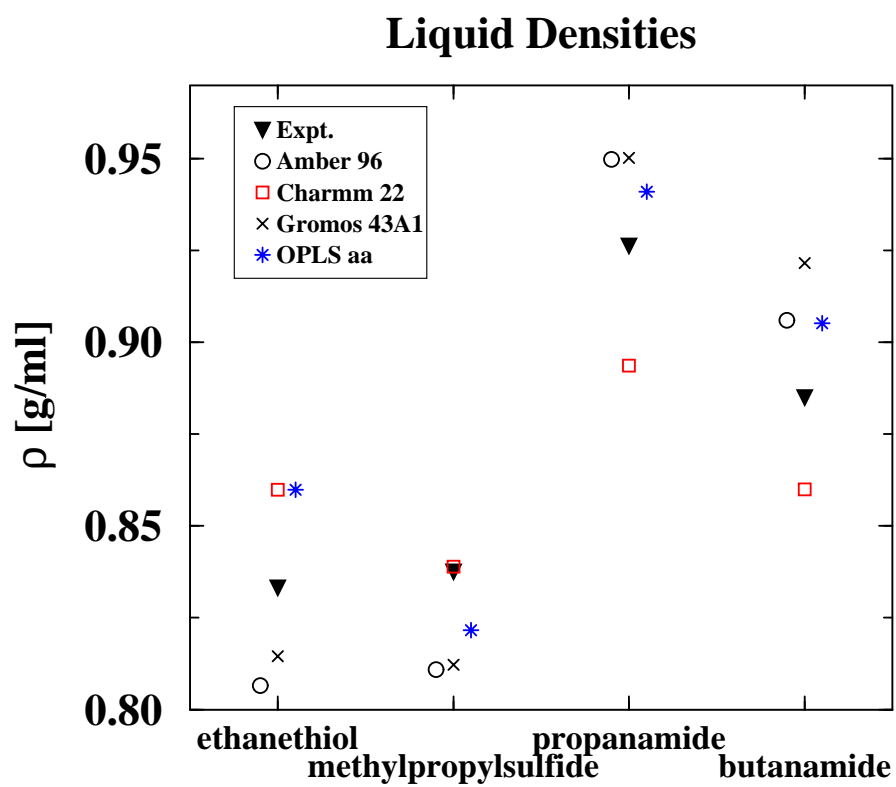


Figure 77. Liquid densities of ethanethiol, methylpropylsulfide, propanamide, and butanamide.

- M.; Smith, J. C.; Stote, R.; Straub, J.; Watanabe, M.; Wiorkiewicz-Kuczera, J.; Yin, D.; Karplus, M.; *J. Phys. Chem. B* **1998**, 102, 3586.
- [3] Jorgensen, W. L.; Maxwell, D. S.; Tirado-Rives, J.; *J. Am. Chem. Soc.* **1996**, 118, 11225.
- [4] Damm, W.; Frontera, A.; Tirado-Rives, J.; Jorgensen, W. L.; *J. Comp. Chem.* **1997**, 18, 1955.
- [5] Rizzo, R. C.; Jorgensen, W. L.; *J. Am. Chem. Soc.* **1999**, 121, 4827.
- [6] Rigby, D.; Sun, H.; Eichinger, B. E.; *Polymer International* **1997**, 44, 311.
- [7] Sun, H.; *J. Phys. Chem. B* **1998**, 102 7338.
- [8] Sun, H.; Ren, P.; Fried, J. R.; *Computational and Theoretical Polymer Science* **1998**, 8, 229.
- [9] Bunte, S. W.; Sun, H.; *J. Phys. Chem. B* **2000**, 104, 2477.
- [10] Scott, W. R. P.; Hunenberger, P. H.; Tironi, I. G.; Mark, A. E.; Billeter, S. R.; Fennen, J.; Torda, A. E.; Huber, T.; Kruger, P.; van Gunsteren, W. F.; *J. Phys. Chem. A* **1999**, 103 3596.
- [11] Martin, M. G.; Siepmann, J. I.; *J. Phys. Chem. B* **1998**, 102, 2569.
- [12] Martin, M. G.; Siepmann, J. I.; *J. Phys. Chem. B* **1999**, 103, 4508.
- [13] Wick, C. D.; Martin, M. G.; Siepmann, J. I.; *J. Phys. Chem. B* **2000**, 104, 8008.
- [14] Chen, B.; Potoff, J.; Siepmann, J. I.; *J. Phys. Chem. B* **2001**, 105, 3090.
- [15] <http://www.cs.sandia.gov/projects/towhee/>
- [16] Panagiotopoulos, A. Z.; *Mol. Phys.* **1987**, 61, 813.
- [17] Panagiotopoulos, A. Z.; Quirke, N.; Stapleton, M.; Tildesley, D. J.; *Mol. Phys.* **1988**, 63, 527.
- [18] Smit, B.; de Smedt, Ph.; Frenkel, D.; *Mol. Phys.* **1989**, 68, 931.
- [19] McDonald, I. R.; *Mol. Phys.* **1972**, 23, 41.
- [20] Chen, B.; Siepmann, J. I.; *J. Phys. Chem. B* **2000**, 104, 8725.

A new efficient method for density functional theory calculations of inhomogeneous fluids

Mark P. Sears, Laura J. D. Frink

Abstract

The accurate computation of the effects of solvation on chemical systems can be done using density functional theories (DFT) for inhomogeneous multicomponent fluids. The DFT models of interest are nonlocal theories which accurately treat hard sphere fluid mixtures; attractive inter-particle potentials (Lennard-Jones) are added as perturbations. In this paper we develop and demonstrate a new efficient method for an accurate nonlocal DFT. The method described here differs from previous work in the use of FFT (Fast Fourier Transform) methods to carry out the convolutions. As with our previous real space work[1, 2] we demonstrate that the Fourier space approach can be solved with a Newton-GMRES approach; however, we now employ a very efficient matrix-free algorithm. A simple but effective preconditioner is presented. The method is demonstrated with calculations performed for one, two, and three dimensional systems, including problems with single and multicomponent fluids. Timing comparisons with previous implementations are given.

Introduction

Density functional theories have been widely applied to study the behavior of confined fluids and fluids near interfaces[6]. Until very recently most of these studies have used very simple surfaces with substantial symmetry and uniform properties. Examples of simple confining geometries include smooth planar walls, cylindrical pores, and spherical cavities, which can all be reduced to 1-dimensional problems. More recently, studies on patterned surfaces have begun to appear in the literature; however, most of these use simplified functionals or have been limited to 2-dimensional problems[9, 11, 10]. We are interested in applying accurate nonlocal DFTs to complex systems such as solvated proteins. In this case the chemistry and geometry of the surface of interest is nonuniform. As a result, a full 3-dimensional solution is required.

We have previously developed a real space code[1, 2] that is based on a form of DFT originally derived by Rosenfeld[12]. That code used massively parallel computers and a variety of specialized algorithms to speed up computation of a Jacobian matrix based on the rather long range integration stencils that result from the nonlocal density functionals of interest[1, 2]. While a variety of novel algorithms were implemented to make 3D-protein systems accessible, the computational requirements are nevertheless substantial.

In this paper, we detail a new Fourier space based approach we have developed for solving the DFTs of interest. As with our previous work, we use a Newton solver for robustness and quadratic convergence guarantees. In contrast to our previous work, we have implemented a matrix free GMRES approach. Below, we discuss the numerical implementation of the Fourier space method, compare Fourier space and real space methods, and demonstrate the power of the Fourier space approach for solving large 3D problems.

The Free Energy Functional

We briefly review the systems of equations solved in the DFT model of a fluid. The basic approach of the model is to consider a functional which accurately represents a fluid composed of a mixture of hard sphere

components and then to add attractive potentials as perturbations. The solution to the model is given as a variational minimum of the grand potential Ω , which is a functional of the density ρ , temperature T , and chemical potential μ :

$$\Omega[\rho_i(\mathbf{r}), T, \mu] = F_{\text{id}}[\rho_i(\mathbf{r}), T, \mu] + F_{\text{hs}}[\rho_i(\mathbf{r})] + F_{\text{u}}[\rho_i(\mathbf{r})] + \int d^3\mathbf{r} \sum_i \rho_i(\mathbf{r}) (V_i^{\text{ext}}(\mathbf{r}) - \mu_i) \quad (140)$$

where the subscript i defines the fluid component and $V_i^{\text{ext}}(\mathbf{r})$ is a one-body external field. The inhomogeneity of the fluid density is a direct result of the spatial variation of the external field.

The first three terms in Eq. 140 are the ideal gas, hard sphere, and two-body perturbative contributions to the free energy, respectively. The ideal gas contribution is

$$F_{\text{id}} = k_B T \int d^3\mathbf{r} \sum_i \rho_i (\ln(\rho_i \Lambda_i^3) - 1) \quad (141)$$

where Λ is the deBroglie length. By redefining the chemical potential ($\mu' = \mu - \log(\Lambda^3)$) Λ becomes unity and drops out of the problem. Either the chemical potential or the bulk density can be used to define the bulk fluid state point.

The Rosenfeld[12] form for the hard-sphere excess free energy is given as a local functional of nonlocal (weighted) densities:

$$F_{\text{hs}} = \int d^3\mathbf{r} \Phi(n_\gamma) \quad (142)$$

where the weighted densities n_γ are given by the convolutions

$$n_\gamma(\mathbf{r}) = \sum_i \int d^3\mathbf{r}' \omega_{i\gamma}(\mathbf{r} - \mathbf{r}') \rho_i(\mathbf{r}'). \quad (143)$$

The weight functions $\omega_{i\gamma}$ can be either scalar or vector. They depend only on so-called fundamental measures of the hard-sphere particles in the fluid: the volume, surface area, and radius of the particles. The vector weight functions probe the density gradient as well. Note that in this paper we use lower case Italic indices for density components and lower case Greek indices to identify weight functions. The detailed form for Φ and the weight functions are presented in appendix A, as is the FFT method for performing convolutions.

The two-body perturbative contribution is taken to be a strict mean field approximation,

$$F_{\text{u}} = \frac{1}{2} \int \int d^3\mathbf{r} d^3\mathbf{r}' \sum_{ij} \rho_i(\mathbf{r}) \rho_j(\mathbf{r}') U_{ij}(\mathbf{r} - \mathbf{r}') \quad (144)$$

where the attractive potential U is described in more detail in appendix C.

A Matrix Free Newton's method

We now describe a solution scheme to find the desired stationary point of the grand potential functional. We define for each independent field f (i.e. density component) a *residual* field r_f given by the functional equation

$$r_f = \frac{\delta \Omega}{\delta f} \quad (145)$$

Clearly, a stationary point is defined by $r_f = 0$ at each point in space for all the fields. In addition to solving these residual equations, boundary conditions must be applied. In contrast to our real space method[1] where implementation of a variety of boundary conditions (periodic, reflective, homogeneous, inhomogeneous) was straightforward, the FFT based convolution method presented here is inherently periodic, and without modification can only handle problems with periodic boundary conditions.

A Picard method could be implemented directly from the residual defined above. The residual for component i can be separated into ideal gas and excess parts:

$$r_i = r_i^{\text{id}} + r_i^{\text{ex}}, \quad (146)$$

and at the solution where $r_i = 0$ we have

$$\rho_i(\mathbf{r}) = \exp \left(-\frac{V_i^{\text{ext}}(\mathbf{r}) - \mu_i + r_i^{\text{ex}}(\mathbf{r})}{kT} \right). \quad (147)$$

To implement the Picard scheme we simply iterate this equation until self consistency is achieved. In practice the convergence rate can be very slow, depending on the specific physics included in the functional and the state point of interest. It has been demonstrated that the convergence of a Newton's method is much faster, but this approach is costly due to the need for computing the Jacobian matrix[1].

The Jacobian of the system of equations defined by Eq. 145 is given by the functional derivatives

$$J_{ff'} = \frac{\delta r_f}{\delta f'} = \frac{\delta^2 \Omega}{\delta f \delta f'} \quad (148)$$

This quantity is defined for each pair of fields f, f' and each pair of points in space x, x' . In the following we treat the spatial coordinates implicitly.

Suppose we are close to a solution, then we can write each field f as the solution f^* plus a small error ϵ_f and then to second order we have

$$r_f[f] = r_f[f^*] + \sum_{f'} J_{ff'} \epsilon_{f'} \quad (149)$$

but of course $r_f[f^*] = 0$ and so ϵ_f is the solution to

$$r_f[f] = \sum_{f'} J_{ff'} \epsilon_{f'}, \quad (150)$$

and the Newton iteration procedure may be written as the replacement of f by $f - \epsilon_f$.

We describe Newton's iteration in this way to point out that the objective is to solve the above equation for the change in the fields. The inverse Jacobian operator is not needed (may not even be well defined), and the Jacobian itself is not required. All that is required is a method for solving the above linear system. In this paper we show that a matrix-free method works quite well: such a method solves the equation using an operational definition of the Jacobian *without storing any part of J* . In other words we assume only the ability to compute the effect of the Jacobian operating on a set of fields. The Jacobian operator can be used directly in an iterative scheme such as GMRES.

As we show in detail below, a powerful result emerges from this matrix free approach: the computation of the operational definition of the Jacobian involves the *same amount of work as the computation of the residual*,

within a small constant factor! This means that Newton's method can be implemented with essentially the same computational effort as a Picard iteration with the potential of converging much more quickly.

The method implemented in our real space code[1] contrasts with the current algorithm primarily in that the real space code computes and saves elements of the Jacobian matrix in a sparse format. The computation is done with finite element techniques, i.e. using finite element shape functions, and the assembled matrix elements therefore form a nodal finite difference stencil. The Jacobian equation is then solved by a sparse matrix package [7] which has a number of solver and preconditioning options. At this level both codes solve the same Newton iteration and as we show later the convergence of the codes with respect to Newton iteration is essentially the same for both. At the lower level the real space code computes and saves a sparse matrix and the matrix vector multiplications are performed by the sparse matrix package, while the matrix-free FFT method implements the matrix-vector multiplications needed for a sparse solve directly in terms of the physical operators. For a true comparison of either method with the Picard approach, we should compare total the number of matrix-vector multiplications (however performed) with the number of Picard iterations.

Overview of the algorithm.

The algorithm basically consists of an outer loop which is the Newtons' iteration. Inside this loop there are three steps: computing the residual, calling the linear solver, and finally updating the solution; this loop is repeated until the residual norm is below some tolerance or a maximum number of steps is reached. The linear solver in turn computes the Jacobian operator some number of times in order to solve the above equation. In the remainder of this section we outline the method for computing the residual and then show the related techniques used to compute the Jacobian operator.

Computing the residuals

In this paper there is one residual field for each density component since we do not include electrostatics. Following the development above, we discuss different physical contributions to the residual independently with the understanding that they will be summed. We make the assumption that the physical fields, potentials, and residuals are described on a simple regular real space mesh. The Fourier mesh described below is only present in order to compute convolutions quickly.

The ideal gas contribution to the residual for density component i is

$$kT \ln(\rho_i(\mathbf{r})) + V_i^{ext}(\mathbf{r}) - \mu_i \quad (151)$$

which can be evaluated directly point by point on the real-space mesh.

The functional derivative of the Rosenfeld form for the hard-sphere excess free energy is

$$\left. \frac{\delta F_{hs}}{\delta \rho_i} \right|_{\mathbf{r}} = \int d^3 \mathbf{r}' \sum_{\gamma} \left. \frac{\partial \Phi}{\partial n_{\gamma}} \right|_{\mathbf{r}'} \frac{\delta n_{\gamma}(\mathbf{r}')}{\delta \rho_i(\mathbf{r})} = \int d^3 \mathbf{r}' \sum_{\gamma} \left. \frac{\partial \Phi}{\partial n_{\gamma}} \right|_{\mathbf{r}'} \omega_{i\gamma}(\mathbf{r} - \mathbf{r}') \quad (152)$$

Note the order of r, r' in this expression compared with Eq. 143, which is just a convolution of $\frac{\partial \Phi}{\partial n_{\alpha}}$ with the weight functions $\omega_{i\gamma}$. For even (i.e. scalar) weight functions the order is irrelevant, but for the vector weight functions the change in order results in a change of sign. We can take this into account during the process of convolution with the FFT method by taking the complex conjugate of the weight function in Fourier space

when the residual is constructed from $\frac{\partial \Phi}{\partial n_\alpha}$. This has no effect on the even weight functions, whose FT is real, and changes the sign of the odd weight functions, whose FT is imaginary. Note that the total amount of work required to compute the residual is $N_w + N_c$ convolutions, where N_w is the number of weight functions and N_c is the number of density components.

Finally, the contribution to the residual of the attractive perturbations is

$$\left. \frac{\delta F_u}{\delta \rho_i} \right|_{\mathbf{r}} = \int d^3 \mathbf{r}' \sum_j \rho_j(\mathbf{r}') U_{ij}(\mathbf{r} - \mathbf{r}') \quad (153)$$

Note that this is a convolution of the potential function U with the density, and can easily be treated with the FFT method described in appendix B.

Computing the operational Jacobian

We now show how to compute the operational definition of the Jacobian, that is the action of the Jacobian on a field. In more detail we are computing the quantities

$$y_i(\mathbf{r}) = \int d^3 \mathbf{r}' \sum_j J_{ij}(\mathbf{r}, \mathbf{r}') x_j(\mathbf{r}') = \int d^3 \mathbf{r}' \sum_j \frac{\delta^2 \Omega}{\delta \rho_i(\mathbf{r}) \delta \rho_j(\mathbf{r}')} x_j(\mathbf{r}'). \quad (154)$$

for some input field x , which will come from the iterative scheme that we use to solve $J\epsilon = r$. We do this without constructing or saving any part of J , thus the method is matrix-free.

The ideal gas contribution to $y_i(\mathbf{r})$ is simply evaluated pointwise as

$$\frac{kT}{\rho_i(\mathbf{r})} x_i(\mathbf{r}) \quad (155)$$

In order to write down the hard sphere contribution to the operational Jacobian we define

$$\Phi_{\alpha\beta}(\mathbf{r}) = \left. \frac{\partial^2 \Phi}{\partial n_\alpha \partial n_\beta} \right|_r \quad (156)$$

Expressions for $\Phi_{\alpha\beta}(\mathbf{r})$ are given in appendix A. Then the hard sphere contribution to the Jacobian becomes

$$\left. \frac{\delta^2 F_{\text{hs}}}{\delta \rho_i \delta \rho_j} \right|_{r, r'} = \int d^3 \mathbf{r}'' \sum_{\alpha\beta} \Phi_{\alpha\beta}(\mathbf{r}'') \frac{\delta n_\alpha(\mathbf{r}'')}{\delta \rho_i(\mathbf{r})} \frac{\delta n_\beta(\mathbf{r}'')}{\delta \rho_j(\mathbf{r}')} \quad (157)$$

$$= \int d^3 \mathbf{r}'' \sum_{\alpha\beta} \Phi_{\alpha\beta}(\mathbf{r}'') \omega_{i\alpha}(\mathbf{r}'' - \mathbf{r}) \omega_{j\beta}(\mathbf{r}'' - \mathbf{r}') \quad (158)$$

where the second derivative of Φ only depends on a single coordinate r'' because Φ is a local function of the weighted densities.

Efficient computation of the hard sphere contribution to the operational Jacobian relies on noticing that it can be evaluated via two successive sets of convolutions. To this end we define two intermediate quantities. The first is a convolution of the input field x with the weight functions ω :

$$t_\beta(\mathbf{r}'') = \int d^3 \mathbf{r}' \sum_j \omega_{j\beta}(\mathbf{r}'' - \mathbf{r}') x_j(\mathbf{r}'). \quad (159)$$

We also define

$$z_\alpha(\mathbf{r}'') = \sum_\beta \left. \frac{\partial^2 \Phi}{\partial n_\alpha \partial n_\beta} \right|_{\mathbf{r}''} t_\beta(\mathbf{r}''). \quad (160)$$

We now see that then we have the hard-sphere contribution to $y_i(r)$ given as a convolution of z_α :

$$\int d^3 \mathbf{r}'' \sum_\alpha \omega_{i\alpha}(\mathbf{r}'' - \mathbf{r}) z_\alpha(\mathbf{r}''). \quad (161)$$

Thus $y(\mathbf{r})$ is computed by first evaluating the convolutions in Eq. 159 followed by a second set of convolutions in Eq. 161. Each requires $N_c + N_w$ individual convolutions for a total of $2N_c + 2N_w$. Note that the order of the variables in the weight functions is reversed in the two convolutions.

We compute and save the quantities $\Phi_{\alpha\beta}(\mathbf{r})$ at each location in the real-space mesh once at the beginning of each Newton's iteration. The cost of computing the hard-sphere contribution to the Jacobian operator is therefore dominated by the two convolutions described here. The total number of FFT operations is $2N_w + 2N_c$ per Jacobian operator computation, or twice the number of FFT operations as were needed for the residual computation. Note also that when N_c is small the cost is dominated by N_w , so the cost of solving for mixtures with a small number of components is hardly larger than that of solving for a single component.

Finally, the attractive contribution to the operational Jacobian is simply given by the convolution of the field x with the interparticle potential U . This becomes a term of the form

$$y_i(\mathbf{r}) = \int d^3 \mathbf{r}' \sum_j U_{ij}(\mathbf{r} - \mathbf{r}') x_j(\mathbf{r}'). \quad (162)$$

Iterative solution with GMRES and Preconditioning

GMRES[14] is a powerful method for solving large systems of linear equations iteratively. The method only requires an implementation of the matrix-vector product, which we provided above. Since the Jacobian is defined in a way that explicitly reveals the fact that it is symmetric, we might think that a simpler method such as conjugate gradients (CG) would be sufficient. CG requires that the matrix also be positive definite however, and this is not so easy to demonstrate. GMRES has a great deal of robustness that CG lacks, and in addition we have intentions to modify this program for situations where the equations are not symmetric, for example when we treat steady state transport[4] or add a state-following algorithm that accesses unstable parts of the phase diagram[3].

GMRES and CG are both Krylov-space iterative methods. In GMRES, as vectors are accumulated they are orthogonalized against all the previously accumulated vectors; this provides much of the stability and robustness relative to CG, which uses a three term recursion relation to implicitly maintain orthogonality. The memory required for GMRES is $N(S + 2)$ where N is the number of independent variables and S is the maximum number of iterations. The method can be restarted, so a fixed number can be chosen for S . Nevertheless, this storage can dominate the required storage for the problem as a whole. Beyond this description we treat GMRES as a black box and refer the interested reader to the published literature on the method.

Like other Krylov-space iterative methods, GMRES can benefit greatly from a good preconditioner. We consider the development of preconditioners to be an open problem for this application. Of course, many of the

preconditioners that are available for finite element methods rely on the existence of explicit matrix elements, which our matrix-free method does not make available. So these preconditioners cannot be used and we are forced to look for physics-based preconditioners.

The approach currently used in the code is very simple. A class of preconditioners is defined by building an approximate inverse to J that is easily computed. If M is such an inverse then we can solve $JMM^{-1}x = y$ instead of $Jx = y$, by solving the modified equation $JMx' = y$ and then computing $x = Mx'$. Here we construct a local function (diagonal matrix) that interpolates between the ideal gas limit and the bulk state point. The preconditioner is

$$\tilde{x}_i = M^{ij}x_j \quad (163)$$

where for a single component

$$M = \frac{\rho}{J_0 - \rho \frac{kT}{\rho_0} + kT} \quad (164)$$

and J_0 is the Jacobian for a constant-density fluid at the bulk state point ρ_0 . This preconditioner interpolates between the bulk fluid state point far from any wall to the ideal gas behavior where the density is small.

A better preconditioner might involve solving a multilevel problem. In this case we would solve the DFT problem on a coarse mesh and then interpolate that solution to the fine mesh. Note that we can do a very good job of interpolation using the FFT method, and if the coarse mesh has twice the spacing then the effort needed to solve on the coarse mesh is 1/8 that on the fine mesh.

Example problems

In this section we give results for several simple one, two, and three dimensional cases. We begin with sample problems where the boundary condition is that of a hard wall, hard cylinder, or hard sphere. A general hard surface (defined as the boundary of some volume) boundary condition can be defined by an external field with

$$V(\mathbf{r}) = \begin{cases} \infty & \text{inside} \\ 0 & \text{outside} \end{cases} \quad (165)$$

Note that for all grid points or nodes inside the volume where $V(\mathbf{r}) = \infty$ the density $\rho(\mathbf{r})$ can be rigorously set to zero. However, when integrating (e.g. computing nonlocal densities) through the discontinuity defined by the surface one should include contributions from elements on the fluid side of the interface only in order to predict surface densities that will satisfy known sum rules (e.g. $\sum_i \rho_i = \beta P$). If one allows for interpolation between the density at the surface node and the density for the first node inside the volume then the sum rules will not be satisfied except in the limit that the grid spacing goes to zero. However all other points in the density distribution will be affected very little. Since we are ultimately interested in systems described by continuous potentials, we have elected not to implement the required code for accurately dealing with true hard potentials in the Fourier algorithm. Therefore the real space results shown below for comparison were done allowing a linear interpolation between the surface nodes of the mesh and the first element inside the volume.

Figures 78 to 80 present a direct comparison of the algorithm presented in this paper with our previous finite element real space implementation. These figures show the fluid density distribution in a periodic array

of planar walls, parallel cylinders, and spheres respectively. In all cases the agreement is extremely good. The bulk state of the fluid is defined by a bulk density of $\rho = .8785$ corresponding to a packing fraction of $\eta = .46$, which is the same state point used in [8]. The wall thickness (radius) is 1σ . For the hard cylinder and hard sphere cases we plot the density along a line extending radially from the surface. The problems were run in a periodic volume of size $L = 12.8\sigma$ for the one and two dimensional problems and $L = 6.4\sigma$ for the three dimensional problem. The mesh cell size for the hard wall and hard cylinder cases is $h = .1\sigma$ and is doubled for the sphere case. The points are from the FFT based calculations and the lines from our finite element calculations; the results in all three cases are almost identical. The inset to Figure 79 shows a contour plot of the density around the cylinder. This contour plot shows that the staircase representation of the cylinder does not induce significant staircase artifacts in the computed density. Rather, uniform cylindrical density bands are observed.

To further illustrate applications of our new algorithm we include three additional one dimensional cases. The first shows an example of a two component hard sphere fluid near a hard wall (see Figure 81). The bulk state is chosen with the bulk densities of $(.0260, .0104)$ for components with hard sphere radii of $(.5, 1.5)$, which regenerates the results of [13].

Figure 82 shows a calculation of a hard-sphere fluid at a Lennard-Jones 9-3 wall, which can be compared with [8]. Details of the wall potential are described in appendix C. Note the large peak next to the wall with a very low minimum next to it. The large peak corresponds to a monolayer of fluid lying in the minimum of the 9-3 potential.

Figure 83 is the most interesting case. We show what happens when a relatively high density fluid is in contact with a Lennard-Jones wall. In this case the fluid is described by the hard-sphere terms as well as a perturbative Lennard-Jones interaction and the state point is chosen to lie in the liquid regime. The bulk density is set to $.75$ in units where the hard sphere diameter is 1. The fluid-wall interaction and the fluid-fluid interaction potential are described in appendix C. In this case large amplitude density oscillations are seen that persist a long distance into the fluid, and again we see that the two codes yield identical results.

Convergence and Performance

In this section we compare the convergence and performance of an implementation of the algorithm described in this paper with that of our real space finite element code. Above we showed that the results of the two codes are essentially identical, here we note that there are three main issues of convergence and performance:

- comparison of convergence of the two codes.
- comparison of the speed (time to solution) of the two codes.
- comparison of memory required by the two codes.

Convergence of the two codes is very similar, as is shown in Figure 84. This plot shows how the residual norm changes as a function of Newton-GMRES iteration, showing the quadratic convergence expected for this

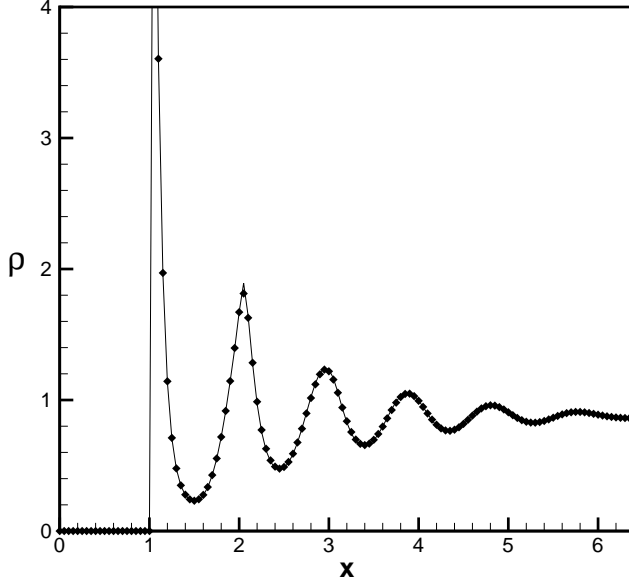


Figure 78. Density profile at a hard wall. The bulk state is $\rho = .8785$ (packing fraction .46).

algorithm. The residual norm is defined by the expression

$$\epsilon = \left(\int dV |r|^2 \right)^{\frac{1}{2}} \quad (166)$$

where r is the residual field. One interesting feature is that the convergence rate improves with increasing dimension. The apparent reason for this is that the curved walls lower the magnitude of the density oscillations in the solution; the effect can be seen by comparing the peak heights in 78, 79, 80. This means that the fluid in these cases is everywhere closer to the bulk state and therefore convergence is improved. For the one dimensional case convergence requires 8 iterations, in two dimensions 7, and in the three dimensional case the algorithm reduces the residual norm by 10 orders of magnitude in only six iterations. In all cases the initial guess for the solution is just a constant density equal to the bulk density outside the wall and zero inside.

Although both codes use approximately the same number of Newton-GMRES iterations to solve the problem, the speed of the two codes is markedly different. The primary difference in performance is due to the following. In the finite element code the weight function convolutions are implemented as finite difference operators. Considering such an operator, we note that each weight function has a finite radius R , so there are a number $O(R^3/h^3)$ points in the finite difference operator in three dimensions, where h is the mesh spacing. The work required to perform a convolution is therefore $O(L^3/h^3)$ since there are L^3 mesh points. In comparison, the FFT method for performing the convolution is almost independent of the radius of the weight functions, so the work in this case is $O(L^3)$. Mesh refinement for the finite element code therefore has a cost $O(1/h^3)$ relative to the FFT method. For one dimension this relative cost is $O(1/h)$ and for two dimensions the relative cost is $O(1/h^2)$.

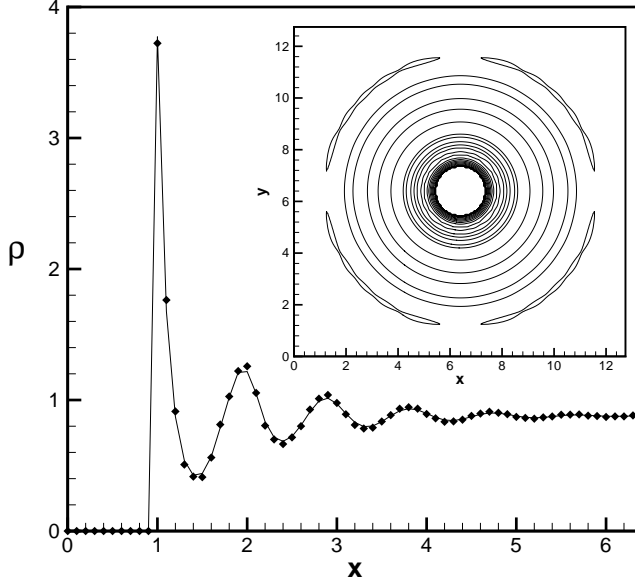


Figure 79. Density profile at a hard cylinder. State is same as fig 1.

Figure 85 shows the relative performance of the two methods running on the same platform (Intel Pentium 4 at 1.3 Ghz), for a scaled set of three dimensional problems. We have plotted time per Newton iteration as a function of the number of points in the mesh, N , and the scaling of the graph is logarithmic. Note that all the algorithms would scale linearly with number of mesh points if the size of the system were increased. However, when the number of points is increased by making the mesh more dense as in Fig.85, there are considerable differences between the algorithms. The performance of the FFT method is approximately $N^{1.2}$ where the performance of the real space method is between $N^{2.2}$ and $N^{1.6}$ depending on the specific algorithm applied. More specifically, the $N^{2.2}$ scaling is found for algorithms dominated by the Jacobian computation while the $N^{1.6}$ scaling is found for algorithms dominated by the GMRES solve.[5]. For comparison, a scaling curve is also shown for the faster real space algorithm on 100 processors of the CPlant commodity cluster at Sandia National Labs. Note that the CPlant processors are slower than the Intel processors used for single processor timings by about a factor of 4. Figure 85 clearly demonstrates that our new matrix free algorithms can be used to compute large $O(10^6)$ unknowns calculations on a single processor workstation in a modest $O(1\text{hour})$ amount of time. When these new algorithms are parallelized and further optimized we expect a further two orders of magnitude speedup.

Finally, table 10 shows a comparison of the approximate memory in gigabytes (GB) required by the two codes for a typical one component fluid in a cubical box with side $L = 12.8\sigma$ at various mesh densities (h in units of σ). This table compares the algorithm presented here (FS) with the RS1 algorithm in Fig.85 for the case of a hard sphere fluid. Clearly, there is a very significant difference between the two codes with respect to required memory.

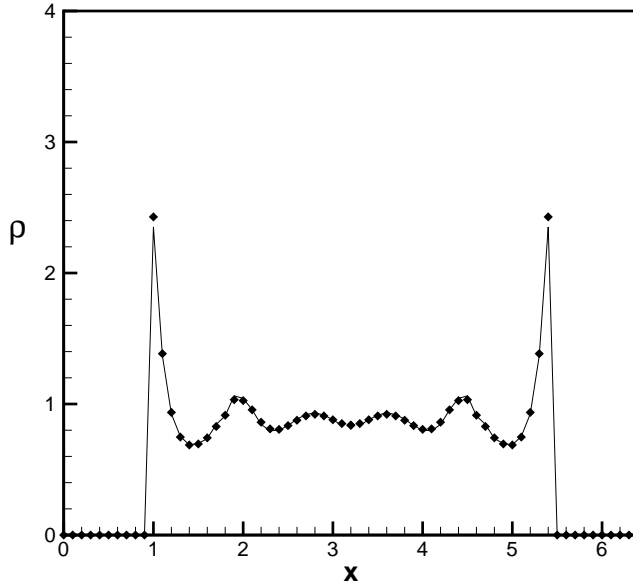


Figure 80. Density profile around a hard sphere. State is same as fig 1..

h	$N \times 10^6$	RS1 (GB)	FS (GB)
.2	0.26	1	.25
.1	2.10	70	2
.05	16.7	4500	16

Table 10. Memory usage in giga bytes (GB).

Conclusions

We have presented an efficient algorithm for treating DFT in complex three dimensional geometries. The Newton-GMRES solution scheme is capable of solving the highly nonlinear optimization problem presented by the minimization of complex DFT model functionals in remarkably few iterations and with quadratic convergence, as shown above. The development of good preconditioners for the solve is still an open question. The efficient FFT based method of computing the residual and the Jacobian operator is based on analysis of the physical operators. The method works without storing a matrix and is both faster than the finite element method and uses significantly less memory.

We have shown that the new matrix-free algorithm accurately reproduces the results of our previous real space finite element code as well as results from the literature. The new algorithm is thus a powerful technique for the treatment of complex fluid mixtures in one, two, and three dimensional inhomogeneous systems.

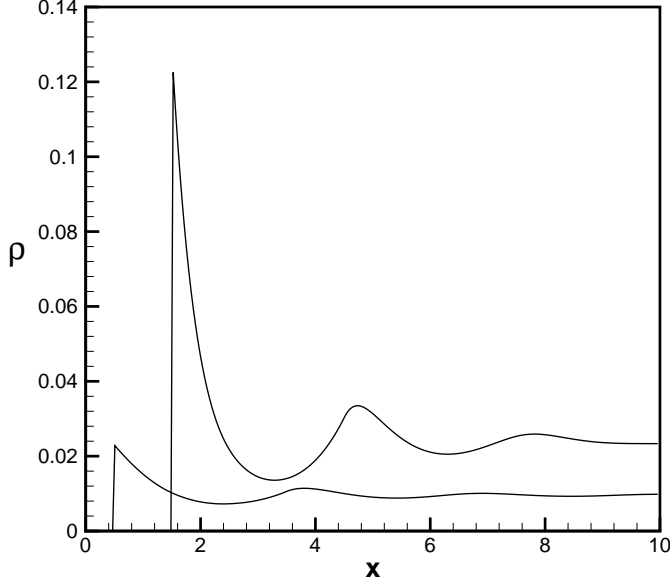


Figure 81. Density profiles for hard sphere mixture. Compare with [13] fig 2a. Bulk density of component 1 (hard sphere radius .5) is .0260 and bulk density of component 2 (hard sphere radius 1.5) is .0104 .

Appendix A: Rosenfeld functional

Here we give for reference the Rosenfeld functional for the excess hard-sphere free energy, its first and second derivatives, the weight functions and their Fourier transforms.

For a fluid component with hard sphere radius R there are four scalar and two vector weight functions, or 10 weight functions altogether for each fluid component. These are

$$\begin{aligned}\omega_0(r) &= \frac{\delta(r-R)}{4\pi R^2}, \omega_1(r) = R \omega_0(r), \omega_2(r) = 4\pi R^2 \omega_0(r), \\ \omega_3(r) &= \theta(r-R), \omega_{1v}(\mathbf{r}) = \frac{\hat{\mathbf{r}}}{4\pi R} \delta(r-R), \omega_{2v}(\mathbf{r}) = 4\pi R \omega_{1v}(\mathbf{r}),\end{aligned}\tag{167}$$

where R is the hard sphere radius of the component. The weight functions ω_{1v} , ω_{2v} and their associated densities n_{1v} , n_{2v} are treated as vector quantities. The Fourier transforms of these functions are

$$\begin{aligned}\tilde{\omega}_0(k) &= \frac{\sin(kR)}{kR}, \tilde{\omega}_1(k) = R \tilde{\omega}_0(k), \tilde{\omega}_2(k) = 4\pi R \tilde{\omega}_0(k), \\ \tilde{\omega}_3(k) &= 4\pi R^3 \frac{\sin(kR) - kR \cos(kR)}{(kR)^3}, \\ \tilde{\omega}_{1v}(\mathbf{k}) &= -i\mathbf{k}R^2 \tilde{\omega}_3(k), \tilde{\omega}_{2v}(\mathbf{k}) = 4\pi R \tilde{\omega}_{1v}(\mathbf{k}),\end{aligned}\tag{168}$$

where $k = |\mathbf{k}|$.

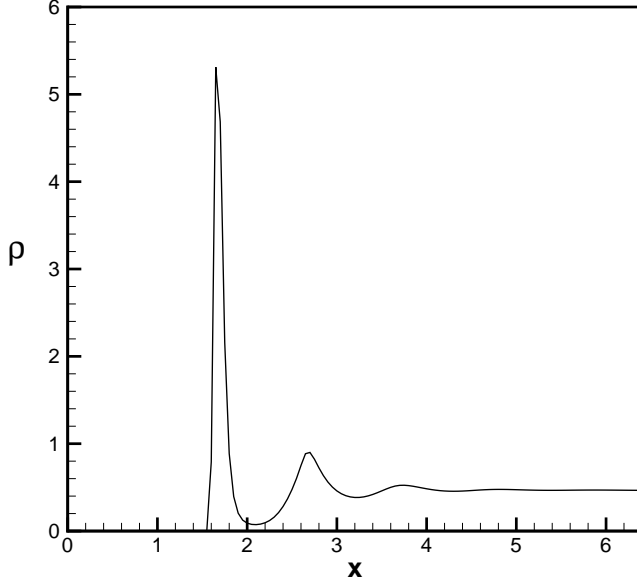


Figure 82. Density profile for hard sphere fluid at LJ 9-3 wall. Compare with [8] fig. 3

The Rosenfeld functional F_{hs} is given by the following expression

$$F_{\text{hs}} = \int d^3\mathbf{r} (\Phi_s + \Phi_v) \quad (169)$$

where the scalar and vector contributions Φ_s and Φ_v are local functions of the weighted densities n_α :

$$\begin{aligned} \Phi_s &= -n_0 \ln(1 - n_3) + \frac{n_1 n_2}{1 - n_3} + \frac{1}{24\pi} \frac{n_2^3}{(1 - n_3)^2} \\ \Phi_v &= -\frac{n_{1v} \cdot n_{2v}}{1 - n_3} - \frac{1}{8\pi} n_2 \frac{n_{2v} \cdot n_{2v}}{(1 - n_3)^2} \end{aligned} \quad (170)$$

The first derivatives of Φ are

$$\begin{aligned} \frac{\partial \Phi}{\partial n_0} &= -\ln(1 - n_3), \quad \frac{\partial \Phi}{\partial n_1} = \frac{n_2}{1 - n_3} \\ \frac{\partial \Phi}{\partial n_2} &= \frac{n_1}{1 - n_3} + \frac{1}{8\pi} \frac{n_2^2}{(1 - n_3)^2} - \frac{1}{8\pi} \frac{n_{2v} \cdot n_{2v}}{(1 - n_3)^2} \\ \frac{\partial \Phi}{\partial n_3} &= \frac{n_0}{1 - n_3} + \frac{n_1 n_2}{(1 - n_3)^2} + \frac{1}{12\pi} \frac{n_2^3}{(1 - n_3)^3} - \frac{n_{1v} \cdot n_{2v}}{(1 - n_3)^2} - \frac{1}{4\pi} n_2 \frac{n_{2v} \cdot n_{2v}}{(1 - n_3)^3} \\ \frac{\partial \Phi}{\partial n_{1v}} &= -\frac{n_{2v}}{1 - n_3}, \quad \frac{\partial \Phi}{\partial n_{2v}} = -\frac{n_{1v}}{1 - n_3} - \frac{1}{4\pi} n_2 \frac{n_{2v}}{(1 - n_3)^2} \end{aligned} \quad (171)$$

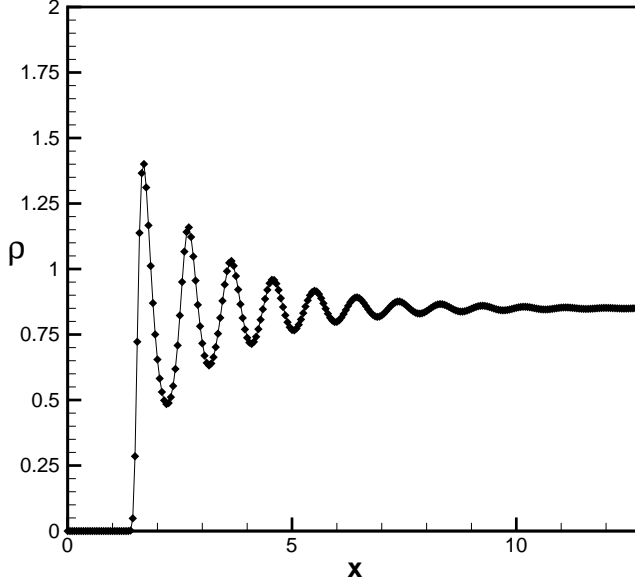


Figure 83. Density profile for LJ fluid at LJ 9-3 wall. See appendix C for details on wall and fluid interaction potentials.

The 21 non-vanishing second derivatives (modulo symmetry) are

$$\begin{aligned}
\frac{\partial^2 \Phi}{\partial n_0 \partial n_3} &= \frac{1}{1 - n_3}, \quad \frac{\partial^2 \Phi}{\partial n_1 \partial n_2} = \frac{1}{1 - n_3}, \quad \frac{\partial^2 \Phi}{\partial n_1 \partial n_3} = \frac{n_2}{(1 - n_3)^2}, \quad \frac{\partial^2 \Phi}{\partial n_2 \partial n_2} = \frac{1}{4\pi} \frac{n_2}{(1 - n_3)^2} \\
\frac{\partial^2 \Phi}{\partial n_2 \partial n_3} &= \frac{n_1}{(1 - n_3)^2} + \frac{1}{4\pi} \frac{n_2^2}{(1 - n_3)^3} - \frac{n_{2v} \cdot n_{2v}}{(1 - n_3)^3}, \quad \frac{\partial^2 \Phi}{\partial n_2 \partial n_{2v}} = -\frac{1}{4\pi} \frac{n_{2v}}{(1 - n_3)^2} \\
\frac{\partial^2 \Phi}{\partial n_3 \partial n_3} &= \frac{n_0}{(1 - n_3)^2} + \frac{n_1 n_2}{(1 - n_3)^3} + \frac{1}{4\pi} \frac{n_2^3}{(1 - n_3)^4} - 2 \frac{n_{1v} \cdot n_{2v}}{(1 - n_3)^3} - \frac{3}{4\pi} n_2 \frac{n_{2v} \cdot n_{2v}}{(1 - n_3)^4} \\
\frac{\partial^2 \Phi}{\partial n_3 \partial n_{1v}} &= -\frac{n_{2v}}{(1 - n_3)^2}, \quad \frac{\partial^2 \Phi}{\partial n_3 \partial n_{2v}} = -\frac{n_{1v}}{(1 - n_3)^2} - \frac{1}{2\pi} n_2 \frac{n_{2v}}{(1 - n_3)^3} \\
\frac{\partial^2 \Phi}{\partial n_{1v} \partial n_{2v}} &= -\frac{1}{1 - n_3} \mathbf{I}, \quad \frac{\partial^2 \Phi}{\partial n_{1v} \partial n_{2v}} = -\frac{1}{4\pi} \frac{n_2}{(1 - n_3)^2} \mathbf{I}
\end{aligned} \tag{172}$$

where \mathbf{I} is the unit tensor.

Appendix B: FFT method for convolutions

If the density components are periodic then the convolutions can be computed rapidly with FFT operations. Let f be a periodic function in a (possibly non-orthogonal) unit cell defined by lattice vectors $\mathbf{l}_x, \mathbf{l}_y, \mathbf{l}_z$ then f can be represented with a Fourier series

$$f(\mathbf{x}) = \sum_{\mathbf{k}} \hat{f}_{\mathbf{k}} e^{i\mathbf{x} \cdot \mathbf{k}} \tag{173}$$

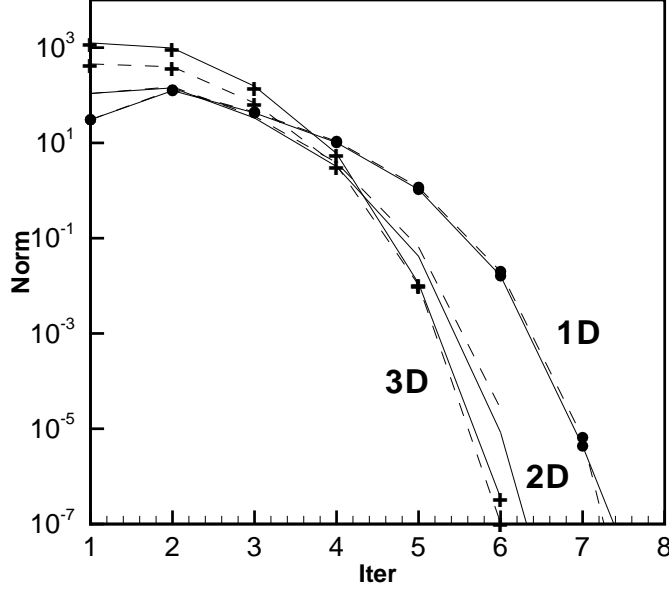


Figure 84. Convergence vs Newton-GMRES iteration for 1D, 2D, 3D problems. See 78, 79, 80

where \mathbf{k} is summed over points of the reciprocal space grid

$$\mathbf{k}(i_x, i_y, i_z) = i_x \mathbf{g}_x + i_y \mathbf{g}_y + i_z \mathbf{g}_z \quad (174)$$

Here the reciprocal lattice vectors are defined as $\mathbf{g}_x = \frac{2\pi}{V} \mathbf{l}_y \times \mathbf{l}_z$, etc., where V is the volume of the unit cell $\mathbf{l}_x \cdot \mathbf{l}_y \times \mathbf{l}_z$, and the sum occurs over all integers i_x, i_y, i_z . If we truncate the representation for $|i_x| \leq N/2$, etc. then the discrete Fourier transform (implemented with the FFT algorithm) can be used to transform to and from the representation on a real space grid

$$\mathbf{x}(q_x, q_y, q_z) = \frac{q_x}{N_x} \mathbf{l}_x + \frac{q_y}{N_y} \mathbf{l}_y + \frac{q_z}{N_z} \mathbf{l}_z \quad (175)$$

where q_x goes from 0 to $N_x - 1$, etc.

Inserting the representation of $f(x)$ into the convolution

$$\tilde{f}(r') = \int d^3 \mathbf{r} \omega(r - r') f(r) \quad (176)$$

we obtain the relation

$$\hat{\tilde{f}}_{\mathbf{k}} = \hat{\omega}(\mathbf{k}) \hat{f}_{\mathbf{k}} \quad (177)$$

where $\hat{\omega}_{\mathbf{k}}$ is the Fourier *transform* of ω :

$$\hat{\omega}(\mathbf{k}) = \int d^3 \mathbf{r} \omega(r) e^{-i\mathbf{r} \cdot \mathbf{k}}. \quad (178)$$

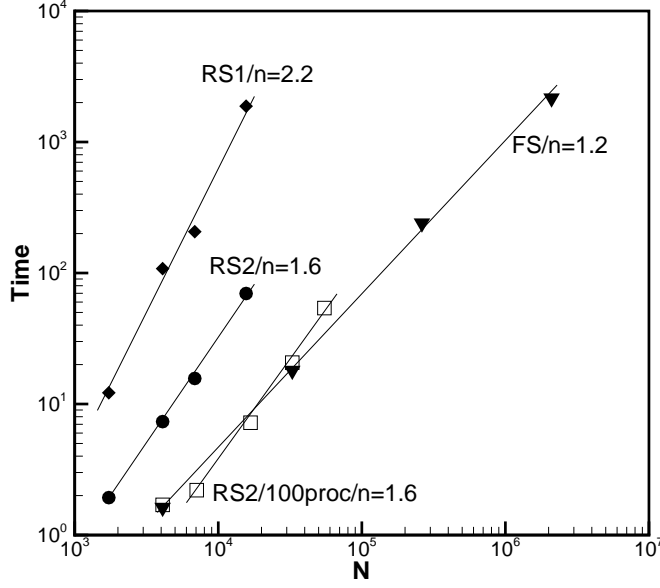


Figure 85. Performance scaling with respect to mesh density (fixed unit cell size) for a three dimensional problem.

Analytic expressions for $\hat{\omega}(\mathbf{k})$ are given above. We can use the FFT algorithm to compute $\hat{f}_{\mathbf{k}}$ even for a non-orthogonal unit cell, and the inverse algorithm can be used to convert the product back to the real-space mesh.

The evaluation of the weighted densities can therefore be accomplished with FFT operations using the real space grid representation of the densities together with the analytic expressions for $\hat{\omega}(\mathbf{k})$. There is one more important point to make here. Suppose we have N_w weight functions (10 for the Rosenfeld functional) and there are N_c density components. Then naively we might suppose that the evaluation of the weighted densities would require $N_w N_c$ transform operations. In fact they can be constructed with $N_w + N_c$ transforms.

This is accomplished by looping over the components. For each density component ρ_i we compute its FFT $\hat{\rho}_i$ and then add $\hat{\omega}_\alpha^c \hat{\rho}_i$ to \hat{n}_α . After the loop over components is complete we apply the inverse FFT to each \hat{n}_α to obtain the weighted densities on the real-space mesh.

As noted above, some care must be taken to perform convolutions with vector valued weight functions.

Interaction and wall potentials

The most commonly used interaction potential between two components i, j is the 12-6 Lennard-Jones (LJ) interaction potential given by

$$U_{ij}^{\text{lj}}(r) = 4\epsilon_{ij} \left(\left(\frac{\sigma_{ij}}{r} \right)^{12} - \left(\frac{\sigma_{ij}}{r} \right)^6 \right) \quad (179)$$

The interaction energy and diameter can be specified (symmetrically) for each pair of components or by means of Lorentz-Berthelot mixing rules which determine the interaction energy and diameter in terms of parameters specified for each component, thus $\sigma_{ij} = \frac{1}{2}(\sigma_i + \sigma_j)$ and $\epsilon_{ij} = \sqrt{\epsilon_i \epsilon_j}$ where ϵ_i and σ_i are the energy and diameter parameters associated with component i .

In order to use this interparticle potential as a mean field perturbation to the hard sphere fluid, we must somehow cut off the repulsive part of the potential at small r . In addition, to accurately treat the long range part of the potential at large r we must cut and shift the potential. We therefore take as the attractive potential the Weeks-Chandler-Anderson[15] split of a cut-and-shifted version of Eq. 179. We then have for the potential U_{ij}

$$U_{ij}(r) = \begin{cases} U_{ij}^{\text{lj}}(r_{\min}) - \Delta_{ij} & r \leq r_{\min} \\ U_{ij}^{\text{lj}}(r) - \Delta_{ij} & r_{\min} < r < r_{\text{cut}} \\ 0 & r \geq r_{\text{cut}} \end{cases} \quad (180)$$

where r_{\min} is defined by the minimum of U_{ij}^{lj} and r_{cut} is some suitable cutoff distance. The shift Δ_{ij} is given by $U_{ij}^{\text{lj}}(r_{\text{cut}})$ and should be small. The resulting function is continuous and has a finite range, but there is a small jump in the derivative at r_{cut} . The Fourier transform of this function is required for the computation of the residual and Jacobian operator; this is computed numerically on a fine one-dimensional mesh and then interpolated onto the problem mesh.

A Lennard-Jones potential can also be used to build a realistic representation of some environment that the fluid interacts with, by smearing the potential over a volume of interest. If this volume is taken to be a slab then we get a 9-3 potential

$$U(z) = 8\pi\epsilon \left(\frac{1}{90} \left(\frac{\sigma}{z} \right)^9 - \frac{1}{12} \left(\frac{\sigma}{z} \right)^3 \right) \quad (181)$$

where z here is the distance to the wall and ϵ, σ are defined as before in terms of parameters for a wall material and a fluid material. The potential inside the wall is infinite and very large just outside the wall; we handle this in the code by clamping the density to zero for $z < z_{\min}$.

This approach can be generalized to define boundary conditions of almost arbitrary complexity. If the potential defined by Eq. 179 is cut off by setting it to a constant for $r < r_{\text{cut}}$ then we can convolve it with a body shape defined by simple geometric primitives (e.g. slabs, cylinders, and spheres) using the FFT convolution method to define the external field for the problem.

For the calculations performed above we only have a single component. In units where $kT = 1$ and the hard sphere diameter is 1 we have $\epsilon = 4.7933$ and $\sigma = .562$. The parameters for the wall are $\epsilon_{\text{wall}} = 19.17$ and $\sigma_{\text{wall}} = .562$.

References

- [1] Laura J. D. Frink and Andrew G. Salinger. Two- and three-dimensional nonlocal density functional theory for inhomogeneous fluids i. algorithms and parallelization. *J. Comp. Phys.*, 159(2):407–424, 2000.
- [2] Laura J. D. Frink and Andrew G. Salinger. Two- and three-dimensional nonlocal density functional theory for inhomogeneous fluids ii. solvated polymers as a benchmark problem. *J. Comp. Phys.*, 159(2):425–439, 2000.
- [3] Laura J. D. Frink and Andrew G. Salinger. A state following algorithm for molecular theory. *J. Comp. Phys.*, To be published.
- [4] Laura J. D. Frink, Aidan Thompson, and Andrew G. Salinger. Applying molecular theory to steady-state diffusing systems. *J. Chem. Phys.*, 112(17):7564–7571, 2000.
- [5] L.J.D. Frink, A.G. Salinger, M.P. Sears, J.D. Weinhold, and A.L. Frischknecht. Numerical challenges in the application of density functional theory to biology and nanotechnology. *J. Phys. Cond. Matter*, to be submitted.
- [6] Douglas Henderson, editor. *Fundamentals of Inhomogeneous Fluids*. Marcel Dekker, 1992.
- [7] S.A. Hutchinson, L.B. Prevost, R.S. Tuminaro, and J.N. Shadid. Aztec user’s guide: Version 2.0. Technical report, Sandia National Laboratories, 1998.
- [8] E. Kierlik and M. L. Rosinberg. Free energy density functional for the inhomogeneous hard-sphere fluid: Application to interfacial adsorption. *Phys. Rev. A*, 42(6):3382–3387, 1990.
- [9] Frink L.J.D. and Salinger A.G. *J. Chem. Phys.*, 110:5969–5977, 1999.
- [10] Rocken P., Somoza A., Tarazona P., and Findenegg G. *J. Chem. Phys.*, 108:8689–8697, 1998.
- [11] Rocken P. and Tarazona P. *J. Chem. Phys.*, 105:2034–2043, 1996.
- [12] Yaakov Rosenfeld. Free energy model for the inhomogeneous hard-sphere fluid mixture and density functional theory of freezing. *Phys. Rev. Lett.*, 63(9):980–983, 1989.
- [13] Yaakov Rosenfeld. Free energy model for inhomogeneous fluid mixtures: Yukawa-charged hard spheres, general interactions, and plasmas. *J. Chem. Phys.*, 98(10):8126–8148, 1993.
- [14] Youcef Saad and Martin H. Schultz. Gmres: A generalized minimal residual algorithm for solving nonlinear linear systems. *SIAM J. Sci. Stat. Comp.*, 7(3):856–869, 1986.
- [15] J. D. Weeks and H. C. Anderson. *J. Chem. Phys.*, 54, 1971.

DISTRIBUTION:

1 MS 0321 Bill Camp, 9200	1 MS 0316 Susan Rempe, 9212
1 MS 0892 Julie Phillips, 1100	1 MS 0316 Shawn Means, 9212
1 MS 0892 John Vitko, 8100	1 MS 0316 Paul Crozier, 9235
1 MS 0887 Mike Cieslak, 1800	1 MS 0316 Mark Sears, 9235
1 MS 9951 Len Napolitano, 8100	1 MS 0316 Marcus Martin, 9235
1 MS 1135 Grant Heffelfinger, 1802	1 MS 0316 Harry Hjalmarson, 9235
1 MS 0318 Paul Yarrington, 9230	1 MS 1349 Frank van Swol, 1834
1 MS 1110 David Womble, 9210	1 MS 1349 John Curro, 1834
1 MS 0310 Robert Leland, 9220	1 MS 1349 Jeff Brinker, 1846
10 MS 0310 Danny Rintoul, 9210	1 MS 1415 Gary Grest, 1114
1 MS 1111 Bruce Hendrickson, 9215	1 MS 0839 Ron Pate, 16000
1 MS 0316 John Aidun, 9235	1 MS 0892 Susan Brozik, 1744
1 MS 0316 Sudip Dosanjh, 9233	1 MS 1413 Darryl Sasaki, 1141
1 MS 1411 Eliot Fang, 1834	1 MS 9018 Central Technical Files, 8945-1
1 MS 1413 Paul Dressendorfer, 1141	2 MS 0899 Technical Library, 9612
1 MS 9951 Joe Schoeniger, 8130	1 MS 0612 Review & Approval Desk, 9612
10 MS 0316 Laura Frink, 9212	3 MS 0161 Patent and Licensing Office, 4916
10 MS 1411 Mark Stevens, 1834	